International Journal of

Thermodynamics

International Centre for Applied Thermodynamics

Publishing Editor

Assoc. Prof. Dr. Abdussamet SUBASI   Assist. Prof. Mustafa Yasin GÖKASLAN

Res. Assist. Ali Murat BİNARK

Language Editor

Assoc. Prof. Dr. Abdussamet SUBASI

Journal Contacts

Editor-in-Chief

Prof. Dr. Lütfullah Kuddusi

ISTANBUL TECHNICAL UNIVERSITY

kuddusi@itu.edu.tr

+902122931300/2452

Department of Mechanical Engineering
Istanbul Technical University
Gumussuyu, 34437 Istanbul Turkey

CONTENTS

Research Article

Thermodynamic and Economic Optimization of Plate-Fin Heat Exchangers Using the Grasshopper Optimization Algorithm

[1]A. Farzin [ID], [2]*S. Mehran [ID], [3]K. Salmalian [ID]

[1,2,3] Department of Mechanical Engineering, Langarud Branch, Islamic Azad University, Langarud, Iran
E-mails: [2]*s_mehran@iaul.ac.ir

Abstract

The present study demonstrates the successful application of the grasshopper optimization algorithm (GOA) to the thermodynamic and economic modeling and optimization of cross-flow plate-fin heat exchangers with offset strip fins. To this end, the $\varepsilon - NTU$ method was played to determine the efficiency and pressure drop. Seven parameters, namely the exchanger length at hot and cold sides, number of hot-side layers, fin frequency, fin-strip length, fin thickness, and fin height, constitute the design parameters for the optimization of the heat exchanger. The efficiency of the heat exchanger, the entropy generation, and the total annual system cost were considered the objective functions. Accordingly, the optimization of each objective function was investigated separately. The efficiency and accuracy of the proposed algorithm were validated using two examples from the literature. Comparison between the obtained results and those in the previous studies indicates that GOA performed better in minimizing total annual cost and entropy generation and maximizing efficiency.

Keywords: Optimization, plate-fin heat exchanger, grasshopper optimization algorithm, total annual cost.

1. Introduction

In recent years, numerous modeling and optimization methods have been implemented in the design of different thermal systems.

A heat exchanger is a device used to recover thermal energy between two or more fluids maintained at different temperatures. The application of various types of heat exchangers is not limited to the chemical industry. They are important also in the food, mineral, power plant, electronic, air conditioning, and automotive industries in addition to household and other areas [1]. Plate-fin heat exchangers are a type of heat exchanger that is widely utilized in various industries due to their good heat transfer efficiency, compactness, and high reliability at high-volume and multi-flow applications [2]. Offset strip fins are among the most common fins used in these heat exchangers. Fig. 1 displays this type of fin. Offset strip fins possess more heat transfer efficiency than pin fins. Also, they are stronger and more reliable than perforated fins [3].

Numerous studies have addressed the optimal design of plate-fin heat exchangers as a result of their widespread application. The design of a plate-fin heat exchanger is a sophisticated process involving many geometric and operational parameters and trial and error methods to meet the thermal energy demand. The hot and cold side lengths, fin height, fin frequency, fin length, fin thickness, and the number of flow channels are the most significant parameters in the design of plate-fin heat exchangers. In these techniques, the operational and geometric parameters are selected in such a way as to meet specific goals in terms of outlet temperature, thermal load, and pressure drop.

In the recent decade, extensive research has been conducted on optimizing plate-fin heat exchangers via metaheuristic algorithms, such as genetic algorithm, particle swarm optimization, differential evolution, simulated annealing algorithm, imperialist competitive algorithm, artificial bee colony algorithm, biogeography-based optimization, and firefly algorithm. This research aimed at minimizing the total annual cost [4-8], maximizing thermal performance [9], minimizing pressure drop [10], increasing the heat transfer rate [11], minimizing the number of entropy generation units [12], minimizing the volume and weight of the plate-fin heat exchanger [13], minimizing the heat transfer surface [14], optimizing the number of flow layers [15], and optimizing the Fanning and Colburn factors [16]. Numerous researchers have attempted the multi-objective optimization of plate-fin heat exchangers given the differences in the mentioned objective [17, 18].

The present study employed the GOA to optimize a plate-fin heat exchanger and to minimize the total annual cost and entropy generation and maximize the efficiency, which is proportional to the total heat transfer surface area, pressure drop, and operating cost. The main objectives of this work are the optimization of the parameters affecting plate-fin heat exchangers, namely the fin height H at the hot and cold sides, fin thickness t at the hot and cold sides, fin frequency n, number of channels($N_c = N_h + 1$), heat exchanger length L, and fin length l, in order to reduce the total annual cost and entropy generation and increase the heat exchanger efficiency in addition to demonstrating the performance of GOA in this optimization.
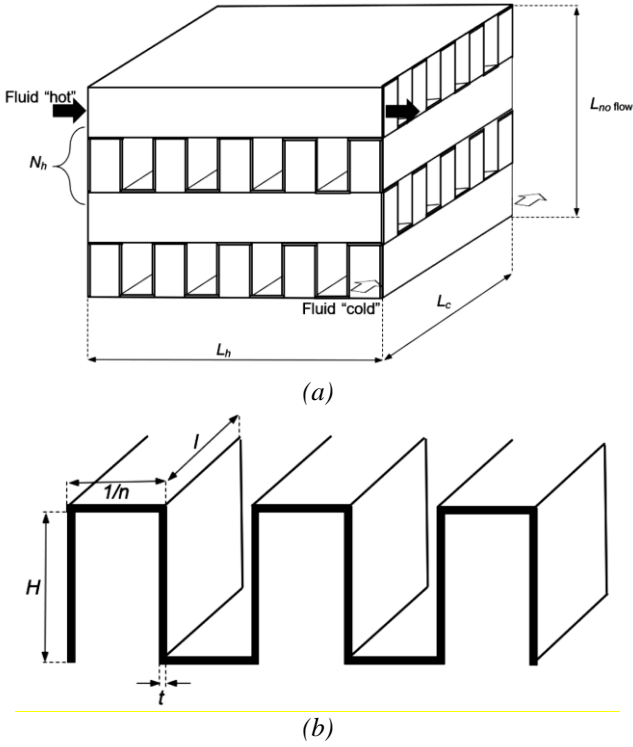
(a)

(b)

Figure 1. (a) View of the plate-fin heat exchanger and (b) the offset strip fin[10].

Based on the proposed method, a complete computer program has been developed in MATLAB Version 2017a for the design of plate-fin heat exchangers of the proposed algorithm. GOA has not been used so far to optimize plate-fin heat exchangers.

2. Mathematical Model

Fig.1 shows a view of a cross-flow plate-fin heat exchanger with offset strip fins of a rectangular cross section. In the analysis, the variation in the physical properties of the fluid with temperature is ignored and both fluids are assumed to behave as an ideal gas in order to simplify the equations. The rest of the assumptions are as follows [19]:

- The number of fin layers on the cold side is assumed to be one more than that on the hot side in order to minimize heat dissipation.
- The heat exchanger operates under stable conditions.
- The coefficient of heat transfer and the distribution are considered constant and uniform.
- The thickness of the plates is considered insignificant, and the thermal resistance and longitudinal heat transfer of the walls are assumed negligible.
- Fouling is negligibly small for a gas-to-gas heat exchanger. Hence, it is neglected.

The present study used the $\varepsilon - NTU$ method to analyze the heat exchanger sizing during optimization since the outlet fluid temperature was unknown. For a cross-flow heat exchanger with two unmixed flows, the rate of heat transfer is expressed as follows [19]:

$$Q = \varepsilon C_{min}(T_{h1} - T_{c1}) = m_h c_{ph}(T_{h1} - T_{h2}) = m_c c_{pc}(T_{c2} - T_{c1}) \quad (1)$$

where ε is the effectiveness of the heat exchanger, Cmin represents the minimum heat duty, and T_{h1} and T_{c1} denote the inlet temperature of the hot and cold fluids, respectively. For the efficiency [16],

$$\varepsilon = 1 - e^{\left(\left(\frac{1}{C_r}\right)NTU^{0.22}\left(e^{(-C_r NTU^{0.78})}-1\right)\right)} \quad (2)$$

In this equation, $C_r = \frac{C_{min}}{C_{max}}$, and the number of units of transfer units NTU is determined from Eq. (3) [16]:

$$\frac{1}{NTU} = C_{min}\left(\frac{Aff_h}{j_h Cp_h Pr_h^{-0.667} \dot{m}_h A_h} + \frac{Aff_c}{j_c Cp_c Pr_c^{-0.667} \dot{m}_c A_c}\right) \quad (3)$$

Moreover, Aff is the free flow area, A denotes the heat transfer surface area, j is the Colburn factor, Cp represents the heat duty, and Pr is the Prandtl number (Pr) for each of the cold and hot flows. For the free flow surface area for the plate-fin heat exchanger geometry [19]

$$Aff_h = (H_h - t_h)(1 - n_h t_h)L_c N_h \quad (4)$$

$$Aff_c = (H_c - t_c)(1 - n_c t_c)L_h N_c \quad (5)$$

where H, t, n, and L represent the fin height, fin thickness, fin frequency, and heat exchanger length, respectively, and N is the number of channels for each flow and is equal to $N_c = N_h + 1$ according to assumptions. Similarly, assuming identical geometry on both sides of the heat exchanger, the heat transfer surface areas are computed as follows [19].

$$A_h = L_h L_c N_h \left(1 + \left(2n_h(H_h - t_h)\right)\right) \quad (6)$$

$$A_c = L_h L_c N_c \left(1 + \left(2n_c(H_c - t_c)\right)\right) \quad (7)$$

Therefore, the total heat transfer surface area of the heat exchanger is expressed as follows:

$$A_{tot} = A_h + A_c \quad (8)$$

There exist numerous equations for evaluating the Colburn factor and the friction factor of offset strip fins. The equations by Manglik and Bergles [20] were used to calculate these factors:

$$j = 0.6522(Re)^{-0.5403}(\alpha)^{-0.1541}(\delta)^{0.1499}(\gamma)^{-0.0677}[1 + 5.3 \times 10^{-5}(Re)^{1.34}(\alpha)^{0.504}(\delta)^{0.456}(\gamma)^{-1.055}]^{0.1} \quad (9)$$

$$f = 9.6243(Re)^{-0.7422}(\alpha)^{-0.1856}(\delta)^{0.3053}(\gamma)^{-0.2659}[1 + 7.7 \times 10^{-7}(Re)^{4.429}(\alpha)^{0.920}(\delta)^{3.767}(\gamma)^{0.236}]^{0.1} \quad (10)$$

where Re is the Reynolds number (Re), $\alpha = {}^S\!/(H - t)$, $\delta = {}^t\!/_l$, $\gamma = {}^t\!/_s$, and $s = (1/n) - t$ denotes the inter-fin distance for the hot and cold flows. These equations hold for the ranges $120 < Re < 10^4$, $0.134 < \alpha < 0.997$, $0.134 < \delta < 0.997$, and $0.041 < \gamma < 0.121$ [20]. The equations for the Colburn and Fanning factors have 20% accuracy compared to the experimental results in the laminar, transient, and turbulence flow regimes. Therefore, there is no need for flow regime description for a given set of operational conditions, and these equations can be useful in most applications [20]. Re is calculated as follows:

$$Re = \frac{Gdh}{\mu} \qquad (11)$$

where $G = \frac{\dot{m}}{Aff}$ represents the mass flux of the flow. The hydraulic radius dh for calculating Re is defined as follows [19]:

$$dh = \frac{4s(H-t)l}{2(sl+(H-t)l+t(H-t))+ts} \qquad (12)$$

In addition, the viscous pressure drop for both hot and cold fluids is obtained as follows [19]:

$$\Delta P = \frac{2fLG^2}{\rho dh} \qquad (13)$$

Considering the Colburn factor, the coefficient of heat transfer is expressed as follows [19]:

$$h = jC_P GPr^{-\frac{2}{3}} \qquad (14)$$

For the no-flow length [18]:

$$L_{no\,flow} = H - 2t_P + N_h(2H + 2t_P) \qquad (15)$$

Based on Bejan's method [19], the entropy generation method is determined from the temperature and pressure as follows:

$$\dot{S} = \dot{m}_h\left[c_{ph}ln\left(\frac{T_{h2}}{T_{h1}}\right) - R_h ln\left(\frac{P_{h2}}{P_{h1}}\right)\right] + \dot{m}_c\left[c_{pc}ln\left(\frac{T_{c2}}{T_{c1}}\right) - R_c ln\left(\frac{P_{c2}}{P_{c1}}\right)\right] \qquad (16)$$

where T_{h2}, T_{c2}, P_{h2}, and P_{c2} are the outlet temperatures and pressures of the hot and cold flows, respectively, and can be determined based on the efficiency of the heat exchanger [16]:

$$\varepsilon = \frac{c_h(T_{h1}-T_{h2})}{c_{min}(T_{h1}-T_{c1})} = \frac{c_c(T_{c2}-T_{c1})}{c_{min}(T_{h1}-T_{c1})} \qquad (17)$$

Accordingly,

$$T_{h2} = T_{h1} - \varepsilon\frac{c_{min}}{c_h}(T_{h1} - T_{c1}) \qquad (18)$$

$$T_{c2} = T_{c1} + \varepsilon\frac{c_{min}}{c_c}(T_{h1} - T_{c1}) \qquad (19)$$

Also, for the outlet fluid pressures,

$$P_{h.2} = P_{h.1} - \Delta P_h \qquad (20)$$

$$P_{c.2} = P_{c.1} - \Delta P_c \qquad (21)$$

3. Optimization Technique

The minimization or maximization of a specific objective function is called optimization. The optimization process is applicable in various fields of science. To solve the optimization problem, different steps must be done. In the first step, the parameters of the problem must be determined. Based on the nature of the parameters, the problem is divided into two categories, discrete or continuous. In the second step, the restrictions that must be applied on the parameters are identified. In the third step, the purpose of the given problem should be examined. In this case, optimization problems are classified into single-objective and multi-objective problems. Finally, based on the type of known parameters, constraints, and number of objectives, a suitable optimizer should be selected to solve the problem in question.

Meta-heuristic optimization algorithms are of great interest in engineering applications; Because they: (i) rely on relatively simple concepts and their implementation is easy; (ii) do not require variable information; (iii) they can bypass the desired local state; (iv) They can be used in a wide range of problems in different fields.

Meta-heuristic algorithms inspired by nature solve optimization problems by imitating biological and physical phenomena. They can be divided into three main categories: evolutionary based, physics based and swarm based methods. Evolutionary methods are inspired by the laws of natural evolution. The search process starts with a randomly generated community and evolves in subsequent generations. The strength of these methods is that the best members always combine with each other to form the next generation. This causes the population to be optimized during the next generations. The most famous evolutionary method is the genetic algorithm (GA)[21], which simulates Darwinian evolution. Physics-based methods imitate the physical laws in the world. The most famous algorithms are: simulated refrigeration (SA)[22], gravitational search algorithm (GSA)[23], central force optimization (CFO)[24] and curved space optimization (CSO)[25]. The third group of methods inspired by nature includes swarm-based techniques that imitate the social behavior of groups of animals. The most famous algorithm is particle swarm optimization, which was first created by Kennedy and Eberhart[26].

Among the stochastic optimization methods, population-based algorithms inspired by nature are the most popular. These methods mimic the problem solving methods found in nature that are often used by living organisms. Surviving is the main goal for all creatures in nature. To achieve this goal, living organisms are evolving and adapting themselves in various ways. In general, crowding-based algorithms have advantages over evolution-based algorithms. For example, swarm-based algorithms preserve information about the search space in subsequent iterations, while evolutionary-based algorithms lose all information as soon as a new population is formed. These methods usually include fewer operators compared to evolutionary approaches (selection, intersection, mutation, elitism, etc.) and hence their implementation is easier.

GOA was employed to solve the heat exchanger optimization problem. Grasshoppers are known as agricultural pests with eleven thousand species found in nature. As seen in Fig.2, a grasshopper moves through egg, nymph, and adult phases in its life cycle.
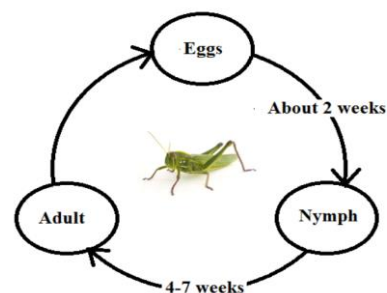

Figure 2. Life cycle of grasshoppers [27].

GOA is a metaheuristic optimization technique and is categorized as a swarm intelligence algorithm based on an initial population similar to particle swarm optimization (PSO). The mathematical model used to simulate grasshopper behavior is as follows [27]:

$$X_i = S_i + G_i + A_i \qquad (22)$$

In the above equation, X_i, S_i, G_i, and A_i are the position, social interaction, gravity force, and wind advection, respectively, of the ith grasshopper. To create random behavior, Eq. (22) can be expressed as follows [27]:

$$X_i = r_1 S_i + r_2 G_i + r_3 A_i \qquad (23)$$

where the coefficients r1, r2, and r3 are random numbers between zero and one. Social interaction represents one of the principal concepts in the behavior of grasshoppers and is expressed as follows [27]:

$$S_i = \sum_{\substack{i=1 \\ j \neq i}}^{N} s(d_{ij}) \, \hat{d}_{ij} \qquad (24)$$

In this equation, d_{ij} is the distance between the ith and jth grasshopper and is calculated as $d_{ij} = |X_j - X_i|$, and $\hat{d}_{ij} = \frac{(X_j - X_i)}{d_{ij}}$ is a unit vector connecting the ith to the jth grasshopper is a function determining the social interaction strength and expresses the effect on the social interaction (attraction and repulsion). It is calculated as follows [27]:

$$s(r) = f e^{\frac{-r}{l}} - e^{-r} \qquad (25)$$

where f represents the intensity of attraction, and l is the attractive length scale. Changes in these parameters lead to social behaviors in artificial grasshoppers and significantly change the comfort, attraction, and repulsion zones. The gravity force in Eq. (22) is calculated as follows [27]:

$$G_i = -g \hat{e}_g \qquad (26)$$

In this equation, g is the gravitational constant, and $\hat{e}_g$ denotes a unit vector toward the center of the Earth. For the direction of wind advection [27]

$$A_i = u \, \hat{e}_\omega \qquad (27)$$

where u is the drift constant, and $\hat{e}_\omega$ denotes a unit vector in the wind direction. Accordingly, Eq. (22) can be expanded as follows [27]:

$$X_i = \sum_{\substack{j=1 \\ j \neq i}}^{N} s(|X_j - X_i|) \frac{(X_j - X_i)}{d_{ij}} - g \hat{e}_g + u \, \hat{e}_\omega \qquad (28)$$

where N represents the number of grasshoppers. Eq (28) is able to simulate a swarm of grasshoppers in 2D, 3D, and hyper dimensional spaces. Given that the grasshoppers reach the comfort zone rapidly and do not converge to a point, this model cannot be directly used to solve optimization algorithms. For this reason, the practical model of Eq. (28) is presented as follows [27]:

$$X_i^d = c \left(\sum_{\substack{j=1 \\ j \neq i}}^{N} c \frac{ub_d - lb_d}{2} s(|X_j^d - X_i^d|) \frac{(X_j - X_i)}{d_{ij}} \right) + \hat{T}_d \qquad (29)$$

lb_d and ub_d represent the upper and lower bounds in the dth dimension, and $\hat{T}_d$ is the value of the best solution in the dth dimension up to a given iteration. c is a decreasing constant and maintains a balance between exploitation and exploration. At first, since the first term in Eq. (29) (exploration term) must be given more weight, c are large. They are gradually reduced and guided toward the best solution. The factor c is updated according to the following equation [27]:

$$c = c_{max} - l \frac{c_{max} - c_{min}}{L} \qquad (30)$$

where, in this study, the highest value c_{max} equals 1, and the lowest value c_{min} equals 0.00001. Moreover, l is the current iteration number, and L denotes the maximum number of iterations in the algorithm. Fig. 3 depicts the steps of GOA, and Fig. 4 represents the block diagram of this algorithm [27].
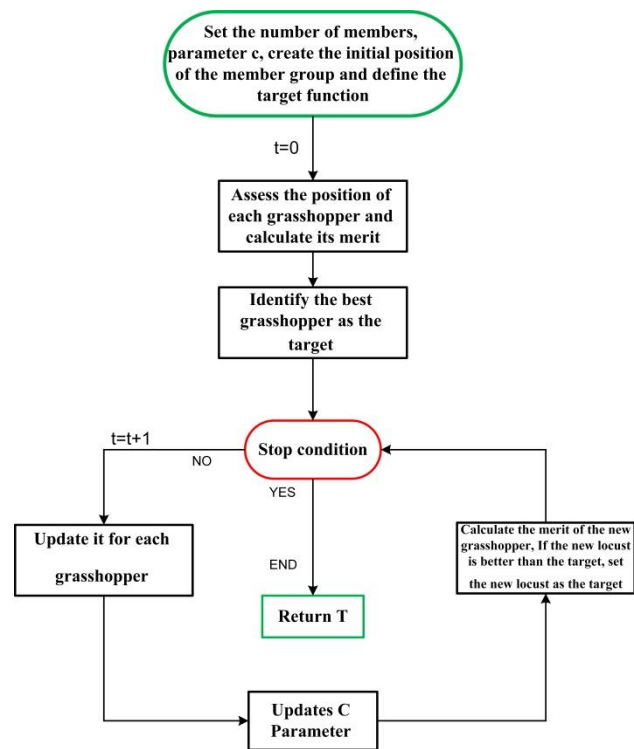
Figure 3. Flowchart of GOA [27].

Step1: Initialize the parameters of algorithm ;
Step2: Produce the population of grasshopper randomly ;
Step3: Assess the position of each grasshopper and calculate its merit ;
Step4: Identify the best grasshopper as the target ;
Step5: Repeat Steps 6 to 12 until the stop condition is established ;
Step6: Repeat steps 7 to 11 for each grasshopper ;
Step7: $c = c_{max} - l \frac{c_{max} - c_{min}}{L}$;
Step8: Update the value of c ;
Step9: Update it for each grasshopper ;
Step10: Calculate the merit of the new grasshopper ;
Step11: If the new grasshopper's merit is better than the target, set the new grasshopper as the target ;
Step12: If the stop condition is not met, go to step 5, otherwise go to end ;
Step13: End

Figure 4. Block diagram of GOA [27].

Hence, based on the presented flowchart, first, the decision parameters and the corresponding region are

specified according to Table 1. Subsequently, the parameters related to GOA are defined. In the present study, the stop criterion is the number of iterations, which is different in different study cases. 18 grasshopper groups were considered for the design of the plate-fin heat exchangers based on the 6 design variables. c is a decreasing constant and maintains a balance between exploitation and exploration. As mentioned previously, for the present work, the highest value c_{max} is equal to 1, while the lowest value c_{min} is equal to 0.00001.

In the next step, the position and cost function value are randomly specified for all the grasshoppers. This equation states that the next position of a grasshopper is determined by its present position, target position, and the positions of all other grasshoppers. The first term in this equation is the current position of the grasshopper based on those of the other grasshoppers. In other words, the positions of all the grasshoppers are considered for defining the positions of the search agents around the target. In short, the first part of the equation simulates the interaction between grasshoppers in nature, while the second part simulates their tendency to move toward the source.

In PSO, there are two vectors for each particle: the position vector and the velocity vector. The positions of the particles are updated according to their current positions, best personal experience, and best global experience. However, in GOA, there is only a position vector for each search agent, which is optimized based on its current position, best global solution, and the positions of other grasshoppers. This means that all the search agents are involved in determining the next position of every search agent. Based on Eq. (30), c is updated in the first step of each iteration. The first adaptive parameter, c, in Eq. (29) decreases the displacements of the grasshoppers around the target. In other words, this parameter strikes a balance between exploration and exploitation around the target and reduces the search space around the target with the aim of increasing the number of iterations in the algorithm. C is a decreasing coefficient to shrink the comfort zone, repulsion zone, and attraction zone.

In the next step, the objective function $\hat{T}_d$ is updated after all the members are evaluated. Based on previous discussions, the mathematical model of the algorithm requires the grasshoppers to converge gradually to the target over the iterations. In the actual search space, there is no target, and the global optimal position, i.e., the main target, is unknown. Thus, one target is found for the grasshoppers in each optimization step. This helps GOA to store the most promising target in the search space in each iteration and to require the grasshoppers to move toward this target. This is done with the hope of finding a better and more accurate target as the best approximation of the global optimal in the search space.

4. Objective Function and Design Parameters

The first step in optimization is to introduce the objective function and the problem. Identifying the objective functions and detecting their dependence on different variables is one of the most important optimization steps.

The present study addresses the single-objective optimization of the heat exchanger and seeks three objectives. The first objective is economic and aims to minimize the total annual cost, the second objective aims to reduce the number of entropy generation units, and the third

objective aims to increase the efficiency based on Eq. (2). For the cost objective function, the sum of the operational and capital (fixed) costs is considered the annual cost. The capital cost is related to the heat transfer surface area, while the operating cost is related to the electricity cost of the compressors. Cost estimation is performed in the same manner as in [15]:

$$C_{in} = A_f . C_A . A_{tot}^{n_1} \tag{31}$$

$$C_{op} = \frac{k_{el}\tau}{\eta} \left[\frac{\Delta P_h m_h}{\rho_h} + \frac{\Delta P_c m_c}{\rho_c} \right] \tag{32}$$

$$TAC = C_{in} + C_{op} \tag{33}$$

where A_f is the annual cost factor and is determined as follows:

$$A_f = \frac{r}{1 - (1+r)^{-y}} \tag{34}$$

All the factors corresponding to the calculation of the total cost are presented in Table 1 [15]. Simplifying Eq. (16)-(21), one may write the following for the entropy growth rate as the objective function

$$N_s = \frac{C_h}{C_{max}} \left[ln \left(1 - \varepsilon \frac{C_{min}}{C_h} \left(1 - \frac{T_{c1}}{T_{h1}} \right) \right) - \frac{R_h}{C_{Ph}} ln \left(1 - \frac{\Delta P_h}{P_{h1}} \right) \right] +$$
$$\frac{C_c}{C_{max}} \left[ln \left(1 + \varepsilon \frac{C_{min}}{C_c} \left(\frac{T_{h1}}{T_{c1}} - 1 \right) \right) - \frac{R_c}{C_{Pc}} ln \left(1 - \frac{\Delta P_c}{P_{c1}} \right) \right] \tag{35}$$

Table 1. Cost parameters for the plate-fin heat exchanger [15].

Parameters for total cost	
Cost per unit arrea, $C_A \left[\$/m^2 \right]$	90
Hourrs of operation, $\tau [hour]$	5000
Electricity price, $k_{el} \left[\$/MWh \right]$	20
Compressor efficiency, η	60%
Exponent of non linear increase with area increase, n_1	0.6
Depreciation time, $y[year]$	10
Inflation rate, r	0.1

Based on the relationship between the objective function and the other equations (dependence on the surface area and pressure drop on the cold and hot sides), they can be considered as follows:

$$Cost\ Function = f(H . t . n . N . L . l) \tag{36}$$

As can be observed, the objective function is a function of fin height, fin thickness, fin frequency, fin length, number of flow channels, and heat exchanger length and cannot be solved analytically. In other words, the objective function is not differentiable (i.e., does not have a closed-form solution); hence, metaheuristic algorithms must be used to approach the optimal solution. Metaheuristic algorithms explore using trial and error. One of their main features is approaching the optimal solution in the search space by managing the search process.

5. Decision Variables and Constraints

The decision variables of the present study are the design variables of the plate-fin heat exchanger, namely the cold- and hot-side fin height H, the cold- and hot-side fin

thickness t, the fin frequency n, the number of channels for each flow $N_c = N_h + 1$, the heat exchanger length L, and the fin length l. These variables are displayed in Fig. 1 and presented in Table 2 according to [15].

Table 2. Range of variation of the design variables [15].

Parameter	Lower	Upper
Hot side flow length, $[m]$	0.1	1
Cold side flow length, $[m]$	0.1	1
Fin height, $[m]$	0.002	0.01
Fin thickness, $[m]$	0.0001	0.0002
Fin frequency	100	1000
Fin offset length, $[m]$	0.001	0.01
Number of hot side layers	1	200

6. Case Studies

Two case studies were used from the literature to examine the applicability of the proposed algorithm. The first was adopted from Shah et al. [3] and the second from Kakac [19]. The first case study involves a cross-flow gas-air heat exchanger with a heat duty of 1069.8 kW, which was designed separately for minimizing the entropy generation unit and the total annual cost. The other performance specifications and the flow thermophysical properties are shown in Table 3. The second case study involves a cross-flow gas-air heat exchanger with a heat duty of 3300 kW, which was designed separately for minimizing the entropy generation unit and maximizing the efficiency.

Table 3. Performance specifications of the case studies.

Parameters	Case Study A[3]		Case Study B[19]	
	Hot Side	Cold Side	Hot Side	Cold Side
Mass flow rate, $\left[kg/s\right]$	1.66	2	25.4	25
Inlet temperature, [°C]	900	200	460	300
Inlet pressure, $[kPa]$	160	200	100	900
Specific heat, $\left[J/kg.K\right]$	1122	1073	1060	1060
Density, $\rho \left[kg/m^3\right]$	0.6296	0.9638	0.54	4.86
Dynamic viscosity, $\mu \left[kg/ms\right]$	4.01E-5	3.36E-5	3.2E-5	3.2E-5
Prandtl number, Pr	0.731	0.694	0.69	0.69
Maximum pressure drop, $\Delta P [kPa]$	9.5	8	7.5	4.5

7. Results and Discussion
7.1 Minimization of Entropy Generation in the First Case Study

For the first case, a preheater cross-flow heat exchanger with exhaust gases as the hot fluid and air as the cold fluid (both single-pass) was considered. In fact, the air entering the furnace is heated by the exhaust gases discharged to the environment, after which the air and the gases exit the heat exchanger and higher and lower temperatures, respectively. The air exiting the heat exchanger constitutes the furnace inlet. The fin type used for the heat exchanger is rectangular, and the heat exchanger is made of aluminum. Based on Eq. (35), heat transfer and pressure drop generate entropy. The entropy generation minimization results are displayed in Table 4.

Fig. 5 displays the graph of entropy convergence as the objective function. A significant reduction was observed in the objective function after 20 iterations. The changes in the objective function became relatively small after about 80

iterations. The minimum entropy generation by the plate-fin heat exchanger appeared after 180 iterations.

Table 4. Optimal entropy generation results in the first case study.

Parameters	Preliminary design[3]	ICA[28]	BA[11]	FOA[10]	GOA
L_h , $[m]$	0.3	1	0.997	0.9	0.998
L_c , $[m]$	0.3	0.88	0.94	1	0.9975
H , $[mm]$	2.49	5	8.33	8.6	2.51
n , $\left[fin/m\right]$	782	240	25702	256.2	987
t, $[mm]$	0.1	0.19	0.166	0.1	0.19981
l, $[mm]$	3.18	9.6	9.51	7.2	3.27
N_h	167	77	56	53	181
ΔP_h , $[kPa]$	9.34	1.23	0.741	0.656	9.4235
ΔP_c , $[kPa]$	6.9	0.67	0.46	0.589	6.5563
$L_{no\ flow}$, $[m]$	1	0.87	0.997	0.967	0.983
ε	-	0.821	0.826	0.827	0.9573
N_s	0.1576	0.137	0.134	0.133	0.1297
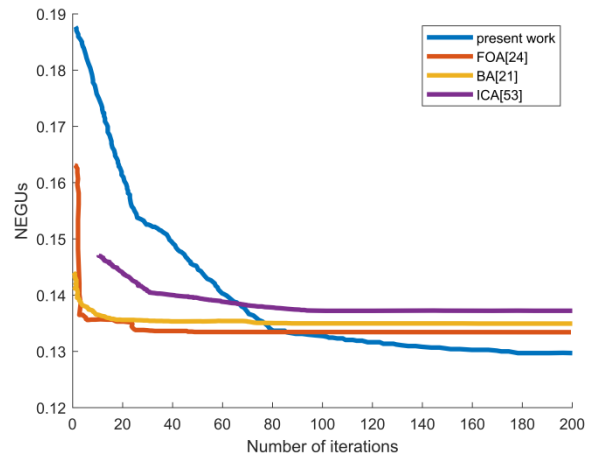
Figure 5. Graph of entropy convergence as the objective function in the first case study.

As seen in the figure, a 17% reduction in entropy generation was achieved by the optimization method compared to the initial design. It was observed that the fin frequency increased and almost reached its maximum value in minimizing the design entropy.

7.2 Minimization of the Total Cost in the First Case Study

The minimization results of the total annual cost for the first case study are displayed in Table 5. Moreover, Fig. 6 displays the graph of the general cost as the objective function. A significant reduction in the objective function was obtained at the beginning of the evaluation (after 10 iterations). Furthermore, the objective function stopped changing after 90 iterations.

7.3 Minimization of Entropy Generation in the Second Case Study

The aim of entropy optimization in heat exchangers is to achieve minimum dissipation of the available energy. A heat exchanger operates based on the temperature difference between two fluids flowing in adjacent channels.

The flowing of the two fluids causes a pressure drop in the channels. The principal mechanisms of exergy destruction, or entropy generation, are heat transfer and pressure drop, which are inevitable in heat exchangers. These devices operate in such a way that a decrease in one leads to an increase in the other.
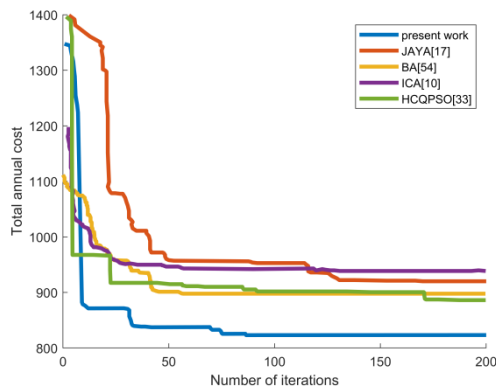
Figure 6. Convergence graph of the total annual cost as the objective function in the first case study.

Table 5. Optimal total cost results in the first case study.

Parameters	BBO [29]	Jaya[6]	BA [30]	HCQPSO[15]	GOA
L_h , $[m]$	0.793	0.84281	0.756	0.6	0.678
L_c , $[m]$	1	1	0.934	0.64	0.784
H , $[mm]$	10	10	9.84	9.06	8.56
n , $\left[{fin}/{m}\right]$	218	198.08	227.73	299.66	243
t , $[mm]$	0.2	0.19881	0.192	0.155	0.192
l , $[mm]$	7	4.9359	7.77	9.2	8.95
N_h	74	71	72	64	86
ΔP_h , $[kPa]$	0.269	0.30019	0.298	0.582	0.3052
ΔP_c , $[kPa]$	0.325	0.32212	0.343	0.48	0.3027
$L_{no\ flow}$, $[m]$	-	-	1.499	1.23	1.5
ε	0.820544	0.82055	-	-	0.82862
Investment cost, $\left[{\$}/{year}\right]$	692.99	672.34	647.1	464.89	584.45
Operation cost, $\left[{\$}/{year}\right]$	230.6	243.32	250.56	423.10	238.8
Total annual cost	923.59	915.66	897.65	888	823.25

In this section, the objective is to find the optimal ratio of these two mechanisms in heat exchangers such that entropy generation during the process is minimized. To this end, factors such as the heat transfer surface area, heat exchanger dimensions, flow rates of the two fluids, heat transfer surface distribution along the heat exchanger, and pressure drop in the heat exchanger are influential. The entropy generation minimization results for the second case study are displayed in Table 6.

7.4 Efficiency Increase in the Second Case Study

The effectiveness of a heat exchanger ε is a measure of its performance and is defined as the ratio of the actual to the ideal heat transfer. In other words, ε expresses the effective thermodynamic performance specifications of the heat exchanger. This parameter is a function of the flow configuration, the ratio of heat capacities, and the number of heat transfer units. The results of maximizing the effectiveness in the second case study are shown in Table 7.

Table 6. Optimal entropy generation results in the second case study.

Parameters	PSO [31]	GA [32]	BA [30]	GOA
L_h , $[m]$	0.925	0.994	0.995	1.216
L_c , $[m]$	0.996	0.887	0.995	2.297
H , $[mm]$	9.98	9.43	9.99	9.85
n , $\left[{fin}/{m}\right]$	0.1	534.9	405.69	412
$t[mm]$	0.1	534.9	405.69	412
$l[mm]$	9.8	63	9.998	9.54
N_h	10	8	10	76
ΔP_h , $[kPa]$	3.331	5.287	1.75	7.408
ΔP_c , $[kPa]$	1.834	2.216	1.143	4.236
$L_{no\ flow}$, $[m]$	0.214	0.169	0.218	1.5297
ε	0.8327	0.8277	0.832	0.7886
N_s	0.053028	0.063332	0.052886	0.040045

Table 7. Optimal efficiency results in the second case study.

Parameters	Preliminary design [3]	BA [30]	GOA
L_h , $[m]$	0.9	1.654	1.5892
L_c , $[m]$	1.8	2.99	2.9973
H , $[mm]$	5.7	5.72	7.88
n , $\left[{fin}/{m}\right]$	500	388.9	473.92
$t[mm]$	0.15	0.169	0.1202
$l[mm]$	6	8.57	9.9638
N_h	149	165	124.47
ΔP_h , $[kPa]$	15	7.5	5.4505
ΔP_c , $[kPa]$	10	3.38	2.4361
$L_{no\ flow}$, $[m]$	1.79	1.99	1.9992
ε	0.778	0.83	0.85574

8. Conclusion

This study presents the successful application of a new algorithm for the optimal design of plate fin heat exchangers. This algorithm is used in most thermal engineering problems that consist of several discrete and continuous variables and a large amount of discontinuity in the objective function.

This algorithm can be employed in most thermal engineering problems involving a large number of discrete and continuous variables. Identifying the objective functions and their dependence on various variables is among the most important optimization steps. Based on applications, seven design parameters were considered to be the optimization variables. Moreover, the $\varepsilon - NTU$ method was utilized for the thermal analysis of the plate-fin heat exchanger. Two case studies were adopted from the literature to validate the accuracy of this algorithm. The results for the total annual cost, entropy generation, and efficiency objective functions indicated the superior performance of GOA compared to the original design and the higher accuracy of GOA compared to other algorithms in converging to the optimal solutions over a given number of iterations. The following conclusions may be drawn from the results:

- The findings demonstrate that the results attained from the GOA are better than the preliminary design considering the respected objective function.
- Grasshoppers effectively explore the promising regions in a given search space.

- Grasshoppers encounter large variations in the initial optimization steps, which helps them search the space more thoroughly.
- Grasshoppers tend to move locally in the final optimization step, which allows them to exploit the search space.
- GOA increases the merit of the members, indicating that this algorithm can effectively improve the merit of the initial random population.
- The target merit increased over iterations, demonstrating that the global optimal approximation becomes more accurate in proportion to the number of iterations.
- As a result, in order to optimally design of heat exchangers by using meta-heuristic algorithms with regard to searching for promising areas, exploiting the entire search space and increasing the competence of members, this method can be considered as a suitable method.

Nomenclature

A	heat exchanger surface area, $[m^2]$
A_f	annual cost factor
A_{ff}	free flow area, $[m^2]$
C	heat capacity rate, $[W/k]$
C_A	cost per unit arrea, $[\$/m^2]$
C_p	specific heat, $[J/kg.K]$
C_r	$\dfrac{C_{min}}{C_{max}}$
C_{op}	operational cost
C_{in}	capital cost
d_h	hydraulic diameter, $[m]$
f	fanning friction factor
$f(x)$	objective function
G	mass flux velocity, $[kg/m^2s]$
GOA	grasshopper optimization algorithm
h	convective heat transfer coefficient, $[W/m^2k]$
H	height of fin, $[m]$
j	Colburn factor
K_{le}	electricity price
l	interrupted length of serrated fin, $[m]$
l_f	lance length of the fin, $[m]$
L	heat exchanger length, $[m]$
m	mass flow rate (kg/s)
n	fin frequency, $[fin/m]$
n_1	exponent of non linear increase with area increase
N_c, N_h	number of fin layers for fluid c and h
N_s	number of entropy generation units (EGU)
NTU	number of transfer units
P	pressure, $[kPa]$
Pr	Prandtl number
Q	heat duty, $[W]$
r	inflation rate
R	specific gas constant, $[J/kg.K]$
Re	Reynolds number
s	fin spacing, $[m]$

$\dot{S}$	rate of entropy generation, $[W/K]$
t	fin thickness, $[m]$
T	Temperature, $[K]$
$T_{h,c}$	outlet and inlet temperatures of the hot and cold flows, $[K]$
TAC	cost objective function
U	overall heat transfer coefficient, $[W/m^2k]$

Greek symbols

μ	viscosity
ρ	density
ε	effectiveness
Δp	Pressure drop
ΔS	entropy difference, $[W/kgK]$
τ	hourrs of operation
γ	t/s
η	compressor efficiency
α	$s/(H-t)$
δ	t/l

Subscripts

c , h	fluid *cold* and hot
1	inlet
2	outlet
max	maximum
min	minimum

References:

[1] A. Farzin, M. Ghazi, A. F. Sotoodeh, M. Nikian, "Economic optimization of heat exchanger networks based on geometric parameters using hybrid genetic-particle swarm algorithm technique", *J. Eng. Des. Tech., 19,* 989-1015, 2021.

[2] P.K. Das, I. Ghosh, "Thermal design of multistream plate fin heat exchangers—a state-of-the-art review", *Heat Trans. Eng., 33,* 284-300, 2012.

[3] R.K. Shah, D.P. Sekulic, *Fundamentals of heat exchanger design*, Hoboken, New Jerse: John Wiley & Sons, Inc., 2003.

[4] X. Zheng, Z. Qi, "A comprehensive review of offset strip fin and its applications", *Appl. Therm. Eng., 139*, 61-75, 2018.

[5] A. Farzin, M. Ghazi, A. Sotoodeh, M. Nikian, "Economic optimization of heat exchangers network based on accuracy design of equipment using whale algorithm", *J. Eng. Des. Tech., 19*, 989-1015, 2021.

[6] R.V. Rao, A. Saroj, P. Ocloń, J. Taler, D. Taler, "Single-and multi-objective design optimization of plate-fin heat exchangers using Jaya algorithm", *Heat Trans. Eng., 39*, 1201-1216, 2018.

[7] R. Song, M. Cui, "Single-and multi-objective optimization of a plate-fin heat exchanger with offset strip fins adopting the genetic algorithm", *Appl. Therm. Eng., 159*, 113881, 2019.

[8] E. Işık, M. Inallı, "Artificial neural networks and adaptive neuro-fuzzy inference systems approaches to forecast the meteorological data for HVAC: the case of cities for Turkey", *Energy, 154*, 7-16, 2018.

[9] K.C. More, R.V. Rao, "Design optimization of plate-fin heat exchanger by using modified Jaya algorithm", *Advanc. Eng. Optim. Thro. Intell. Techn. Proceedings of AEOTIT,* 165-172. 2020.

[10] E.H.V. Segundo, V.C. Mariani, L. Coelho, "Design of heat exchangers using falcon optimization algorithm", *Appl. Therm. Eng., 156*, 119-144, 2019.

[11] H. Zarea, F.M. Kashkooli, A.M. Mehryan, M.R. Saffarian, E.N. Beherghani, "Optimal design of plate-fin heat exchangers by a Bees Algorithm", *Appl. Therm. Eng., 69*, 267-277, 2014.

[12] X. Peng, Z. Liu, C. Qiu, J. Tan, "Effect of inlet flow maldistribution on the passage arrangement design of multi-stream plate-fin heat exchanger", *Appl. Therm. Eng.,* 103, 67-76, 2016.

[13] R.V. Rao, A. Saroj, "A self-adaptive multi-population based Jaya algorithm for engineering optimization", *Swarm. Evol. comput., 37*, 1-26, 2017.

[14] K. Guo, N. Zhang, R. Smith, "Optimisation of fin selection and thermal design of counter-current plate-fin heat exchangers", *Appl. Therm. Eng., 78*, 491-499, 2015.

[15] O.E. Turgut, "Hybrid chaotic quantum behaved particle swarm optimization algorithm for thermal design of plate fin heat exchangers", *Appl. Math. Mod., 40,* 50-69, 2016.

[16] Z. Wang and Y. Li, "A combined method for surface selection and layer pattern optimization of a multistream plate-fin heat exchanger", *Appl. Energy, 165*, 815-827, 2016.

[17] J. Wen, K. Li, X. Zhang, C. Wang, S. Wang, J. Tu, "Optimization investigation on configuration parameters of serrated fin in plate-fin heat exchanger based on fluid structure interaction analysis", *Int. J. Heat Mass Trans.,119*, 282-294, 2018.

[18] H. Hajabdollahi, "Multi-objective optimization of plate fin heat exchanger using constructal theory", *Int. J. Heat Mass Trans., 108*, 104283, 2019.

[19] S. Kakaç, H. Liu, A. Pramuanjaroenkij, *Heat Exchangers: Selection, Rating, and Thermal Design,* 3rd *Ed*. Boca Raton: CRC press, 2020.

[20] R.M. Manglik A.E. Bergles, "Heat transfer and pressure drop correlations for the rectangular offset strip fin compact heat exchanger", *Exp. Therm. Fluid Sci., 10*, 171-180, 1995.

[21] J.H. Holland, "Genetic Algorithms", *Sci. Americ., 267*, 66-73, 1992. [Online]. Available: http://www.jstor.org/stable/24939139.

[22] V. Černý, "Thermodynamical approach to the traveling salesman problem: An efficient simulation algorithm", *J. Opt. Theor. Applic., 45*, 41-51, 1985/01/01 1985, doi: 10.1007/BF00940812.

[23] E. Rashedi, H. Nezamabadi-pour, S. Saryazdi, "GSA: A Gravitational Search Algorithm", *Inf. Sci., 179*, 2232-2248, 2009/06/13/ 2009, doi: https://doi.org/10.1016/j.ins.2009.03.004.

[24] R. Formato, "Central force optimization: a new metaheuristic with applications in applied electromagnetics". *Prog. Electromagn. Res.*, 77: 425–491, 2007.

[25] F.F. Moghaddam, R.F. Moghaddam, M. Cheriet, "Curved space optimization: a random search based on general relativity theory", *arXiv preprint arXiv:1208.2214,* 2012.

[26] J. Kennedy R. Eberhart, "Particle swarm optimization", in *Proceedings of ICNN'95-international conference on neural networks*, *4*, 1942-1948, 1995.

[27] A. Farzin, M. Ghazi, A.F. Sotoodeh, M. Nikian, "Economic optimization of a shell-and-tube heat exchanger (STHE) based on new method by Grasshopper Optimization Algorithm (GOA)", *Iranian J. Mar. Tech., 7*, 112-124, 2020.

[28] M. Yousefi, A.N. Darus, H. Mohammadi, "Second law based optimization of a plate fin heat exchanger using imperialist competitive algorithm", *Int. J. Phys. Sci., 6*, 4749-4759, 2011.

[29] A. Hadidi, "A robust approach for optimal design of plate fin heat exchangers using biogeography based optimization (BBO) algorithm", *Appl. Energy, 150*, 196-210, 2015.

[30] S. Banooni, H. Zarea, and M. Molana, "Thermodynamic and economic optimization of plate fin heat exchangers using the bees algorithm", *Heat Trans. Asian Res., 43*, 427-446, 2014.

[31] R. Rao, V. Patel, "Thermodynamic optimization of cross flow plate-fin heat exchanger using a particle swarm optimization algorithm", *Int. J. Therm. Sci., 49*, 1712-1721, 2010.

[32] M. Mishra, P. Das, S. Sarangi, "Second law based optimisation of crossflow plate-fin heat exchanger design using genetic algorithm", *Appl. Therm. Eng., 29*, 2983-2989, 2009.

Research Article

Thermodynamic and Environmental Analysis of Hydrocarbon Refrigerants as Alternatives to R134a in Domestic Refrigerator

*S. A. Kadhim

Mechanical Engineering Department, University of Technology- Iraq, Baghdad, Iraq
E-mail: 20292@uotechnology.edu.iq

Abstract

The process of phasing out of medium and high global warming potential refrigerants is accelerating in all areas of refrigeration, particularly since the European F-Gas Regulation No. 517/2014 and the ensuing Kigali amendment went into effect. Hydrocarbon refrigerants are being considered as suitable alternatives due to their low global warming potential and excellent thermal properties, but due to their flammability, safety precautions must be followed. This theoretical study contributes to the evaluation of the thermal and environmental impact of hydrocarbon refrigerants as drop-in alternatives to R134a in domestic refrigerator. In order to conduct an analysis of energy, exergy, and environmental factors, R134a and all hydrocarbons refrigerants proposed by ASHRAE—R290, R600, R600a, R601, R601a, and R1270—were examined as operating fluids used in a domestic refrigerator with a cooling capacity of 157 W and constant condenser temperature of 40°C and variable evaporator temperature every 5°C between -5 and -30°C. The results revealed that all the alternative refrigerants except R601 and R601a have higher thermal and environmental performance than R134a and can be used after refrigerator compressor replacement.

Keywords: Domestic refrigerator; R134a; R290; R600; R600a; R601; R601a; R1270; TEW1.

1. Introduction

Due to its low cost, excellent thermodynamic and thermophysical properties, and lack of ozone depletion potential (ODP), R134a is a type of HydroFluoroCarbons (HFCs) that is still used as a refrigerant in refrigerators, particularly in developing countries. On the other hand, it has a high Global Warming Potential (GWP) [1]. Therefore, HFCs are being phased out according to the Kyoto Protocol [2]. HydroCarbons (HCs) are being considered as potential alternatives due to their low GWP and also have good thermophysical properties [3]. In reality, HCs were utilized as refrigerants in refrigerating units in the beginning of the 20th century. Nevertheless, nonflammable ChloroFluoroCarbons CFCs took their place due to the technical and safety issues with the usage of HCs at the given moment [4]. Their flammable properties are the fundamental disadvantage of HCs, which restrict their usage as refrigerants. Experts advise using a small amount of refrigerant in a refrigerating unit to help reduce this issue. Before the installation of large-volume refrigeration equipment, there are a number of safety rules and measures that should be followed. Some of the primary precautionary guidelines that have to be followed while utilizing HCs include containing them in a sealed system, decreasing the charge of HCs for particular uses, reducing the level of concentration of HCs in the ambient air (less than the flammability limit), utilizing a suitable ventilating source, and removing any potential source of ignition [5, 6].

In order to assess the possibility of using HC refrigerants as the best performing alternatives to HFC refrigerants, many researchers have conducted thermodynamic, environmental,

or both investigations of these refrigerants as they are used in refrigeration systems [7-11]. In an identical refrigeration facility with a hermetic compressor, under the same operating conditions, Sánchez et al. [12] carried out experiment research to examine the performance of low-GWP refrigerants as alternatives to R134. This included two evaporating temperature levels (0 and -10ºC) at three condensing temperatures (25, 35, and 45ºC) for every one of them. Among these refrigerants, R290 and R600 were tested as HCs. The results showed that the R290 has the best results in terms of cooling capacity and coefficient of performance, but it is not preferred to be utilized as a direct drop-in substitute due to the difference of a displacement to decrease the similar cooling capacity, this applies to R600. Shaik and Srinivas [13] conducted a thermodynamic analysis on a domestic refrigerator that used R134a as a refrigerant, and compared it with alternative environmentally friendly refrigerants, including R290 and R600a without any modification to the refrigerator. Their results showed that these refrigerants had a performance slightly lower than R134a at various evaporator and condenser temperatures. Hastak and Kshirsagar [14] presented an experimental study to evaluate the thermal performance of R600a and R436a (R290:R600a, 54:46 by weight) in a household refrigerator using R134a refrigerant, an HC compressor in place of an HFC compressor and optimal capillary. The results revealed that alternative refrigerants have lower power consumption and higher COP, and that the mixture refrigerant is a better alternative, especially in the long term. Siddegowda et al. [15] predicted some thermodynamic properties for a group of hydrocarbon refrigerants as alternatives to replace R134a

using SRK EOS software. They performed a simulation of an 89 W domestic refrigerator using a ten state point vapour compression cycle with condenser temperature at 55°C and evaporator temperatures ranging from -5 to -30°C. Their findings indicate that R290 and R1270 are suitable and suggested as R134a replacements with smaller compressors. de Paula et al. [16] published a mathematical modeling of a vapor compression refrigerating unit with a minimal capacity for cooling that uses many different refrigerants, including R290 and R600a as substitutes for R134a. They completed the environmental analysis using the entire equivalent warming impact, and the thermo-economic evaluation using the performance coefficient, the exergy efficacy, and the overall plant cost ratio. According to their examination of the thermodynamic, economic, and environmental factors, the system including R290 performs better than the other systems under the examined thermodynamic circumstances in terms of energy, efficiency, the environment, and the economy. Using three different vapor compression system configurations—a single-stage cycle, a cycle having an inner heat exchanger, and a two-stage cycle having vapor injection—Ghanbarpour et al. [17] presented an empirical investigation for evaluating the energy and exergy performances as well as the environmental impact. All operating with HCs R290, R600a, and R1270 as alternatives to R134a. According to their findings, alternative HC refrigerants might perform as well as R134a in every configuration while reducing carbon emissions by 50% when used. Sharma and Dwivedi [18] compared the performance of the R134a and R600a experimentally in a similar vapor compression refrigeration system. In order to compare the refrigerants, the performance coefficient, refrigeration effect, and Carnot coefficient of performance were computed. The exergy destruction and second law efficiency for the main components were then estimated. They discovered that R600a is a better refrigerant.

Following this in-depth review of the literature, it becomes clear that HC refrigerants are excellent alternatives to R134a in vapour compression refrigeration systems, especially domestic refrigerators, but the focus is usually on R290 and R600a, with few studies that take into account both thermodynamic (energy and exergy) and environmental analysis. This study presents a theoretical evaluation of the performance of all hydrocarbon refrigerants recommended by ASHRAE: R290, R600, R600a, R601, R601a, and R1270 as drop-in alternatives for R134a in a domestic refrigerator with cooling capacity of 157 W. Evaluation is done by performing an energy analysis based on compression ratio, compressor work, volumetric refrigeration capacity, and coefficient of performance, followed by an exergy analysis

based on total exergy destruction rate, exergy efficiency, and sustainability index, and finally an environmental analysis based on total equivalent warming impact.

2. Comprehensive Properties of Hydrocarbon Refrigerants

When choosing a refrigerant, take into account its thermophysical characteristics as well as environmental, economic, and technological considerations [19]. ODP and GWP are important environmental features that help decrease environmental effect, but they must also have strong thermophysical and economic properties in order to be used. Table 1 shows the definitions of HCs and R134a used in this study as well as their thermophysical, safety and environmental properties. As a first impression after taking a look at the table, all refrigerants have optimal thermophysical properties for vapor compression refrigeration systems except R601 and R601a because of their high natural boiling temperature. Refrigerants are classified in terms of safety, toxicity and flammability [20]. The refrigerants' flammability is indicated by numbers, as follows: (1) is non-flammability, (2) is medium flammability, and (3) is higher flammability, while letters are an indication of toxicity, (A) is lower toxicity, and (B) is higher toxicity. Therefore, all HC refrigerants have low toxicity, but the problem of flammability remains, which must be taken into account when using these refrigerants according to the instructions, some of which were mentioned in the introduction section. Finally, in view of the environmental properties, HC refrigerants are very suitable because they do not have ODP and have a low GWP (less than 150 [2]).

3. Configuration and Assumptions

The performance is analyzed on the basis of data, most of which were taken from a 200-liter domestic refrigerator with a working fluid R134a, as shown in Table 2. The refrigerator operates on the actual vapor-compression refrigeration cycle and with some assumptions that will be mentioned later. Can Figure 1shows the path of the cycle on P-h diagram compared to the ideal cycle.

To make the analysis simpler, some of the presumptions from related earlier studies have been used as follows [26, 27]:
(1) Each component is in a steady state and is flowing steadily.
(2) The isentropic efficiency of a compressor is a function of the compression ratio.
(3) The throttling processes in the expansion device are isenthalpic.

Table 1. Thermophysical, safety and environmental properties of the studied refrigerants. [20-23]

Property	R134a	R290	R600	R600a	R601	R601a	R1270
Chemical Name	1,1,1,2-Tetrafluoroethane	Propane	Butane	Isobutane	Pentane	Isopentane	Propene (propylene)
Chemical Formula	CF_3CH_2F	$CH_3CH_2CH_3$	$CH_3CH_2CH_2CH_3$	$CH(CH_3)_2CH_3$	$CH_3(CH_2)_3CH_3$	$(CH_3)_2CHCH_2CH_3$	$CH_3CH=CH_2$
Molecular Mass (gmol⁻¹)	102.03	44.096	58.122	58.122	72.15	72.15	42.08
Critical Temperature (°C)	101.06	96.74	151.98	134.66	196.5	187.2	91.061
Critical Pressure (kPa)	4059.3	4251.2	3796.0	3629.0	3367.0	3378	4554.8
Normal Boiling Point (°C)	−26.074	−42.11	−0.49	−11.75	36.1	27.8	−47.62
Safety Group	A1	A3	A3	A3	A3	A3	A3
ODP	none	none	none	none	none	none	none
GWP$_{100}$ (kg CO_2-eq/kg refrigerant)	1300	5	4	20	11	20	1.8
Atmospheric life time (year)	13.4	0.034	-	0.016	-	0.009	0.001

(4) No pressure drop and heat losses in the cycle are considered.

(5) The volumetric efficiency of the compressor is 1.

(6) The refrigerator's freezer is the subject of analyses.

Table 2. Data adopted in thermodynamic and environmental analysis.

| Parameter	Unit	Data
Cooling capacity (Q_e)	W	157
Condenser temperature (T_c)	°C	40
Evaporator temperature (T_e)	°C	-30 to -5
Subcooling temperature	°C	5
Superheat temperature	°C	5
Cooled air temperature in the freezer cabinet (T_{ca})	K	$8+T_e$
Ambient temperature (T_a)	K	303
Mechanical efficiency of the compressor (η_{mech})	-	0.81
Electrical efficiency of the compressor (η_{elec})	-	0.93
Refrigerant weight of R134a (N)	kg	0.135
Leakage rate (L)	kg/year	10% for R134a [24]
Refrigerator lifetime (n)	year	15
Recovery factor (α)	-	0.7 [17]
Carbon emission factor (β)	kg CO_2-eq. / kWh	0.5 Middle East [25]
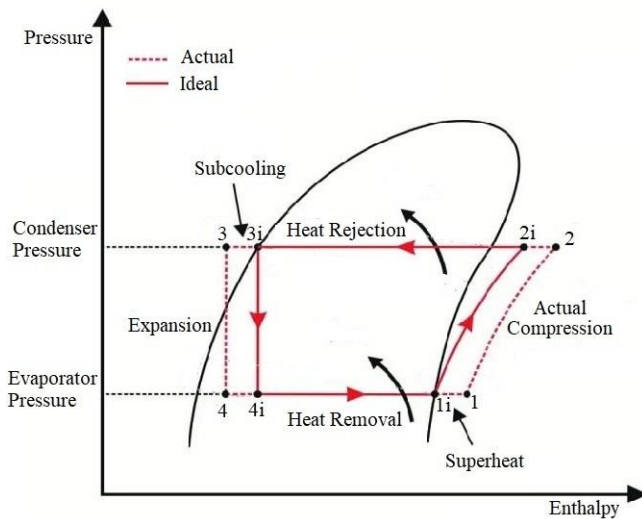
Figure 1. The proposed cycle path on P-h diagram.

4. Mathematical Analysis
4.1 Energy Analysis

Performance is evaluated in terms of energy aspects based on the first law of thermodynamics. According to the assumptions that were mentioned in the previous section, the energy expenditure is represented in the compressor work, which can be expressed by Eq. (1) [28]:

$$W_{com} = \frac{m(h_2 - h_1)}{\eta_{mech}\,\eta_{elec}} = \frac{m(h_{2s} - h_1)}{\eta_{mech}\,\eta_{elec}\,\eta_{is}} \tag{1}$$

The refrigerant mass flow rate is determined depending on the value of cooling capacity and is given by Eq. (2):

$$m = \frac{Q_e}{h_1 - h_4} \tag{2}$$

Eq. (3) is used to express the isentropic efficiency, which depends on the compression ratio [29]:

$$\eta_{is} = 0.874 - 0.0135 P_r \tag{3}$$

The compression ratio is an important parameter for determining the compressor design and size. In this cycle, it represents the ratio of high pressure (condenser pressure) to the ratio of low pressure (evaporator pressure) as expressed in Eq. (4):

$$P_r = \frac{P_c}{P_e} \tag{4}$$

The volumetric refrigeration capacity is another parameter to evaluate performance, especially concerning the compressor design and size, it can be expressed in Eq. (5) [27]:

$$VRC = \frac{Q_e}{m\,v_1} \tag{5}$$

In general, the vapor-compression refrigeration cycle performance is expressed by the coefficient of performance, which represents as the ratio of the heat removal by the evaporator (cooling capacity) to work rate done in the compressor as expressed in Eq. (6) [30]:

$$COP = \frac{Q_e}{W_{com}} \tag{6}$$

4.2 Exergy Analysis

It is possible to assess the effectiveness of the vapor-compression refrigeration cycle using the energy analysis approach. It cannot, however, assess the cycle's severity of irreversibility. In order to further assess the irreversibility of the cycle while replacing the refrigerant, the exergy analysis approach is used.

Typically, Eq. (7) is used to represent the exergy balance for the steady process control volume [28]:

$$EX_d = \sum EX_{in} - \sum EX_{out} + \sum Q \left[1 - \frac{T_a}{T_s}\right]_{in} - \sum Q \left[1 - \frac{T_a}{T_s}\right]_{out} + \sum W_{in} - \sum W_{out} \tag{7}$$

Eq. (8) gives the exergy rate of every state point within the cycle, assuming that kinetic as well as potential energy variations were ignored [31], [32]:

$$EX = m[(h - h_o) - T_a(s - s_o)] \tag{8}$$

Where, h_o and s_o are the enthalpy and entropy at ambient temperature.

According to Eq. (7) and Eq. (8), the exergy destruction rate of the cycle components are measured as follows:

In the compressor
$$EX_{d,com} = EX_1 - EX_2 + \sum W_{in} = m[(h_1 - h_o) - T_a(s_1 - s_o)] - m[(h_2 - h_o) - T_a(s_2 - s_o)] + W_{com} = m[(h_1 - h_2) - T_a(s_1 - s_2)] + W_{com} \tag{9}$$

In the condenser

$$EX_{d,c} = EX_2 - EX_3 - \sum Q\left[1 - \frac{T_a}{T_s}\right]_{out} = m[(h_2 - h_o) - T_a(s_2 - s_o)] - m[(h_3 - h_o) - T_a(s_3 - s_o)] - Q_c\left[1 - \frac{T_a}{T_a}\right] = m[(h_2 - h_3) - T_a(s_2 - s_3)] \tag{10}$$

In the expansion device

$$EX_{d,exp} = EX_3 - EX_4 = m[(h_3 - h_o) - T_a(s_3 - s_o)] - m[(h_4 - h_o) - T_a(s_4 - s_o)] = m\,T_a(s_4 - s_3) \qquad (11)$$

In the evaporator

$$EX_{d,e} = EX_4 - EX_1 + \sum Q\left[1 - \frac{T_a}{T_s}\right]_{in} = m[(h_4 - h_o) - T_a(s_4 - s_o)] - m[(h_1 - h_o) - T_a(s_1 - s_o)] + Q_e\left[1 - \frac{T_a}{T_{ca}}\right] = m[(h_4 - h_1) - T_a(s_4 - s_1)] + Q_e\left[1 - \frac{T_a}{T_{ca}}\right] \qquad (12)$$

The total exergy destruction rate can be expressed in Eq. (13):

$$EX_{d,tot} = EX_{d,com} + EX_{d,c} + EX_{d,exp} + EX_{d,e} \qquad (13)$$

The total exergy efficiency of the cycle can be expressed in Eq. (14) [33]:

$$\eta_{ex,tot} = 1 - \frac{EX_{d,tot}}{W_{com}} \qquad (14)$$

The effective use of resources is necessary for sustainability evaluation, which is carried out using the sustainability index approach, which is connected to energy efficiency. Exergy evaluation can be crucial for increasing productivity because it enables any user to fully utilize the advantages of their resources while reducing drawbacks like environmental harm [34]. In order to acquire the sustainability evaluation represented in Eq. (15), the sustainability index approach based on energy efficiency is a valuable tool. [35]:

$$SI = \frac{1}{1 - \eta_{ex}} \qquad (15)$$

4.3 Environmental Analysis

There are several metrics for evaluating the environmental impact left by the systems, one of which and the most used is the total equivalent warming impact metric. Such environmental metric, which has a mathematical expression in Eq. (16), includes both direct as well as indirect greenhouse gas releases from a refrigerating system [36]:

$$TEWI = [GWP\,L\,n + GWP\,N(1 - \alpha) + E_y\,\beta\,n]\,10^{-3} \qquad (16)$$

5. Results and Discussion

In this section, the results are presented and discussed in three stages: energy analysis results, exergy analysis results, and environmental analysis results. The results were built considering that the condenser temperature is constant at 40°C, While the evaporator temperature ranges between -30 and -5°C, performance parameters are calculated every 5°C. The thermal properties of the cycle (P,v,h,s) are determined using Coolselector®2 software, and the equations are simulated using MATLAB software.

Figure 2 shows the compression ratio of R134a and alternative refrigerants over a range of evaporator temperatures. For all refrigerants, the compression ratio increases with the increase in the temperature difference

between the condenser and the evaporator, and this increase requires a larger compressor work and thus higher costs. For R134a, the minimum compression ratio is 4.1742 and the maximum compression ratio is 12.0379 at evaporator temperatures of -5 and -30°C, respectively. According to such results, the results of the alternative refrigerants can be divided into three levels: excellent, represented by R290 and R1270, acceptable, represented by R600 and R600a, and bad, represented by R601 and R601a. For R290 and R1270, the minimum and maximum compression ratios are 3.3719 and 3.2855, and of 8.1585 and 7.7883 at evaporator temperatures of -5 and -30°C, respectively. That is, the minimum and maximum compression ratios are reduced by 19% and 21%, and by 32% and 35% when using R290 and R1270, respectively. For R600 and R600a, the minimum and maximum compression ratios are 4.4477 and 4.0550, and of 13.4220 and 11.3991 at evaporator temperatures of -5 and -30°C, respectively. That is, the minimum and maximum compression ratios are reduced by 3% and 5%, respectively when using R600a, they increase by 6% and 10%, respectively when using R600, this is an acceptable result. For R601 and R601a, the minimum and maximum compression ratios are 5.9639 and 5.4693, and of 22.6863 and 19.4231 at evaporator temperatures of -5 and -30°C, respectively. That is, the minimum and maximum compression ratios are increased by 30% and 24%, and by 47% and 38% when using R601 and R601a, respectively. This means that it is difficult to use R601 and R601a in instead of R134a without mixing, because it requires a compressor with a very high displacement to secure the required cooling capacity.
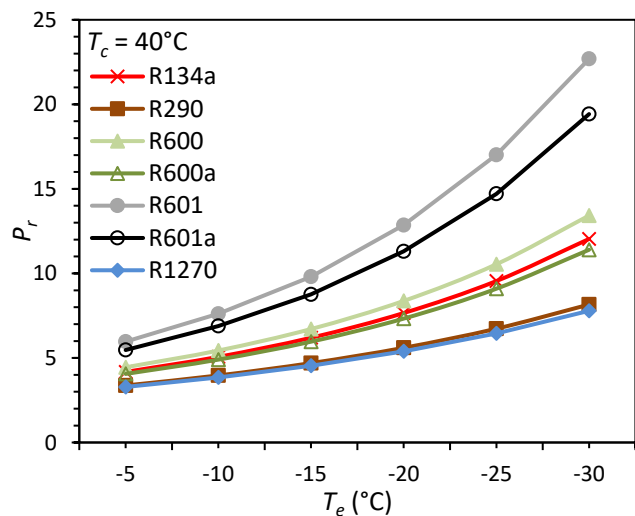
Figure 2. Variation of compression ratio with evaporator temperature for several refrigerants.

Figure 3 shows the volumetric refrigeration capacity of R134a and alternative refrigerants at different evaporator temperatures. This parameter gives a visualization of the compressor displacement and required refrigerant charge to secure the cooling capacity. The volumetric refrigeration capacity decreases with the increase in the temperature difference between the condenser and the evaporator for all refrigerants. For R134a, the maximum volumetric refrigeration capacity is 1779.80 kJ/m3 and the minimum volumetric refrigeration capacity of 583.22 kJ/m3 at evaporator temperatures of -5 and -30°C, respectively. According to this result, the results of the alternative refrigerants can be divided into three levels: excellent,

represented by R290 and R1270, acceptable, represented by R600 and R600a, and bad, represented by R601 and R601a. For R290 and R1270, the maximum and minimum volumetric refrigeration capacities are 2475.20 and 3007.00 kJ/m3, and are 963.36 and 1209.10 kJ/m3 at evaporator temperatures of -5 and -30°C, respectively. That is, the maximum and minimum volumetric refrigeration capacities are increased by 28% and 41%, and by 39% and 52% when using R290 and R1270, respectively. This means that it is possible to use R290 and R1270 instead of R134a, but with use a compressor with a lower displacement (smaller in size) and change in the charge amount to secure the same performance. For R600 and R600a, the maximum and minimum volumetric refrigeration capacities are 681.17 and 957.10 kJ/m3, and of 214.93 and 320.08 kJ/m3 at evaporator temperatures of -5 and -30°C, respectively. That is, the maximum and minimum volumetric refrigeration capacities are decreased by 61% and 46%, and by 63% and 45% when using R600 and R600a, respectively. This means that when using R600 and R600a instead of R134a, a higher displacement compressor and a different charge amount should be used to guarantee the same performance. For R601 and R601a, the maximum and minimum volumetric refrigeration capacities are 190.08 and 255.59 kJ/m3, and are 48.06 and 68.61 kJ/m3 at evaporator temperatures of -5 and -30°C, respectively. That is, the maximum and minimum volumetric refrigeration capacities are decreased by 89% and 86%, and by 92% and 88% when using R600 and R600a, respectively. This means that it is difficult to use R601 and R601a instead of R134.

Figure 3. Variation of volumetric refrigeration capacity with evaporator temperature for several refrigerants.

Figures 2 and 3 provide more design indicators than thermal ones. To clearly evaluate the thermal performance when using alternative refrigerants, compressor work and coefficient of performance results are investigated. Figure 4 shows compressor work behavior at different evaporator temperatures using R134a and alternative refrigerants. It is clear that the compressor work increases with the increase in the temperature difference between the condenser and the evaporator for all refrigerants, in other words, power consumption increases as the evaporator temperature decreases. All refrigerants show convergent values at an evaporator temperature from -5 to -20°C, with preference given to the R600 and R600a, it recorded the lowest values for the compressor work. Differences begin to appear

after that, especially at -30°C, the compressor work reaches to the maximum, and there are clear differences between work values of the refrigerants. At the evaporator temperature of 30°C, the compressor work arrived to 115.5 W using R134a, while arrived to 108.7, 112.9, 111.4, 135.4, 127.2, and 107.8 W using R290, R600, R600a, R601, R601a, and R1270, respectively. This means that the compressor work decreased by 5.88%, 2.25%, 3.55%, and 6.66% using R290, R600, R600a, and R1270, respectively, while increased by 14.69% and 9.19% using R601 and R601a, respectively.
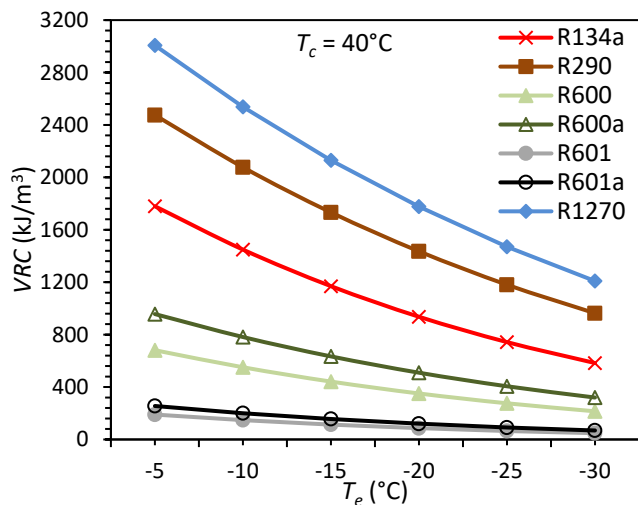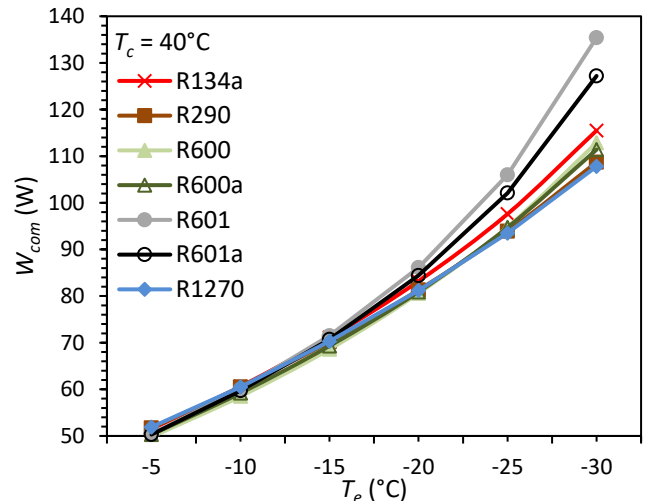

Figure 4. Variation of compressor work with evaporator temperature for several refrigerants.

Figure 5 shows coefficient of performance with different evaporator temperatures using R134a and alternative refrigerants. It is clear that the coefficient of performance decreases with the increase in the temperature difference between the condenser and the evaporator for all refrigerants, this is due to the increased work required from the compressor. All refrigerants show convergent values at an evaporator temperature from -5 to -20°C, with preference given to the R600 and R600a, it recorded the highest values for the coefficient of performance. Differences begin to appear more after that, especially at -30°C where the coefficient of performance is 1.3591 using R134a, while it is 1.4448, 1.3912, 1.4097, 1.1593, 1.2344, and 1.4565 using R290, R600, R600a, R601, R601a, and R1270, respectively. This means that the coefficient of the performance increased by 5.93%, 2.30%, 3.59%, and 6.68% using R290, R600, R600a, and R1270, respectively, while decreased by 14.70% and 9.17% using R601 and R601a, respectively.

Exergy analysis was performed based on three parameters: total exergy destruction rate, exergy efficiency, and sustainability index. Figure 6 shows the total exergy destruction rate as a function of different evaporator temperatures using R134a and HCs. It is clear that the exergy destruction rate increases with the increase in the temperature difference between the condenser and the evaporator, in other words, thermal losses increase due to irreversibility as the evaporator temperature decreases. All refrigerants have convergent values of the total exergy destruction rate at evaporator temperature from -5 to -20°C, with preference given to the R600 and R600a, it recorded the lowest values. Differences begin to appear more after that, especially at -30°C, the destruction rates reach their highest levels due to the increased intensity of irreversibility. At an

evaporator temperature of -30 °C, it is observed that the total exergy destruction rate using R134a is 83 W, while it is 76.1, 80.3, 78.8, 106.6, 94.7, and 75.3 W when using R290, R600, R600a, R601, R601a, and R1270. This means that the total exergy destruction rate was decreased by 8.31%, 3.25%, 5.33%, and 10.22% using R290, R600, R600a, and R1270 respectively, while increased by 22.13% and 12.35% using R601 and R601a, respectively.
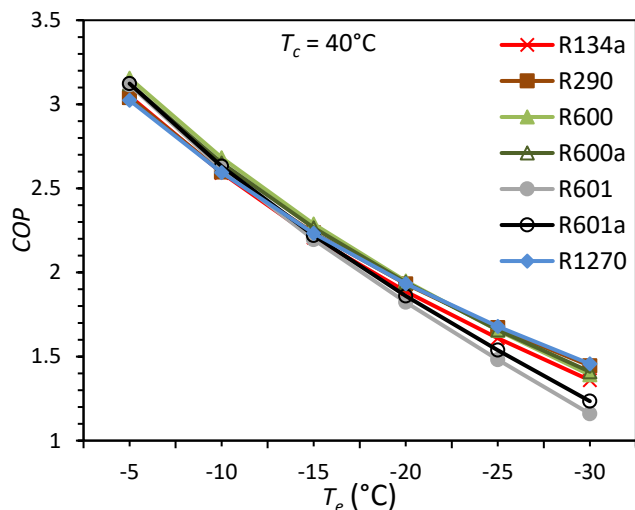

Figure 5. Variation of coefficient of performance with evaporator temperature for several refrigerants.
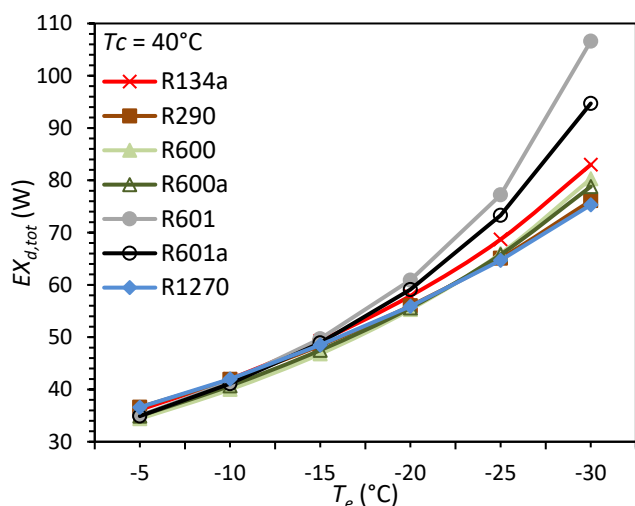

Figure 6. Variation of total exergy destruction rate with evaporator temperature for several refrigerants.

Figure 7 shows the change in efficiency with evaporator temperatures when R134 and alternative HC refrigerants are used. Contrary to all the parameters that were presented, the exergy efficiency did not show direct or inverse behavior, it increased with the evaporator temperature to a certain extent and then decreased, as this behavior applies to all refrigerants. This behavior was reported in [9], and it is explained by the fact that, according to Eq. (14), the exergy efficiency depends on both the compressor work and the total exergy destruction rate. When increasing, it means that the increase in the compressor work is greater than the increase in the total exergy destruction rate, and vice versa when decreasing. At evaporator temperatures of -15°C, R134a's maximum exergy efficiency was recorded to be 0.3071, while that of R290, R600, and R600a was 0.3109, 0.3183, and 0.3152. At evaporator temperatures of -20°C, R1270's maximum exergy efficiency was recorded to be 0.3112,

while that of R601 and R601a was 0.3091 and 0.3107, respectively. At 30°C, the exergy efficiency of alternative refrigerants is higher than the exergy efficiency of R134a, except for R601 and R601a.
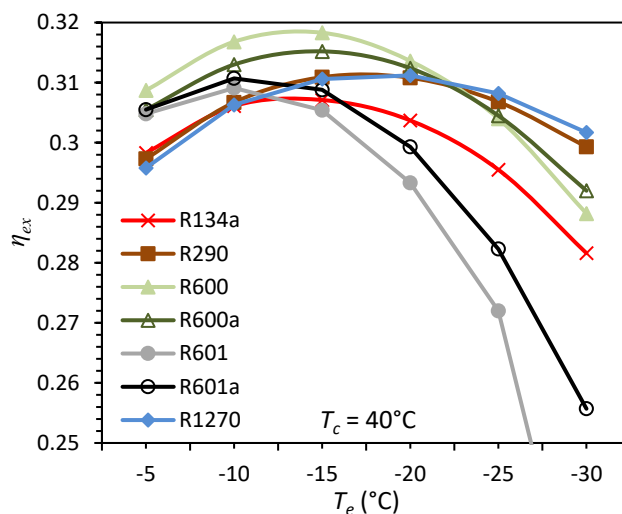
Figure 7. Variation of exergy efficiency with evaporator temperature for several refrigerants.

Depending on the exergy efficiency values, the sustainability index is determined, which showed different values between a same refrigerant and between refrigerants according to change evaporator temperatures, as shown in Figure 8.

The best sustainability index was observed for R134a to be 1.4431, while that of R290, R600, and R600a was 1.4513, 1.4669, and 1.4602 respectively at evaporator temperatures -15°C, while was observed for R1270 to be 1.4517 at evaporator temperatures -20°C, and that of R601 and R601a was 1.4473 and 1.4508 respectively at evaporator temperatures -10°C.

Total equivalent warming impact is an effective parameter in evaluating the environmental impact of refrigeration systems because it diagnoses carbon emissions from the system itself as well as from the energy source supplied to the system. Therefore, reducing power consumption when replacing the refrigerant has environmental benefits in addition to economic benefits. According to Eq. (16), the first and second terms represent direct emissions for which the refrigerator is responsible, and the third term represents indirect emissions. All refrigerants are considered to have the same weight of charge (135 g). As for the leakage rate of HC refrigerants, it is determined according to the leakage rate of R134a listed in Table 2, where the leakage rate of HC refrigerant represents the ratio of its high pressure to high pressure of R134a multiplied by the leakage rate of R134a. While the annual energy consumption is determined depending on the compressor work, considering that the refrigerator operates 24 hours a day.

Figure 9 shows the change in total equivalent warming impact of the used refrigerants with the evaporator temperature. It is clear that the total equivalent warming impact increases with decreasing the evaporator temperature due to indirect emissions that increase as a result of power consumption and irreversibility losses. Except for R601, which records higher values at -25 and -30°C evaporator temperatures, and R601a, which records higher value at -30°C, all HC refrigerants have a lower total equivalent warming impact than R134. Overall, In the evaporator

Figure 8. Variation of sustainability index with evaporator temperature for several refrigerants.

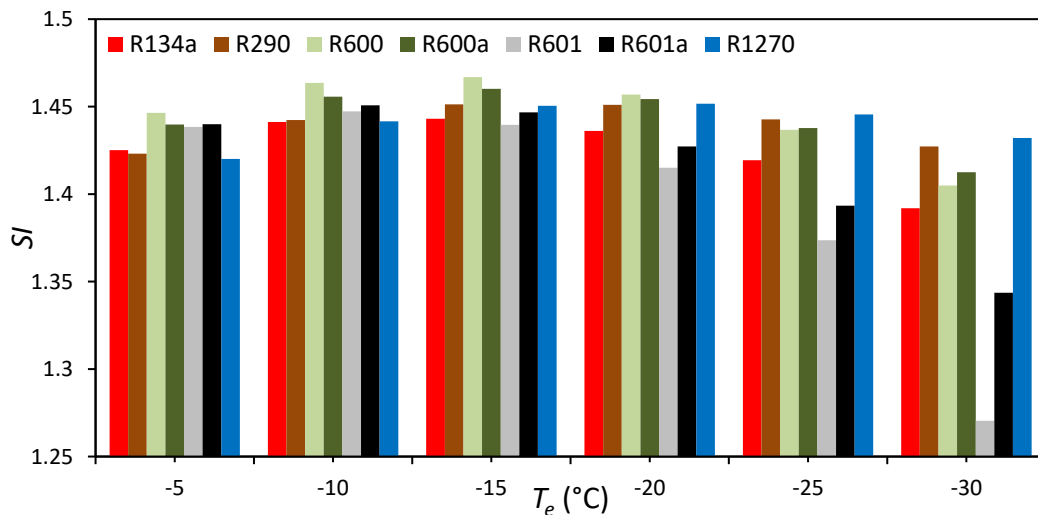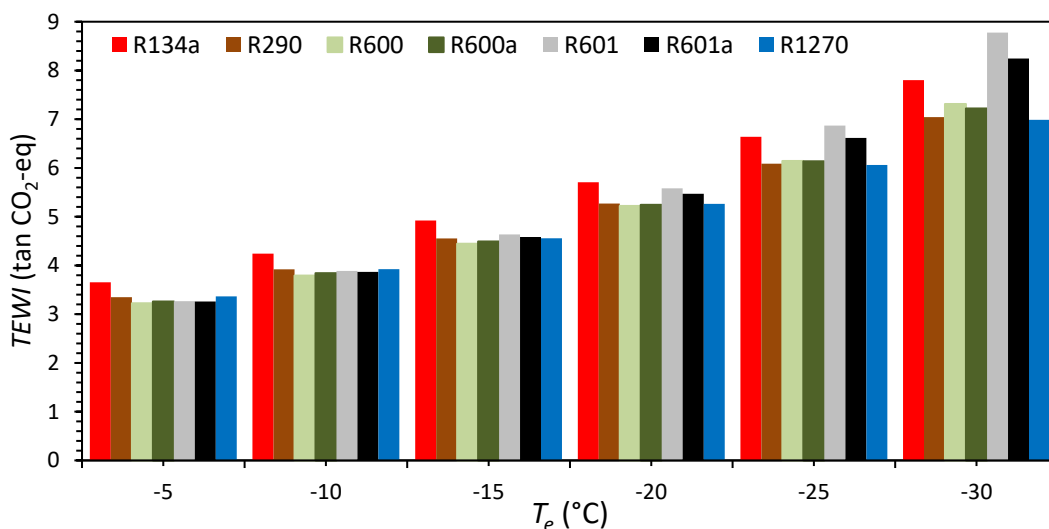*Figure 9. Variation of Total equivalent warming impact with evaporator temperature for several refrigerants.*

temperature range of -5 to -20°C, R600 was shown to have the lowest total equivalent warming impact, followed by R600a, and at -25 and -30°C, R1270 was shown to have the lowest total equivalent warming impact, followed by R290.

6. Conclusions and Recommendations

This study contributes to the thermal and environmental evaluation of HC refrigerants: R290, R600, R600a, R601, R601a, and R1270 as working fluids in a domestic refrigerator instead of high-GWP R134a. A triple analysis of energy, exergy, and environmental was performed with constant operating conditions for ambient and condenser temperatures of 30 and 40°C, respectively, and variable operating conditions for evaporator temperatures from -5 to -30°C. The results can be summarized according to the calculated parameters:

(1) There are prominent differences in the compression ratios, and the refrigerants can be arranged from lowest to highest compression ratio under the same conditions as follows: R1270, R290, R600a, R134a, R600, R601a, and R601.

(2) There are prominent differences in the volumetric refrigeration capacities, and the refrigerants can be arranged from the highest to lowest volumetric refrigeration capacity under the same conditions as follows: R1270, R290, R134a, R600a, R600, R601a, and R601.

(3) In the evaporator temperature range of -5 to -20°C, R600 has the lowest compressor work (power consumption) and total exergy destruction rate, followed by R600a. However, at -25 and -30°C, R1270 has the lowest compressor work and total exergy destruction rate followed by R290.

(4) In the evaporator temperature range of -5 to -20°C, R600 has the highest coefficient of performance followed by R600a. However, at -25 and -30°C, R1270 has the highest coefficient of performance, followed by R290.

(5) In the evaporator temperature range of -5 to -20°C, R600 and R600a had the best energy efficiency and sustainability index, while R1270 and R290 had the best results at -25 and -30°C.

(6) With the exception of R601, which recorded higher values at -25 and -30°C evaporator temperatures and also R601a, which recorded a higher value at -30°C, all HC refrigerants have a lower total equivalent warming impact than R134 under the same conditions. R1270 has the lowest total equivalent warming impact, followed by R290 at -25 and -30°C, and R600 also has the lowest total equivalent warming impact, followed by R600a in the -5 to -20°C evaporator temperature range.

According to the results of this study, it is recommended to use R600 or R600a instead of R134a but with a higher displacement compressor and a change in amount of the charge. Also, it is recommended to use R1270 or R290 instead of R134a, but with a lower displacement compressor

and a change in amount of the charge. With safety instructions adherence when using HC refrigerants. It is not recommended to use R601 and R601a refrigerants in domestic refrigerators.

Nomenclature

COP	Coefficient of performance
EX	Exergy rate (W)
E_y	Annual energy consumption (kWh/year)
h	Specific enthalpy (kJ/kg)
L	Leakage rate (kg/year)
m	Refrigerant mass flow rate (kg/s)
N	Refrigerant weight (kg)
n	Refrigerator lifetime (year)
p	Pressure (bar)
P_r	Pressure ratio
Q	Heat rate (W)
Q_e	Cooling capacity (W)
SI	Sustainability index
s	Specific entropy (kJ/kg.K)
T	Temperature (°C)
$TEWI$	Total equivalent warming impact (tan CO_2-eq)
VRC	Volumetric refrigeration capacity (kJ/m³)
v	Specific volume (m³/kg)
W	Work rate (W)

Greeks Symbol

α	Recovery factor at the end of life
β	Carbon emission factor (kg CO_2-eq./kWh)
η	Efficiency

Subscripts

o	Reference state
1-4	State points of refrigerant for actual cycle
$2s$	State point at constant entropy
1i-4i	State points of refrigerant for ideal cycle
a	Ambient
c	Condenser
ca	Cooled air in the freezer cabinet
com	Compressor
d	destruction
e	Evaporator
$elec$	Electrical
ex	Exergy
exp	Expansion device
in	Inlet
is	Isentropic
$mech$	Mechanical
out	Outlet
s	Space
tot	Total

Abbreviations

ASHRAE	American Society of Heating, Refrigerating and Air-Conditioning Engineers
CFCs	ChloroFluoroCarbons
GWP	Global Warming Potential
HCs	HydroCarbons
HFCs	HydroFluoroCarbons
ODP	Ozone Depletion Potential

References:

[1] J. Gill and J. Singh, "Energy analysis of vapor compression refrigeration system using mixture of R134a and LPG as refrigerant," *Int. J. Refrig.*, vol. 84, pp. 287–299, 2017. doi: 10.1016/j.ijrefrig.2017.08.001

[2] K. Protocol, "Kyoto protocol", UNFCCC Website." 1997. Available online: http://unfccc.int/kyoto_protocol/items/2830

[3] I. M. G. Almeida, C. R. F. Barbosa, and F. de A. O. Fontes, "Thermodynamic and thermophysical assessment of hydrocarbons application in houshould refrigerator," *Rev. Eng. Térmica*, vol. 9, no. 1–2, pp. 19–27, 2010. doi: 10.5380/reterm.v9i1-2.61926

[4] G. Venkatarathnam and S. Srinivasa Murthy, "Refrigerants for vapour compression refrigeration systems," *Resonance*, vol. 17, pp. 139–162, 2012. doi: 10.1007/s12045-012-0015-x

[5] K. Harby, "Hydrocarbons and their mixtures as alternatives to environmental unfriendly halogenated refrigerants: An updated overview," *Renew. Sustain. Energy Rev.*, vol. 73, pp. 1247–1264, 2017. doi: 10.1016/j.rser.2017.02.039

[6] R. Zhai, Z. Yang, Y. Zhang, Z. Lv, and B. Feng, "Effect of temperature and humidity on the flammability limits of hydrocarbons," *Fuel*, vol. 270, p. 117442, 2020. doi: 10.1016/j.fuel.2020.117442

[7] M. Mohanraj, S. Jayaraj, C. Muraleedharan, and P. Chandrasekar, "Experimental investigation of R290/R600a mixture as an alternative to R134a in a domestic refrigerator," *Int. J. Therm. Sci.*, vol. 48, no. 5, pp. 1036–1042, 2009. doi: 10.1016/j.ijthermalsci.2008.08.001

[8] W. S. Mohammad and A. O. Jassim, "Experimental and Theoretical Investigation of Propane/Butane and Propane/Isobutane Mixtures as an Alternative to R134a in a Domestic Refrigerator," *Eng. Technol. J.*, vol. 32, no. 5 Part (A) Engineering, 2014.

[9] K. Chopra, V. Sahni, and R. S. Mishra, "Energy, exergy and sustainability analysis of two-stage vapour compression refrigeration system," *J. Therm. Eng.*, vol. 1, no. 4, pp. 440–445, 2015. doi: 10.18186/jte.95418

[10] C. H. de Paula, W. M. Duarte, T. T. M. Rocha, R. N. de Oliveira, and A. A. T. Maia, "Optimal design and environmental, energy and exergy analysis of a vapor compression refrigeration system using R290, R1234yf, and R744 as alternatives to replace R134a," *Int. J. Refrig.*, vol. 113, pp. 10–20, 2020. doi: 10.1016/j.ijrefrig.2020.01.012

[11] E. Gundabattini, C. Masselli, D. S. Gnanaraj, S. Tadikonda, V. Karnati, and V. K. Vemireddy, "Improving the Energy Performances of the Refrigeration Systems with Subcooling Using the Eco-Friendly Refrigerant R600a: Initial Experimental Results.," *Instrumentation, Mes. Métrologies*, vol. 19, no. 2, pp. 73–81, 2020. doi: 10.18280/i2m.190201

[12] D. Sánchez, R. Cabello, R. Llopis, I. Arauzo, J. Catalán-Gil, and E. Torrella, "Energy performance evaluation of R1234yf, R1234ze (E), R600a, R290 and R152a as low-GWP R134a alternatives," *Int. J. Refrig.*, vol. 74, pp. 269–282, 2017. doi: 10.1016/j.ijrefrig.2016.09.020

[13] M. Shaik Sk and K. Srinivas, "Theoretical analysis of a Low GWP Refrigerants as a Drop in substitute of R134a in a Domestic Refrigerator," *Iran. J. Energy & Environ.*,

vol. 9, no. 2, pp. 130–136, 2018. doi: 10.5829/ijee.2018.09.02.08

[14] S. S. Hastak and J. M. Kshirsagar, "Comparative performance analysis of R600a and R436a as an alternative of R134a refrigerant in a domestic refrigerator," in *IOP Conference Series: Materials Science and Engineering*, 2018, vol. 377, no. 1, p. 12047. doi: 10.1088/1757-899X/377/1/012047

[15] P. Siddegowda, G. Mundur Sannappagowda, V. Jain, and S. Javare Gowda, "Hydrocarbons as Alternate Refrigerants to Replace R134a in Domestic Refrigerators.," *Rev. des Compos. des Matériaux Avancés*, vol. 29, no. 2, pp.95–99, 2019. doi: 10.18280/rcma.290204

[16] C. H. de Paula, W. M. Duarte, T. T. M. Rocha, R. N. de Oliveira, R. de Paoli Mendes, and A. A. T. Maia, "Thermo-economic and environmental analysis of a small capacity vapor compression refrigeration system using R290, R1234yf, and R600a," *Int. J. Refrig.*, vol. 118, pp. 250–260, 2020. doi: 10.1016/j.ijrefrig.2020.07.003

[17] M. Ghanbarpour, A. Mota-Babiloni, B. E. Badran, and R. Khodabandeh, "Energy, exergy, and environmental (3E) analysis of hydrocarbons as low GWP alternatives to R134a in vapor compression refrigeration configurations," *Appl. Sci.*, vol. 11, no. 13, p. 6226, 2021. doi: 10.3390/app11136226

[18] S. Sharma and V. K. Dwivedi, "Comparative Assessment of Environment-Friendly Alternative to R134a in Vapour Compression Refrigeration System using Exergy Destruction," *J. Eng. Res.*, vol. 10, 2022. doi: 10.36909/jer.ICMET.17205

[19] A. Kilicarslan and N. Müller, "A comparative study of water as a refrigerant with some current refrigerants," *Int. J. energy Res.*, vol. 29, no. 11, pp. 947–959, 2005. doi: 10.1002/er.1084

[20] ASHRAE, *ASHRAE fundamentals (SI)*. 2017.

[21] NIST, *NIST reference fluid thermodynamic and transport properties database (REFPROP)*, v. 9.0. National Institute of Standards and Technology, Gaithersburg, MD, 2010.

[22] J. C. Calm, G. C. Hourahan, A. Vonsild, D. Clodic, and D. Colbourne, *2014 Report of the refrigeration, air conditioning, and heat pumps technical options committee*, Ch. 2: Refrigerants. United Nations Environment Programme (UNEP) Ozone Secretariat, Nairobi, 2015.

[23] IPCC, *Climate change 2013: The physical science basis*. Cambridge University Press, 2013.

[24] M. A. Islam, K. Srinivasan, K. Thu, and B. B. Saha, "Assessment of total equivalent warming impact (TEWI) of supermarket refrigeration systems," *Int. J. Hydrogen Energy*, vol. 42, no. 43, pp. 26973–26983, 2017. doi:10.1016/j.ijhydene.2017.07.035

[25] Carbonfootprint, *CARBON FOOTPRINT COUNTRY SPECIFIC ELECTRICITY GRID GREENHOUSE GAS EMISSION FACTORS Last Updated: March 2022. March*, pp. 1–11, 2022. https://www.carbonfootprint.com

[26] M. Direk, A. Kelesoglu, and A. I. Ahmet, "Theoretical performance analysis of an R1234yf refrigeration cycle based on the effectiveness of internal heat exchanger," *Hittite J. Sci. Eng.*, vol. 4, no. 1, pp. 23–30, 2017. doi: 10.17350/HJSE19030000044

[27] Q. Chen, L. Zhou, G. Yan, and J. Yu, "Theoretical investigation on the performance of a modified refrigeration cycle with R170/R290 for freezers application," *Int. J. Refrig.*, vol. 104, pp. 282–290, 2019. doi: 10.1016/j.ijrefrig.2019.05.037

[28] S. Khatoon and M. N. Karimi, "Thermodynamic analysis of two evaporator vapor compression refrigeration system with low GWP refrigerants in automobiles," *Int. J. Air-Conditioning Refrig.*, vol. 31, no. 1, p. 2, 2023. doi: 10.1007/s44189-022-00017-1

[29] M. Elakdhar, E. Nehdi, and L. Kairouani, "Analysis of a compression/ejection cycle for domestic refrigeration," *Ind. & Eng. Chem. Res.*, vol. 46, no. 13, pp. 4639–4644, 2007. doi: 10.1021/ie070377e

[30] H. M. Ali, S. A. Kadhim, and O. A. A. M. Ibrahim, "Evaluating Refrigerant Purity Characteristics: An Experimental Approach to Assess Impact on Vapor-Compression Refrigeration System Performance," *Int. J. heat & Technol.*, vol. 41, no. 4, pp. 883–890, 2023. doi: 10.18280/ijht.410410

[31] N. Bilir and H. K. Ersoy, "Performance improvement of the vapour compression refrigeration cycle by a two-phase constant area ejector," *Int. J. energy Res.*, vol. 33, no. 5, pp. 469–480, 2009. doi: 10.1002/er.1488

[32] H. M. Ali and L. A. Mahdi, "Exergy analysis of chest freezer working with R-134a and R-600a at steady state conditions," *Int. J. Energy Prod. Manag.*, vol. 8, no. 2, pp. 63–70, 2023. doi: 10.18280/ijepm.080202

[33] M. Pitarch, E. Hervas-Blasco, E. Navarro-Peris, and J. M. Corberan, "Exergy analysis on a heat pump working between a heat sink and a heat source of finite heat capacity rate," *Int. J. Refrig.*, vol. 99, pp. 337–350, 2019. doi: 10.1016/j.ijrefrig.2018.11.044

[34] M. A. Rosen, I. Dincer, and M. Kanoglu, "Role of exergy in increasing efficiency and sustainability and reducing environmental impact," *Energy Policy*, vol. 36, no. 1, pp. 128–137, 2008. doi: 10.1016/j.enpol.2007.09.006

[35] H. Caliskan, A. Hepbasli, I. Dincer, and V. Maisotsenko, "Thermodynamic performance assessment of a novel air cooling cycle: Maisotsenko cycle," *Int. J. Refrig.*, vol. 34, no. 4, pp. 980–990, 2011. doi: 10.1016/j.ijrefrig.2011.02.001

[36] A. Mota-Babiloni, J. R. Barbosa Jr, P. Makhnatch, and J. A. Lozano, "Assessment of the utilization of equivalent warming impact metrics in refrigeration, air conditioning and heat pump systems," *Renew. Sustain. Energy Rev.*, vol. 129, p. 109929, 2020. doi: 10.1016/j.rser.2020.109929

Research Article

Evaluation of the Effect of Ethyl Alcohol Content In A Ternary Ethanol/Biodiesel/Diesel System

J.K.A. Bezerra[1]* (iD), R.R da Silva[2] (iD), E. L. de Barros Neto[3] (iD), G. G. de Medeiros[3] (iD), L. J. N. Duarte[4] (iD), H. N. M. de Oliveira[3] (iD)

[1] Doctoral student in Chemical Engineering, Graduate Chemical Engineering Program, Federal University of Rio Grande do Norte (UFRN) RN, Brazil.
[2] Graduated student in Chemical Engineering, Graduate Chemical Engineering Program, Federal University of Rio Grande do Norte (UFRN) RN, Brazil.
[3] Chemical Engineering Department, Federal University of Rio Grande do Norte (UFRN) RN, Brazil.
[4] Petroleum Engineering Department, Federal University of Rio Grande do Norte (UFRN) RN, Brazil.
E-mail: [1]*jessycakn@hotmail.com

Abstract

Increasing concern about climate change and the need to reduce dependence on fossil fuels have driven the search for more sustainable energy alternatives. One way to reduce emissions is by adding oxygenated compounds such as biodiesel and alcohols to diesel fuel. However, this can lead to phase separation between the fuels and have serious consequences for engine performance. In this context, the present study aimed to evaluate the effect of ethanol content on the miscibility of components in mixtures containing ethanol + biodiesel + diesel through the study of liquid-liquid equilibrium. The results from ternary phase diagrams revealed that the amount of water present in ethanol has a significant effect on the miscibility of the mixture components, with larger biphasic regions observed in systems with lower ethanol content. For the 95% ethanol diagram, the reliability of experimental data on equilibrium lines was assessed through the Othmer-Tobias and Hand correlations, which showed correlation coefficients (R^2) of 0.996 and 0.995, respectively. The results obtained from the NRTL and UNIQUAC thermodynamic models demonstrated excellent agreement with the experimental data, with a deviation of only 1.78 and 0.78% for the NRTL and UNIQUAC models.

Keywords: Liquid-liquid equilibrium; ethanol; biodiesel; UNIQUAC; NRTL; othmer-tobias correlation.

1. Introduction

Growing energy demands and the harm caused by fossil fuels have been an increasing concern in recent years. Although fossil fuels constitute a large part of energy consumption worldwide, they exhibit several disadvantages, such as environmental pollution and greenhouse gas emissions responsible for global warming. In this respect, numerous scientific studies have focused on promoting biofuels, considered sustainable and with a smaller carbon footprint [1], [2], [3].

In this category, biodiesel is a promising alternative to mitigate the damage caused by diesel fuel used in road transport. This biofuel can be produced from several renewable sources and has similar characteristics to oil-derived diesel. In addition, biodiesel combustion in diesel engines produces fewer greenhouse gases, such as carbon dioxide, carbon monoxide and hydrocarbons, thereby reducing atmospheric emissions from non-renewable fuels [4], [5]. Adding oxygenated compounds, such as ethanol, to diesel oil has also proved to be an interesting alternative since it has renewable origins, strengthens combustion and consequently engine performance [6], [7], [8].

In this respect, partial substitution of fossil diesel by biodiesel has been investigated, demonstrating good perspectives due to its technical and environmental capacity [9]. In addition to these advantages, ethanol also increases the octane rating of gasoline and withstands a higher compression rate. On the other hand, the limitations of these biofuels must be respected when added to fossil diesel, such as mixture immiscibility as a function of composition and temperature [10], [11].

A liquid-liquid equilibrium (LLE) study is essential to understanding how components interact and are distributed between the liquid phases present in the mixture. Thermodynamic modeling using models such as UNIQUAC and NRTL (which apply the local composition theory) is a valuable tool in predicting and understanding phase behavior in complex multicomponent systems [12], [13]. A thorough understanding is crucial to developing optimized mixtures capable of ensuring the stability and performance inherent to fuels [14].

In this respect, the present study aimed at assessing the effect of ethyl alcohol content in a ternary system consisting of Ethanol + Biodiesel + Diesel, including a liquid-liquid

---

equilibrium study to assess mixture miscibility and fuel stability when using different ethanol contents.

2. Materials and Methods

2.1 Raw Material

In the LLE, were used biodiesel produced according to the methodology of Bezerra et al.[15]. pure diesel (Nordeste Logística from Guamaré, Brazil) and ethyl alcohol (Dinâmica Química Contemporânea, 99.5%) were diluted at concentrations of 98.5, 97.5, 96.5 and 95.5%. Table 1 shows the the materials used in this study.

2.2 Isothermal Phase Diagram

Binodal curves were determined using the cloud point method, similar to mass titration, widely applied for these determinations [16], [17]. Titrations were performed in a glass cell, where the temperature was kept constant by water circulation supplied by a thermostatic bath (Figure 1). This method involves slowly adding a component to a monophasic mixture containing known amounts of each component up to the cloud point, where a second phase is visually detected. In order to determine the uncertain pattern of a binodal curve, in terms of molar fraction (x), the binodal compositions were assessed in duplicate and the u deviation values (x) for each system are presented in the footnotes of each table. The experimental data obtained for binodal curves provide useful information to select compositions in the biphasic region to be used as global composition for tie-line measurements.
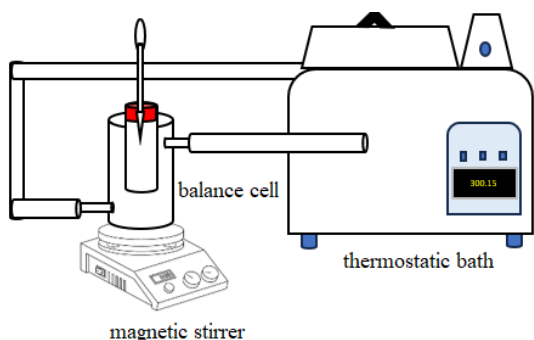
Figure 1. Schematic drawing of the system.

2.3 Tie-lines compositions

Because of the extensive area of the curve, tie-line compositions were assessed for the 95.5% diagram. Samples were prepared by weighing 30 mL of each component and the mixture was submitted to constant agitation in a magnetic agitator for three hours. Samples of each phase were collected with a syringe and their densities measured in an automatic densimeter (Anton Paar DMA 4500M). Tie-line construction required the addition of a known amount of one of the components present in the mixture in order to guarantee that the samples remained in a single phase (homogeneous mixture).

The LLE data of the ternary systems were plotted using the Origin Pro 2018 program. Based on the equilibrium lines, the distribution (β) and selectivity (S) coefficients were calculated to determine the efficiency of the solvent in extraction. The values of these parameters were obtained using Equations (1), (2) and (3), where β_2 represents the distribution coefficient of biodiesel, β_3 the distribution coefficient of diesel, S the selectivity coefficient; w_{21} the mass fraction of biodiesel in the ethanol-rich phase; w_{23} the mass fraction of biodiesel in the B12 diesel-rich phase; w_{33} the mass fraction of diesel in the diesel-rich phase and w_{31} the mass fraction of diesel in the ethanol-rich phase.

$$\beta_2 = \frac{w_{21}}{w_{23}} \tag{1}$$

$$\beta_3 = \frac{w_{31}}{w_{33}} \tag{2}$$

$$S = \frac{\beta_2}{\beta_3} \tag{3}$$

2.4 Thermodynamic Models

The thermodynamic consistency of experimental LLE data was assessed using Othmer-Tobias [18] and Hand correlations [19]. These correlations consider the mass fractions of components present in the ethanol and diesel-rich phases to reproduce the equilibrium lines and ensure data reliability. The fractions were calculated using Equations (4) and (5), where w_{11} is the mass fraction of ethanol in the ethanol-rich phase, w_{33} the mass fraction of diesel in the diesel-rich phase, w_{21} the mass fraction of biodiesel in the ethanol-rich phase and w_{23} the mass fraction of biodiesel in the diesel-rich phase.

Table 1. Materials used in this study.

Chemical Name	IUPAC Name	Source	Mass fraction	Analysis method
Biodiesel	Biodiesel	[15]	>0.98	GC[a]
Ethyl alcohol	Ethanol	Dinâmica Química Contemporânea	>0.99	GC[a]
Diesel[b]	Diesel	Nordeste Logística	>0.99	-

[a]Gas chromatography purities were provided by the manufacturers and the chemicals used without any additional treatment.
[b]Diesel sample (see supplementary materials).

$$ln\left(\frac{1 - w_{33}}{w_{33}}\right) = a + b\left(\frac{1 - w_{11}}{w_{11}}\right) \tag{4}$$

$$ln\left(\frac{w_{23}}{w_{33}}\right) = a + b\left(\frac{w_{21}}{w_{11}}\right) \tag{5}$$

In addition, thermodynamic modeling was assessed using the NRTL and UNIQUAC models based on excess Gibbs energy. Experimental data reliability was attested by the binary interaction parameters of the ternary systems composed of ethanol, biodiesel and diesel. The regression parameters of the NRTL and UNIQUAC models were determined using an objective function, according to Equation (6), which compares experimental mass compositions calculated from the different phases and equilibrium lines, where j, i, and k indicate the phase, the component and equilibrium line, respectively; M the number of equilibrium lines; w^{exp} the experimental mass composition and w^{cal} the calculated mass composition. The TML computational tool was used to determine the binary interactions of the parameters [20].

$$OF = \sum_{k=1}^{M}\sum_{j=1}^{2}\sum_{i=1}^{3}\left[\left(w_{ijk}^{exp} - w_{ijk}^{cal}\right)^2\right] \tag{6}$$

To evaluate the accuracy of the two models, the root-mean-square deviation (RMSD) was calculated by Equation (7), where k, j, i, w^{exp} and w^{cal} are the same as expressed in Equation (6).

$$RMSD(\%) = 100x\left[\sum_{k=1}^{M}\sum_{j=1}^{2}\sum_{i=1}^{3}\frac{\left(w_{ijk}^{exp} - w_{ijk}^{cal}\right)^2}{6M}\right]^{\frac{1}{2}} \tag{7}$$

The UNIQUAC model uses van der Waals® molecular volume parameters and surface area (q) for each component of the mixture. These parameters are calculated by adding the individual terms of each subgroup present in the molecules of the components, as defined by Equations (8) and (9) [21], where i is the component of the system; k, group identification; $v_k^{(i)}$, the number of k subgroups of component i; R_k, the UNIFAC volume and Q_k, the UNIFAC surface parameter. For biodiesel, the parameters were determined considering a weighted mean that considers the composition of the main esters present.

$$r_i = \sum_k v_k^{(i)}R_k \tag{8}$$

$$q_i = \sum_k v_k^{(i)}Q_k \tag{9}$$

Table 2. Experimental (Liquid-Liquid) Equilibrium Data from the Binodal Curve of the Systems: Ethanol (1) + Biodiesel (2) + Diesel (3) for Mass Fractions (w) at a Temperature 300.15 K and 101.3 kPa.

ethanol 99.5% (system 1)			ethanol 98.5% (system 2)			ethanol 97.5% (system 3)			ethanol 96.5% (system 4)			ethanol 95.5% (system 5)		
w_1	w_2	w_3	w_1	w_2	w_3	w_1	w_2	w_3	w_1	w_2	w_3	w_1	w_2	w_3
0.813	0.006	0.181	0.894	0.006	0.100	0.888	0.013	0.099	0.048	0.429	0.523	0.091	0.856	0.053
0.676	0.034	0.290	0.739	0.075	0.186	0.740	0.075	0.185	0.090	0.362	0.548	0.016	0.886	0.098
0.549	0.084	0.367	0.621	0.113	0.266	0.596	0.148	0.256	0.142	0.332	0.526	0.014	0.788	0.198
0.415	0.171	0.414	0.528	0.118	0.354	0.509	0.151	0.340	0.210	0.314	0.476	0.014	0.690	0.296
0.322	0.194	0.484	0.420	0.160	0.420	0.408	0.184	0.408	0.288	0.289	0.423	0.014	0.591	0.395
0.245	0.185	0.570	0.332	0.171	0.497	0.317	0.208	0.475	0.357	0.239	0.405	0.014	0.493	0.493
0.167	0.166	0.667	0.253	0.157	0.590	0.227	0.244	0.529	0.474	0.203	0.323	0.014	0.395	0.591
0.089	0.116	0.795	0.158	0.212	0.630	0.150	0.250	0.600	0.631	0.158	0.211	0.014	0.296	0.690
0.050	0.0	0.950	0.085	0.155	0.760	0.079	0.216	0.705	0.766	0.086	0.148	0.014	0.200	0.786
			0.043	0.143	0.814	0.035	0.049	0.916	0.856	0.045	0.099	0.014	0.099	0.887
			0.026	0.049	0.925	0.043	0.096	0.861	0.012	0.395	0.593	0.047	0.893	0.060
						0.072	0.187	0.741	0.024	0.293	0.683	0.075	0.831	0.094
									0.016	0.198	0.786	0.083	0.753	0.164
									0.022	0.097	0.881	0.161	0.641	0.198
									0.028	0.049	0.923	0.238	0.557	0.205
												0.318	0.478	0.204
												0.395	0.396	0.209
												0.484	0.322	0.194
												0.590	0.255	0.155
												0.701	0.182	0.117
												0.824	0.094	0.082
												0.895	0.047	0.058

3. Results and Discussion
3.1 Ternary Diagram Fuel Blends

The experimental miscibility curves of the ternary system [Ethanol (1) + Biodiesel (2) + Diesel (3)], at ethanol concentrations of 99.5% (system 1), 98.5% (system 2), 97.5% (system 3), 96.5% (system 4) and 95.5% (system 5), constructed at a temperature of 300.15 K, are presented in Tables 1 and 2 and plotted on the ternary diagrams of Figure 2. Ternary diagrams are generally used for extraction or purification, and to observe stable and relevant regions in fuel formulation studies [22].

The appearance of the phase diagrams plotted in Figure 2 demonstrates that the reciprocal solubility of the constituents of the mixture defines the size of the monophasic and biphasic regions. The ternary diagrams show that as ethanol content declines, there is a significant increase in the biphasic region. This behavior is associated with the rise in the amount of water present and consequent increase in ethanol molecule polarity, thereby reducing miscibility of the constituents [23], [24].

This shows the importance of a larger ethanol content when using it as an additive in fuel formulations aimed at optimizing miscibility and minimizing phase separation problems, which directly influence engine performance and efficiency [22].

Of the ternary systems studied, system 5 (ethanol 95.5%) contained an extensive biphasic region (Figure 2e), especially due to the hydrophilic and polar nature of water, present in larger amounts (5%wt), exhibiting unequal electron density distribution. Despite dissolving very well in nonpolar compounds such as gasoline, the polar extremity of ethanol molecules is characterized by the presence of a hydroxyl group (-OH). Adding water strengthens ethanol polarity due to the strong dipole-dipole interactions between them [11]. On the other hand, diesel is a mixture of nonpolar hydrocarbons composed primarily of hydrophobic alkanes. The presence of water in ethanol is even more incompatible with diesel, given that the polar nature of ethanol is intensified. Phase separation compromises fuel quality [25].
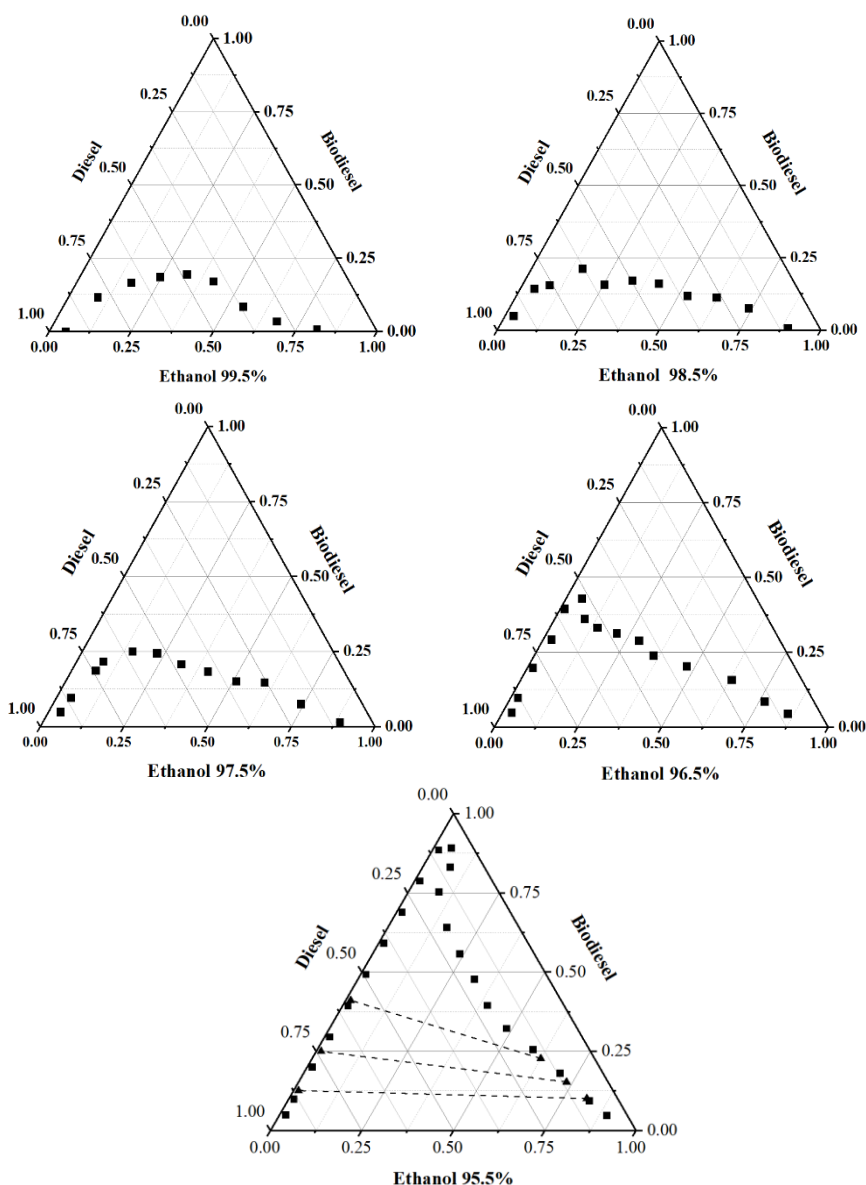

Figure 2. Ternary diagrams for LLE of different systems with Ethanol (1) + Biodiesel (2) + Diesel (3) solubility (■) and tie lines point in system 5 (▲---▲) for a mass fraction (w) at 300.15 K and 101.3 kPa.

3.2 Distribution Coefficients and Selectivity

The distribution and selectivity coefficients were performed only for system 5 (Ethanol 95.5%) because of the large biphasic region. The compositions of the equilibrium lines in the diesel and ethanol-rich phases are presented in Table 3. Greater affinity between biodiesel and diesel when compared with ethanol is evident in the slope of the equilibrium lines, indicating that the amount of biodiesel present in the diesel-rich phase is higher than in the ethanol-rich phase. The different component distribution between the phases shows a preference for a greater proportion of biodiesel to mix and solubilize in diesel when compared to ethanol [26].

The miscibility behavior of the constituents was assessed using the distribution coefficients (Figure 3), which are parameters capable of describing the distribution of a component between the two immiscible liquid phases, and selectivity coefficient (Figure 4), which quantifies the solvent extraction power of the system components [27]. The values obtained exhibited a biodiesel distribution coefficient less than 1 ($\beta_2 < 1$), which means that a larger amount of biodiesel is distributed in the diesel-rich phase, corroborating the equilibrium line results. Selectivity exhibited values above 1, underscoring diesel's preference for biodiesel and its extraction capacity, and in agreement with the other results presented. Bezerra et al. [16], obtained distribution coefficient values less than 1 and selectivity greater than 1 for systems containing biodiesel + glycerol + methanol and methyl palmitate + glycerol + methanol. Bezerra et al. [15] assessed the use of biodiesel as an additive to stabilize alcohol mixtures in diesel, proposing new formulations based on LLE studies between methanol/ethanol/butanol + biodiesel + diesel, obtaining distribution coefficient values less than 1 and selectivity greater than 1.

Table 3. *Phase Equilibrium Composition of the constituents: Ethanol 95.5% (1) + Biodiesel (2) + Diesel (3) for Mass Fractions (w) at 300.15 K and 101.3 kPa.*

diesel rich-phase				ethanol rich-phase			
w_1	w_2	w_3	densities (g.cm^{-3})	w_1	w_2	w_3	densities (g.cm^{-3})
0.014	0.411	0.575	0.841	0.626	0.223	0.151	0.820
0.014	0.250	0.736	0.834	0.733	0.153	0.114	0.815
0.014	0.126	0.860	0.829	0.815	0.101	0.084	0.811

[a]Standard uncertainties u are $u(T) = 0.5$ K, $u(P) = 1$ kPa, and $u(w) = 0.003$.

3.3 Thermodynamic Models
3.3.1 Hand and Othmer-Tobias Correlations

The reliability and consistency of the data obtained from the equilibrium lines were assessed using Othmer-Tobias and Hand correlations. The linearity of these correlations indicates the degree of consistency of the experimental data [28]. The correlation coefficients (R^2) for both equations were close to 1 (greater than 0.99), as shown in Table 4, which demonstrates the thermodynamic consistency of the experimental data. Linear behavior is also evident in the graphs presented in Figure 5. Similar results were reported by Toledo et al. [29] when studying the system (Peanut Biodiesel + Glycerol + Ethanol).
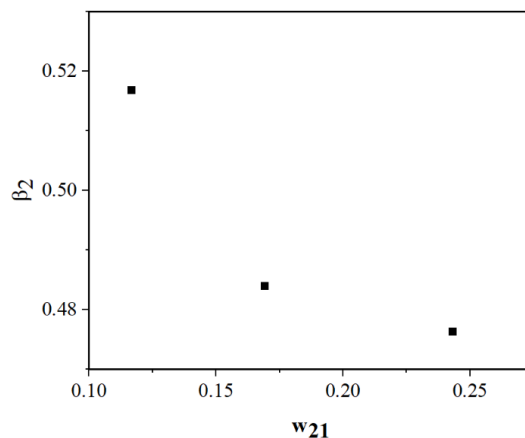
Figure 3. *Experimental solute distribution coefficient (β_2) as a function of ethanol 95.5% mass fraction for system 5 at 300.15 K and 101.3 kPa.*
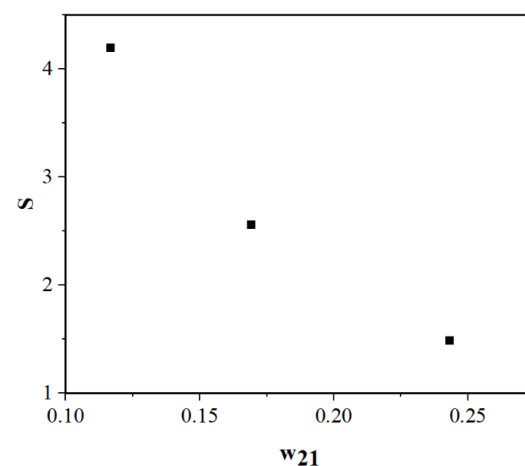
Figure 4. *Experimental selectivity value (S) as a function of ethanol mass fraction for system 5 at 300.15 K and 101.3 kPa.*

Table 4. *Othmer-Tobias and Hand Equation coefficients and the linear coefficient (R^2) for system 5.*

Correlation	a	b	R^2
Othmer-Tobias	0.688	1.397	1
Hand	1.238	1.283	0.999

3.3.2 NRTL and UNIQUAC Models

Liquid-liquid equilibrium data predictability was established using the NTRL and UNIQUAC thermodynamic models. These models can predict the molar fractions of the components in each phase, considering the intermolecular forces and molecular characteristics of each substance [21]. The values of structural parameters r and q used in the UNIQUAC model are presented in Table 5. These parameters can estimate the contributions of the groups present in the individual components, and their values are influenced by the molecular structure of each component [21]. The binary parameters Aij, Aji and aij of the UNIQUAC and NRTL correlations were estimated and are shown in Table 6.
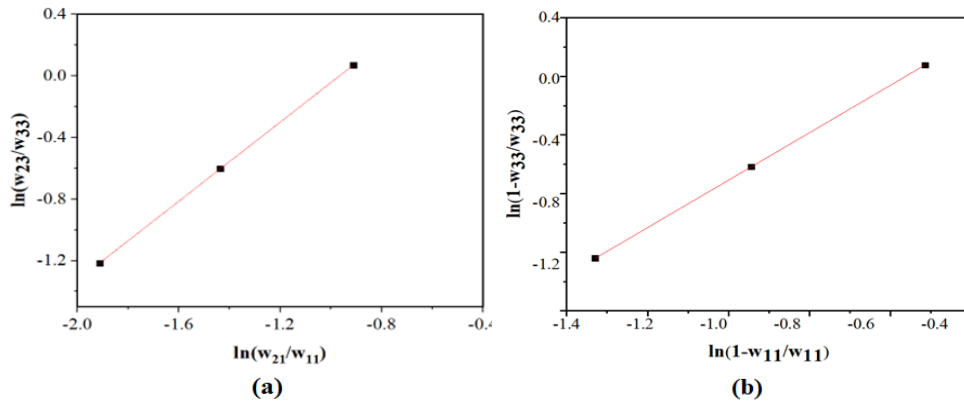
Figure 5. Thermodynamic consistency [(a) Hand and (b) Othmer-Tobias] of the experimental data for system 5 with ethanol 95.5%.

Table 5. UNIQUAC Structural Parameters (r and q) for Pure Components.

Component	r	q
Ethanol	2.575	2.588
Biodiesel	13.073	10.760
Diesel	9.677	8.004

Figure 6 shows that the experimental data were satisfactorily fit to the UNIQUAC and NRTL models, confirmed by the low root mean square deviations of 0.78 and 1.78%, respectively. These results indicate that the UNIQUAC model better fit the experimental data, demonstrating more accurate agreement between the model predictions and real observations. Santos et al.[26] reported that the experimental data of the ternary system (methyl oleate + methanol + water) fit the UNIQUAC and NRTL models satisfactorily and the former resulted in better data predictions when compared to NRTL. Evangelista Neto *et al.* [17] correlated the experimental equilibrium data of the ternary system (Chicken Fat biodiesel + Methanol + Glycerol) with the UNIQUAC model and obtained low RMSD values of 0.78 and 0.89%, respectively. These results corroborated the data obtained in the present study. Machado *et al.*, [30] assessed the estimated parameters of the UNIFAC subgroup for ethanol in predicting the LLE of the biodiesel systems, exhibiting an RMSD of 1.2%. Bezerra *et al.*[15], assessed the stimated parameters of UNIQUAC and NRTL for ternary phase diagrams for LLE of (a) methanol (1) + biodiesel (2) + diesel (3) (system 1) and (b) ethanol (1) + biodiesel (2) + diesel (3) (system 2) at 300.15 K and the results corroborated the data obtained in the present study.

Table 6. Binary parameters and Root-Mean-Square Deviation (RMSD) of system 5 [Ethanol 95.5% (1) + Biodiesel (2) + Diesel (3)].

Model	i-j	Aij	Aji	aij	RMSD (%)
UNIQUAC	1-2	-288.57	2994.5		
	1-3	294.01	168.22		0.77
	2-3	-54.89	122.99		
NRTL	1-2	149.12	337.41	0.429	
	1-3	177.33	1879.5	0.2	1.78
	2-3	2174.6	-48.15	0.47	
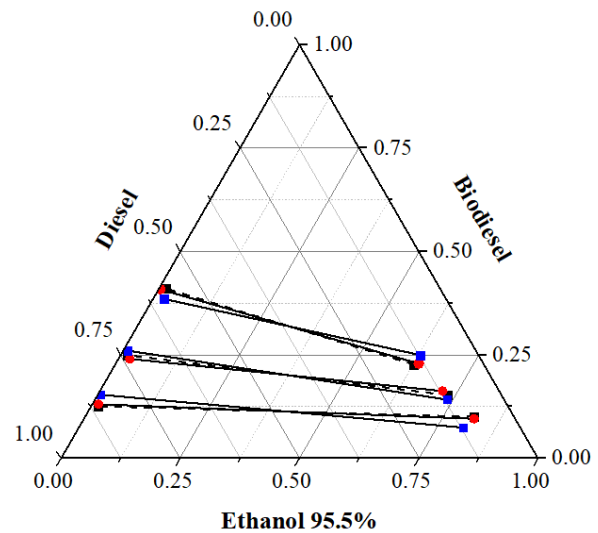
Figure 6. Ternary phase diagram for LLE of Ethanol 95.5% (1) + Biodiesel (2) + Diesel (3) at 300.15 K. Experimental tie line points for system 5 (■), NRTL model (■) and UNIQUAC model (●).

4. Conclusion

LLE analysis in the systems containing ethanol, biodiesel and diesel revealed that ethanol content plays a crucial role in the miscibility of components. Adding ethanol with higher concentrations of water resulted in a large phase separation region in the mixture, indicating lower miscibility among the constituents, due to the polar and hydrophilic nature of water. On the other hand, adding ethanol with higher purity grades promoted better miscibility, evidenced by smaller phase separation regions. The consistency of equilibrium data was assessed for system 1 using Othmer-Tobias and Hand correlations, whose correlation coefficients were higher than 0.99, demonstrating the reliability of the data. For system 5, the experimental equilibrium data and the results obtained using the NRTL and UNIQUAC thermodynamic models were compared. Both models were able to suitably represent the experimental data, with a slight advantage for the UNIQUAC model, with an average deviation of 0.78%, and 1.78% for the NRTL. These results underscore the significant influence of ethanol content on the solubilization capacity of the components and provide valuable information for the development of more stable, efficient, and sustainable fuel formulations, contribute to reducing the damage caused by fossil fuels to the environment. And, the

experimental data measured in this study for the biodiesel system may be useful in building a database for researchers involved in biodiesel process development and optimization.

Nomenclature:

Symble	Variable
β	distribution coefficient
S	selectivity coefficient
w^{exp}	experimental mass composition
w^{cal}	mass composition
$r[cm^3.g^{-1}]$	van der Waals molecular volume
$q[m^2.g^{-1}]$	molecular surface area
v_k,	the number of k subgroups
R_k,	UNIFAC group volume parameter
Q_k,	UNIFAC surface parameter.

Subscripts

1	Ethanol
2	Biodiesel
3	Diesel
j	phase
i	component
k	tie lines
M	number of tie lines

Abbrevations

LLE	Liquid-Liquid Equilibrium
GC	Gas Chromatography
OF	Objective Function
RMSD	Root-mean-square deviation
R^2	Regression coefficient

References

[1] M. H. M. Ashnani, A. Johari, H. Hashim, and E. Hasani, "A source of renewable energy in Malaysia, why biodiesel?," *Renew. Sustain. Energy Rev.*, vol. 35, pp. 244–257, 2014, doi: 10.1016/j.rser.2014.04.001.

[2] A.B.M. Sharif Hossain, A. Salleh, A. N. Boyce, P. Chowdhury and M. Naqiuddin, "Biodiesel Fuel Production from Algae as Renewable Energy". *J. Biochem. Biotechnol.*, vol. 4, no. 3, pp. 250–254, 2008.

[3] N. Gaurav, S. Sivasankari, G. S. Kiran, A. Ninawe, and J. Selvin, "Utilization of bioresources for sustainable biofuels: A Review," *Renew. Sustain. Energy Rev.*, vol. 73, no. January, pp. 205–214, 2017, doi: 10.1016/j.rser.2017.01.070.

[4] F. Fangfang, A. Alagumalai, and O. Mahian, "Sustainable biodiesel production from waste cooking oil: ANN modeling and environmental factor assessment," *Sustain. Energy Technol. Assessments*, vol. 46, no. May, p. 101265, 2021, doi: 10.1016/j.seta.2021.101265.

[5] J. Xue, T. E. Grift, and A. C. Hansen, "Effect of biodiesel on engine performances and emissions," *Renew. Sustain. Energy Rev.*, vol. 15, no. 2, pp. 1098–1116, 2011, doi: 10.1016/j.rser.2010.11.016.

[6] H. Kuszewski, "Experimental investigation of the autoignition properties of ethanol–biodiesel fuel blends," *Fuel*, vol. 235, no. September 2018, pp. 1301–1308, 2019, doi: 10.1016/j.fuel.2018.08.146.

[7] Y. Yoshimoto, E. Kinoshita, L. Shanbu, and T. Ohmura, "Influence of 1-butanol addition on diesel combustion with palm oil methyl ester/gas oil blends," *Energy*, vol. 61, pp. 44–51, 2013, doi: 10.1016/j.energy.2012.11.039.

[8] H. Venu, "An experimental assessment on the influence of fuel-borne additives on ternary fuel (diesel–biodiesel–ethanol) blends operated in a single cylinder diesel engine," *Environ. Sci. Pollut. Res.*, pp. 14660–14672, 2019, doi: 10.1007/s11356-019-04739-5.

[9] S. A. Shahir, H. H. Masjuki, M. A. Kalam, A. Imran, I. M. R. Fattah, and A. Sanjid, "Feasibility of diesel-biodiesel-ethanol/bioethanol blend as existing CI engine fuel: An assessment of properties, material compatibility, safety and combustion," *Renew. Sustain. Energy Rev.*, vol. 32, pp. 379–395, 2014, doi: 10.1016/j.rser.2014.01.029.

[10] J. Baeyens, Q. Kang, L. Appels, R. Dewil, Y. Lv, and T. Tan, "Challenges and opportunities in improving the production of bio-ethanol," *Prog. Energy Combust. Sci.*, vol. 47, pp. 60–88, 2015, doi: 10.1016/j.pecs.2014.10.003.

[11] P. Kwanchareon, A. Luengnaruemitchai, and S. Jai-In, "Solubility of a diesel-biodiesel-ethanol blend, its fuel properties, and its emission characteristics from diesel engine," *Fuel*, vol. 86, no. 7–8, pp. 1053–1061, 2007, doi: 10.1016/j.fuel.2006.09.034.

[12] H. An, W. M. Yang, and J. Li, "Effects of ethanol addition on biodiesel combustion: A modeling study," *Appl. Energy*, vol. 143, no. x, pp. 176–188, 2015, doi: 10.1016/j.apenergy.2015.01.033.

[13] R. N. Bonacorso, "Estudo do equilíbrio líquido-líquido de sistemas contendo misturas de diesel/biodiesel/etanol/1- butanol," P.h.D dissertation, Dept. Chem. Eng., Universidade Federal de Santa Maria, RS, Brazil, 2021.

[14] Z. Yang, C. Ren, S. Jiang, Y. Xin, Y. Hu, and Z. Liu, "Theoretical predictions of compatibility of polyoxymethylene dimethyl ethers with diesel fuels and diesel additives," *Fuel*, vol. 307, no. x, p. 121797, 2022, doi: 10.1016/j.fuel.2021.121797.

[15] J. K. A. Bezerra, L. J. N. Duarte, H. N. M. de Oliveira, G. G. de Medeiros, and E. L. de Barros Neto, "Experimental Study of Liquid–Liquid Equilibrium and Thermodynamic Modeling for Systems Containing Alcohols + Biodiesel + Diesel," *J. Chem. Eng. Data*, vol.68, 1739-1747, 2023, doi: 10.1021/acs.jced.3c00261.

[16] J. BEZERRA, M. R. D. A. ANDRADE, E. R. SİLVA, L. D. J. N. DUARTE, G. G. MEDEİROS, and E. L. De BARROS NETO, "Thermodynamic Modeling of Liquid-Liquid Equilibrium in Ternary Systems with Biodiesel and Isolated Ester (Methyl Palmitate)," *Int. J. Thermodyn.*, vol. 25, no. 4, pp. 56–65, 2022, doi: 10.5541/ijot.1136615.

[17] A. A. Evangelista Neto, J. C. C. Sobrinho, H. N. M. Oliveira, H. F. S. Freitas, F. F. M. Silva, and E. L. Barros Neto, "Liquid-Liquid Equilibrium Data for the Pseudo-Ternary Biodiesel of Chicken Fat + Methanol +

Glycerol," *Brazilian J. Pet. Gas*, vol. 12, no. 2, pp. 123–133, 2018, doi: 10.5419/bjpg2018-0012.

[18] D. F. Othmer and E. Tobias, "Liquid-liquid extraction data - Tie Line Correlation," *Ind. Eng. Chem.* vol.34, no.5, 1942, doi: https://doi.org.ez18.periodicos.capes.gov.br/10.1021/ie50390a600.

[19] D. B. Hand, "Dineric distribution," *J. Phys. Chem.* vol.34, no.9, 1961–2000, 1930, doi:https://doi.org/10.1021/j150315a009.

[20] L. Stragevitch, "Equilíbrio Líquido-Líquido de Misturas de Não Eletrólitos." P.h.D thesis, Dept. Chem. Eng. Universidade Estadual de Campinas, Brazil, 1997.

[21] R. C. Reid; J. M. Prausnitz; B.E. Poling, "The Properties of Gases and Liquids", *McGraw-Hill, Inc*. 4th ed. New York, 1987. ISBN 0-07-051799-1

[22] S. Vasanthaseelan, "Comprehensive Analysis for Developing Novel Fuel Blend by Ternary Analysis using Diesel –Canola Methyl Ester (Canol Biodiesel) – Ethanol; Liquid – Liquid Equilibrium," *Int. J. Sci. Eng. Res.*, vol. 7, no. 2, pp. 281–285, 2016.

[23] Y. Jiang, S. Lin, H. Yan, H. Guo, and Q. Li, "Liquid-liquid equilibrium data measurement and thermodynamic modelling for ternary mixtures composed of water, diethylene glycol dimethyl ether and different solvents at 298.2 K," *J. Chem. Thermodyn.*, vol. 165, pp. 0–7, 2022, doi: 10.1016/j.jct.2021.106669.

[24] J. C. Nunes *et al.*, "Experimental Data and Phase Equilibrium Modeling in Ternary and Pseudoquaternary Systems of Sunflower Oil for Biodiesel Production," *J. Chem. Eng. Data*, vol. 64, no. 2, pp. 412–420, 2019, doi:

10.1021/acs.jced.8b00276.

[25] D. Babu and R. Anand, "Effect of biodiesel-diesel-n-pentanol and biodiesel-diesel-n-hexanol blends on diesel engine emission and combustion characteristics," *Energy*, vol. 133, pp. 761–776, 2017, doi: 10.1016/j.energy.2017.05.103.

[26] T. Santos, J. F. Gomes, and J. Puna, "Liquid-liquid equilibrium for ternary system containing biodiesel, methanol and water," *J. Environ. Chem. Eng.*, vol. 6, no. 1, pp. 984–990, 2018, doi: 10.1016/j.jece.2017.12.068.

[27] X. Meng, X. Liu, J. Gao, D. Xu, L. Zhang, and Y. Wang, "Liquid-Liquid Equilibrium of Isobutyl Acetate + Isobutyl Alcohol + Imidazolium-Based Ionic Liquids at 298.15 and 308.15 K," *J. Chem. Eng. Data*, vol. 64, no. 2, pp. 778–783, 2019, doi: 10.1021/acs.jced.8b01045.

[28] J. J. Silva, D. M. de Mello, R. F. Pires, and S. C. Dantas, "Estudo termodinâmico do equilíbrio líquido-líquido para o sistema acetato de etila + ácido acético + água," *Res. Soc. Dev.*, vol. 11, no. 7, p. e9311729685, 2022, doi: 10.33448/rsd-v11i7.29685.

[29] I. E. P. Toledo *et al.*, "Liquid-Liquid Equilibrium of the System {Peanut Biodiesel + Glycerol + Ethanol} at Atmospheric Pressure," *J. Chem. Eng. Data*, vol. 64, no. 5, pp. 2207–2212, 2019, doi: 10.1021/acs.jced.8b01185.

[30] G. D. Machado, M. Castier, A. P. Voll, V. F. Cabral, L. Cardozo-Filho, and D. A. G. Aranda, "Ethanol and methanol Unifac subgroup parameter estimation in the prediction of the liquid-liquid equilibrium of biodiesel systems," *Fluid Phase Equilib.*, vol. 488, pp. 79–86, 2019, doi: 10.1016/j.fluid.2019.01.012.

Research Article

Analytical Modeling of Counter-Current Drying Process

*M.T. Pamuk[ID]

Okan University, İstanbul, Turkey
E-mail: *turgaypamuk@hotmail.com

Abstract

In this analytical study, spray drying of detergent particles of diameters 0.4-1 mm by using counter-current air heated at around 300ºC is investigated using Matlab©. Particle drying using hot gases is a mature process with a vast variety of applications ranging from dried food to powdered detergent production. The study shows a strong relationship between the drying process (final water content) and particle size, drying gas temperature, as well as the tower dimensions since cross-sectional area of the tower has a direct control on vertical gas velocity, thus heat and mass transfer coefficients while the height of tower is closely related to residence time of particles in tower which guarantees the targeted drying level. The conclusions of this study can be a guide to have a better set of drying parameters such as inlet temperatures and humidity/water content as well as exit temperatures and humidity/water content and valuable information on how these relate to heat energy consumption necessary to heat the air from atmospheric conditions to the desired drying gas temperature. It is also worth indicating that the measurement of the absolute humidity in tower exhaust is a good parameter to control the drying process in an effective way.

Keywords: Heat transfer; convection; mass transfer; spray drying; counter-current dryers.

1. Introduction

Particle drying is a complex phenomenon involving coupled heat and mass transfer as well as particle kinematics caused by vigorous mixing in a drying tower. Heat transfer occurs mainly in convection mode while mass transfer is an outcome of water vapor migration due to evaporation of water caused by concentration difference between the water content on the surface of the particle and the drying medium. As the drying takes place at the surface of the particle, there also occurs a mass transfer of water from the internal part of the particles to its surface due to the concentration gradient. This process continues until the particle dries to the targeted water content. Research in the area is vast ranging from analytical studies to experiments as well as numerical simulations. Mujumdar and Jog [1] proposed a simple procedure for the design of a spray drying tower especially suitable for drying of skim milk where drying gas temperature is at the vicinity of 200ºC and the powder dimension is about 100μm. Despite the simplicity of the design process and the assumptions, they point out that their model can accurately predict the required tower and nozzle dimensions as well as power requirements. The model studied in this paper is checked with their data for comparison. However, some deviations are found mainly because their tower has concurrent flow as opposed to counter-current studied herein. Wawrzyniak et al. [2] presented in their paper both theoretical and experimental determination of hydrodynamics of drying air in the industrial counter-current spray dryer. They compared experimental and theoretical results and showed that the developed CFD model of counter current spray drying process can be used for a reliable estimation of the tower

performance. Ali [3] investigated the simple plug-flow model in a pilot counter-current spray drying tower in his PhD thesis by comparing the results of numerical simulations to those of experiments performed by previous researches. According to his findings; the simple plug-flow model has the advantage of being cheap in computational resources and can be used to determine the influence of various operating parameters. Afolabi and Onifade [4] developed a fundamental model that can be used to predict the air residence time distribution of spray droplets in a counter-current spray dryer. Their simulation results show that most of spray evaporation is completed within a short-time interval meaning that the mean size of the pure liquid spray increases with time due to the rapid completion of evaporation of the smaller droplet sizes in the spray. They also indicate that there is a close agreement between the simulated result and experimental data. Ali et al. [5] implemented a steady state, three-dimensional, multiphase CFD simulation of a pilot-plant counter-current spray drying tower with an emphasis put on the modeling of particle-wall interaction. They found that the particle-wall interaction was one of the critical factors influencing the predicted average dried powder characteristics. Crosby et al. [6] investigated the effects of particle size on drying performance. They concluded that cascade control of the mean particle size, based on manipulating the mass flow rate of gas, resulted in tighter, more responsive control. They also indicate that changes in slurry rate caused complications, as the impact on particle size growth in the dryer is non-linear and difficult to predict. Gonzalez-Gallego et al. [7] investigated a co-current flow spray drying tower for maltodextrin drying using an analytical and numerical model in their study. They indicate

that their proposed model differs from a classic counter-flow model as it can predict dynamic changes even with a dispersed phase with variable velocity and it is able to predict composition, temperature and velocity of both phases, continuous and disperse, at axial points in the tower. Hernandez et al. [8] presented a novel CFD model in which different levels of deposition and Reynolds numbers for swirling-flow industrial-scale spray-drying towers are taken into account. They initially compared steady-state and transient simulations, then calibrated their CFD model using the experimental swirl intensity values under different levels of deposits. The methodology is only applicable to steady-state solutions, since the dynamic equilibrium between deposition and re-entrainment is achieved and the deposits are constant, in terms of time. They point out that it does not consider the simultaneous interaction between the deposits generated and the effect that they create on the flow. Xia et al. [9] investigated the heat and mass transfer performances of the spray drying tower under different pressures in order to explore the optimum pressure in the drying tower. They developed a three-stage heat and mass transfer model for single-droplet in their simulation to show the effect of pressure on tower height and inlet air temperature required for droplet to be completely dried. They found that the optimal pressure is increased with the increase of inlet air temperature. However, when the tower height is fixed, the inlet air temperature required for drying droplet firstly decreases and then increases with the increase of pressure. They also indicate that it is feasible to achieve complete drying in spray drying process by reducing the pressure in the tower with low inlet temperature. Jamil Ur Rahman et al [10] presented in their research an experimental analysis of a counter flow spray drying process using water and skim milk as feed. They performed their study by examining the droplet size distribution of sprays and the temperature profiles in the dryer. They evaluated the influence of air inlet temperature, air mass flow rate, feed flow rate, and droplet size on air temperatures in the dryer. Their results show that it is possible to have a process intensified spray drying technology in a counter-current setup using an elevated air temperature of 260–360°C. They point out the main problem for the high-temperature milk spray drying in a small volume is the accommodation and control of various size droplets with different velocities and drying rates, and the separation of such droplets/particles before they impinge the walls. However, the introduction of swirling flows at these locations should reduce the problem. Sefidan et al. [11] investigated in their study the spray drying process of whole milk by providing statistics on droplet conditions at exit and first impact with the surfaces of the chamber using a numerical model. They validated a four-stage droplet evaporation model against an experiment and then coupled to an Euler–Lagrange model for simulating the milk droplet trajectories inside a dryer. Their results show that larger droplets remain for a shorter residence time in the tower and contain more moisture on exiting. According to their findings regarding the drying conditions, the residence time is not affected by a decrease in the airflow inlet temperature from 200°C to 150°C. However, since the evaporation rate decreased, the result was more droplets leaving the dryer with a higher moisture content. Jubaer et al [12] assessed in their work, five different turbulence models in CFD simulations of a lab scale counter-current spray drying process. They concluded that the tested turbulence models with default settings are unlikely to provide a good agreement between the simulation and measured data, particularly for a lab scale dryer, where the flow field might not be entirely turbulent, despite the available low Reynold number corrections. They also point out that their work will prove extremely useful in simulating spray drying applications in a lab scale as well as industrial spray dryers, since the choice of an appropriate turbulence model can considerably improve the accuracy of the prediction. Hernandez et al. [13] evaluated in their study the single droplet drying (SDD) of detergents. They used experimental data are to validate a theoretical multistage model. According to their findings, drying appears to take place in three stages: The first stage being a surface drying stage with a shrinkage of the droplet until the surface gets saturated, the second stage where the drying is governed by the diffusive resistance of water through the pores and the third stage controlled by boiling temperature until the final equilibrium moisture content is achieved. Chen et al. [14] proposed a one-dimensional mathematical model for the drying process of calcium chloride solution in a co-current spray separation tower based on the four-stage drying model of single droplet. Their simulation results show that air mass flow rate, inlet solution concentration and solution mass flow rate have a greater effect on the thermal efficiency than other inlet parameters while the inlet solution concentration plays a pivotal role on the drying strength. According to their conclusions, the air mass flow rate, inlet solution concentration and solution mass flow rate have greater effect on the thermal efficiency than other parameters. Also, there exists an optimal dry air mass flow rate at which the drying strength and volumetric heat transfer coefficient are the maximum values, while the dry air mass flow rate has negative effect on the thermal efficiency, and the most significant impact on the volumetric heat transfer coefficient is the inlet solution concentration heat transfer coefficient.

In this study, the physical and process data of an example tower are considered for the analysis of the drying performance of a counter-current spray dryer. It is believed such an analytical study presented herein can make it possible to fine tune the tower to optimum operating conditions especially towards the energy efficiency of the drying tower.

2. Analytical Model

In spray drying of particles such as powdered detergent, high water content (typically 20-40%) material is forced through nozzles of small diameters at high pressure by means of special pumps into a drying tower (Figures 1 and 2). The numerical values on both figures are either directly excerpted from production data of Ali [4] or estimated/calculated by using his data. The wet particle in a drying tower meet air at average temperatures well over 200°C flowing in the opposite direction, usually in a swirling motion to enhance the heat and mass transfer and to help increase the residence time of the particle in the tower.

Particle kinematics plays an important role in spray drying. Newton's second law states that the sum of all external forces on a body must be equal to a dynamic force which is the product of mass and acceleration. While the initial vertical velocity of the particles leaving the nozzles are quite high (typically at an order of 50-100 m/s), they tend to decelerate to much lower velocities in a short time due to drag forces between the particles and gas in opposite flow as well as a net force between the gravitational and buoyancy forces. As a result of deceleration, particles slow down a

velocity of less than 10 m/s. Particles' residence time is then determined by this deceleration as well as the increased path length due to the swirling motion of the hot drying air supplied from specially directed gas inlets at the cone section of the bottom of the tower.
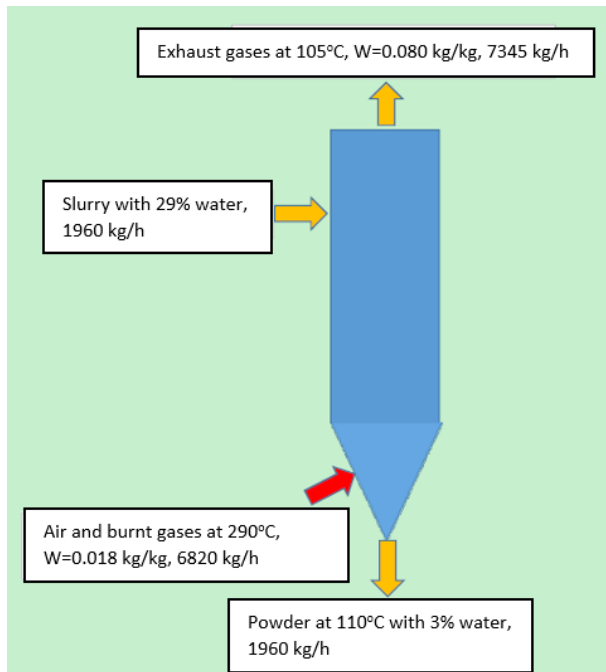

Figure 1. Counter-current drying tower (Mass balance). (Figure is in color in online version of paper).
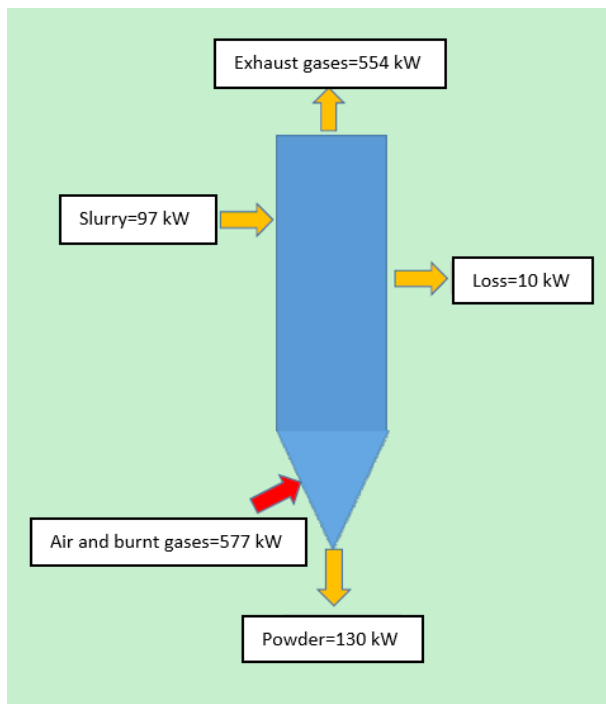

Figure 2. Counter-current drying tower (Heat balance). (Figure is in color in online version of paper).

It should be noted that the swirling strength determining the residence time is an effective vortex indicator in wall turbulence, and it can be determined based on three-dimensional (3D) velocity fields. In this context, drying throughput of the tower is strongly related to its volume which is calculated by the tower diameter and height. The smaller the diameter, the higher the vorticity, thus a larger tower height and a longer residence time. Preliminary design of a drying tower requires an extensive study of particle

kinematics. Figure 3 shows the velocity streamlines for fluid phase in a counter-current drying tower (from an unpublished work of the author).
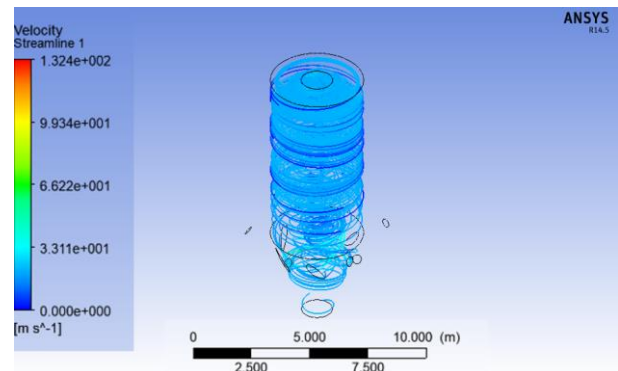
Figure 3. Velocity streamlines. (Figure is in color in online version of paper).

Once the dimensions of the tower determined using kinematic principles, methods of heat and mass transfer are implemented as drying is a result of these two principles. On one hand, convection occurs between the particle and the drying medium which is most of the time a mixture of air and hot gases as given in Equation 1 [15]:

$$\dot{Q}_{conv} = hA_o (T_o - T_\infty) \tag{1}$$

where h is convection coefficient which is dependent on many factors such as geometry and surface characteristics of the particle, flow and/or particle velocity and fluid properties. T_o and T_∞ are particle surface and fluid temperatures, respectively. On the other hand, water content of the particle is reduced due to the evaporation caused by concentration gradients and differences as given in Equations 2 and 3 respectively, as given by Çengel [15]:

$$\dot{m}_{diff} = -D_{AB}A\frac{dC}{dx} \tag{2}$$

$$\dot{m}_{conv} = h_{mass} A_o (\rho_o - \rho_\infty) \tag{3}$$

where h_{mass} is convective mass transfer coefficient and ρ is water vapor density with the subscripts o (outer surface) and ∞ (far field). Equation 2 is Fick's law which is analogous to Fourier's law in that they both are diffusion phenomena where the diffusion coefficients and variation of properties through the thickness of material (variation per unit length of the material or gradient) are the driving effects. Fourier's law gives conduction heat transfer (*e.g. kJ/s*) while Fick's law gives mass transfer (*e.g. kg/s*) depending on the diffusion coefficient (mass diffusivity) D_{AB} and concentration gradient dC/dx. A is the area perpendicular to flow in both equations. Equation 3 is analogous to Equation 1 in that they both utilize convective coefficients and differences of temperatures and concentrations. A_o is the surface area of the particle in both equations. If particle is assumed to be a sphere, Equation 2 is valid for the drying phenomenon taking place within the particle due to the water concentration variation through the radius of the particle (concentration gradient) while Equation 3 is valid for the evaporation phenomenon from the surface of the particle and the fluid due to the water concentration difference between the particle surface and the fluid. D_{AB} is strongly related to physicochemical properties of the particle

material and usually readily available while h_{mass} is much more complicated to determine.

Particles lose most of their water content according to Equations 2 and 3 as they travel from the nozzle from where they are sprayed towards the bottom of the tower under the influences of the net vertical force (gravitational and buoyancy) and drag force caused by the upward swirling air. If these two equations are set equal to each other, it is interesting to point out the analogy between lumped heat transfer and lumped mass transfer in which it is possible to describe a parameter similar to Biot number in transient heat transfer. Parti [16] performed an analytical study regarding the similarity between mass transfer Biot number and heat transfer Biot number and concluded that all the results and statements on heat transfer are applicable for mass transfer substituting the heat transfer Biot number by mass transfer Biot number.

The heat and mass transfer for the particles within the tower is a transient process as neither humidity nor the temperature of the particle remains constant throughout the process, although the particle temperature variation is much less compared to water content variation. The evaporation process causing a reduction in particle's mass and convective heat transfer causing a change in particle's temperature with the inclusion of particle's internal energy variation due to the time dependent nature of physical phenomenon can be simplified by introducing the following mathematical model (Equation 4) which belongs to the coupled heat and mass transfer [7]:

$$L \frac{dm}{dt} + hA_o (T_o - T_\infty) = mc \frac{dT}{dt} \qquad (4)$$

where L is latent heat of water, or in other words energy required for the water phase to change to gas phase during the evaporation and m and c are the mass and the specific heat of the particle, respectively. Particle temperature may remain almost constant for most of the process due to the thermal balance between the evaporative cooling and convective heat gain, although their temperature tends to increase fast as their water content become very low towards the end of the process.

Initial gas temperature T_∞ can be calculated by considering the adiabatic flame temperature of the combustion products of natural gas (*mostly methane, CH_4*) as given in Equation 5 [17]:

$$CH_4 + 2O_2 + 2(3.76)N_2 \rightarrow CO_2 + 2H_2O + 2(3.76)N_2 \qquad (5)$$
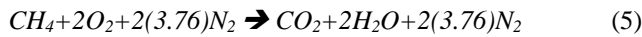
where *891 kJ/mol* energy is released. The coefficient 3.76 comes from the molar ratio of N_2 to O_2 in the atmospheric air. Above equation belongs to stoichiometric combustion of methane where the stoichiometric air/fuel ratio is $AF_{sto}=m_{air}/m_{methane}=274.6/16=17.2$. It should be noted that the chemical energy of combustion is less than *891 kJ/mol* (*HHV*) due to the fact that product water is vapor, not liquid, thus it absorbs latent heat required for vaporization. If the heat of vaporization of water is taken to be $i_{fg}=2260$ *kJ/kg=40.7 kJ/mol*, then for *2 mols* of product water to evaporate, the stoichiometric combustion requires *2x40.7=81.4 kJ* per mol of natural gas. Therefore, net heat energy released during the chemical reaction is taken to be *891-81.4~809 kJ/mol (LHV)*.

Two different analyses are performed within this study:
1. Overall mass and heat balance to and from the drying tower
2. Heat and mass interaction of individual particles as they travel within the tower

In all drying processes, the target is a predefined water content of the final product (w_p). Mass flow rate of wet product, or slurry ($\dot{m}_s$) is measured using a mass flow meter before it is supplied to tower. The process requires that either water content of slurry (w_s) or mass flow rate of dry product ($\dot{m}_p$) be known. Assuming w_s is known, following relation between $\dot{m}_s$ and $\dot{m}_p$ is obtained from Equation 6:

$$\dot{m}_p = \dot{m}_s(1 - w_s)/(1 - w_p) \qquad (6)$$

For the first part of the first analysis, Figures 1 and 2 need to be taken into account for mass and energy balances:

$$\dot{m}_s + \dot{m}_{gas} = \dot{m}_p + \dot{m}_{exh} \qquad (7)$$

$$\dot{m}_s i_s + \dot{m}_{gas} i_{gas} = \dot{m}_p i_p + \dot{m}_{exh} i_{exh} + \dot{Q}_{loss} \qquad (8)$$

where $\dot{Q}_{loss}$ is the heat lost to the surroundings from the external surface of the drying tower which may be as high as *20%* of the heat input, depending on the overall thermal resistance at tower's wall including its thermal insulation and the temperature difference between the average gas temperature in the tower and ambient temperature as well as cold air entrained at the dry product (powder) exit at the bottom due to the vacuum (in the order of *250 Pa*) at the tower top created by the suction at the exhaust side. Considering this heat loss, assuming the burner combustion efficiency and energy carried away by exhaust gases and dry product, an overall drying process thermal efficiency of η_{dry} *~50%* can be taken into account for initial calculations. However, this needs to be verified by implementing Equation 8. Enthalpies in Equation 8 can be calculated from $C_p T$ for wet and dry products as well as gas while for exhaust gas from Equation 9 as given by McQuiston et al. [18]:

$$i_{exh} = T_{exh} + W_{exh}(2501.3 + 1.86 T_{exh}) \qquad (9)$$

where i is the specific enthalpy.

Using ideal gas law $\rho = P/(RT)$, density of natural gas is calculated, then the mass flow rate of natural gas can be obtained as $\dot{m}_{CH_4} = \rho \dot{V}_{CH_4}$ where $\dot{V}_{CH_4}$ is the volumetric flowrate of natural gas.

By revisiting Equation 5, the adiabatic flame temperature of the stoichiometric combustion can be calculated using Equation 10 and 11 as given by Pulkrabek [17].

$$\dot{m}_{CH_4} + \dot{m}_{air} = \dot{m}_{CO_2} + \dot{m}_{H_2O} + \dot{m}_{N_2} = \dot{m}_{sto} \qquad (10)$$

$$\dot{m}_{CO_2} C_{p,CO_2} \Delta T_{adia} + \dot{m}_{H_2O} C_{p,H_2O} \Delta T_{adia} + \dot{m}_{N_2} C_{p,N_2} \Delta T_{adia}$$

$$= \dot{m}_{CH_4}(LHV) \qquad (11)$$

Constant temperature specific heats seen in Equation 11 are usually temperature dependent especially at temperatures such as found in flames. Using constant pressure specific heat values for C_{p,CO_2}, C_{p,H_2O} and C_{p,N_2} as *48.2 kJ/mol.K, 31.6 kJ/mol.K* and *29.4 kJ/mol.K* respectively, the

calculation yields an adiabatic temperature of about $T_{adia}=2350^oC$. It is therefore possible to calculate the mass flow rate of ambient (excess) air $\dot{m}_{exc}$ as given in Equation 12 and 13:

$$\dot{m}_{gas}i_{gas} = \dot{m}_{sto}C_pT_{adia} + \dot{m}_{exc}i_{exc} \tag{12}$$

$$\dot{m}_{gas}= \dot{m}_{sto} + \dot{m}_{exc} \tag{13}$$

and the air enthalpies can be calculated as in Equation 12 and $C_p=32.4$ $kJ/mol.K$, a weighted average of C_{p,CO_2}, C_{p,H_2O} and C_{p,N_2}. Once $\dot{m}_{exc}$ is known, all the mass flowrates can be calculated.

The humidity content of the above drying gas is very small when considered as relative humidity at the given temperature and its adverse effect on drying is negligible. However, as the evaporation from particles takes place, the water vapor content (humidity) in gas flowing towards the exit increases substantially as can be seen from Equations 14 and 15, as evaporated water will be added in gas flow.

$$\dot{m}_w = \dot{m}_{wet} - \dot{m}_{dry} \tag{14}$$

$$\dot{m}_{exh} = \dot{m}_{gas} + \dot{m}_w \tag{15}$$

For the second analysis, Matlab© is used for the calculation of the overall heat and mass transfer between the particle and the gas. Equation 4 can be solved iteratively by taking the final humidity target to terminate the calculation. The most critical part of this equation is the dying rate, or dm/dt that must be calculated by considering Equation 2. A better presentation of this equation is given in Equation 16 which is given for a hollow spherical particle:

$$\dot{m}_{diff} = 4\pi r_1 r_2 D_{AB}\frac{\rho_1-\rho_2}{r_2-r_1} \tag{16}$$

Internal surface of the hollow cylinder can be taken to be saturated at the given particle temperature which makes it possible to determine ρ_1. However, the surface water content ρ_2 is not readily available. On the other hand, at the particle-gas interface mass flow rates due to diffusion and convection must be equal, i.e. $\dot{m}_{diff} = \dot{m}_{conv}$. This equality makes it possible to eliminate ρ_2 in Equations 3 and 16, however h_{mass} is still an unknown, but it can be calculated using Chilton-Colburn analogy:

$$\frac{h_{heat}}{h_{mass}} = \rho C_p \left(\frac{\alpha}{D_{AB}}\right)^{2/3} \tag{17}$$

where α is the thermal diffusivity, D_{AB} is the diffusion coefficient of vapor in the air (different from D_{AB} in the particle which is the diffusion coefficient of water in the particle) and can be calculated from Equation 18:

$$D_{AB}=1.87x10^{-10}\frac{T^{2.072}}{P} \tag{18}$$

h_{heat} is calculated from Nusselt number ($Nu=hd/k$) for flow about spherical surfaces as proposed by Whitaker [19]

$$Nu = 2 + \left(0.4Re^{1/2} + 0.06Re^{2/3}\right)Pr^{0.4}\left(\frac{\mu}{\mu_s}\right) \tag{19}$$

which is valid for $0.71 \leq Pr \leq 380$,

$$3.5 \leq Re \leq 7.6x10^4 \ and \ 1.0 \leq \left(\frac{\mu}{\mu_s}\right) \leq 3.2$$

Above equations are evaluated sequentially and iteratively once the required reduction in water content of the final product calculated, as well as the corresponding energy requirement. The iterative calculation scheme (flowchart) is given in Figure 4.

3. Results and Discussion

For simulation purposes, standard atmospheric pressure and temperature ($P_a =101.3$ kPa and $T_a = 20^oC$) with a relative humidity of $RH_a = 50\%$ ($W_a=0.0072$ kg of $water$ per kg of dry air) are assumed. In order to have realistic simulation results, following production data of Ali [3] is used. Due to the confidentiality requirements set forth by author's institution, some of the following data have been deducted and may not reflect the actual data. For instance, tower area is calculated by using mass fluxes ($kg/m^2.s$) and enthalpy flow rates provided, using the relationships $m''=\dot{m}/A$ and $\dot{Q}_{gas} = \dot{m}i_{gas}$. Once the cross sectional area of the tower is determined, its height is calculated by using the scale of tower drawing.

Input data and stoichiometry calculations:
D = 1.65 m (estimated tower diameter)
H = 16.5 m (estimated tower height)
C_s = 2100 J/kg.C (Data, slurry specific heat)
C_p = 1500 J/kg.C (Data, powder specific heat)
ρ_s = 1200 kg/m³ (Data, slurry density)
$\dot{m}_s$ = 1960 kg/h (Data, estimated)
w_s = 29% (Data)
w_p = 3% (final water content, typical range 2-3%)
$\dot{m}_p$ = 1435 kg/h (Equation 6)
T_s = 85^oC (Data)
T_{gas}= 290^oC (Data)
T_{exh} =105^oC (Data)
d =750μm (assumed, average particle diameter)
Analyses:
As is shown in Figure 1, overall mass and heat balance to and from the drying tower: Mass balance can be obtained from Equation 7:

1960 + 6820 = 1435 + 7345 (checks)

Similarly, as is shown in Figure 2, heat balance can be obtained from Equation 20

$$\dot{m}_s i_s + \dot{m}_{gas}i_{gas} \rightarrow \dot{m}_p i_p + \dot{m}_{exh}i_{exh} + \dot{Q}_{loss} \tag{20}$$

97 + 577 = 130 + 534 + $\dot{Q}_{loss}$

It then turns out that $\dot{Q}_{loss}=10$ kW (~1.8% of the energy input which includes the effect of air entrainment also). Drying towers must be insulated against heat loss through the outer tower walls. The loss percentage is therefore a matter of insulation level, thus the loss of 20% represents a very poorly insulated tower. Using the tower data from the published work, we can deduce that the heat insulation of the tower used in this study is good. Particle flow rate:

$$\dot{n}_p=\dot{m}_s/m_p=\dot{m}_s/[\rho_s(4\pi r^3/3)]= 2.05x10^6 \ particles/s.$$
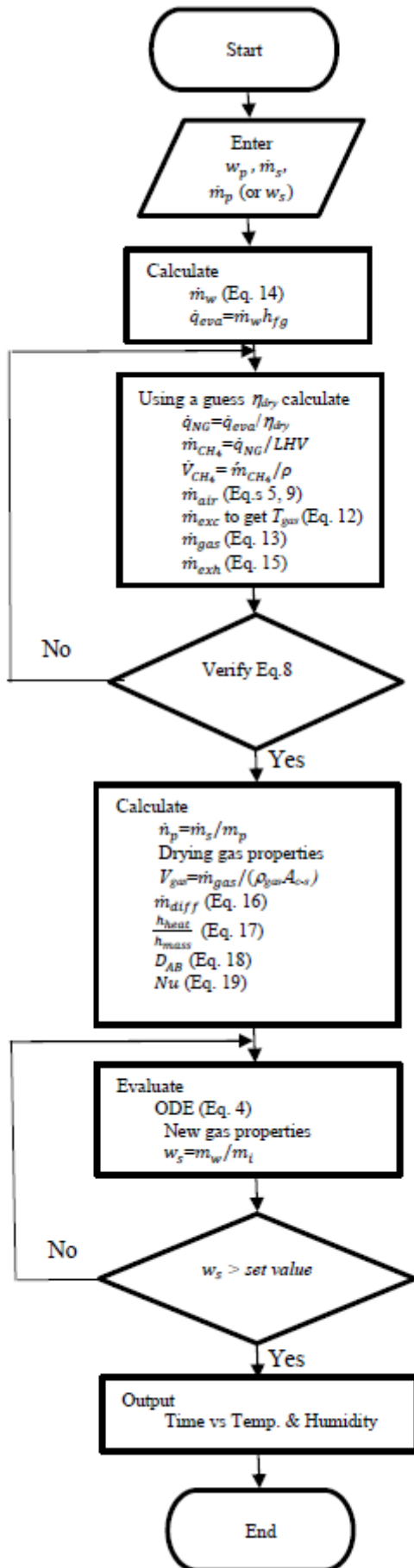
Figure 4. Flowchart of the iterative calculation scheme.

From this point on, the iterative process mentioned above is performed and following simulation results are obtained:

Figure 5 gives the temperature variation of particle and drying air for an average particle diameter of *750 μm*. The drying gas temperature is shown to be at the same instant of particle's dying process time, i.e., gas temperature at *t=0* is the gas exit temperature, not the inlet temperature. When targeted w_s is reached, the iterative calculation is terminated, therefore plot for *t > 5.3* s is not shown.

Drying time and the particle temperature at the exit strongly depends on particle diameter. To illustrate this dependence, it is interesting to investigate Figures 6 and 7. In Figure 6, the particle diameter is 400 *μm* while Figure 7 belongs to a particle with a diameter of 1000 *μm*. Same reasoning for *d=750 μm* for terminating the iterative calculation applies also to these cases. It is important to note that the temperature of the particle drops drastically at the beginning of the drying process due to the evaporative cooling caused by very high rate of mass transfer from the particle to its surroundings. As the drying proceeds, convective heat transfer becomes more accentuated where heat flows from the gas to particle causing its temperature to increase. It is vital to have a control on the exit humidity and the temperature of the particle, thus its size as well as drying gas properties are very important. This effect is seen in Figure 8 where $f=\dot{Q}_{evap}/\dot{Q}_{conv}$.
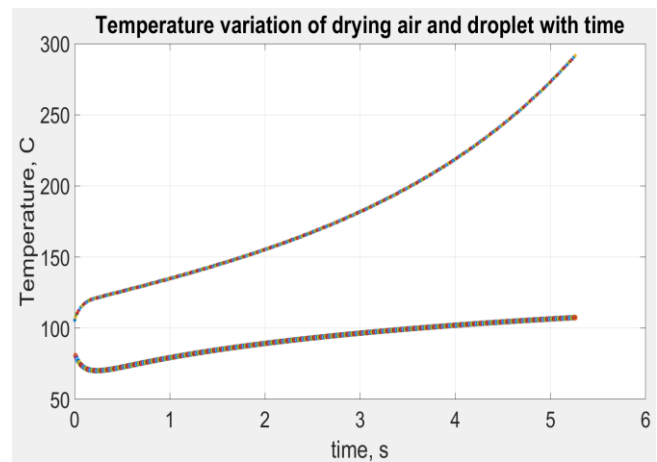
Figure 5. Temperature variation of drying air (top) and particle (d=750 μm). (Figure is in color in online version of paper).
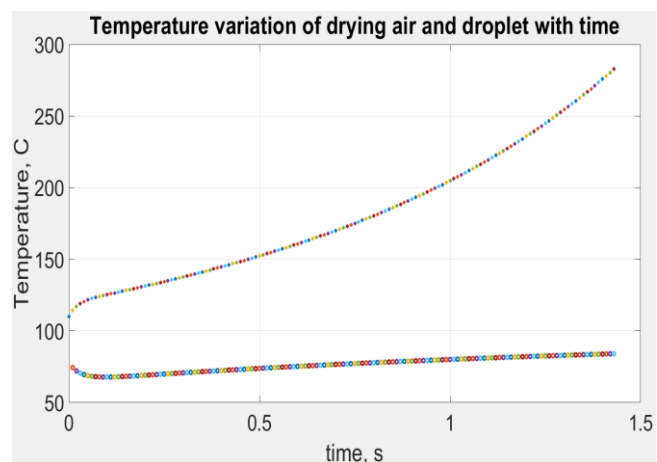
Figure 6. Temperature variation of drying air (top) and particle (d=400 μm). (Figure is in color in online version of paper).
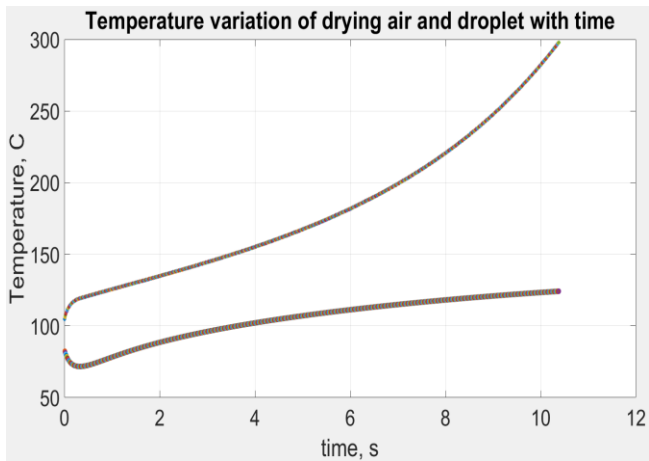
Figure 7. *Temperature variation of drying air (top) and particle (d=1000 μm). (Figure is in color in online version of paper).*
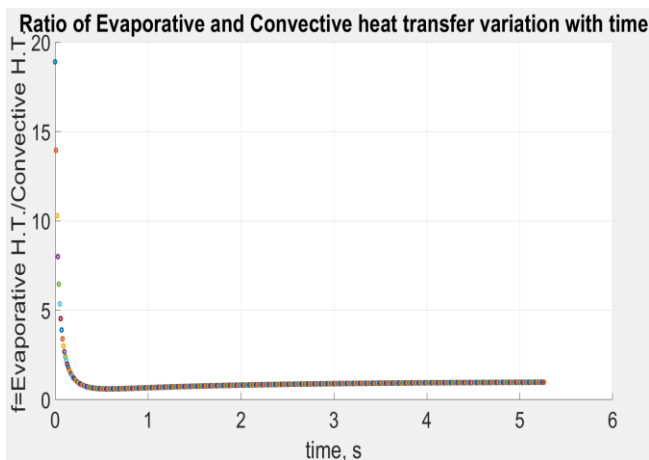
Figure 8. *Ratio of evaporative heat transfer to convective heat transfer (d=750 μm). (Figure is in color in online version of paper).*

In Figure 9, variation of Nusselt number variation is seen. The value of the Nusselt number decreases almost monotonically by 15%, due to the increasing dynamic viscosity of drying gas with temperature.

In Figure 10, variation of heat and mass transfer (*x1000*) coefficients are seen. While heat transfer coefficient increases with increasing time (or gas temperature), mass transfer coefficient remains relatively constant.

In Figure 11, evaporation rate variation in particles is seen. The initial very high water (humidity) concentration difference causes the mass transfer to be very high, however it falls very fast due to the particle's evaporative cooling, also causing its temperature to decrease. Later, with the increasing temperature difference between the particle and the drying gas, the drying process speeds up.

In Figure 12, variation of water mass fraction in particles is seen. As the particle loses water content by evaporation, the drying phenomenon accelerates due to the increasing temperature in drying gas as well as increasing concentration (humidity) difference between the particle surface and the gas.

In Figure 13, particle mass variation is seen. Its trend is very similar to Figure 12, as expected.

In Figure 14, absolute humidity variation (*W*) of drying gas is seen. Its trend is also similar to Figure 12.

In Figure 15, relative humidity variation (*RH*) of drying gas is seen. At the exhaust side it is around 12% while it is almost completely dry at the inlet.
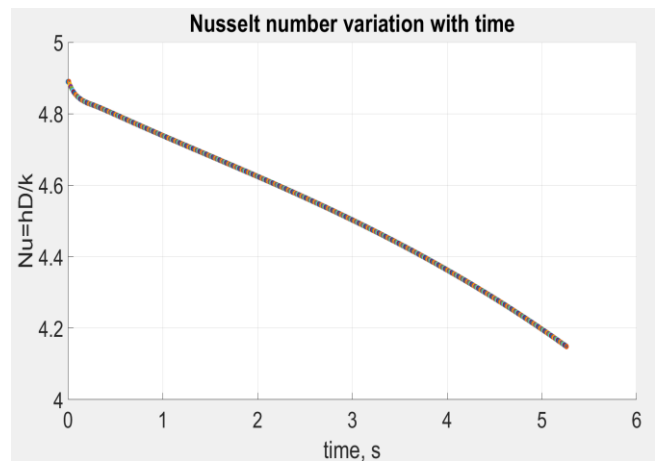
Figure 9. *Nusselt number variation for particle (d=750 μm). (Figure is in color in online version of paper).*
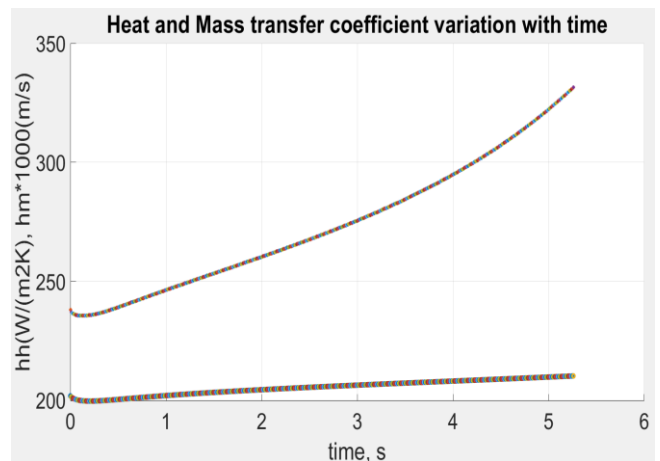
Figure 10. *Comparison of heat (top) and mass transfer (x1000) coefficients (d=750 μm). (Figure is in color in online version of paper).*
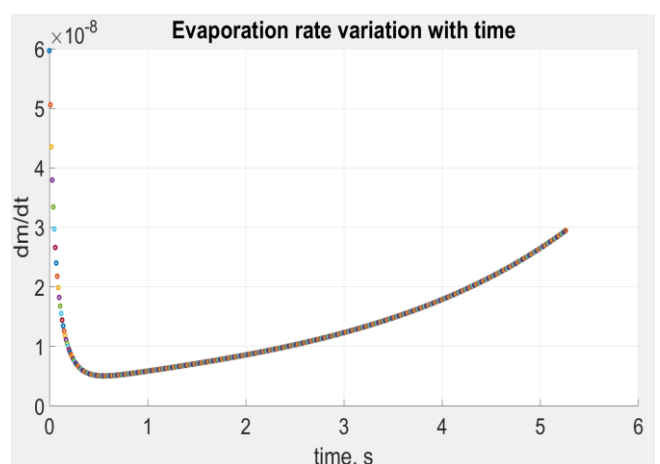
Figure 11. *Evaporation rate variation for particle (d=750 μm). (Figure is in color in online version of paper).*

The script was run for various final water contents of the final product to see the effect on the required drying time. It is observed that the drying time is inversely proportional to the final water content. The increase in drying time, or in other words energy consumption is about 3.3% when the final product water content is reduced from 3.6% to 2.4%.

Another interesting result obtained from a parametric study of the analytical model is the effect of the variation of excess air supply. When the air flowrate (stoichiometric + excess) is varied between 85%-105% of that of the problem at hand, the variation in the drying time is only within 0.4% of the 5.27 s obtained from the standard data. However variations in hot gas and final product temperatures are in the vicinity of 35°C. Especially the final product temperature may be very critical as required by the subsequent processes.
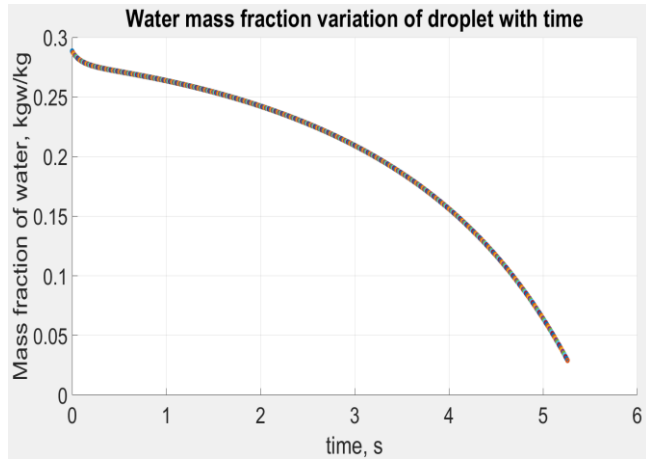
Figure 12. Water mass fraction variation in particle (d=750 μm). (Figure is in color in online version of paper).
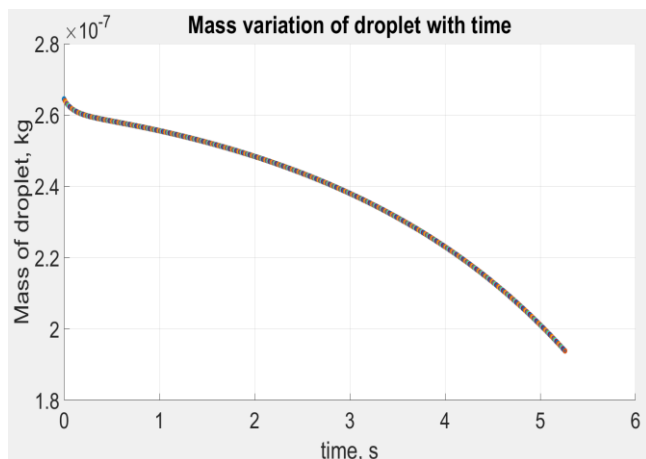
Figure 13. Mass variation in particle (d=750 μm). (Figure is in color in online version of paper).
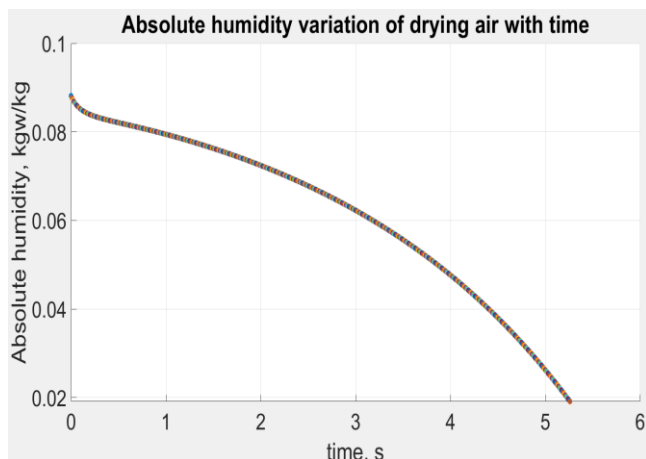
Figure 14. Absolute humidity variation in drying gas (d=750 μm). (Figure is in color in online version of paper).
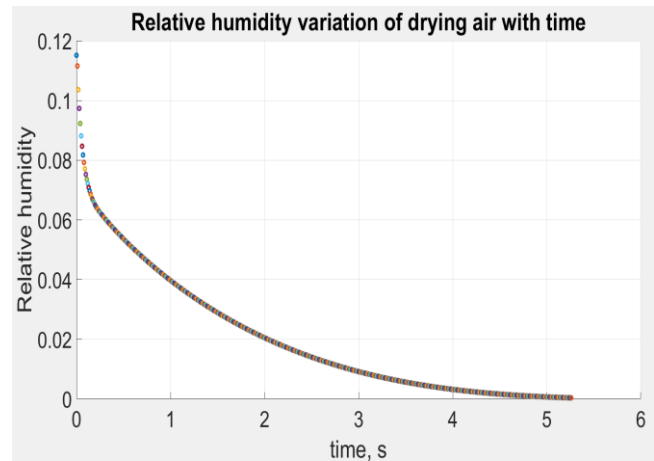
Figure 15. Relative humidity variation in drying gas (d=750 μm). (Figure is in color in online version of paper).

When the numerical results such as drying time, humidity and temperatures are compared to those provided by Ali [3], similar trends are observed. According to the researcher's plot for "residence time distribution of particles (Fig. 5.7)" provides a value about 5 s for a particle diameter of 750 μm which coincides with the required drying time.

4. Conclusion

In this study, spray drying of detergent particles of diameters *0.4-1 mm* by using counter-current air heated at around *300°C* is investigated. Due to the complexity of the drying phenomenon, best operating parameters are usually difficult to determine resulting in poor quality of final product, being either too wet or over-dried and consumption of too much heating energy. The simulation results presented in this paper based on a mathematical model that takes into account many aspects of drying kinetics show that, by observing basic parameters, it is possible to fine tune the tower to optimum operating conditions which will not only increase the tower performance but decrease the energy consumption as well. It is recommended that the absolute humidity in tower exhaust be measured to be used as a control parameter for energy input.

Nomenclature

A	area [m²]
c	specific heat [J/kg-C]
C	concentration []
d	particle diameter [μm]
D	tower diameter [m]
D_{AB}	mass diffusion coefficient [m²/s]
$\vec{F}$	Force vector [N]
h	convective heat transfer coefficient [W/m²C]
h_{mass}	convective mass transfer coefficient [W/m²C]
H	tower height [m]
HHV	higher heating value [kJ]
i	enthalpy [kJ/kg]
L	latent heat [J/kg]
LHV	lower heating value [kJ]
m	mass [kg]
$\dot{m}$	mass flow rate [kg/s]
$\dot{n}$	discrete phase flow rate [particles/s]
Nu	Nusselt number [-]
$\dot{Q}$	heat transfer rate [W]
r	particle radius [m]
P	pressure [Pa]

Pr	Prandtl number [-]
Re	Reynolds number [-]
T	temperature [C]
$\vec{v}$	velocity vector [m/s]
V	scalar velocity [m/s]
$\dot{V}$	volumetric flow rate [m^3/s]
w	water content by weight [kg/kg or %]
W	absolute humidity [kg-w/kg-a]

Greek letters

α	thermal diffusivity [m^2/s]
μ	dynamic viscosity [Pa.s]
ρ	density [kg/m^3]

Subscripts

conv	convection
adia	adiabatic
b	buoyancy
diff	difference
d	drag
dry	dry (material)
exc	excess
exh	exhaust
fg	fluid-gas (in phase change)
g	gravitational
gas	gas
loss	loss
NG	natural gas
o	outer (surface)
p	particle
s	slurry
sto	stoichiometric
w	wet
wat	water
∞	far field

References:

[1] A. S. Mujumdar and V. Jog, "Simple Procedure for Design of a Spray Dryer," *Journal of the Institution of Engineers (India): Chemical Engineering Division*, vol. 57, pp. 134-138, Jun. 1977.

[2] P. Wawrzyniak, M. Podyma, I. Zbicinski, Z. Bartczak and J. Rabaeva, "Modeling of Air Flow in an Industrial Counter current Spray-Drying Tower," *Drying Technology,* vol. 30, no. 2, pp. 217-224, Nov. 2011, doi:10.1080/07373937.2011.618282.

[3] M. Ali, "Numerical Modeling of a Counter-Current Spray Drying Tower," Ph.D. dissertation, Ins. of Particle Sci. and Eng., School of Chemical and Process Eng., The Univ. of Leeds, Woodhouse, Leeds LS2 9JT, UK, 2014.

[4] E.A. Afolabi and K. R. Onifade, "Simulation of Air Residence Time Distributions of Spray Droplets in A Counter-Current Spray Dryer," *ARPN Journal of Engineering and Applied Sciences*, vol. 9, no. 2, pp. 145-152, Feb. 2014.

[5] M. Ali, T. Mahmud, P.J. Heggs, M. Ghadiri, A. Bayly, H. Ahmadian and L. M. de Juan, "CFD Simulation of a Counter-Current Spray Drying Tower with Stochastic Treatment of Particle-Wall Collision," *Procedia Engineering*, vol. 102, pp. 1284-1294, Jan. 2015, doi:10.1016/j.proeng.2015.01.259.

[6] M. J. Crosby, L. M. De Juan, E. Martin and G. Montague, "Particle size control of detergents in mixed flow spray dryers," *The Journal of Engineering*, vol. 2015, no. 3, pp. 102–107, Feb. 2015, doi:10.1049/joe.2014.0250.

[7] S. Gonzalez-Gallego, S. López and H. Alvarez, "A phenomenological-based model for a spray drying tower,"

Brazilian Journal of Chemical Engineering, Apr. 2023. [Online]. Available: https://link.springer.com/content/pdf/10.1007/s43153-023-00323-0.pdf

[8] B. Hernandez, B. Fraser, L.M. de Juan and M. Martin, "Computational Fluid Dynamics (CFD) Modeling of Swirling Flows in Industrial Counter-Current Spray-Drying Towers under Fouling Conditions," *Industrial & Engineering Chemistry Research,* vol. 57, pp. 11988-12002, Aug. 2018, doi:10.1021/acs.iecr.8b02202.

[9] Y. Xia, J. Lu, S. Jin and Q. Cheng, "Effect of pressure on heat and mass transfer performance in spray drying tower with low inlet temperature," *Applied Thermal Engineering,* vol. 218, pp. 1-15 Jan. 2023, doi:10.1016/j.applthermaleng.2022.119260.

[10] U. Jamil Ur Rahman, A.K. Pozarlik and G. Brem, "Experimental analysis of spray drying in a process intensified counter flow dryer," *Drying Technology*, vol. 40, no. 15, pp. 3128-3148, Dec. 2021, doi:10.1080/07373937.2021.2004160.

[11] A.M. Sefidan, M. Sellier, J.N. Hewett, A. Abdollahi and G.R. Willmott, "Numerical model to study the statistics of whole milk spray drying," *Powder Technology*, vol. 411, pp. 1-14, Oct. 2022, doi:10.1016/j.powtec.2022.117923.

[12] H. Jubaer, S. Afshar, J. Xiao, D.C. Xiao, C. Selomulya and M.W. Woo, "On the effect of turbulence models on CFD simulations of a counter-current spray drying process," *Chemical Engineering Research and Design,* vol. 141, pp. 592-607, Jan. 2019, doi:10.1016/j.cherd.2018.11.024.

[13] B. Hernandez, R. Mondragon, M.A. Pintoa, L. Hernandez, J. E. Julia, J.C. Jarque, S. Chiva and M. Martin, "Single droplet drying of detergents: Experimentation and modelling," *Particuology,* vol. 58, pp. 35-47, Oct. 2021, doi:10.1016/j.partic.2021.01.012.

[14] L. Chen, C. Chen, J. Yu and S. Jin, "Study on the heat and mass transfer characteristics of spray separation tower at low temperature and normal pressure," *International Journal of Heat and Mass Transfer,* vol. 153, pp. 1-17, Jun. 2020, doi:10.1016/j.ijheatmasstransfer.2020.119662.

[15] Y.A. Çengel and A.J. Ghajar, "Mass Transfer", in *Heat and Mass Transfer: Fundamentals & Applications,* 5th ed., New York, NY, USA: McGraw-Hill, 2015, ch. 14, sec. 1-6, pp. 835-854.

[16] M. Parti, "Mass Transfer Biot Numbers," *Periodica Polytechnica Ser. Mech. Eng.,* vol. 38, no. 2-3, pp. 109-122, Feb. 1994.

[17] W.W. Pulkrabek, "Thermochemistry of fuels" in *Engineering Fundamentals of the Internal Combustion Engine*, 2nd ed., Essex, UK: Pearson, 2014, ch. 4, sec. 1, pp. 153-155.

[18] F.C. McQuiston, J.D. Parker and J.D. Spitler, "Moist Air Properties and Conditioning Processes" in *Heating Ventilating and Air Conditioning – Analysis and Design*, 6th ed., Hoboken, NJ, USA: Wiley, 2005, ch. 3, sec. 2, pp. 51-53.

[19] S. Whitaker, "Forced convection heat transfer correlations for flow in pipes, past flat plates, single cylinders, single spheres, and for flow in packed beds and tube bundles," *AIChE Journal*, vol. 18, no. 2, pp. 361-371, Mar. 1972.

Research Article

The Inflationary with Inverse Power-Law Potential in Tsallis Entropy

*M. F. Karabat [ID]

Prof. Dr. Aziz Sancar Science and Art Center
E-mail: mfarukkarabat@gmail.com

Abstract

In this article, we focus on the inflation dynamics of the early Universe using an inverse power law potential scalar field ($V_{(\phi)} = V_0 \phi^{-n}$) within the framework of Tsallis entropy. First, we derive the modified Friedmann equations from the non-additive Tsallis entropy by applying the first law of thermodynamics to the apparent horizon of the Friedmann–Robertson–Walker (FRW) Universe. We assume that the inflationary era of the Universe consists of two phases; the slow roll inflation phase and the kinetic inflation phase. We obtained the scalar spectral index n_s and tensor-to-scalar ratio r and compared our results with the latest Planck data for these phases. By choosing the appropriate values for the Tsallis parameters, which bounded by $\beta < 2$, and the inverse power-term of the potential n, we determined that the inflation era of the Universe in Tsallis entropy can only occur in the second phase (kinetic inflation), while the slow-roll inflation phase is incompatible with the Planck data.

Keywords: Tsallis entropy; inflationary; inverse power-law potential.

1. Aims and Scope

In recent years many astrophysical and cosmological studies confirm that an accelerated expansion of the Universe is taking place [1- 5]. According to our standard big bang theory there are two possible stages of accelerated expansion: one of them the early stage of the evolution of the Universe namely the inflation and the other is a current stage that we live in. In the framework of this scenario, it is possible to explain this cosmic acceleration in two ways. The first is to continue Einstein's General Theory of Relativity and introduce new energy components such as dark energy [6- 9] and an inflation field [10]. The second is to introduce a modified gravity such as F(R) gravity [11- 17], F(G) gravity [18], Galileon gravity [19-20] and Weyl gravity [21-22] etc.

On the other hand, thermodynamic gravity has been extensively discussed for a long time [23-24]. In the light of these studies, we can say that there are many indications that the concepts of gravity and entropy are related within the framework of the standard thermodynamics, which based on Boltzmann-Gibbs entropy, such as black hole mechanics [25], the Bekenstein-Hawking formula [26- 28] and the holographic principle [29-30]. However, in the framework of the Boltzmann-Gibbs entropy the energy of system is generally extensive and the entropy is additive. Therefore, it is generally known that the entropy of an entire system is not equal to the sum of the entropies of its subsystems. In another word, if we generalize this case to our Universe, the entropy of the whole Universe not necessarily equal the entropies of its subsystems. Hence, it is well known that standard Boltzmann-Gibbs additive entropy should be generalized, especially in the case of non-additive systems such as gravitational systems. [31-33]. This such approach makes use of the extended entropy instead of the additive systems.

Recently, a generalized form of non-additive entropy has been proposed by Tsallis and Cirto [34] and assuming that the Universe is a spherically symmetrical system, they showed that the Tsallis entropy is proportional to a power of the horizon field, namely $S_A \sim A^\beta$. İn this context, they argued that the microscopic mathematical expression of the thermodynamical entropy of a black holes should be as

$$S_A = \gamma A^\beta , \tag{1}$$

which is known as the Tsallis entropy, where β is the non-additive Tsallis entropy parameter, $\gamma > 0$ is a costant and A is the black hole horizon area A $= 4\pi r^2$. Herein, in the context of Tsallis cosmology scenario the Bekenstein-Hawking area law formula ($S_A = \frac{A}{4G}$) for the black hole entropy, slightly modified as $S_A = \gamma A^\beta$. It is clear that for $\beta = 1$ it reduces to the Bekenstein-Hawking conventional form or corresponding to the standard entropy. It can be seen that the cosmological application of the above (1) non-additive thermodynamics leads to the new modified Friedmann equations since it contains extra terms that appear for the first time in the general case when the Tsallis generalized entropy becomes the usual one.

In this paper, we examined the inflationary dynamics of the very early Universe (high energy era) within the framework of apparent horizon thermodynamics with the inverse power-law potential function. In this sense, first of all, we considered the Tsallis entropy corrections in the Friedmann equations and investigated the inflation dynamics of this framework also assuming phases of slow-roll inflation and kinetic inflation. We then specifically considered the Tsallis entropy as the horizon entropy and the scalar field as the matter content inside of the horizon. Taking these

assumptions into account, we investigated whether the above aforementioned phases can be achieved appropriately or not. It is worth noting that here we considered the slow-roll parameter expressions and the spectral index of the scalar perturbations valid for the canonical scalar field theory. This is a concise study of inflationary dynamics for the Tsallis' corrected General Theory of Relativity case.

In this regard, we assumed that the inflationary epoch of the Universe could consist of two phenomenological phases before the quintessence era begin, namely slow-roll and kinetic inflation. With such considerations, we calculated the observable parameters (the scalar spectral index n_s and tensor-to-scalar ratio r). Here, we used the exponent of the inverse power law term of the potential ($V_{(\phi)} = V_0 \phi^{-n}$) n and the Tsallis parameter within the limits of $0 < n < 1$, $\beta < 2$, respectively, with the e-folding number N. With these parameters, we determined how the inflationary period of the Universe behaves with respect to the Tsallis entropy scenario. In this context, we compared our results with the observational consistency of the scalar spectral of the primordial curvature perturbations n_s and the tensor-to-scalar ratio r with the latest Planck 2020 observable indices [35] for both phases aforementioned above.

Consequently, our investigations shows that in the context of the Tsallis entropy scenario under the inverse power-law potential scalar field function the slow-roll inflation phase incompatible with Planck 2020 observable satellite data since we have some β parameter constraints ($\beta < 2$). However, we observed that the kinetic inflation phase exists, which is in good agreement with Planck observable data.

This paper is organized as follows; in the next section applying the first law of thermodynamics to the apparent horizon of the Universe, we derive the modified Friedmann equations from Tsallis entropy. In the section 3, we analyzed the early inflationary dynamics of Tsallis cosmology. In the section 4, we discuss the early inflationary dynamics of Tsallis cosmology with the inverse power-law potential function, $V_{(\phi)} = V_0 \phi^{-n}$, $n > 0$, under the slow-roll condition and we determined that the slow-roll phase incompatible with Planck's observable data since the some restrict of the Tsallis entropy does not allow. In the section 5, we explored the kinetic energy (second phase) phase of the inflationary era of the Universe. We proceed in this section by considering the second phase of inflation driven by an inverse power-law potential. However, we seen that the Tsallis parameter β take the large negative values and therefore the entropy decreases in the kinetic inflation phase. We conclude final section with a discussion.

2. Modified Friedmann Equations in Tsallis Cosmology

In this section, we derive the modified Friedmann equations assuming a homogeneous and isotropic flat FRW Universe from the Tsallis Cosmology. Following [36],

$$ds^2 = h_{\mu\nu}dx^\mu dx^\nu - \tilde{r}^2[d\theta^2 + \sin^2\theta d\phi^2], \quad (2)$$

where $h_{\mu\nu} = (-1, a^2 / 1 - kr^2)$, $\tilde{r} = a(t)$ and $x^0 = t$, $x^1 = r$ represents the two dimensional metric. The parameter k is introduced to explain the spatial curvature of the metric and takes values $k = -1, 0, 1$ in case of the closed, spatially flat, an open Universe, respectively. In the framework of the thermodynamics laws, we assume that the boundary of the Universe is the apparent horizon and with its radius

$$\tilde{r}_A = \frac{1}{\sqrt{H^2 + k/a^2}}, \quad (3)$$

where $H \equiv \frac{\dot{a}}{a}$ and the dot represents the time derivative. Here the surface gravity and the apparent horizon has a related temperature [37, 38]

$$T = \frac{1}{2\pi r_A}. \quad (4)$$

We now suppose that the energy and matter content of the Universe is in the form of perfect fluid and represented by a scalar field ϕ. The corresponding Lagrangian is given by

$$\mathcal{L}_\phi = X - V_\phi \text{ and } X = -\frac{1}{2}h^{\mu\nu}\partial_\mu\phi\partial_\nu\phi, \quad (5)$$

where X and V_ϕ are the kinetic energy and the potential terms, respectively. The corresponding stress-energy tensor in four dimensions reads

$$T_{\mu\nu} = (\rho_\phi + p_\phi)u_\mu u_\nu + ph_{\mu\nu}, \quad (6)$$

where ρ_ϕ and p_ϕ represent the energy density and pressure, respectively. These are expressed as follows

$$\rho_\phi = \frac{\dot{\phi}^2}{2} + V_\phi, \quad (7)$$

$$p_\phi = \frac{\dot{\phi}^2}{2} - V_\phi. \quad (8)$$

In turn, the conservation equation, $\nabla_\mu T^{\mu\nu} = 0$, which shows the continuity equation

$$\dot{\rho}_\phi + 3H(\rho_\phi + p_\phi) = 0, \quad (9)$$

combining (7), (8) and (9), we obtain the Klein–Gordon equation of the canonical scalar field form

$$\ddot{\phi} + 3H\dot{\phi} + V_\phi = 0. \quad (10)$$

The work density is defined as [39]

$$W = -\frac{1}{2}T^{\mu\nu}h_{\mu\nu} \quad (11)$$

$$W = \frac{1}{2}(\rho_\phi - p_\phi), \quad (12)$$

where the equation (12) is in the simple form. The first law of thermodynamics at the apparent horizon is

$$dE = TdS + WdV, \quad (13)$$

where $E = \rho V$ is the total energy content of the Universe of 3- dimensional spherical volume $V = 4\pi \tilde{r}_A^3/3$ and horizon surface area $A = 4\pi\tilde{r}_A^2$.

The Eqs. (1), (4), (9), (11) and (12) into the (13) and after some algebra, we obtain the first modified Friedmann equation in Tsallis entropy [36]

$$\left(H^2 + \frac{k}{a^2}\right)^{2-\beta} = \frac{8\pi G}{3}\rho_\phi, \quad (14)$$

where we define $\gamma \equiv \frac{(2-\beta)4\pi^{1-\beta}}{4\beta G}$ and $\kappa^2 = 8\pi, G = 1$. Taking the first derivative with respect to the time of (14), using Eq. (9) and with the relation $\dot{H} = \frac{\ddot{a}}{a} - H^2$ one can get the second modified Friedmann equations [36]

$$(4-2\beta)\frac{\ddot{a}}{a}\left(H^2 + \frac{k}{a^2}\right)^{1-\beta} + (2\beta - 1)\left(H^2 + \frac{k}{a^2}\right)^{2-\beta} = -8\pi p_\phi. \tag{15}$$

3. Inflation in Tsallis Cosmology

Let us now proceed to the study of the inflationary era of the Universe within the framework of the general scalar theories. In this context, the expressions called slow-roll parameters takes the following values

$$\epsilon = -\frac{\dot{H}}{H^2}, \tag{16}$$

$$\eta = -\frac{\ddot{H}}{2H\dot{H}}. \tag{17}$$

It should be noted that, according to the slow-roll conditions both of these parameters take the very small values during the inflation $\epsilon \ll 1$, $\eta \ll 1$. On the other hand, applying the slow-roll condition to ensure inflation during the inflationary period depends only on $\epsilon \ll 1$. That is, this case is the only necessary and sufficient condition to existence an inflation. Therefore, when we apply slow-roll conditions ($\dot{\phi}^2 \ll 1$ and $\ddot{\phi} \ll 1$) on the Friedmann equations the Eq. (14) becomes [40]

$$H^2 \cong \left(\frac{8\pi}{3}\right)^{\frac{1}{2-\beta}} V_{(\phi)}^{\frac{1}{2-\beta}}. \tag{18}$$

Applying Eqs. (18) to the second Friedmann Eqs. (15) and with (10), we get the following equation [40]:

$$\dot{H} \cong -\frac{3\dot{\phi}^2}{2(2-\beta)}\left(\frac{8\pi}{3}\right)^{\frac{1}{2-\beta}} V_{(\phi)}^{\frac{\beta-1}{2-\beta}}. \tag{19}$$

Using the equations (18) and (19), the slow-roll parameters given by (16), (17) becomes [40]

$$\epsilon = \frac{\dot{\phi}^2}{2(2-\beta)} V_{(\phi)}^{-1}, \tag{20}$$

$$\eta = -\frac{1}{2}\left(\frac{8\pi}{3}\right)^{\frac{1}{2\beta-4}} \frac{V_{(\phi)}^{\frac{-1}{4-2\beta}}}{\dot{\phi}}\left[2\ddot{\phi} + \frac{\dot{\phi}^2(\beta-1)}{(2-\beta)}\frac{V_\phi}{V_{(\phi)}}\right]. \tag{21}$$

The some observable indices like the spectral index for the primordial curvature perturbation, (n_s) and the tensor-to-scalar ratio (r) can be defined by the slow-roll parameters at the leading order as:

$$n_s \cong 1 - 6\epsilon + 2\eta, \tag{22}$$

$$r = 16\epsilon. \tag{23}$$

It is well known the slow-roll parameters are determined by the value of the inflation scalar field $\emptyset$, where the comoving scale $k = aH$ exits the horizon during inflation, and k shows the comoving wave vectors [41]. It is worth noting here that to solve for $\emptyset$, the slow-roll approach is often used to calculate the e-foldings number (N), which describes the amount of inflation between two times, t_i and t_f, after the horizon exit and it defined as

$$N = \int_{t_i}^{t_f} H(t)dt, \tag{24}$$

where t_i and t_f are the quantities indicate that the beginning and ending times of the inflation period, respectively, and also t_f denotes the end of inflation defined by $\epsilon(\phi)_{end} = 1$. Here, we consider $t_i = t_c$ as the horizon crossing time and also equivalently the scalar field $\phi_i = \phi_c$. So, the above equation (24) can be expressed as

$$N = \int_{\phi_i}^{\phi_f} H\dot{\phi}^{-1}d\phi. \tag{25}$$

It is worth noting here that about 40 to 60 e-foldings numbers ($N = 40 - 60$) are required to solve the most well known flatness and horizon problems of our cosmological model. [42- 43].

4. Inverse Power-Law Scalar Potentials in the Tsallis Slow-Roll Inflation

We consider the inverse power-law potential which arises in supersymmetric theories and are given by the following form

$$V_{(\phi)} = V_0\phi^{-n}, \tag{26}$$

where both $V_0 > 0$ and $n > 0$ are constants parameters. In the standard inflationary cosmology such potentials leads to the intermediate inflation with scale factor $a(t) \propto exp(At^f)$ where $A > 0$ and $0 < f = 4/(n+4) < 1$ [44-47] are completely incompatible by Planck 2015 data [48].

In order to examine this potential term of the scalar field $(V_{(\phi)} = V_0\phi^{-n})$, we need to defined $\dot{\phi}$ (velocity) by using slow-roll inflation scenario. So the above Eqs. (10) can be write as

$$\dot{\phi} \cong -\frac{V_\phi}{3H}. \tag{27}$$

And insertion the Eqs. (18) into (27), the following is obtained:

$$\dot{\phi} = \frac{nV_0^{\frac{3-2\beta}{4-2\beta}}}{3(\frac{8\pi}{3})^{\frac{1}{4-2\beta}}}\phi^{\frac{2\beta n+2\beta-3n-4}{4-2\beta}}. \tag{28}$$

It is well known that inflation ends when $\epsilon(\phi_{end})\sim 1$. Hence, using Eqs. (28) and (26), we get the following expression

$$\phi_f = \left[\frac{6(2-\beta)(\frac{8\pi}{3})^{\frac{1}{2-\beta}}}{n^2V_0^{\frac{1-\beta}{2-\beta}}}\right]^{\frac{2-\beta}{2\beta+\beta n-4-n}}. \tag{29}$$

Similarly, we get the e-foldings number (N) from the relevant equations above as follows:

$$N = \frac{3(2-\beta)(\frac{8\pi}{3})^{\frac{1}{2-\beta}}}{n(n-\beta n-2\beta+4)V_0^{\frac{3-2\beta}{4-2\beta}}}\left[\phi_f^{\frac{n-\beta n-2\beta+4}{2-\beta}} - \phi_c^{\frac{n-\beta n-2\beta+4}{2-\beta}}\right]. \tag{30}$$

From this Eq. (30) one can get the following expression

$$\phi_c = \left[\frac{V_0^{\frac{1-\beta}{2-\beta}}(\frac{8\pi}{3})^{\frac{-1}{2-\beta}}}{6(2-\beta)}\right]^{\frac{2-\beta}{n-\beta n-2\beta+4}} [n^2 - 2nN(n - \beta n - 2\beta +$$

$$4)]^{\frac{2-\beta}{n-\beta n-2\beta+4}} . \tag{31}$$

This equation (31) expresses the scalar field at the horizon crossing. We can now write expressions corresponding to the observable indices, the scalar spectral index n_s (22) and the tensor-scalar ratio r (23). These equations can be expressed in terms of power term n and e-foldings number N as follows:

$$n_s = 1 - \left[\frac{6n-4(n+2)(2-\beta)}{n-2N(n-\beta n-2\beta+4)}\right], \tag{32}$$

$$r = \frac{16n}{n-2N(n-\beta n-2\beta+4)} . \tag{33}$$

It can be seen that the slow-roll indices depend only on the power term n and the Tsallis parameter β, and it is independent of V_0, as we expected. The Planck 2020 data [35], which set the following limits on n_s and r

$$n_s = 0.9649 \pm 0.0042 \ (68\%CL) \tag{34}$$

from Planck TT, TE, EE + lowE + lensing,

$$r < 0.064 \ (95\%CL) \tag{35}$$

from Planck TT, TE, EE + lensing + lowEB.

Table 1.The table shows some of the values of n_s and r with increasing values of n when N has large values ($N \geq 220$).

$V_{(\phi)} = V_0\phi^{-n}$					
$\beta = 1.9$					
$N \geq 220$	$n = 0.6$	$n = 0.7$	$n = 0.8$	$n = 0.9$	$n = 1$
n_s	0.9829	0.9835	0.9839	0.9842	0.9844
r	0.0639	0.0589	0.0557	0.0534	0.0517

From the table 1, it can be seen that the slow-roll inflation does not occur as the observable indices lies outside the range allowed by the Planck 2020 data [35]. This is a notable difference with the power-law potential based on Tsallis entropy [40], where the results allow for the slow-roll inflation phase. The Table 1 shows that the observable indices approach the Planck observation limits with very large values $N \geq 220$ and the large value of $\beta, \beta = 1.9$. On the other hand, the point to remember here is that the Tsallis parameter is limited to a specific values ($\beta < 2$), due to the positive definition of the energy density. For example, choosing $\beta = 2.13$ with an corresponding value of $n = 0.2$, then we would get a value in a range that allowed by Planck data [35], but this case leads to the emergence of negative energy density.

5. Inverse Power-Law Scalar Potentials in the Tsallis Kinetic Inflation

In this section, we move on to kinetic inflation, the second phase of the early inflation of the Universe after the slow-roll inflation. So we will now proceed to study this kinetic phase of the Universe, which has kinetic energy and assuming that kinetic energy is a function of the scalar field

potential. In this context, we assume that the kinetic energy has the following form

$$\dot{\phi}^2 = nV_{(\phi)}. \tag{36}$$

Using Eqs. (36), the Eqs. (18) and (19) becomes;

$$H^2 \cong \left(\frac{8\pi}{3}\right)^{\frac{1}{2-\beta}} \left(\frac{n+2}{2}\right)^{\frac{1}{2-\beta}} \phi^{\frac{-n}{2-\beta}}, \tag{37}$$

$$\dot{H} \cong -\frac{3\dot{\phi}^2}{2(2-\beta)}\left(\frac{8\pi}{3}\right)^{\frac{1}{2-\beta}}\left(\frac{n+2}{2}\right)^{\frac{\beta-1}{2-\beta}}\phi^{\frac{n-\beta n}{2-\beta}} . \tag{38}$$

Now we can write the new slow-roll parameters considering these Eqs. (37) and (38) as follows

$$\epsilon = -\frac{\dot{H}}{H^2} = \frac{3n}{(2-\beta)(n+2)}, \tag{39}$$

$$\eta = -\frac{\ddot{H}}{2H\dot{H}} = \frac{n^{\frac{3}{2}}}{(4-2\beta)}\left(\frac{8\pi}{3}\right)^{\frac{-1}{4-2\beta}}\left(\frac{n+2}{2}\right)^{\frac{-1}{4-2\beta}}\phi^{\frac{2\beta+n\beta-n-4}{4-2\beta}}. \tag{40}$$

Here, at the end of kinetic inflation this parameter take the value $\eta(\phi)_{end} = 1$, so we obtain as follows

$$\phi_f = \left[\frac{(4-2\beta)}{n^{\frac{3}{2}}}(\frac{8\pi}{3})^{\frac{1}{4-2\beta}}\left(\frac{n+2}{2}\right)^{\frac{1}{4-2\beta}}\right]^{\frac{4-2\beta}{2\beta+\beta n-4-n}}. \tag{41}$$

Using the relevant equations above and taking integration over the scalar field (25), we can get the e-foldings number as

$$N = \frac{(4-2\beta)(\frac{8\pi}{3})^{\frac{1}{4-2\beta}}(\frac{n+2}{2})^{\frac{1}{4-2\beta}}}{n^{\frac{1}{2}}(n-\beta n-2\beta+4)}\left[\phi_f^{\frac{n-\beta n-2\beta+4}{4-2\beta}} - \phi_c^{\frac{n-\beta n-2\beta+4}{4-2\beta}}\right]. \tag{42}$$

From this Eq. one can get the following expression

$$\phi_c = \left[\frac{(\frac{8\pi}{3})^{\frac{1}{4-2\beta}}(\frac{n+2}{2})^{\frac{1}{4-2\beta}}}{4-2\beta}\right]^{\frac{4-2\beta}{n-2\beta-\beta n+4}} \left[n^{\frac{3}{2}} - n^{\frac{1}{2}}N(n - 2\beta - \beta n +\right.$$

$$4)\Big]^{\frac{4-2\beta}{n-2\beta-\beta n+4}}. \tag{43}$$

This equation represents the scalar field at the horizon crossing. The observable indices, the scalar spectral index and the tensor-scalar ratio can be expressed as

$$n_s = 1 - \left[\frac{18n(n-N(n-2\beta-\beta n+4))-2n(2-\beta)(n+2)}{(2-\beta)(n+2)(n-N(n-2\beta-\beta n+4))}\right], \tag{44}$$

$$r = \frac{48n}{(2-\beta)(n+2)} . \tag{45}$$

We see that the kinetic inflation phase depends on the parameters, β, n and N. In additionally, it can be clearly seen from Eqs. (44) and (45) that observational consistency is achieved for the appropriate β and n values, unlike the previous slow-roll phase.

These results are in good agreement with the Planck data [35]. We show the observable index values (n_s, r) in the tables below. Here we see that (table 2, table 3) the best values for observable indices are in the range $0 < n < 1$. As a result, we observe that with the constraint of the inverse power term n ($0 < n < 1$), the kinetic inflation occurs in a

wide range of observable indices values, unlike the slow-roll inflation.

Table 2. The table shows the corresponding β values when $n = 0.1$.

$V_{(\phi)} = V_0\phi^{-n}$					
$n = 0.1$					
$N = 60$	$\beta = -34$	$\beta = -38$	$\beta = -42$	$\beta = -50$	$\beta = -60$
n_s	0.9761	0.9785	0.9804	0.9834	0.9861
r	0.0634	0.0571	0.0519	0.0439	0.0368

Table 3. The table shows some values of the n_s and r corresponding to the varying values of n and β .

$V_{(\phi)} = V_0\phi^{-n}$	$n = 0.01$	$n = 0.2$	$n = 0.3$	$n = 0.6$	$n = 0.6$
$N = 60$	$\beta = -2$	$\beta = -68$	$\beta = -97$	$\beta = -176$	$\beta = -180$
n_s	0.9775	0.9765	0.9762	0.9766	0.9771
r	0.0597	0.0623	0.0632	0.0622	0.0608

6. Conclusion

In the above study, using the inverse power-law potential, $V_{(\phi)} = V_0\phi^{-n}$, we explored the inflation period of the early Universe in terms of Tsallis entropy. In this context, we considered the evolution of the FRW Universe and assumed that its matter content was represented by a perfectly fluid homogeneous scalar field. Afterwards, by using the first law of thermodynamics to the apparent horizon of a FRW Universe, we derived the modification of the FRW equations from the non-additive Tsallis entropy.

For both the slow-roll and kinetic inflation phases constituting the first stage of the Universe, taking into account the inverse power-law potential, we calculated the two slow-roll parameters (ϵ, η) to obtain the observational indices (r, n_s). Finally, we compared our results with the latest Planck observation data with appropriate values of the Tsallis parameter β and the inverse power-term of the potential n. In conclusion, we determined that, unlike the slow-roll inflation, the kinetic inflation phase occurs, which is well agreement in the Planck data. In the slow-roll inflation phase, according to the obtained results, we have found that the observation does not occur due to limited Tsallis parameter, $\beta < 2$ and the e-folding number requiring $N \geq 220$.

Nomenclature

β: The non-additive Tsallis entropy parameter
ϕ: Scalar field
S_A: Tsallis entropy
N: E-folding number
r: Tensor-to-scalar ratio
n_s: Scalar spectral index
T: Temperature
V_0: Constant parameter
ϵ: Slow-roll parameter
η: Slow-roll parameter
γ: Constant
n: Exponent of the inverse power law potential
k: Spatial curvature of the metric
A: Black hole horizon area
$\tilde{r}_A$: Radius
H: Hubble constant
$\mathcal{L}$: Lagrangian
$T_{\mu\nu}$: Stress-energy tensor

ρ_ϕ: Energy density
p_ϕ: Pressure
W: Work density
E: Energy
V: Volume

References:

[1] A. G. Riess et al., ''Observational evidence from supernovae for an accelerating Universe and a cosmological constant,'' *Astron. J. 116*, 1009, 1998.

[2] S. Perlmutter et al., ''Measurements of Omega and Lambda from 42 High-Redshift supernovae,'' *Astrophys. J. 517*, 565, 1998.

[3] P. A. R. Ade et al., ''Joint Analysis of BICEP2/Keck Array and Planck Data'' *Astron. Astrophys. 571*, A16, 2014.

[4] R. G. Vishwakarma, ''Mon. Not. Roy,'' *Astron. Soc. 331*, 776, 2002.

[5] S. L. Briddle, O. Lahav, J. P. Ostriker, P.J. Steinhardt, "Precision cosmology? Not just yet,'' *Science, vol.299*, pp.1532–1533, 2003.

[6] P. J. E. Peebles, B. Ratra, "Cosmic Discordance: Planck and luminosity distance data exclude LCDM'' *Rev. Mod. Phys. 75*, 559, 2003.

[7] Y. F. Cai, E. N. Saridakis, M. R. Setare and J. Q. Xia., "Holographic dark energy through Tsallis entropy,'' *Phys. Rept. 493,* 1, 2010.

[8] P. J. E. Peebles, B. Ratra, ''The cosmological constant and dark energy,'' *Rev. Mod. Phys. 75,* 559, 2003, arXiv:astro-ph/0207347.

[9] Y. F. Cai, E. N. Saridakis, M. R. Setare, J. Q. Xia, "Quintom cosmology: theoretical implications and observations,'' *Phys. Rept. 493,* 1, 2010, arXiv:0909.2776 [hep-th].

[10] N. Bartolo, E. Komatsu, S. Mattarrese and A. Riotto., ''Non-Gaussianity from Inflation: Theory and Observations,'' *Phys. Rept. 402*, 103, 2004.

[11] S. Nojiri, S. D. Odintsov, ''Modified f(R) gravity consistent with realistic cosmology: from matter dominated epoch to dark energy Universe,'' *Phys. Rev. D 74*, 086005, 2006.

[12] S. Nojiri, S. D. Odintsov, ''Unified cosmic history in modified gravity: from F(R) theory to Lorentz non-invariant models,'' *Phys. Rept. 505*, 59, 2011.

[13] S. Nojiri, S. D. Odintsov, ''Modified gravity with negative and positive powers of curvature: Unification of inflation and cosmic acceleration,'' *Phys. Rev. D 68,* 123512, 2003, arXiv:hep-th/0307288.

[14] S. Nojiri, S. D. Odintsov, "Introduction to modified gravity and gravitational alternative for dark energy,'' *Int. J. Geom. Meth. Mod. Phys. 4*, 115, 2007.

[15] S. Capozziello, M. D. Laurentis, ''Introduction to modified gravity and gravitational alternative for dark energy,'' *Phys. Rept. 509*, 167, 2011, arXiv:1108.6266 [gr-qc].

[16] Y. F. Cai, S. Capozziello, M. D. Laurentis, E.N. Saridakis, ''f (T) teleparallel gravity and cosmology,''

Rept. Prog. Phys. 79, 106901, 2016, arXiv:1511.07586 [gr-qc].

[17] S. Nojiri, S. D. Odintsov, "Modified Gauss–Bonnet theory as gravitational alternative for dark energy," *Phys. Lett. B 631,* 1, 2005, arXiv:hep-th/0508049.

[18] S. Nojiri, S. D. Odintsov, Petr V. Tretyakov. "From inflation to dark energy in the non-minimal modified gravity," *Progress of Theoretical Physics Supplement 172,* 81-89, 2008,

[19] C. Deffayet, G. Esposito-Farese, A. Vikman, "Covariant galileon," *Phys. Rev. D 79,* 084003, 2009, arXiv:0901.1314 [hep-th].

[20] G. Leon, E.N. Saridakis, "Dynamical analysis of generalized Galileon cosmology," *JCAP 1303,* 025, 2013, arXiv:1211.3088 [astro-ph.CO].

[21] P. D. Mannheim, D. Kazanas, "Exact vacuum solution to conformal Weyl gravity and galactic rotation curves," *Astrophys. J. 342,* 635, 1989.

[22] E. E. Flanagan, "Fourth order Weyl gravity," *Phys. Rev. D 74,* 023002, 2006, arXiv:astro-ph/0605504.

[23] T. Padmanabhan, "Gravity and the thermodynamics of horizons," *Phys. Rep. 406,* 49, 2005.

[24] E. Verlinde, "On the origin of gravity and the laws of Newton," J. *High Energy Phys. 1104,* 029, 2011.

[25] J. M. Bardeen, B. Carter, S. Hawking, "The four laws of black hole mechanics," *Commun. Math. Phys. 31,* 161, 1973.

[26] J. D. Bekenstein, "Black holes and entropy," *Phys. Rev. D 7,* 2333, 1973.

[27] J. B. Hartle, S. W. Hawking. "Path-integral derivation of black-hole radiance," *Physical Review D* 13.8, 2188, 1976.

[28] L. Buoninfante, G. G. Luciano, L. Petruzziello, F. Scardigli, "Bekenstein bound and uncertainty relations," *Phys. Lett. B 824,* 136818, 2022.

[29] G. T. Hooft, "Dimensional reduction in quantum gravity," *arXiv preprint gr-qc/9310026,* 1993.

[30] L. Susskind, "The world as a hologram," *J. Math. Phys. 36,* 6377, 1995.

[31] G. Wilk, Z. Wlodarczyk, "Interpretation of the nonextensivity parameter q in some applications of Tsallis statistics and Lévy distributions," *Physical Review Letters* 84.13, 2770, 2000.

[32] M. L. Lyra, C. Tsallis, "Non-extensivity and multifractality in low-dimensional dissipative systems,"

Phys. Rev. Lett. 80, 53, 1998.

[33] C. Tsallis, R. S. Mendes, A. R. Plastino, "The role of constraints within generalized non-extensive statistics," *Physica A: Statistical Mechanics and its Applications* 261.3-4, 534-554, 1998.

[34] C. Tsallis, L. J. L. Cirto, "Black hole thermodynamical entropy," *Eur. Phys. J. C 73,* 2487, 2013.

[35] Y. Akrami et al., Planck. "Planck 2018 results-X. Constraints on inflation," *Astron. Astrophys. 641,* A10, 2020.

[36] A. Sheykhi, "Modified Friedmann equations from Tsallis entropy," *Physics Letters B 785,* 118, 2018.

[37] K. Huang, *Statistical Mechanics,* John Wiley & Sons, 2008.

[38] T. Padmanabhan, "Thermodynamical aspects of gravity: new insights," *Reports on Progress in Physics* 73.4, 046901, 2010.

[39] M. Akbar, R. G. Cai, "Thermodynamic behavior of Friedmann equation at apparent horizon of FRW Universe," *Phys. Rev. D 75,* 08400, 2007, arXiv:0609128 [hep-th].

[40] A. I. Keskin, "The inflationary era of the universe via Tsallis cosmology," *Int. J. Geom. Methods Mod. Phys. 19,* 2250005, 2022.

[41] R. Brandenberger, P. Peter, "Bouncing cosmologies: progress and problems," *Found. Phys. 47,* 797, 2017, https:// doi.org/10.1007/s10701-016-0057-0.

[42] L. Randall, M. Soljacic, "Supernatural inflation: Inflation from supersymmetry with no (very) small parameters," A.H. Guth, *Nucl. Phys. B 472,* 377, 1996.

[43] V. Barger, H. S. Lee, D. Marfatia, "WMAP and inflation," *Phys. Lett. B 565,* 33, 2003.

[44] J. D. Barrow, "Graduated inflationary universes," *Physics Letters B 235,* 40, 1990.

[45] J. D. Barrow, A. R. Liddle, "Perturbation spectra from intermediate inflation," *Physical Review D 47,* R5219, 1993.

[46] J. D. Barrow, A. R. Liddle, C. Pahud, "Intermediate inflation in light of the three-year WMAP observations," *Physical Review D 74,* 127305, 2006.

[47] J. D. Barrow, N. J. Nunes, "Dynamics of "logamediate" inflation," *Physical Review D 76,* 043501, 2007.

[48] P. A. R. Ade, et al., "Planck 2015 results-XX. Constraints on inflation," *Astronomy & Astrophysics 594,* A20, 2016.

Research Article

Calculation of Azeotropic Properties for Ternary Mixtures with the PC-SAFT Equation of State

[1]F. Zemmouri ⓘD, [2*]H. Madani ⓘD [3]I. Anoune ⓘD, [4]A. Merzougui ⓘD

[1,2,3] Laboratory of Studies on Industrial Energy Systems, Faculty of Technology, University of Batna 2, 05000 Algeria.
[1,4] Department of Chemical Engineering, University Mohamed Khider, Biskra, 07000, Algeria.
E-mails: [1]zemmourifayza@yahoo.com, [2*]h.madani@univ-batna2.dz, [3]imad.announe@gtft.dz, [4]a.merzougui@univ-biskra.dz

Abstract

In this study, a novel approach employing the Perturbed-Chain Statistical Associating Fluid Theory (PC-SAFT) Equation of State was introduced to investigate azeotropic behavior in ternary mixtures and explore their liquid-vapor equilibria. The temperature range spans (243.15–323.5) K, covering a broad spectrum of conditions relevant to industrial and chemical processes. Our analysis focuses on six different ternary mixtures: Difluoromethane (R32) + 1,1-difluoroethane (R152a) + 2,3,3,3-tetrafluoropro-1-ene (R1234yf); Isobutane (R600a) + 1,1-difluoroethane (R152a) + 1,1,2,2-tetrafluoroethane (R134); 1,1,1,2-tetrafluoroethane (R134a) + 2,3,3,3-tetrafluoropro-1-ene (R1234yf) + isobutane (R600a); 1,1,1,2-tetrafluoroethane (R134a) + 2,3,3,3-tetrafluoropro-1-ene (R1234yf) + dimethyl ether (DME); isobutene (R600a) + 1,3,3,3-tetrafluoropropene (R12345ze(E)) + trifluoroiodomethane (R13I1); and difluoromethane (R32) + fluoroethane (R161) + 1,3,3,3-tetrafluoropropene (R1234ze(E)). Among these, only three mixtures exhibit azeotropic behavior.

The PC-SAFT equation of state, incorporating an expansion form tailored for Vapor-Liquid Equilibrium (VLE) calculations within ternary mixtures, determined azeotropic composition and pressure based on the Gibbs-Konovalov theorem, which characterizes azeotropic behavior under constant temperature. Our estimations of the VLE and azeotropic composition and pressure closely align with experimental data. The maximum relative error in pressure does not exceed 4.2% for the R600a + R152a + R134 mixture and remains less than 6.56% for the liquid composition of R1234ze(E) within the (R600a + R1234ze(E) + R13I1) ternary mixture. These results underscore the reliability and accuracy of the PC-SAFT equation of state in modeling azeotropes within ternary mixtures.

Keywords: Ternary mixture; azeotrope; PC-SAFT; equation of state.

1. Introduction

In the field of refrigeration science, a paramount concern revolves around the preservation of the global environment. Extensive research endeavors have been initiated with the overarching objective of identifying novel refrigeration mixtures that wield a minimal environmental impact, particularly with respect to mitigating global warming and curbing ozone layer depletion. In recent years, heightened attention has been directed towards two interrelated challenges: the phenomenon of climate warming and the depletion of the ozone layer. In response to these pressing issues, various regulatory frameworks and protocols, such as the Montreal Protocol of 1987 and the Kyoto Protocol of 1997, have been established to delineate stringent guidelines governing the usage and management of refrigerants.

In various industrial contexts, the use of both pure compounds and complex mixtures is essential. Achieving efficient industrial process design relies heavily on a thorough comprehension of the thermophysical properties and phase behavior exhibited by these components and mixtures. Within the specific scientific purview, Gross and Sadowski [1,2] have contributed significantly by formulating the Perturbed-Chain Statistical Associating

Fluid Theory (PC-SAFT) equation of state. In marked contrast to the foundational SAFT equation of state initially postulated by Huang and Radosz [3,4] alongside its multiple well-established modified versions [5,12] In the PC-SAFT approach, a hard-chain reference system is employed instead of the conventional hard-sphere reference system when applying the standard second-order high-temperature perturbation theory of Barker and Henderson [13] to obtain the dispersion contribution. Additional binary interaction parameters are integrated to rectify molecular interactions, yielding results that demonstrate robust extrapolation capabilities.

Our primary objective is the development of an innovative and robust method for predicting azeotrope positions in complex multicomponent mixtures. Extensive research conducted within our research group [14], [15] has laid the foundation for this endeavor. In this study, a novel approach is introduced for the direct determination of azeotropes, both empirically from experimental data and theoretically through the employment of the PC-SAFT thermodynamic model. Six ternary mixtures were investigated: (R32 + R152a + R1234yf), (R600a + R152a + R134), (R134a + R1234yf + R600a), (R134a + R1234yf +
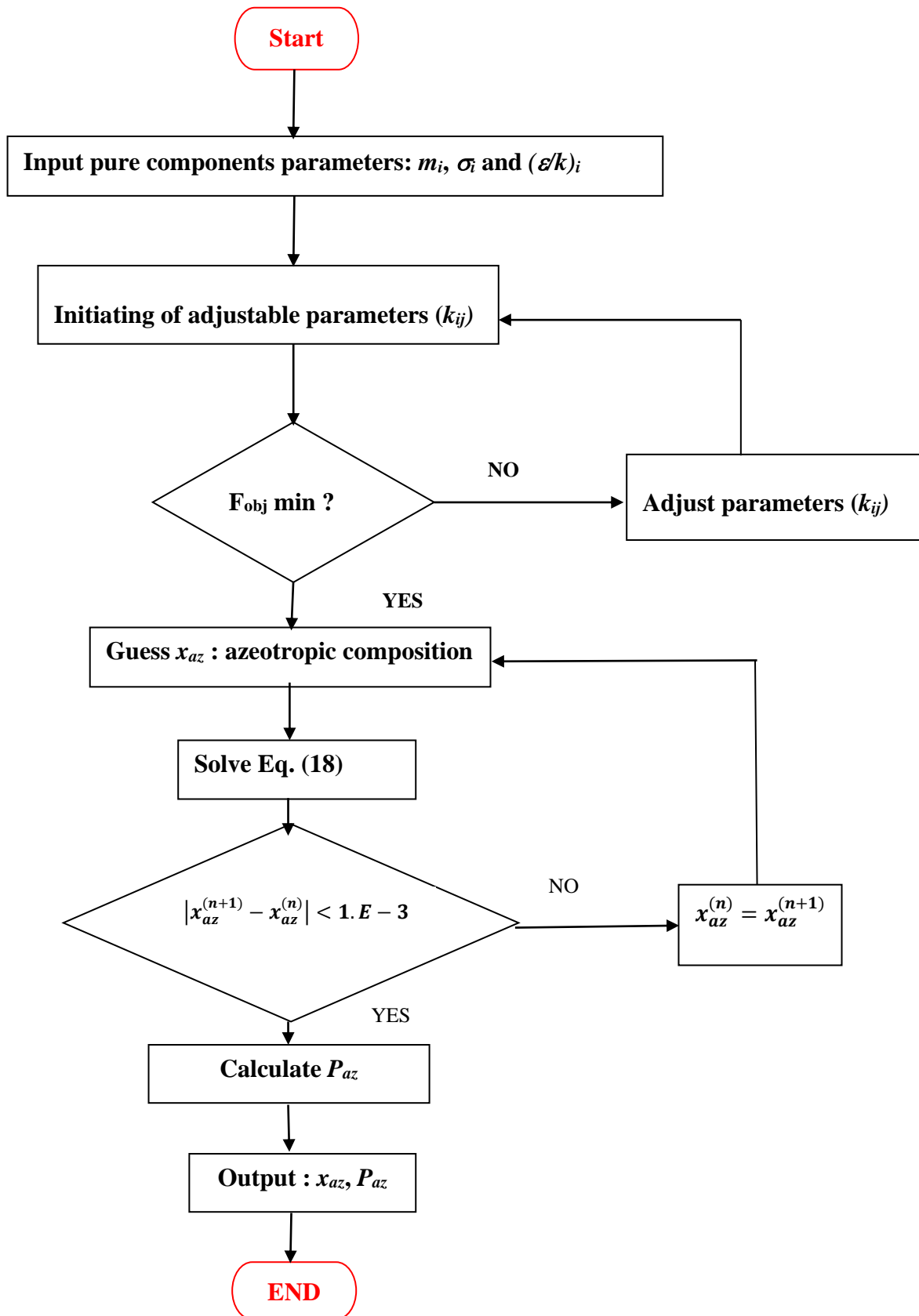
Figure 1. The calculation procedure for azeotropic properties by PC-SAFT model.

DME), (R600a + R1234ze(E) + R13I1), and (R32 + R161 + R1234ze(E)), with three of these mixtures displaying azeotropic behavior. It is worth noting that the examined mixtures in our study are environmentally friendly, characterized by low Global Warming Potential (GWP) and zero Ozone Depletion Potential (ODP).

2. PC-SAFT Model

The definition of the residual Helmholtz free energy $\tilde{a}^{res}$ (reduced quantity) is given by:

$$\tilde{a}^{res} = \frac{A^{res}}{NkT} \tag{1}$$

where, A^{res} is the Helmholtz free energy, N is the Avogadro

Table 1. Parameters and properties of investigated components.

Component	R13I1	R152a	R600a	R1234ze(E)	R134	R134a	R32	R1234yf	DME	R161
Environment characterization [a]										
GWP	0	124	3	7	1500	1430	675	4	1	12
ODP	0	0	0	0	0	0	0	0	0	0
Critical properties and acentric factor [b]										
Tc (K)	396.44	386.41	407.81	382.51	391.74	374.21	351.60	367.85	400.10	375.31
Pc (MPa)	3.9530	4.5168	3.6290	3.6350	4.6400	4.0590	5.8300	3.3823	5.370	5.028
ω	0.1760	0.2752	0.1840	0.3130	0.2930	0.3270	0.2769	0.2760	0.204	0.209
Pure-component parameters [c]										
m	2.29706	3.05606	2.38497	3.43117	3.26450	3.53622	3.01995	3.06453	2.48190	2.61983
σ [°A]	3.70077	3.17498	3.79437	3.26153	3.08382	3.08618	2.84472	3.43605	3.27078	3.20027
ε/k [K]	205.748	176.207	207.923	166.181	173.717	160.601	160.998	167.544	200.370	183.182

[a] From ref. [14–15].

[b] From ref. [18–23].

[c] From ref. [17].

Table 2. Experimental and calculated VLE in the system R32(1) + R152a(2) + R1234yf(3) [18].

T[K]	P_{exp}[MPa]	P_{cal}[MPa]	x_{1exp}	y_{1exp}	y_{1cal}	y_{2exp}	y_{2cal}	ΔP[MPa]	Δy_1	Δy_2
283.15										
	0.532	0.534	0.131	0.265	0.266	0.380	0.372	0.002	0.001	-0.008
	0.500	0.506	0.146	0.298	0.301	0.589	0.576	0.006	0.003	-0.013
	0.594	0.584	0.170	0.347	0.336	0.151	0.158	-0.010	-0.011	0.006
	0.663	0.669	0.363	0.574	0.578	0.322	0.321	0.006	0.003	-0.001
	0.783	0.772	0.425	0.628	0.626	0.098	0.093	-0.011	-0.002	-0.005
	0.834	0.836	0.559	0.727	0.734	0.132	0.131	0.002	0.007	0.001
293.15										
	0.714	0.715	0.129	0.252	0.254	0.385	0.380	0.002	0.002	-0.005
	0.674	0.675	0.144	0.280	0.282	0.601	0.596	0.001	0.002	-0.005
	0.789	0.783	0.167	0.330	0.324	0.157	0.160	-0.006	-0.006	0.002
	0.884	0.882	0.360	0.557	0.558	0.338	0.336	-0.002	0.001	-0.002
	1.034	1.032	0.421	0.608	0.611	0.096	0.095	-0.003	0.002	-0.001
	1.106	1.109	0.556	0.718	0.721	0.139	0.137	0.003	0.003	-0.002
303.15										
	0.937	0.940	0.127	0.237	0.239	0.396	0.392	0.003	0.002	-0.004
	0.890	0.890	0.143	0.265	0.266	0.617	0.612	0.000	0.002	-0.004
	1.030	1.024	0.166	0.313	0.308	0.163	0.165	-0.006	-0.006	0.002
	1.154	1.150	03357	0.539	0.539	0.356	03353	-0.004	0.000	-0.003
	1.340	1.338	0.416	0.590	0.591	0.102	0.102	-0.002	0.002	0.000
	1.438	1.441	0.554	0.705	0.707	0.148	0.146	0.003	0.001	-0.002
313.15										
	1.209	1.211	0.125	0.224	0.225	0.407	0.405	0.002	0.000	-0.001
	1.153	1.154	0.141	0.251	0.253	0.632	0.628	0.001	0.002	-0.004
	1.319	1.314	0.164	0.295	0.291	0.169	0.170	-0.005	-0.005	0.001
	1.481	1.478	0.355	0.521	0.522	0.373	0.371	-0.003	0.000	-0.002
	1.704	1.705	0.411	0.570	0.570	0.110	0.109	0.001	0.001	0.000
	1.838	1.843	0.551	0.691	0.691	0.159	0.157	0.005	0.001	-0.002
323.15										
	1.535	1.535	0.123	0.211	0.214	0.418	0.416	0.000	0.003	-0.002
	1.469	1.469	0.135	0.238	0.235	0.645	0.645	0.000	-0.003	0.000
	1.665	1.655	0.162	0.278	0.274	0.175	0.175	-0.009	-0.004	0.000
	1.870	1.878	0.351	0.502	0.504	0.392	0.390	0.009	0.002	-0.002
	2.133	2.137	0.406	0.550	0.548	0.117	0.117	0.004	-0.001	0.000
	2.310	2.325	0.546	0.673	0.674	0.171	0.171	0.015	0.001	-0.001

number, k is the Boltzmann constant and T is the absolute temperature.

In the PC-SAFT model, proposed by Gross and Sadowski [1], the residual Helmholtz free energy $\tilde{a}^{res}$ for non-associating compounds consists of the hard-chain reference contribution and the dispersion contribution, illustrated as:

$$\tilde{a}^{res} = \tilde{a}^{hc} + \tilde{a}^{disp} \qquad (2)$$

The hard-chain reference contribution, in Eq. (2), is expressed by:

$$\tilde{a}^{hc} = \left(\sum_{i=1}^{nc} x_i m_i\right)\tilde{a}^{hs} - \sum_{i=1}^{nc} x_i(m_i - 1)\ln g_{ii}^{hs}(\sigma_{ii}) \qquad (3)$$

Where, m_i is the segment number parameter and x_i are the mole fractions of component i.
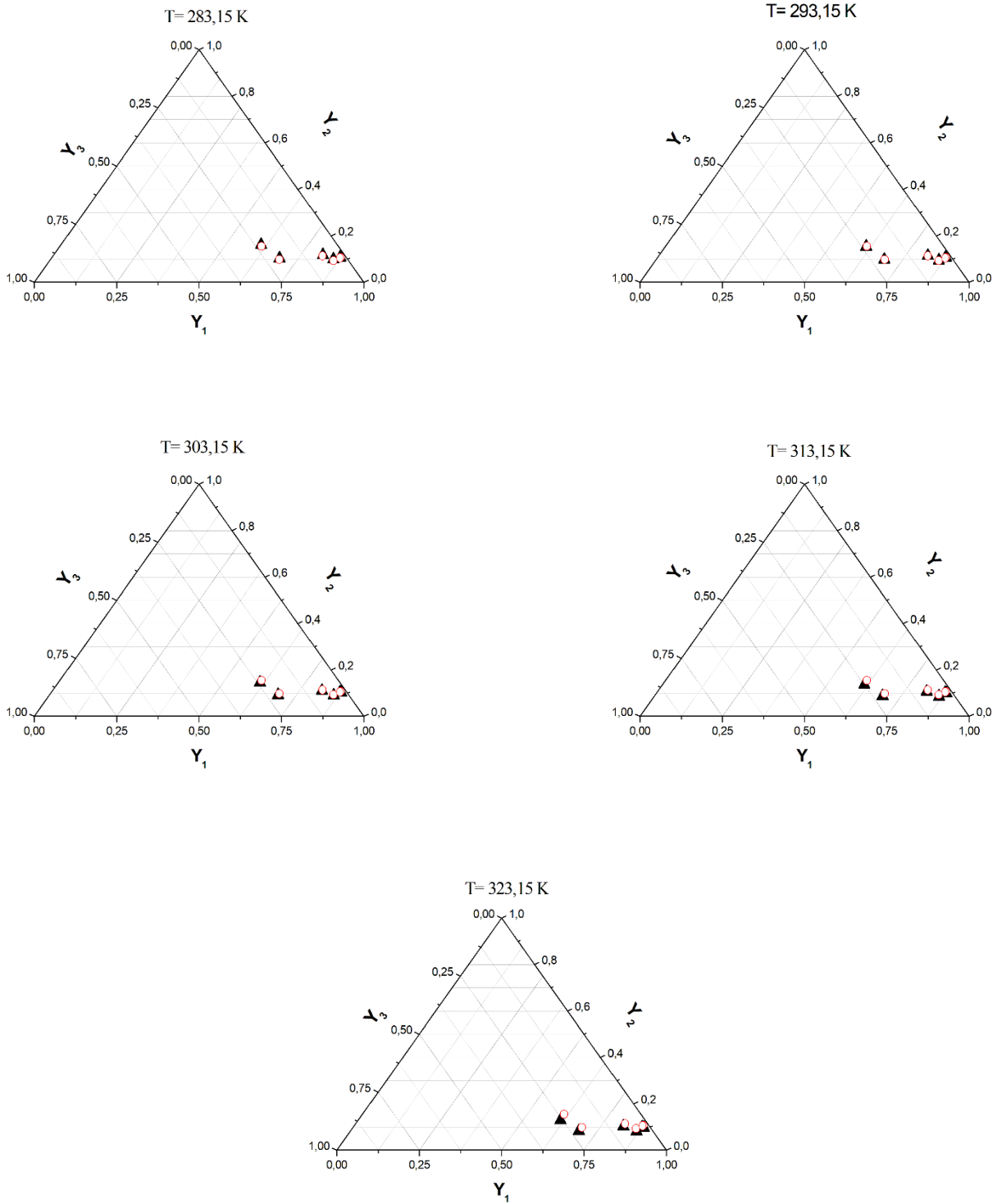
Figure 2. VLE of ternary mixture R32(1) + R152a(2) + R1234yf(3).
(▲): Experimental data [18]; (○): PC-SAFT prediction.

The hard-sphere term $\tilde{a}^{hs}$ is defined as follows:

$$\tilde{a}^{hs} = \frac{A^{hs}}{NkT}$$
$$= \frac{1}{\xi_0}\left[\frac{3\xi_1\xi_2}{(1-\xi_3)} + \frac{\xi_2{}^3}{\xi_3(1-\xi_3)^2} + \left(\frac{\xi_2{}^3}{\xi_3{}^2} - \xi_0\right)\ln(1-\xi_3)\right] \quad (4)$$

The coefficients ξ_0, ξ_1, ξ_2 and ξ_3 are defined by Eq. (6) below.

g_{ii}^{hs} is the radial distribution function of the hard-sphere fluid; it can be calculated by:

$$g_{ii}^{hs} = \frac{1}{(1-\xi_3)} + \left(\frac{d_i d_j}{d_i+d_j}\right)\frac{3\xi_2}{(1-\xi_3)^2} + \left(\frac{d_i d_j}{d_i+d_j}\right)^2\frac{2\xi_2{}^2}{(1-\xi_3)^3} \quad (5)$$

Table 3. Experimental and calculated VLE in the system R32(1) + R161(2) + R1234ze(E)(3) [19].

T[K]	P_{exp}[MPa]	P_{cal}[MPa]	x_{1exp}	y_{1exp}	y_{1cal}	y_{2exp}	y_{2cal}	ΔP[MPa]	Δy_1	Δy_2
283.15										
	0.588	0.590	0.075	0.138	0.139	0.778	0.783	0.002	0.001	0.005
	0.498	0.493	0.116	0.260	0.265	0.387	0.391	-0.005	0.005	0.004
	0.466	0.460	0.124	0.303	0.303	0.211	0.226	-0.006	0.000	0.015
	0.541	0.535	0.216	0.452	0.454	0.170	0.169	-0.006	0.002	0.000
	0.640	0.638	0.233	0.399	0.407	0.456	0.451	-0.002	0.008	-0.004
	0.613	0.608	0.266	0.479	0.490	0.271	0.265	-0.005	0.010	-0.006
	0.726	0.727	0.408	0.621	0.624	0.213	0.226	0.002	0.003	0.013
	0.734	0.735	0.473	0.710	0.717	0.076	0.073	0.001	0.007	-0.003
	0.878	0.880	0.605	0.752	0.759	0.184	0.179	0.002	0.007	-0.005
293.15										
	0.787	0.793	0.074	0.132	0.134	0.780	0.782	0.006	0.002	0.002
	0.669	0.666	0.113	0.247	0.245	0.387	0.392	-0.003	-0.001	0.005
	0.628	0.622	0.121	0.280	0.281	0.223	0.228	-0.006	0.001	0.004
	0.722	0.716	0.211	0.427	0.427	0.172	0.174	-0.006	0.000	0.003
	0.851	0.853	0.228	0.383	0.386	0.458	0.460	0.002	0.003	0.002
	0.817	0.813	0.262	0.464	0.467	0.269	0.271	-0.003	0.003	0.002
	0.962	0.964	0.399	0.592	0.599	0.239	0.236	0.002	0.008	-0.002
	0.975	0.975	0.469	0.693	0.697	0.078	0.076	0.000	0.003	-0.001
	1.165	1.169	0.601	0.741	0.745	0.190	0.186	0.005	0.005	-0.004
303.15										
	1.033	1.034	0.074	0.126	0.784	0.779	0.784	0.001	0.001	0.005
	0.881	0.868	0.112	0.233	0.386	0.385	0.386	-0.013	0.000	0.000
	0.828	0.813	0.119	0.261	0.223	0.223	0.223	-0.015	0.002	0.000
	0.944	0.929	0.207	0.405	0.173	0.173	0.173	-0.015	-0.001	0.000
	1.109	1.101	0.216	0.348	0.487	0.494	0.487	-0.008	0.009	-0.008
	1.065	1.049	0.257	0.443	0.271	0.272	0.271	-0.015	0.003	-0.001
	1.246	1.240	0.391	0.571	0.242	0.245	0.242	-0.007	0.009	-0.003
	1.267	1.259	0.463	0.675	0.078	0.080	0.078	-0.008	0.002	-0.002
	1.515	1.511	0.597	0.729	0.191	0.196	0.191	-0.004	0.005	-0.004
313.15										
	1.332	1.344	0.073	0.121	0.122	0.779	0.781	0.012	0.001	0.002
	1.140	1.137	0.110	0.219	0.217	0.383	0.387	-0.003	-0.002	0.004
	1.072	1.063	0.117	0.245	0.244	0.222	0.225	-0.008	-0.001	0.004
	1.210	1.201	0.202	0.379	0.377	0.174	0.177	-0.009	-0.002	0.002
	1.422	1.429	0.212	0.333	0.337	0.499	0.496	0.006	0.005	-0.003
	1.365	1.362	0.255	0.423	0.424	0.276	0.278	-0.004	0.001	0.002
	1.591	1.605	0.392	0.551	0.563	0.251	0.245	0.014	0.011	-0.007
	1.620	1.621	0.463	0.655	0.656	0.082	0.081	0.001	0.001	-0.001
	1.938	1.945	0.593	0.716	0.717	0.202	0.201	0.007	0.002	-0.001
323.15										
	1.691	1.706	0.072	0.115	0.116	0.778	0.780	0.015	0.001	0.002
	1.450	1.448	0.108	0.203	0.203	0.381	0.384	-0.003	-0.001	0.002
	1.365	1.356	0.115	0.229	0.227	0.221	0.222	-0.009	-0.002	0.002
	1.528	1.519	0.198	0.354	0.353	0.175	0.177	-0.009	-0.002	0.001
	1.794	1.803	0.206	0.316	0.317	0.504	0.505	0.009	0.001	0.001
	1.722	1.720	0.251	0.403	0.402	0.279	0.280	-0.003	0.000	0.001
	1.991	2.000	0.377	0.527	0.531	0.258	0.256	0.010	0.003	-0.002
	2.036	2.046	0.462	0.634	0.636	0.084	0.082	0.010	0.002	-0.002
	2.437	2.449	0.588	0.700	0.700	0.210	0.209	0.012	0.001	-0.001

The coefficients ξ_n are calculated through the relation:

$$\xi_n = \frac{\pi}{6}\rho \sum_{i=1}^{n_C} x_i m_i d_i^n, \ n \in [0,1,2,3] \tag{6}$$

The dispersion contribution term is given by:

$$\tilde{a}^{disp} = -2\pi\rho\left(\sum_{i=0}^{6} a_i(\bar{m})\eta^i\right)\overline{m^2 \varepsilon \sigma^3} - \pi\rho\bar{m}C_1\left(\sum_{i=0}^{6} b_i(\bar{m})\eta^i\right)\overline{m^2 \varepsilon^2 \sigma^3} \tag{7}$$

where:

$$\bar{m} = \left(\sum_{i=1}^{n_C} x_i m_i\right) \tag{8}$$

and

$$\rho = \frac{6}{\pi}\eta\left(\sum_{i=1}^{n_C} x_i m_i d_i^3\right)^{-1} \tag{9}$$

Here, ρ is the total number density of molecules, η is the reduced segment density, which is equal to ξ_3 and d_i is the temperature-dependent segment of component i expressed by:

$$d_i = \sigma_i\left[1 - 0.12 \exp\left(-3\frac{\varepsilon_i}{kT}\right)\right] \tag{10}$$

Table 4. Experimental and calculated VLE in the system R134a(1) + R1234yf(2) + DME(3) [22].

T[K]	P_{exp}[MPa]	P_{cal}[MPa]	x_{1exp}	x_{2exp}	y_{1exp}	y_{1cal}	y_{2exp}	y_{2cal}	ΔP[MPa]	Δy_1	Δy_2
253.15											
	0.167	0.156	0.066	0.822	0.069	0.071	0.850	0.814	-0.012	0.002	-0.035
	0.152	0.148	0.35	0.280	0.353	0.325	0.361	0.345	-0.004	-0.028	-0.016
	0.149	0.143	0.332	0.193	0.327	0.313	0.264	0.261	-0.006	-0.015	-0.003
	0.167	0.156	0.081	0.737	0.085	0.085	0.788	0.737	-0.011	0	-0.051
	0.153	0.154	0.100	0.562	0.096	0.098	0.624	0.588	0.002	0.002	-0.036
263.15											
	0.238	0.226	0.065	0.828	0.069	0.070	0.847	0.826	-0.012	0.001	-0.021
	0.218	0.213	0.354	0.285	0.358	0.336	0.352	0.346	-0.004	-0.022	-0.006
	0.212	0.206	0.335	0.193	0.335	0.321	0.258	0.254	-0.006	-0.013	-0.005
	0.237	0.225	0.082	0.745	0.085	0.085	0.785	0.750	-0.011	0.001	-0.035
273.15	0.220	0.222	0.100	0.563	0.097	0.099	0.623	0.592	0.002	0.001	-0.030
	0.328	0.320	0.064	0.829	0.071	0.072	0.849	0.829	-0.008	0.002	-0.02
	0.305	0.301	0.356	0.281	0.360	0.346	0.347	0.342	-0.004	-0.014	-0.006
	0.298	0.291	0.335	0.196	0.341	0.326	0.255	0.255	-0.007	-0.015	0.001
	0.330	0.318	0.077	0.752	0.090	0.085	0.776	0.760	-0.012	-0.005	-0.016
283.15	0.310	0.312	0.093	0.570	0.090	0.096	0.636	0.600	0.002	0.005	-0.035
	0.448	0.440	0.064	0.830	0.070	0.069	0.855	0.833	-0.008	0.000	-0.022
	0.421	0.415	0.356	0.289	0.362	0.350	0.340	0.339	-0.006	-0.011	-0.001
	0.410	0.401	0.337	0.198	0.345	0.332	0.251	0.247	-0.009	-0.012	-0.004
	0.450	0.437	0.071	0.756	0.076	0.076	0.789	0.767	-0.013	0.000	-0.022
293.15	0.427	0.428	0.092	0.580	0.092	0.093	0.637	0.608	0.001	0.002	-0.029
	0.599	0.591	0.065	0.834	0.068	0.069	0.858	0.840	-0.008	0.001	-0.018
	0.568	0.556	0.359	0.295	0.362	0.357	0.339	0.339	-0.012	-0.005	-0.001
	0.552	0.539	0.340	0.203	0.351	0.340	0.251	0.245	-0.012	-0.011	-0.006
	0.582	0.586	0.070	0.763	0.073	0.073	0.799	0.776	0.004	0	-0.023
303.15	0.576	0.572	0.092	0.585	0.093	0.093	0.638	0.613	-0.003	0	-0.024
	0.773	0.783	0.062	0.833	0.070	0.070	0.846	0.837	0.010	0.000	-0.009
	0.742	0.742	0.363	0.297	0.352	0.368	0.351	0.343	0.000	0.016	-0.009
	0.730	0.715	0.351	0.206	0.356	0.355	0.242	0.251	-0.015	-0.002	0.008
	0.762	0.777	0.071	0.776	0.084	0.079	0.797	0.786	0.016	-0.004	-0.011
313.15	0.748	0.759	0.102	0.600	0.104	0.108	0.637	0.626	0.011	0.004	-0.011
	0.966	0.947	0.304	0.314	0.299	0.303	0.371	0.375	-0.019	0.003	0.005
	1.016	1.022	0.061	0.843	0.073	0.072	0.854	0.845	0.006	-0.001	-0.009
	1.043	1.019	0.204	0.604	0.221	0.217	0.649	0.626	-0.024	-0.004	-0.024
	0.955	0.951	0.364	0.288	0.357	0.364	0.362	0.351	-0.004	0.007	-0.012
	0.929	0.919	0.370	0.218	0.367	0.368	0.273	0.282	-0.010	0.001	0.009
	0.993	1.014	0.071	0.783	0.081	0.081	0.801	0.792	0.021	0.000	-0.009
	0.968	0.988	0.100	0.617	0.104	0.107	0.667	0.644	0.020	0.002	-0.023

T is the absolute temperature; k is the Boltzmann constant; σ_i is the segment diameter and ε_i is the depth of the pair potential.

The coefficients $a_i(\bar{m})$ and $b_i(\bar{m})$ depend on the chain length and are calculated as follows:

$$a_i(\bar{m}) = a_{0i} + \frac{\bar{m}-1}{\bar{m}} a_{1i} + \frac{\bar{m}-1}{\bar{m}} \frac{\bar{m}-2}{\bar{m}} a_{2i} \qquad (11)$$

$$b_i(\bar{m}) = b_{0i} + \frac{\bar{m}-1}{\bar{m}} b_{1i} + \frac{\bar{m}-1}{\bar{m}} \frac{\bar{m}-2}{\bar{m}} b_{2i} \qquad (12)$$

where, the universal constants a_{ki} and b_{ki} ($k = 0, 1, 2$) are available in the literature [1].

The expression of the term C_l in Eq. (7) is given by the following:

$$C_1 = \left[1 + \bar{m} \frac{8\eta - 2\eta^2}{(1-\eta)^4} + (1-\bar{m}) \frac{20\eta - 27\eta^2 + 12\eta^3 - 2\eta^4}{[(1-\eta)(2-\eta)]^2} \right]^{-1} \qquad (13)$$

The abbreviations are as follows:

$$\overline{m^2\varepsilon\sigma^3} = \sum_i \sum_j x_i x_j m_i m_j \left(\frac{\epsilon_{ij}}{kT}\right) \sigma_{ij}^3 \qquad (14)$$

$$\overline{m^2\varepsilon^2\sigma^3} = \sum_i \sum_j x_i x_j m_i m_j \left(\frac{\epsilon_{ij}}{kT}\right)^2 \sigma_{ij}^3 \qquad (15)$$

To determine the parameters for a pair of unlike segments, conventional combining rules are employed:

$$\sigma_{ij} = \frac{1}{2}(\sigma_i + \sigma_j) \qquad (16)$$

$$\varepsilon_{ij} = \sqrt{\varepsilon_i \varepsilon_j}(1 - k_{ij}) \qquad (17)$$

where k_{ij} are the binary interaction parameters.

Table 5. Experimental and calculated VLE in the system R134a(1) + R1234yf(2) + R600a(3) [21].

T[K]	P_{exp}[MPa]	P_{cal}[MPa]	x_{1exp}	x_{2exp}	y_{1exp}	y_{1cal}	y_{2exp}	y_{2cal}	ΔP[MPa]	Δy_1	Δy_2
283.15											
	0.460	0.454	0.172	0.354	0.268	0.254	0.429	0.427	-0.006	-0.013	-0.002
	0.462	0.464	0.217	0.421	0.277	0.267	0.440	0.448	0.002	-0.010	0.008
	0.464	0.463	0.254	0.266	0.361	0.366	0.316	0.313	-0.001	0.005	-0.003
	0.465	0.465	0.278	0.223	0.397	0.410	0.259	0.265	0.000	0.013	0.006
	0.470	0.473	0.352	0.112	0.499	0.533	0.138	0.134	0.004	0.034	-0.004
	0.476	0.474	0.399	0.376	0.441	0.406	0.364	0.355	-0.002	-0.035	-0.009
	0.475	0.477	0.408	0.249	0.465	0.463	0.263	0.247	0.002	-0.002	-0.016
	0.477	0.472	0.669	0.203	0.634	0.621	0.184	0.186	-0.005	-0.013	0.003
	0.476	0.448	0.675	0.274	0.640	0.634	0.237	0.267	-0.028	-0.006	0.029
293.15											
	0.613	0.607	0.172	0.354	0.253	0.250	0.428	0.425	-0.005	-0.003	-0.003
	0.623	0.623	0.217	0.421	0.275	0.266	0.446	0.448	0.000	-0.009	0.003
	0.622	0.618	0.254	0.266	0.351	0.360	0.302	0.313	-0.003	0.009	0.010
	0.624	0.620	0.278	0.223	0.386	0.402	0.259	0.265	-0.004	0.016	0.006
	0.630	0.629	0.352	0.112	0.488	0.523	0.133	0.135	-0.001	0.035	0.002
	0.641	0.639	0.399	0.376	0.441	0.411	0.365	0.359	-0.002	-0.030	-0.006
	0.642	0.641	0.408	0.249	0.470	0.464	0.275	0.249	-0.001	-0.006	-0.025
	0.647	0.638	0.669	0.203	0.641	0.632	0.191	0.190	-0.009	-0.009	-0.001
	0.645	0.610	0.675	0.274	0.651	0.643	0.243	0.268	-0.035	-0.008	0.025
303.15											
	0.808	0.799	0.172	0.354	0.247	0.246	0.419	0.424	-0.008	-0.001	0.004
	0.820	0.824	0.217	0.421	0.276	0.266	0.452	0.449	0.003	-0.009	-0.003
	0.819	0.813	0.254	0.266	0.347	0.354	0.308	0.314	-0.006	0.007	0.006
	0.822	0.814	0.278	0.223	0.386	0.394	0.264	0.267	-0.008	0.009	0.004
	0.830	0.820	0.352	0.112	0.489	0.512	0.138	0.138	-0.009	0.023	0.000
	0.849	0.850	0.399	0.376	0.440	0.416	0.369	0.364	0.001	-0.025	-0.005
	0.848	0.848	0.408	0.249	0.473	0.463	0.281	0.255	-0.001	-0.010	-0.027
	0.859	0.849	0.669	0.203	0.646	0.640	0.191	0.197	-0.010	-0.006	0.006
	0.858	0.821	0.675	0.274	0.653	0.648	0.252	0.273	-0.036	-0.005	0.022
313.15											
	1.042	1.036	0.172	0.354	0.244	0.240	0.410	0.422	-0.006	-0.004	0.012
	1.062	1.071	0.217	0.421	0.270	0.263	0.456	0.450	0.010	-0.007	-0.007
	1.057	1.052	0.254	0.266	0.344	0.346	0.318	0.315	-0.005	0.002	-0.004
	1.063	1.052	0.278	0.223	0.377	0.385	0.271	0.268	-0.011	0.008	-0.002
	1.071	1.056	0.352	0.112	0.486	0.500	0.139	0.139	-0.015	0.013	0.001
	1.102	1.109	0.399	0.376	0.438	0.416	0.372	0.367	0.007	-0.022	-0.005
	1.100	1.102	0.408	0.249	0.468	0.460	0.282	0.258	0.001	-0.008	-0.024
	1.120	1.109	0.669	0.203	0.653	0.646	0.192	0.199	-0.011	-0.007	0.007
	1.116	1.079	0.675	0.274	0.659	0.653	0.258	0.274	-0.037	-0.006	0.017
323.15											
	1.321	1.312	0.172	0.354	0.241	0.236	0.421	0.418	-0.009	-0.005	-0.003
	1.351	1.364	0.217	0.421	0.271	0.262	0.458	0.449	0.013	-0.008	-0.009
	1.341	1.332	0.254	0.266	0.346	0.339	0.316	0.314	-0.009	-0.007	-0.002
	1.350	1.330	0.278	0.223	0.372	0.377	0.278	0.268	-0.020	0.005	-0.010
	1.359	1.329	0.352	0.112	0.479	0.488	0.138	0.140	-0.030	0.009	0.002
	1.407	1.422	0.399	0.376	0.440	0.419	0.375	0.371	0.015	-0.021	-0.004
	1.404	1.404	0.408	0.249	0.463	0.459	0.290	0.260	0.000	-0.004	-0.030
	1.436	1.427	0.669	0.203	0.661	0.652	0.194	0.203	-0.009	-0.009	0.010
	1.429	1.400	0.675	0.274	0.667	0.657	0.261	0.277	-0.030	-0.009	0.016

3. Numerical Procedure and Results

Azeotropic mixtures present a compelling option for refrigerants since they exhibit behavior closely resembling that of pure substances. Numerous approaches and methods have been explored for predicting azeotropic positions and vapor-liquid equilibrium in ternary mixtures. In this paper, a PC-SAFT model to predict the azeotropic positions of ternary mixture refrigerants was developed. The obtained results were compared with experimental data and confirmed the validity of our method.

The PC-SAFT model was used to determine the azeotropic composition (x_{az}) and azeotropic pressure (P_{az}) for ternary systems. The identification of azeotropic behavior in mixtures was based on the application of the Gibbs-Konovalov theorem [16]. This theorem postulates that under constant temperature conditions, the vapor and liquid phases possess identical compositions ($x_i = y_i$), and the bubble and dew point curves exhibit a local extremum:
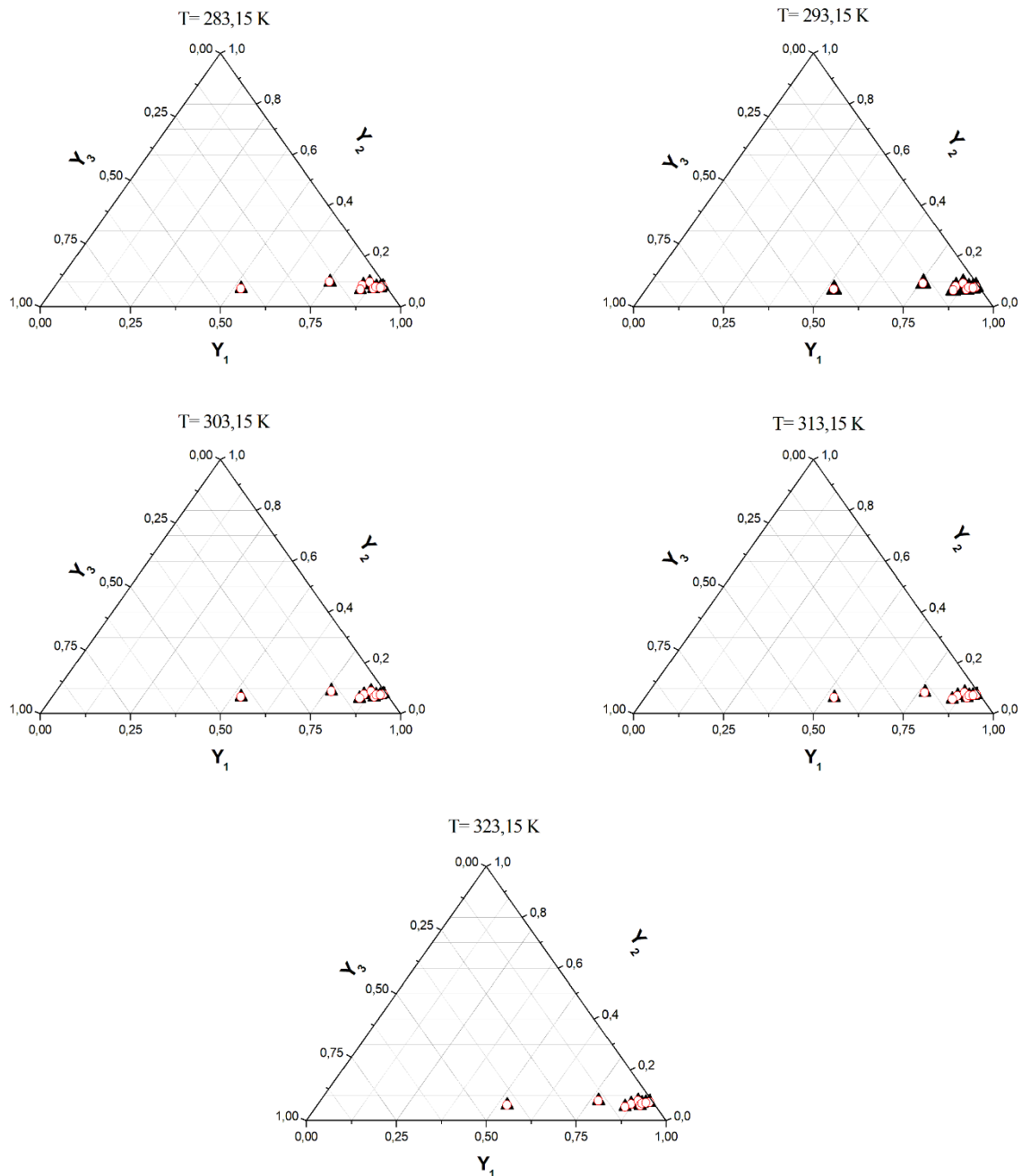
for $i = 1$ to n_c;

Figure 3. VLE of ternary mixture R32(1) + R161(2) + R1234ze(E)(3).
(▲): Experimental data [19]; (○): PC-SAFT prediction.

$$\left(\frac{\partial P}{\partial x_i}\right)_{T,x_j} = -\frac{\partial}{\partial x_i}\left[\left(\frac{\partial \tilde{a}^{res}}{\partial T}\right)_V\right]_{T,x_j} = 0 \quad (18)$$

Eq. (18) serves as the criterion for assessing azeotropic properties. The process for computing azeotropic points (x_{az}, P_{az}) based on the proposed approach is presented in Figure 1.

In the case of non-associating compounds, the PC-SAFT equation parameters for the pure components m_i, σ_i, and $(\varepsilon/k)_i$ are indispensable for establishing azeotropic properties in ternary mixtures. Anoune et al [17] offer a correlation that enables the determination of PC-SAFT parameters for the pure components under investigation, using only the critical temperature (T_C), critical pressure (P_C), and acentric factor (ω) as input data. The PC-SAFT

parameter values of the selected compounds are displayed in Table 1.

We note that the binary interaction parameters k_{ij} were obtained by minimizing the following objective function:

$$F_{obj} = \frac{100}{N}\left[\sum_1^N\left(\frac{P_{exp}-P_{cal}}{P_{exp}}\right)^2 + \sum_1^N\left(\frac{x_{exp}-x_{cal}}{x_{exp}}\right)^2\right] \quad (19)$$

The interaction parameters k_{ij} were optimized by minimizing objective function by simplex using the Newton Raphson iterative method. The objective function F_{obj} was minimized using Dichotomy method [17].
The deviations, $MRD(U)$, and $Bias(U)$ applied to both the mole fractions in the liquid and vapor phases as well as to the
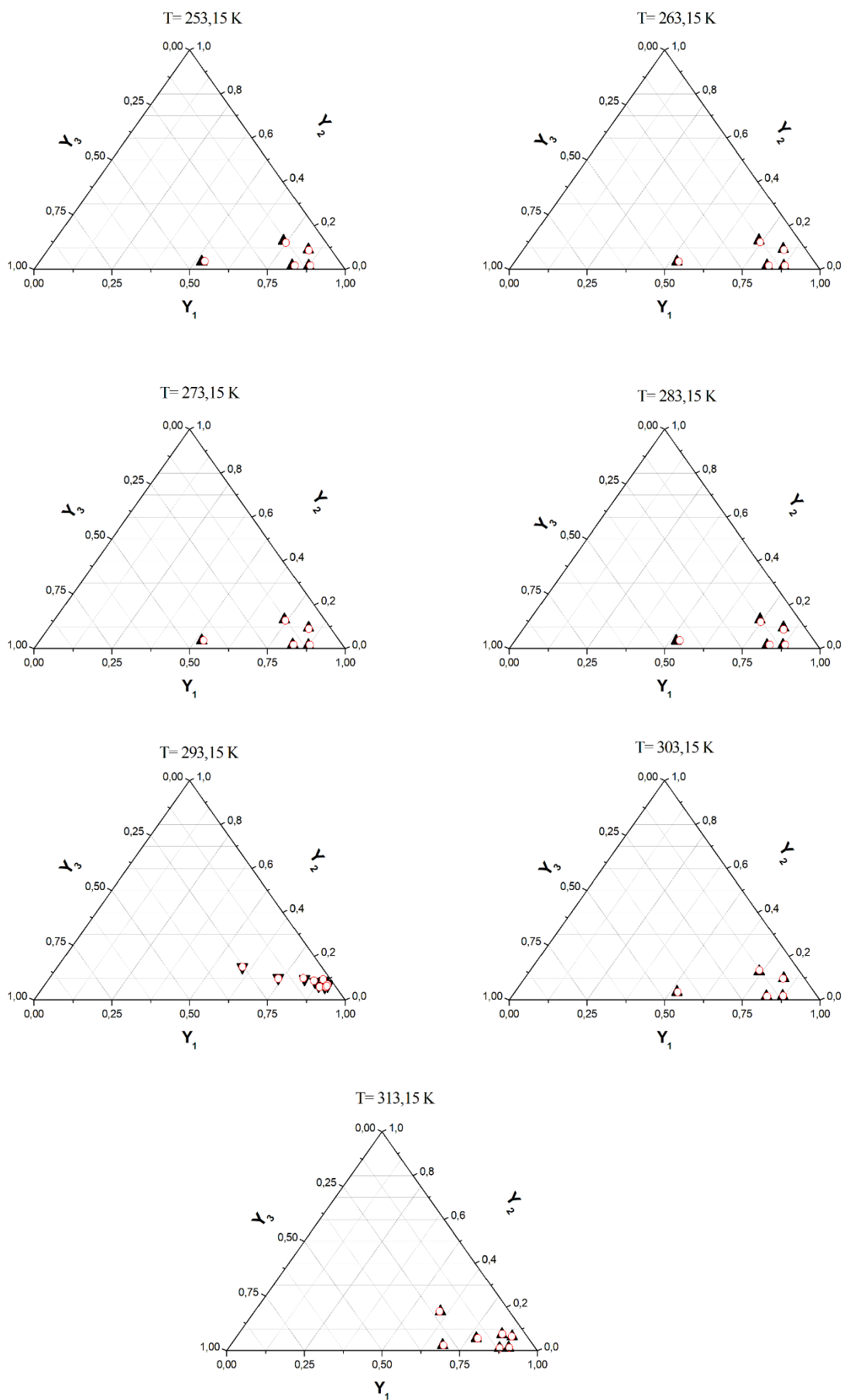
Figure 4. VLE of ternary mixture R134a(1) + R1234yf(2) + DME(3).
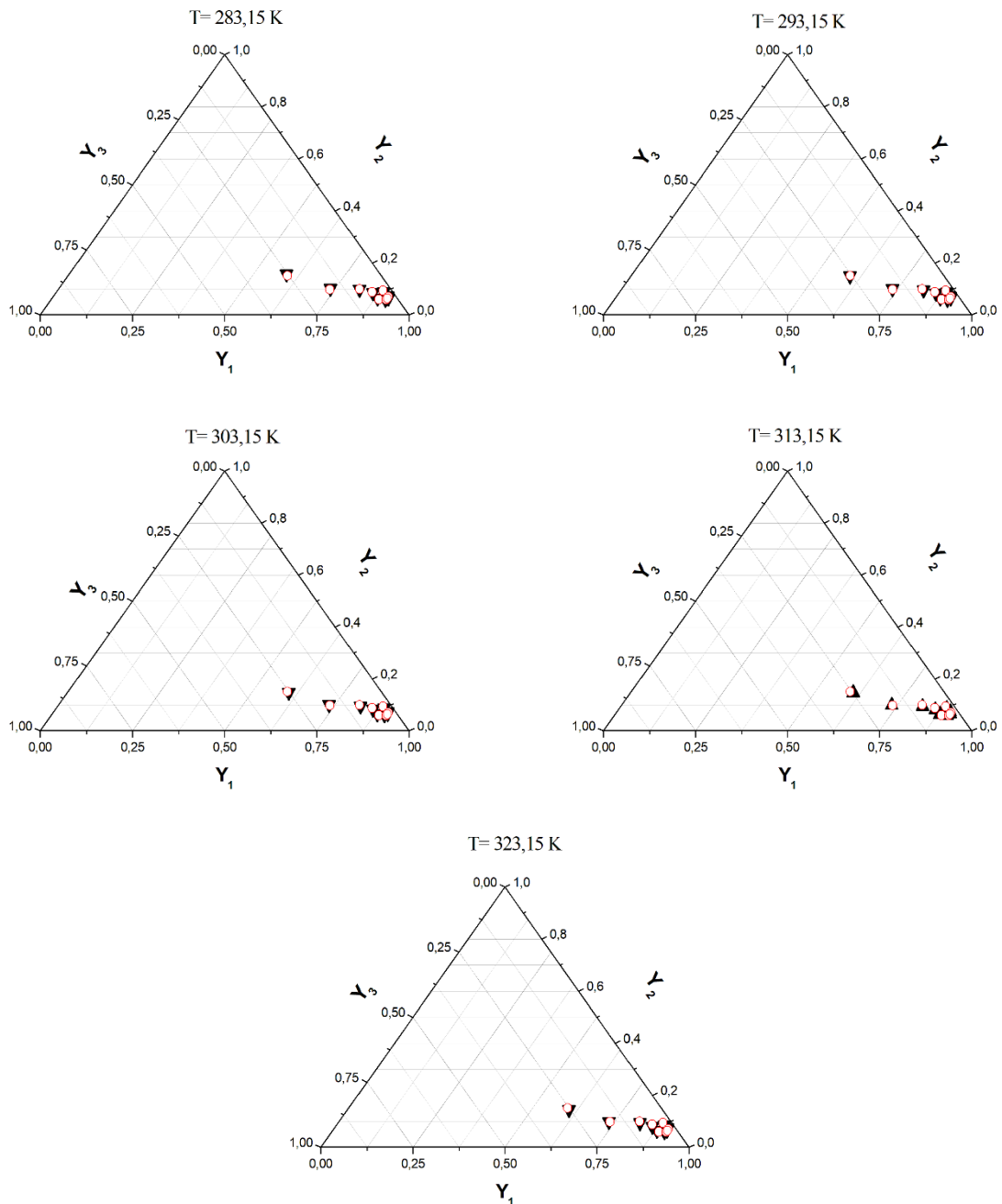*(▲): Experimental data [22]; (○): PC-SAFT prediction.*

*Figure 5. VLE of ternary mixture R134a(1) + R1234yf(2) + R600a(3).
(▲): Experimental data [21]; (○): PC-SAFT prediction.*

saturated pressure of mixtures are defined as follows:

$$MRD(U) = \frac{100}{N} \sum \left| \left(\frac{(U_{exp} - U_{cal})}{U_{exp}} \right) \right| \qquad (20)$$

$$Bias(U) = \frac{100}{N} \sum \left(\frac{(U_{exp} - U_{cal})}{U_{exp}} \right) \qquad (21)$$

where N is the number of data points, and U is P, x_i or y_i.

3.1 VLE in Ternary Mixtures

The VLE data for the six ternary mixtures investigated are tabulated in Tables (2–7) and graphically presented in Figures (2–7) at different temperatures. Additionally, the binary interaction parameter k_{ij}, the objective function F_{obj}, the relative deviation MRD, and the Bias obtained by fitting experimental VLE data with the PC-SAFT model are reported in Table 8.

It is noteworthy that the predictions for pressure exhibit strong agreement with the experimental values. Specifically, the relative deviation remains below 1% for three mixtures: R32 + R152a + R1234yf [18], R32 + R161 + R1234ze(E) [19] and R600a + R1234ze(E) + R13I1[20]. In the case of the R134a + R1234yf + R600a [21] mixture, the relative error does not exceed 1.15% at 283.15 K. The highest relative deviation is observed for the R134a + R1234yf + DME [22] mixture, reaching 4.26% at 253.15 K. For the R600a + R152a + R134 [23] mixture at the same temperature, the error remains within 2.78%. In conclusion, these results demonstrate a strong concurrence between the calculated values and the experimental data taken from the literature.

3.2 Azeotropic Prediction

Among the six ternary mixtures examined only three exhibit azeotropic behavior. These mixtures are as follows:

Table 6. Experimental and calculated VLE in the system R600a(1) + R152a(2) + R134(3) [23].

T[K]	P_{exp}[MPa]	P_{cal}[MPa]	x_{1exp}	x_{2exp}	y_{1exp}	y_{1cal}	y_{2exp}	y_{2cal}	ΔP[MPa]	Δy_1	Δy_2
253.15											
	0.129	0.130	0.799	0.098	0.500	0.403	0.228	0.248	0.001	-0.097	0.020
	0.145	0.145	0.572	0.066	0.417	0.356	0.078	0.074	0.000	-0.061	-0.004
	0.143	0.137	0.415	0.336	0.396	0.374	0.347	0.356	-0.006	-0.022	0.009
	0.143	0.137	0.367	0.409	0.382	0.368	0.403	0.418	-0.006	-0.014	0.015
	0.143	0.137	0.365	0.410	0.379	0.369	0.413	0.417	-0.006	-0.010	0.004
	0.143	0.138	0.327	0.470	0.368	0.361	0.447	0.465	-0.005	-0.007	0.018
	0.142	0.138	0.320	0.493	0.360	0.356	0.471	0.488	-0.004	-0.004	0.017
	0.142	0.138	0.313	0.497	0.359	0.355	0.471	0.488	-0.004	-0.004	0.017
	0.142	0.138	0.312	0.498	0.360	0.355	0.469	0.489	-0.004	-0.005	0.020
	0.139	0.136	0.152	0.326	0.349	0.379	0.234	0.233	-0.003	0.030	-0.001
	0.143	0.138	0.379	0.227	0.398	0.389	0.207	0.202	-0.005	-0.009	-0.005
	0.143	0.139	0.458	0.194	0.409	0.378	0.199	0.196	-0.004	-0.031	-0.003
263.15											
	0.199	0.198	0.739	0.123	0.473	0.396	0.236	0.247	-0.001	-0.077	0.011
	0.214	0.213	0.597	0.066	0.419	0.363	0.079	0.080	0.000	-0.056	0.001
	0.211	0.203	0.414	0.337	0.387	0.369	0.350	0.359	-0.008	-0.018	0.009
	0.211	0.203	0.374	0.404	0.374	0.361	0.407	0.419	-0.007	-0.013	0.012
	0.209	0.203	0.365	0.419	0.372	0.359	0.417	0.432	-0.006	-0.013	0.015
	0.210	0.204	0.338	0.463	0.360	0.352	0.452	0.468	-0.006	-0.008	0.016
	0.210	0.204	0.318	0.495	0.350	0.346	0.477	0.494	-0.005	-0.004	0.017
	0.209	0.204	0.313	0.497	0.352	0.346	0.474	0.493	-0.005	-0.006	0.019
	0.209	0.204	0.310	0.499	0.350	0.345	0.475	0.493	-0.005	-0.005	0.018
	0.205	0.202	0.177	0.311	0.328	0.363	0.243	0.232	-0.003	0.035	-0.011
	0.211	0.205	0.380	0.226	0.389	0.380	0.210	0.205	-0.006	-0.009	-0.005
	0.211	0.206	0.462	0.193	0.404	0.375	0.202	0.199	-0.005	-0.029	-0.003
273.15											
	0.282	0.279	0.739	0.123	0.483	0.413	0.233	0.243	-0.002	-0.070	0.010
	0.303	0.303	0.595	0.066	0.422	0.371	0.080	0.080	0.000	-0.051	0.000
	0.302	0.291	0.416	0.336	0.388	0.364	0.348	0.361	-0.011	-0.024	0.013
	0.302	0.292	0.374	0.404	0.367	0.355	0.411	0.422	-0.010	-0.012	0.011
	0.300	0.292	0.365	0.418	0.366	0.353	0.419	0.433	-0.008	-0.013	0.014
	0.300	0.293	0.337	0.463	0.353	0.344	0.455	0.471	-0.007	-0.009	0.016
	0.300	0.294	0.318	0.495	0.343	0.337	0.481	0.498	-0.007	-0.006	0.017
	0.300	0.294	0.314	0.497	0.343	0.336	0.480	0.498	-0.006	-0.007	0.018
	0.299	0.293	0.310	0.499	0.335	0.336	0.485	0.497	-0.006	0.001	0.012
	0.293	0.288	0.173	0.313	0.306	0.337	0.254	0.243	-0.005	0.031	-0.011
	0.302	0.295	0.380	0.227	0.382	0.372	0.214	0.210	-0.007	-0.010	-0.004
	0.301	0.295	0.462	0.193	0.401	0.373	0.204	0.201	-0.006	-0.028	-0.003

R600a + R1234ze(E) + R13I1 at temperatures of 243.15 K, 263.15 K, and 283.15 K, R600a + R152a + R134 at temperatures of 253.15 K, 263.15 K, and 273.15 K. Lastly, R134a + R1234yf + R600a demonstrates azeotropic behavior at temperatures of 313.15 K and 323.13 K.

Table 9 presents both the experimental and PC-SAFT model-calculated compositions and pressures for these ternary azeotrope mixtures. The relative errors between the experimental and calculated azeotropic compositions and pressures are calculated using the following relations:

$$\Delta x_{az} = \frac{|x_{az}^{exp} - x_{az}^{cal}|}{x_{az}^{exp}} \times 100 \tag{22}$$

For pressure:

$$\Delta P_{az} = \frac{|P_{az}^{exp} - P_{az}^{cal}|}{P_{az}^{exp}} \times 100 \tag{23}$$

For the (R600a + R1234ze(E) + R13I1) ternary mixture, the maximum relative errors do not exceed (Δx_1=5.26%, Δx_2=6.56%) for molar fractions and 1.39% for pressure (see

Table 9). Similarly, for the (R600a + R152a + R134) mixture, the relative errors do not exceed (Δx_1=3.48%, Δx_2=3.71%) for molar fractions and 4.20% for pressure. As for the (R134a + R1234yf + R600a) ternary mixture, the maximum relative errors in molar fractions are (Δx_1=3.44% and Δx_2=1.97%), with a maximum relative pressure error of ΔP=0.98%.

The relative errors found when comparing the experimental and calculated values for each ternary system are well within acceptable limits. This comparison stands out well when considering the research conducted by Maalem et al [14]. They used three different models (relative volatility, NRTL, and Wilson) to predict azeotropic compositions and pressures for the same ternary mixtures. This suggests that the PC-SAFT model is effective in predicting azeotropic points in ternary systems.

4. Conclusion

A comprehensive study on six different ternary mixtures at different temperatures to predict their azeotropic behavior was conducted. To achieve this, the Perturbed-Chain SAFT (PC-SAFT) equation of state, with estimated binary
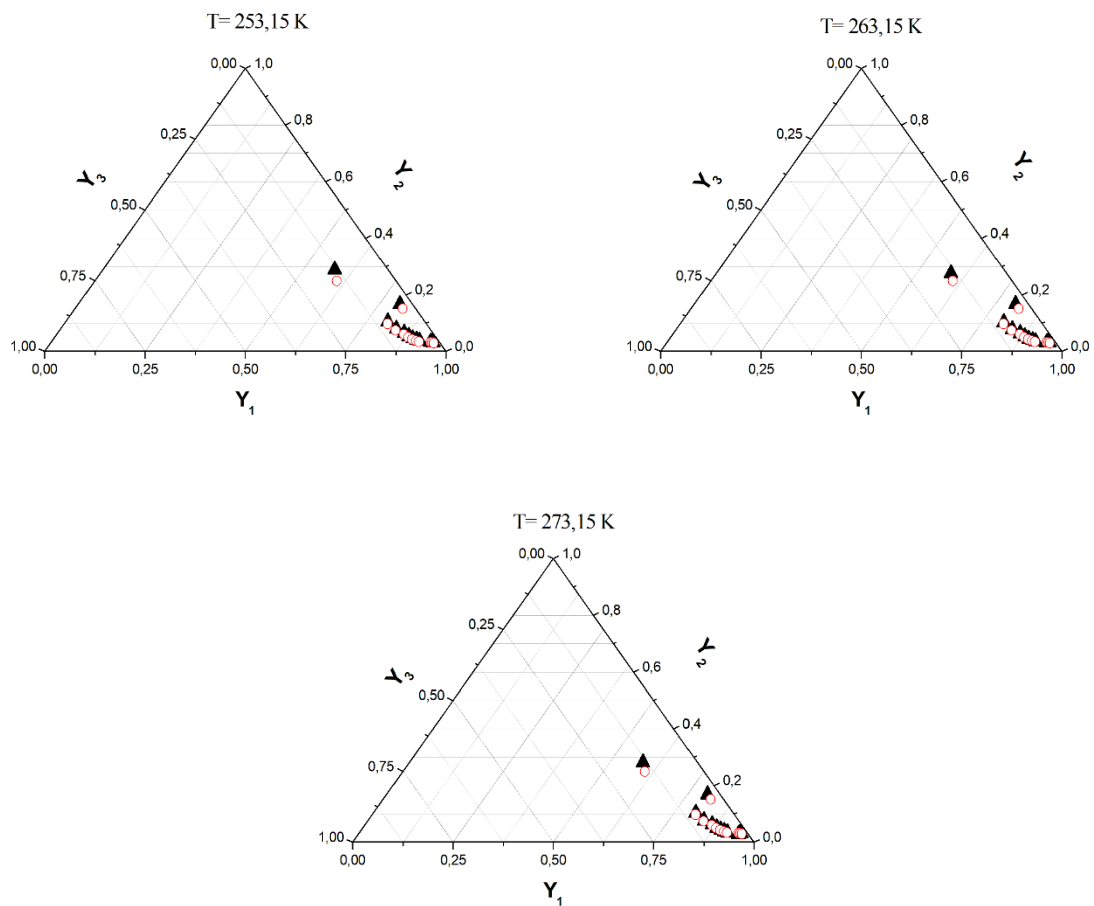
Figure 6. VLE of ternary mixture R600a(1) + R152a(2) + R134(3).
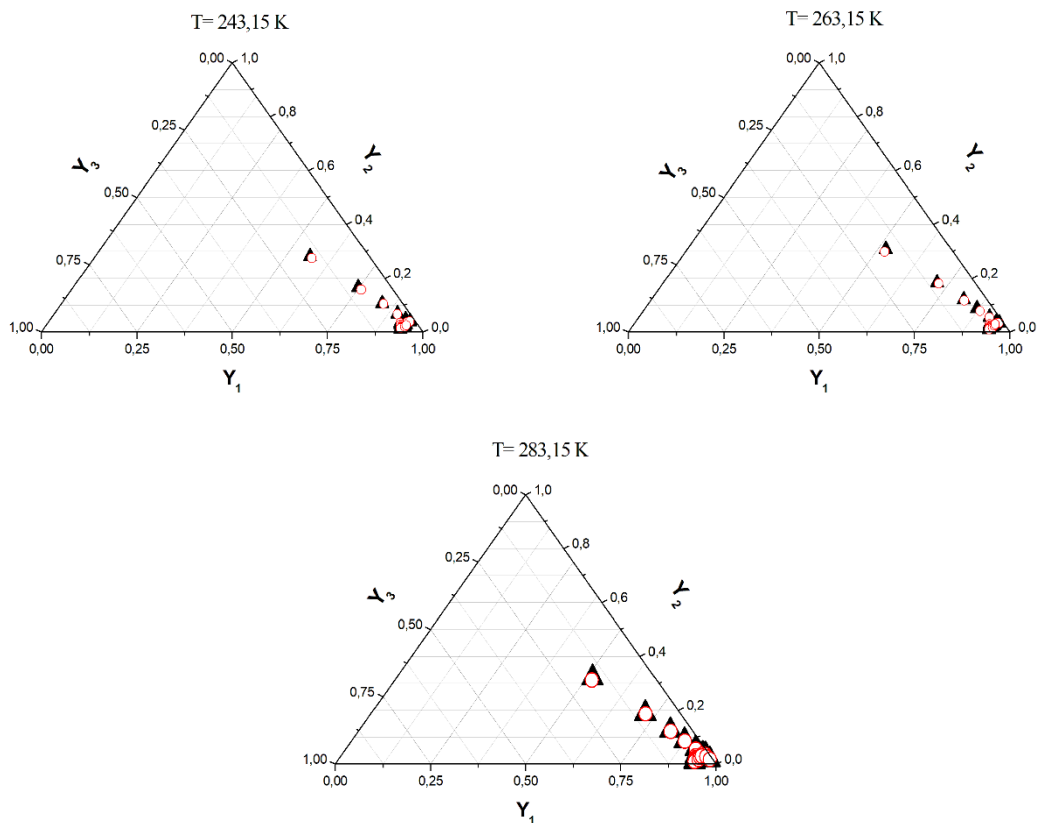(▲): Experimental data [23]; (○): PC-SAFT prediction.

Figure 7. VLE of ternary mixture R600a(1) + R1234ze(E)(2) + R13I1(3).
(▲): Experimental data [20]; (○): PC-SAFT prediction.

Table 7. Experimental and calculated VLE in the system R600a(1) + R1234ze(E)(2) + R13I1(3) [20].

T[K]	P_{exp}[MPa]	P_{cal}[MPa]	x_{1exp}	x_{2exp}	y_{1exp}	y_{1cal}	y_{2exp}	y_{2cal}	ΔP[MPa]	Δy_1	Δy_2
243.15											
	0.070	0.070	0.669	0.129	0.498	0.481	0.276	0.268	0.000	-0.017	-0.008
	0.072	0.072	0.571	0.112	0.442	0.415	0.231	0.218	0.000	-0.027	-0.013
	0.073	0.072	0.504	0.096	0.379	0.372	0.192	0.181	-0.001	-0.007	-0.011
	0.074	0.074	0.383	0.087	0.301	0.294	0.148	0.151	0.000	-0.007	0.003
	0.075	0.075	0.246	0.069	0.248	0.203	0.123	0.113	0.000	-0.045	-0.010
	0.073	0.074	0.307	0.055	0.248	0.246	0.092	0.096	0.000	-0.002	0.004
	0.079	0.079	0.312	0.262	0.258	0.253	0.328	0.326	0.000	-0.005	-0.002
	0.079	0.080	0.277	0.350	0.244	0.240	0.390	0.386	0.001	-0.004	-0.004
	0.079	0.080	0.258	0.400	0.236	0.235	0.423	0.417	0.001	-0.001	-0.006
	0.080	0.080	0.209	0.518	0.219	0.220	0.492	0.484	0.001	0.001	-0.008
	0.077	0.078	0.135	0.685	0.186	0.187	0.606	0.586	0.001	0.001	-0.020
	0.075	0.075	0.099	0.792	0.159	0.169	0.683	0.673	0.000	0.010	-0.010
	0.081	0.079	0.268	0.553	0.273	0.279	0.520	0.520	-0.001	0.006	0.000
	0.080	0.078	0.465	0.389	0.399	0.375	0.461	0.467	-0.001	-0.024	0.006
263.15											
	0.156	0.155	0.765	0.166	0.592	0.572	0.329	0.342	0.000	-0.020	0.013
	0.157	0.158	0.664	0.136	0.511	0.496	0.276	0.266	0.001	-0.015	-0.010
	0.161	0.161	0.569	0.122	0.442	0.428	0.222	0.224	0.000	-0.014	0.002
	0.163	0.163	0.459	0.104	0.401	0.353	0.198	0.180	0.000	-0.048	-0.018
	0.164	0.165	0.373	0.088	0.300	0.294	0.145	0.147	0.001	-0.006	0.002
	0.166	0.165	0.254	0.062	0.238	0.211	0.110	0.101	-0.001	-0.027	-0.009
	0.164	0.163	0.302	0.050	0.246	0.247	0.083	0.086	-0.001	0.001	0.003
	0.176	0.177	0.302	0.269	0.249	0.248	0.338	0.333	0.001	-0.001	-0.005
	0.178	0.180	0.27	0.350	0.233	0.234	0.402	0.393	0.001	0.001	-0.009
	0.179	0.180	0.249	0.403	0.224	0.225	0.437	0.429	0.001	0.001	-0.008
	0.180	0.181	0.204	0.513	0.219	0.207	0.489	0.499	0.001	-0.012	0.010
	0.177	0.176	0.128	0.694	0.164	0.166	0.629	0.622	0.000	0.002	-0.007
	0.172	0.172	0.093	0.778	0.136	0.14	0.701	0.692	0.000	0.004	-0.009
	0.180	0.180	0.262	0.552	0.264	0.264	0.545	0.538	-0.001	0.000	-0.007
	0.177	0.176	0.465	0.389	0.393	0.377	0.462	0.471	-0.001	-0.016	0.009
	0.170	0.166	0.657	0.252	0.496	0.487	0.399	0.410	-0.004	-0.009	0.011
283.15											
	0.305	0.303	0.774	0.169	0.621	0.603	0.319	0.328	-0.002	-0.018	0.009
	0.306	0.307	0.664	0.136	0.523	0.517	0.254	0.253	0.001	-0.006	-0.001
	0.312	0.313	0.569	0.122	0.457	0.444	0.213	0.215	0.001	-0.013	0.002
	0.321	0.316	0.492	0.106	0.397	0.387	0.180	0.181	-0.005	-0.010	0.001
	0.323	0.320	0.373	0.086	0.308	0.300	0.140	0.141	-0.003	-0.008	0.001
	0.326	0.322	0.280	0.067	0.235	0.232	0.104	0.107	-0.004	-0.003	0.003
	0.321	0.317	0.309	0.048	0.251	0.255	0.080	0.081	-0.005	0.004	0.001
	0.346	0.346	0.309	0.271	0.254	0.254	0.340	0.338	0.001	0.000	-0.002
	0.354	0.352	0.270	0.349	0.234	0.231	0.402	0.398	-0.001	-0.003	-0.004
	0.355	0.355	0.250	0.401	0.223	0.221	0.441	0.437	0.000	-0.002	-0.004
	0.358	0.357	0.206	0.519	0.198	0.201	0.523	0.520	-0.001	0.003	-0.003
	0.354	0.352	0.130	0.688	0.153	0.154	0.649	0.642	-0.002	0.001	-0.007
	0.347	0.344	0.091	0.781	0.122	0.123	0.726	0.721	-0.003	0.001	-0.005
	0.360	0.355	0.260	0.548	0.253	0.251	0.554	0.551	-0.005	-0.002	-0.003
	0.350	0.344	0.480	0.375	0.401	0.388	0.456	0.464	-0.006	-0.013	0.008
	0.332	0.324	0.651	0.248	0.508	0.500	0.389	0.390	-0.007	-0.008	0.001
	0.311	0.308	0.626	0.121	0.491	0.489	0.229	0.224	-0.003	-0.002	-0.005
	0.321	0.320	0.392	0.089	0.297	0.314	0.156	0.147	-0.001	0.017	-0.009

interaction parameters was employed.

In the initial phase of our research, the PC-SAFT Equation of state was utilized to calculate Vapor Liquid Equilibrium (VLE) data for all six ternary mixtures under investigation. Overall, the values of MRD and Bias confirm a reasonable agreement with the experimental data. A strong correlation between the phase behavior of these mixtures and the thermodynamic model founded indicates the model's effectiveness.

Among the six mixtures, only three exhibited azeotropic characteristics. The pressure and composition of the azeotropes, denoted as P_{az} and x_{az}, respectively, were determined by using adjustable parameters, including k_{ij}, m_i, σ_i, and $(\varepsilon/k)_i$.

The present results obtained from the model proposed by Maalem et al [14] performs a high degree of agreement with the aforementioned sources.

Table 8. Binary interaction parameter k_{ij}. objective function F_{obj}. Relative deviation MRD. and Bias obtained by fitting experimental VLE data with PC-SAFT model.

T (K)	BiasP %	MRDP %	Biasy_1 %	Bias y_2 %	MRDy_1 %	MRD y_2 %	k_{12}	k_{13}	k_{23}	F_{obj}
R32(1) + R152a(2) + R1234yf(3)										
283.15	0.07	0.96	0.09	1.04	1.08	2.45	0.00861	0.03255	0.01542	0.13036
293.15	0.09	0.31	-0.06	0.58	0.69	1.09	0.00507	0.03760	0.01455	0.02269
303.15	0.08	0.26	-0.01	0.53	0.60	0.95	0.00450	0.03893	0.01482	0.01850
313.15	0.00	0.19	0.09	0.42	0.42	0.61	0.00505	0.03992	0.01456	0.00957
323.15	-0.13	0.32	0.16	0.17	0.83	0.32	0.00811	0.04021	0.01261	0.01326
R32(1) + R161(2) + R1234ze(E)(3)										
283.15	0.40	0.61	-1.05	-0.51	1.08	2.76	0.00727	0.02104	-0.0104	0.15238
293.15	0.10	0.46	-0.58	-0.20	0.74	1.23	0.00851	0.02179	-0.0077	0.02874
303.15	0.93	0.96	-0.85	0.84	0.88	1.02	0.00660	0.02183	-0.0099	0.04426
313.15	-0.06	0.52	-0.32	0.10	0.73	1.15	0.00936	0.02314	-0.0059	0.03056
323.15	-0.14	0.49	-0.04	0.03	0.43	0.71	0.01006	0.02406	-0.0054	0.01230
R134a(1) + R1234yf(2) + DME(3)										
253.15	3.78	4.26	1.69	4.40	3.27	4.40	0.01934	0.00091	0.01095	0.63646
263.15	2.72	3.05	1.36	3.09	2.67	3.09	0.01759	-0.00471	0.00574	0.34519
273.15	1.81	2.03	1.22	2.24	4.39	2.40	0.02000	-0.01051	0.00118	0.34904
283.15	1.58	1.67	0.91	2.34	1.88	2.34	0.01566	-0.01181	-0.0009	0.16384
293.15	1.13	1.39	0.60	2.23	1.29	2.23	0.01251	-0.01472	-0.0039	0.11679
303.15	-0.56	1.38	-0.58	0.63	2.92	2.03	0.01856	-0.02076	-0.0072	0.20068
313.15	0.13	1.51	-0.30	1.15	1.22	2.40	0.02484	-0.03970	-0.0086	0.11849
R134a(1) + R1234yf(2) + R600a(3)										
283.15	0.83	1.15	0.94	-0.59	3.45	3.39	0.00349	0.11838	0.07477	0.46282
293.15	1.07	1.07	0.12	-0.63	3.20	3.36	0.00492	0.11511	0.07366	0.42899
303.15	0.97	1.10	0.49	-0.52	2.45	3.06	0.00980	0.11096	0.07272	0.31578
313.15	0.68	1.04	0.84	-0.01	2.00	2.98	0.01169	0.10852	0.07404	0.23295
323.15	0.63	1.08	1.36	0.66	2.07	3.42	0.01587	0.10432	0.07198	0.28224
R600a(1) + R152a(2) + R134(3)										
253.15	2.65	2.78	4.41	-1.89	5.83	3.41	0.09233	0.12320	-0.0319	0.90612
263.15	2.31	2.31	3.89	-1.75	5.68	3.15	0.09222	0.12312	-0.0308	0.73767
273.15	2.11	2.11	3.74	-1.65	5.47	2.87	0.09210	0.12258	-0.0294	0.63810
R600a(1) + R1234ze(E)(2) + R13I1(3)										
243.15	-0.18	0.82	2.36	1.74	3.76	2.86	0.07235	0.02131	0.03798	0.49045
263.15	0.08	0.53	2.53	0.82	3.28	2.90	0.07132	0.01999	0.03641	0.37321
283.15	0.76	0.86	0.65	0.20	1.72	1.41	0.06856	0.01744	0.03533	0.09772

Table 9. Experimental and calculated compositions and pressures of the ternary mixtures' azeotrope and relative error.

T(K)	$x_{1,exp}$	$x_{2,exp}$	$x_{3,exp}$	$x_{1,cal}$	$x_{2,cal}$	$x_{3,cal}$	Δx_1(%)	Δx_2(%)	$P_{az,exp}$	$P_{az,cal}$	ΔP_{az}(%)
R134a(1) + R1234yf(2) + R600a (3)[21]											
313.15	0.669	0.203	0.028	0.646	0.199	0.155	3.438	1.970	1.120	1.109	0.982
323.15	0.669	0.203	0.028	0.652	0.203	0.145	2.541	0.000	1.436	1.427	0.627
R600a(1) + R152a(2) + R134(3) [23]											
253.15	0.365	0.410	0.225	0.369	0.417	0.214	1.096	1.707	0.143	0.137	4.196
263.15	0.374	0.404	0.222	0.361	0.419	0.220	3.476	3.713	0.211	0.203	3.791
273.15	0.365	0.418	0.217	0.353	0.433	0.214	3.288	3.589	0.300	0.292	2.667
R600a(1) + R1234ze(E)(2) + R13I1(3) [20]											
243.15	0.209	0.518	0.273	0.220	0.484	0.296	5.263	6.564	0.080	0.080	0.000
263.15	0.262	0.552	0.186	0.264	0.538	0.198	0.763	2.536	0.180	0.180	0.000
283.15	0.260	0.548	0.192	0.251	0.551	0.198	3.462	0.547	0.360	0.355	1.389

Nomenclature

Symbols

$\tilde{a}$	Reduced Helmholtz free energy.
A	Helmholtz free energy.
C	Cubic term of the Helmholtz free energy equation.
d	Segment diameter of component.
EoS	Equation of State.
F_{obj}	Objective function.
GWP	Global Warming Potential
k	Boltzmann constant.
k_{ij}	Binary interaction parameter.
m	Mean segment number in the mixture.

N	The Avogadro number.
P	Pressure [MPa].
RE	Relative Error ($\Delta x_{az}, \Delta P_{az}$).
SAFT	Statistical Associating Fluid Theory.
T	Temperature [K].
U	Represents P, x or y.
VLE	Vapor Liquid Equilibrium.
x	Liquid mole fraction.
y	Vapor mole fraction.

Greek letters

σ	Segment diameter.
ω	Acentric factor.
ρ	Molar density.

ε/k The segment-segment interaction energy parameter

Subscripts and superscripts

Az   Azeotrope property.

c   Pure-component critical property.

cal   Calculated property.

exp   Experimental property.

disp   Contribution due to dispersive attraction

hc   Hard-chain.

hs   Hard sphere.

res   Residual property.

i,j   Molecular species.

References:

[1] J. Gross and G. Sadowski, "Application of perturbation theory to a hard-chain reference fluid: an equation of state for square-well chains," *Fluid Phase Equilib.*, 168, 183–199, 2000, doi: 10.1016/S0378-3812(00)00302-2.

[2] J. Gross and G. Sadowski, "Perturbed-Chain SAFT: An Equation of State Based on a Perturbation Theory for Chain Molecules," *Ind. Eng. Chem. Res.*, 40, 1244–1260, 2001, doi: 10.1021/ie0003887.

[3] S. H. Huang and M. Radosz, "Equation of state for small, large, polydisperse, and associating molecules," *Ind. Eng. Chem. Res.*, 29, 2284–2294, 1990, doi:10.1021/ie00107a014.

[4] S. H. Huang and M. Radosz, "Equation of state for small, large, polydisperse, and associating molecules: extension to fluid mixtures," *Ind. Eng. Chem. Res.*, 30, 1994–2005, 1991, doi: 10.1021/ie00056a050.

[5] T. Kraska and K. E. Gubbins, "Phase Equilibria Calculations with a Modified SAFT Equation of State. 1. Pure Alkanes, Alkanols, and Water," *Ind. Eng. Chem. Res.*, 35, 4727–4737, 1996, doi: 10.1021/ie9602320.

[6] A. Gil-Villegas, A. Galindo, P. J. Whitehead, S. J. Mills, G. Jackson, and A. N. Burgess, "Statistical associating fluid theory for chain molecules with attractive potentials of variable range," *J. Chem. Phys.*, 106, 4168–4186, 1997, doi: 10.1063/1.473101.

[7] A. G. Lowri, A. D. Alej, "The thermodynamics of mixtures and the corresponding mixing rules in the SAFT-VR approach for potentials of variable range," *Mol. Phys.*, 93, 241–252, 1998, doi: 10.1080/002689798169249.

[8] J. B. Felipe, F. V. Lourdes, "Prediction of Binary and Ternary Diagrams Using the Statistical Associating Fluid Theory (SAFT) Equation of State," *Ind. Eng. Chem. Res.*, 37, 660–674, 1998.

[9] Y.-H. Fu, S. I. Sandler, "A Simplified SAFT Equation of State for Associating Compounds and Mixtures," *Ind. Eng. Chem. Res.*, 34, 1897–1909, 1995, doi: 10.1021/ie00044a042.

[10] G. M. Kontogeorgis, E. C. Voutsas, I. V. Yakoumis, D. P. Tassios, "An Equation of State for Associating Fluids," *Ind. Eng. Chem. Res.*, 35, 4310–4318, 1996, doi: 10.1021/ie9600203.

[11] Ii. Polishuk, "Generalization of SAFT + Cubic equation of state for predicting and correlating thermodynamic properties of heavy organic substances," *J. Supercrit. Fluids*, 67, 94–107, 2012, doi: 10.1016/j.supflu.2012.02.009.

[12] E. K. Karakatsani, T. Spyriouni, and I. G. Economou, "Extended statistical associating fluid theory (SAFT) equations of state for dipolar fluids," *AIChE Journal*, 51, 2328–2342, 2005, doi: 10.1002/aic.10473.

[13] J. A. Barker, D. Henderson, "Perturbation Theory and Equation of State for Fluids. II. A Successful Theory of Liquids," *J. Chem. Phys.*, 47, 4714–4721, 1967, doi: 10.1063/1.1701689.

[14] Y. Maalem, A. Zarfa, Y. Tamene, S. Fedali, H. Madani, "Prediction of thermodynamic properties of the ternary azeotropic mixtures," *Fluid Phase Equilib.*, 517, 112613, 2020, doi: 10.1016/j.fluid.2020.112613.

[15] B. Bentama, H. Grine, I. Anoune, H. Madani, C. Bougriou, "Calculation of azeotropic properties for binary mixtures with the PC-SAFT equation of state," *Fluid Phase Equilib.*, 565, 113631, 2023, doi: 10.1016/j.fluid.2022.113631.

[16] L. A. Serafimov, O. B. Razova, A. V. Frolkova, T. V. Chelyuskina, "The Gibbs-Konovalov law at simple singular points of two-phase multicomponent system diagrams," *Russ. J. of Phys. Chem. A*, 82, 946–950, 2008, doi: 10.1134/S0036024408060149.

[17] I. Anoune, Z. Mimoune, H. Madani, A. Merzougui, "New modified PC-SAFT pure component parameters for accurate VLE and critical phenomena description," *Fluid Phase Equilib.*, 532, 112916, 2021, doi: 10.1016/j.fluid.2020.112916.

[18] T. Yang, X. Hu, X. Meng, J. Wu, "Vapor–Liquid Equilibria for the Binary and Ternary Systems of Difluoromethane (R32), 1,1-Difluoroethane (R152a), and 2,3,3,3-Tetrafluoroprop-1-ene (R1234yf)," *J. Chem. Eng. Data*, 63, 771–780, 2018, doi: 10.1021/acs.jced.7b00950.

[19] X. Hu, T. Yang, X. Meng, J. Wu, "Isothermal vapor liquid equilibrium measurements for difluoromethane (R32) + fluoroethane (R161) + trans-1,3,3,3-tetrafluoropropene (R1234ze(E)) ternary mixtures," *Int. J. Refrig.*, 79, 49–56, 2017, doi: 10.1016/j.ijrefrig.2017.04.019.

[20] Y. Zhao *et al.*, "Vapor Liquid Phase Equilibrium for Azeotropic Isobutane + *trans* -1,3,3,3-Tetrafluoropropene + Trifluoroiodomethane System at Temperatures from 243.150 to 283.150 K," *J. Chem. Eng. Data*, 63, 812–821, 2018, doi: 10.1021/acs.jced.7b00964.

[21] P. Hu, W.-B. Zhu, L.-X. Chen, X.-D. Cai, Z.-S. Chen, "Vapor–liquid equilibria measurements of 1,1,1,2-tetrafluoroethane (HFC-134a)+2,3,3,3-tetrafluoroprop-1-ene (HFO-1234yf)+isobutane (HC-600a) ternary system," *Fluid Phase Equilib.*, 414, 111–116, 2016, doi: 10.1016/j.fluid.2016.01.028.

[22] X. Han, Z. Gao, J. Lei, B. Yang, Y. Zhao, G. Chen, "Isothermal Vapor–Liquid Equilibrium of the Ternary Mixture of 1,1,1,2-Tetrafluoroethane + 2,3,3,3-Tetrafluoroprop-1-ene + Dimethyl Ether at Temperatures from 253.15 K to 323.15 K," *J. Chem.*

Eng. Data, 60, 2219–2225, 2015, doi: 10.1021/je501167d.

[23] Y. Zhao, M. Gong, X. Dong, H. Guo, J. Wu, "The investigation on the vapor + liquid equilibrium for the ternary mixture isobutene (R600a) + 1,1-difluoroethane (R152a) + 1,1,2,2-tetrafluoroethane (R134) at temperatures from 253.150 to 273.150 K," *Fluid Phase Equilib.*, 408, 72–78, 2016, doi: 10.1016/j.fluid.2015.08.020.

Research Article

Validation of Bluff-body Swirling Flame with RANS Turbulent Model and Comparison of the Results with LES Turbulent Model

[1]O. V. Kazancı [ID], [2]Y. E. Böke [ID]

[1]İstanbul Technical University, Mechanical Eng. Faculty, Mechanical Engineering Division
34437, İstanbul, Türkiye.
[2]İstanbul Technical University, Mechanical Eng. Faculty, Mechanical Engineering Division
34437, İstanbul, Türkiye.
E-mail: [1]*kazanci@itu.edu.tr

Abstract

The energy required for technological advancement is primarily derived from hydrocarbon combustion, which is a key topic in thermodynamics. The stability of the flame in hydrocarbon combustion is a critical parameter that impacts both burner design and combustion efficiency. Various methods have been employed in the literature to achieve a stable flame, with swirl flow being one technique that enhances combustion performance in engineering applications. This study focuses on the numerical analysis of the SM1 flame from Sydney swirl flames. Initially, the flow incorporating the two-equation Re-Normalization Group (RNG) k-ε and Shear Stress Transport (SST) k-ω turbulence models, along with the chemical reactions of CH_4 combustion using the GRI 3.0 reaction mechanism, was modeled and compared with experimental data. Subsequently, the numerical results obtained from the Shear Stress Transport k-ω turbulence model, which demonstrated the best agreement with experimental data, were compared with results from a numerical analysis in the literature using the Large Eddy Simulation (LES) turbulence model. The predictive capabilities of these two turbulence models, along with their behavior in the flow region, were evaluated. The comparison revealed that for stable flames within the Sydney swirl flame family, the Shear Stress Transport k-ω turbulence model, which provides results in a more efficient manner, is sufficient compared to the computationally expensive Large Eddy Simulation turbulence model. This choice is made possible by utilizing a solution algorithm tailored to the flow characteristics and appropriate boundary conditions.

Keywords: *Swirling flow; thermodynamics; non-premixed combustion; Reynolds Averaged Navier-Stokes; Large Eddy Simulation.*

1. Introduction

Nowadays, the problem of environmental pollution caused by the combustion of fossil fuels demands significant attention. In recent years, the focus has shifted towards finding effective solutions to increase combustion efficiency and reduce emissions [1]. To address this issue, researchers are exploring various combustion methods that can ensure efficient fuel utilization, such as non-premixed turbulent flames involving introducing a swirl into the flow to stabilize the flames. The current emphasis on environmental pollution caused by fossil fuel combustion has led researchers to prioritize improving combustion efficiency and pollutant removal. In understanding this complex relationship, previous studies have highlighted the importance of considering thermodynamic properties of gas combustion. The relationship between gas combustion and thermodynamics is a complex one, influenced by a range of factors. Brinkley highlights the importance of understanding the thermodynamic properties of combustion gases in power plant design, with a focus on thermal equilibrium [2]. Sugawara further explores this, discussing the changes in temperature, velocity, and pressure of combustion gas in a combustion chamber, and their relationship with the fuel-air

ratio [3]. Lots of researchers delve into the chemical kinetics of combustion to identify the invariance of the adiabatic temperature for certain combustion mixtures. Lee and Guirao add to this by discussing the gas dynamic effects of fast exothermic reactions, emphasizing the interplay between gas dynamics and chemistry in combustion phenomena [4]. These studies collectively underscore the intricate relationship between gas combustion and thermodynamics, shaped by a range of physical and chemical factors.

In non-premixed systems, the air-fuel mixture is provided before the combustion reaction. Efficient mixing and stable combustion over wide operating ranges are essential for the design of a properly functioning combustor. In many non-premixed systems, fuel is injected into the region of high turbulent flow to increase mixing and geometric or aerodynamic flame stabilizer mechanisms are used to ensure flame stability. The bluff body is one of the classic geometric flame stabilizers. The recirculation zone that occurs behind the bluff body in the flow allows the hot combustion products to be carried upwards, thus ensuring re-combustion and flame persistence. In aerodynamic flame stabilizers, recirculation bubbles, often referred to as vortex breakdown bubbles, are created by the circularity of the flow field. In

some combustors, both types of flame stabilizers can be used to improve air-fuel mixing and flame stability. Such flames are used in industrial applications such as gas turbines and furnaces due to their superiority over non-cyclic turbulent flames [5]. The salient features of swirl stable turbulent flames are increased fuel and combustor mixing, flame stability, flame extinction characteristics, and low emission rates [6].

Swirl stabilized flows and flames have been studied in many experimental studies in the literature. TNF workshops are one of the most comprehensive of these experimental studies [7]. The TNF workshops have well-designed experiments for many different non-premixed flame configurations. Simple jet flames, bluff-body stabilized jet flames and swirl stabilized jet flames are some of the flame types studied in these workshops. The bluff-body stabilized jet flames, a sub-topic of the TNF workshop, provide flames suitable for turbulence-chemistry interaction studies such as piloted burners. Bluff-body burners are also quite similar to real-world combustors that are employed in several industrial settings. Because it retains relatively basic and well-defined boundary constraints while incorporating some of the complexity inherent with real-world combustors, this geometry makes an appropriate compromise for use as a model issue. In TNF Workshops, the bluff-body burner was experimentally studied for several test-cases named HM1e, HM1, HM2, HM3, and HM3e. Swirl stabilized burner, another topic of TNF Workshop, constitutes a natural extension of the bluff-body burner, emerging through the incorporation of a 60 mm inner diameter annulus appended to the bluff-body. This annular addition facilitates the introduction of swirled air, which is delivered tangentially through systematically arranged inlets located at the base of the burner. The swirl-stabilized flame configuration is the most complex test case to determine the accuracy of various turbulence and combustion models because it has two recirculation zones in a specific combination of low swirl number and higher primary axial velocity as opposed to bluff-body stabilized flows, which only have one. There is a Sydney swirl flow project subgroup within the TNF workshops swirl stabilized burner flames. In this subgroup, there are two isothermal swirling flow studies (N29S054 and N16S159) and eight reacting swirling flow (SM1, SM2, SMA1, SMA2, SMA3, SMH1, SMH2 and SMH3) studies for three different fuel types. In first group, SM1 and SM2 flames utilize methane as a fuel and have been tested in the same burner. A swirl coefficient of 0.5 has been employed for both flames. The fuel jet velocity for SM2 is significantly higher than that of SM1. The air jet velocity is consistent for both flames. The impact of the elevated fuel jet velocity has been comparatively investigated. In second group, a mixture of methane and air at a ratio of 1:2 was utilized as the fuel in the flames SMA1, SMA2, and SMA3. The swirl coefficient is 0.66 for SMA1 flame and 1.59 for both SMA2 and SMA3 flames. The study investigated the effects of two different air jet velocities for a constant fuel jet velocity and the effects of two different fuel jet velocities for a constant air jet velocity. In last group, the flames SMH1, SMH2, and SMH3 were fueled with a mixture of methane and hydrogen in a 1:1 ratio. The swirl coefficient is 0.32 for SMH1 flame and 0.54 for both SMH2 and SMH3 flames. The study systematically examined the influence of two distinct air jet velocities while maintaining a constant fuel jet velocity, as well as the effects of two different fuel jet velocities under conditions of constant air jet velocity. The results of these experimental

studies have been presented to the literature in several studies with in-depth analysis [8, 9].

The configuration of swirl-stabilized flames is one of the most difficult experimental studies to verify with different turbulence and combustion models [10]. Many working groups have been working on the modeling and verification of these isothermal and reacting experimental studies for about 20 years. In these studies, personal numerical codes and commercial package programs have been used [11, 12] and the results have been published [13].

In their study, Rahman et al. tried to capture the critical flow properties of isothermal turbulent flows stabilized by swirling flow. They investigated the effects of the quality of the mesh structure in critical regions, mesh structure, discretization methods, and various turbulence models on the accurate calculation of flow properties [13]. Researchers underscore the crucial role of mesh resolution in accurately capturing a sizable vortex breakdown bubble. The findings show that 3D RANS simulations can be a useful option for industry, offering a more affordable alternative to the computationally demanding LES. Engineers can gain practical guidance on choosing numerical modeling configurations for complex 3D flow issues.

In a study with 2D axisymmetric geometry, Radwan et al. used Standard and Realizable k-ε, Standard k-ω, and Reynolds Stress Model turbulence models to analyze isothermal turbulent flows of Sydney swirl flow project [11]. In particular, the study aimed to calculate the overall flow behavior and compare it with the experimental model. The numerical investigations showed that among the tested RANS models, Standard k-ω demonstrated acceptable performance in predicting the swirling flow features in both low and high swirl level cases. In addition, the study concluded that the tested RANS models, particularly the one with acceptable performance, can be used as a tool to predict the characteristics of swirling flow in combustor configurations similar to the Sydney swirl burner. Also, researchers implied that the numerical simulations and experimental validation conducted in this study can serve as a reference for future studies on unconfined swirl flow, providing a basis for further research and development in this area.

Yang et al. investigated the SM1 flame, with 2D axisymmetric geometry, using customized Standard k-ε and Realizable k-ε turbulence models in ANSYS Fluent [14]. The researchers stated that the customized Standard k-ε turbulence model is more consistent with the experimental results. Similarly, West et al. tried to calculate the mean and fluctuating velocity values in the flow field using DES (Detach Eddy Simulation) based on SST [15]. Swirl-type regeneration burner was investigated by Fu et al. with four different two-equation turbulence models [16]. The researchers emphasized that SST k-ω and Realizable k-ε models give better results in the flow field. Kashir et al. conducted a comparative study using SST k-ω and Realizable k-ε models in a 2D axisymmetric region [6]. They reported that both models give satisfactory results in the flow field, mixing ratios, temperature, and mass fractions of carbon monoxide in agreement with experimental data. Researchers implied that the prediction of temperature and carbon monoxide mass fraction in the flow field can aid in the design of combustion systems with better control over temperature distribution and reduced CO emissions. They also added that the findings of this study can be used to optimize the design and operation of bluff-body stabilized

swirl flames in practical combustion systems, such as gas turbines and industrial burners [6].

For the swirling flow in the near-burner zone, Weber et al. examined the outcomes of the Reynolds stress model (RSM), k−ε, and an algebraic stress model (ASM) [17]. They found that in the burner quarl area, where the inviscid expansion of flow takes place, the k-ε model introduces a significant inaccuracy. Nonetheless, whirling vortices may be well predicted by RSM and ASM models that use the quadratic upstream differencing (QUICK) discretization scheme for convective components. In another study Gupta and Kumar investigated the dynamics of the three-dimensional flow in a cyclone with tangential inlet and tangential exit using particle tracking velocimetry (PTV) and a three-dimensional computational model [18]. They compared the k-ε and RNG k-ε turbulence numerical models for their suitability in studying the dynamics of pure liquid flowing in a cyclone. According to their findings, the traditional k–ε model is not as good at predicting the flow field as the RNG k–ε model. As a result, they observed secondary recirculating flow and the accurate prediction of its characteristics can help in the development of more efficient separation processes in cyclones, which is important for industries that rely on particle separation and filtration [18].

Christo and Dally used several k−ε models to study the turbulent non-premixed methane/hydrogen flame [19]. They noted that the best agreement with experimental data is shown by the standard k−ε model findings combined with the modified dissipation constant. They also implied that accurate modeling of turbulence, combustion, and chemical kinetics is crucial for predicting the performance of jet in hot flames.

Safavi and Amani conducted one of the most recent studies on the Sydney flames [6]. They compared various steady regime and time-dependent turbulence models such as 2D RANS (Reynolds Averaged Navier Stokes) (RNG k-ε, SST k-ω, Transition SST and RSM (Reynolds Stress Model)), LES (Germano's Dynamic SGS (Sub Grid Scale)), 3D hybrid models (based on SST k-ω) SAS (Scale Adaptive Simulation), Realizable k-ε DES and SST k-ω DES. The results are analyzed focusing on the all flow field and vortex breakdown bubble, which is characteristic of swirl stabilized flames.

Lu et al. modeled the SM1 swirling flame using the Standard k-ε turbulence model with modified coefficients, steady diffusion flamelet combustion model, and DO (discrete ordinate) radiation model [20]. As a result of the analyses, they reported that the turbulence model is inadequate in the regions where the shear stress of the flow is dominant, but in general, it captures the experimental results. Wang et al. demonstrated that Large Eddy Simulation (LES) conducted on a grid of moderate density effectively replicates the precessing vortex core structures in unconfined swirl flow, exhibiting accuracy in both reactive and non-reactive conditions [21]. They also concluded that the observation of vortex structures and spiral-type vortices outside the flame front can provide insights into the flow dynamics and flame behavior, which can be utilized in the development of more efficient and stable combustion systems.

Wegner et al. investigated 3D flow patterns in a non-premixed swirl combustor called the TECFLAM project [22]. They compared time-dependent RANS simulation with experimental results and results obtained with the LES

turbulence model. The researchers observed that the time-dependent RANS turbulence model models the flow velocity and vortex core frequency with high accuracy. However, they stated that this turbulence model underestimates the amount of energy in the motion of the precessing vortex core compared to the LES turbulence model. Chen et al. investigated the reactive swirl flow in a combustor with Standard k-ε, RNG k-ε, SST k-ω, and LES turbulence models [23]. They reported that the results obtained with the LES turbulence model are much better than the RANS turbulence models for the flow field and scalar quantities. They also added that the best results among the RANS turbulence models were obtained with the SST k-ω turbulence model.

Apart from RANS simulations, there are also studies on Sydney swirling flames in the literature by Malalasekara et al [24], El-Asrag and Menon [25], Hu et al [26], Xu et al [27], Luo et al [28], Yang and Kaer [12] using the LES turbulence model. In these studies, it was observed that the results obtained from the LES turbulence model were in good agreement with the experimental results in the Sydney swirling combustor. However, the LES turbulence model is not a widely preferred method due to its high cost in core hours. The RANS approach, which is shorter in computer time and lower in cost, has been the predominantly preferred technique in CFD studies to date [29].

The literature survey conducted in this study has shown that RANS analyses with 2D axisymmetric geometry cannot adequately capture the primary flow characteristics of Sydney swirling flames. The vortex breakdown bubble and the upper recirculation zone are three-dimensional in nature and 2D geometries cannot adequately resolve the flow physics of these structures. Therefore, three-dimensional geometries are better choices for solving such flows and are more suitable for use in analysis. A limited number of three-dimensional RANS analyses of Sydney swirling flames are available in the literature, but these studies have focused on predicting the velocity behavior in various flow regimes obtained from isothermal experimental results. In this study, unlike other studies in the literature, the three-dimensional velocity and combustion behavior of SM1, a reactive Sydney swirling flame, is evaluated. It is also aimed to develop a numerical model compatible with the experimental results, to reduce computer time and to provide resources for swirl flame studies.

In the first part of this study, the results obtained from the two-equation RANS (RNG k-ε, SST k-ω) turbulence models (RNG k-ε, SST k-ω), which give successful results in solving swirling flow problems in three-dimensional geometry, are compared with experimental data for the SM1 swirling reactive flow from the Sydney swirl flame family. In the second part of the study, the results of the SST k-ω turbulence model, which gives more consistent results with the experimental data, are compared with the results of the LES turbulence model analysis results which is published. RANS analyses were obtained with the ANSYS Fluent 2020 R1 program. The results of the LES turbulence model are taken from the data shared by Malalasekara et al. in their study [24]. In the literature, there is no such study has been encountered comparing the validations with three-dimensional RANS and LES turbulence models for the SM1 flame. The comparison of the analyses shows that the agreement of the two-equation SST k-ω turbulence model with the experimental data is very similar to the results of the LES turbulence model. For the stable flames of the Sydney

swirl flame family, it is concluded that the use of the two-equation SST k-ω turbulence model, which can be obtained in a shorter time instead of the LES turbulence model, which is much more expensive in terms of core hours, is sufficient and provides analysis without spending much resources by using the solution algorithm suitable for the characteristics of the flow and the correct boundary conditions.

2. Experimental Setup

The Sydney swirl burner selected for the analyses has a radius (D) 50mm ceramic surface. In the center of the ceramic surface is a 3.6mm diameter fuel inlet. Swirl flow is provided by a 5mm wide annular region around the ceramic surface. The swirl of the airflow in the burner is achieved aerodynamically by air entering at a 15° angle through 3 tangential inlets located below the air inlet. The combustor is located in the center of a 130x130mm wind tunnel that provides secondary flow to have well-defined boundary conditions. A detailed drawing of the combustor can be seen in Fig. 1 [8].

There are four velocities that are important in the flow characteristics of this combustor. These velocities are the axial velocity U_j of the fuel jet, the axial and tangential velocities U_s and W_s of the air coming circularly from the annular cross-section, and the axial velocity U_e of the secondary airflow coming from the wind tunnel. The geometric swirl value, which indicates the intensity of the cyclic motion in the combustion air, is expressed by S_g. This value is directly proportional to the momentum swirl value S ($S=0.9S_g$). In this study, the SM1 flame from the Sydney swirl flame family was verified. Pure CH_4 was used as fuel in the SM1 flame. The velocity values of the SM1 flame are given in Table 1.

Detailed information about the Sydney swirl burner and experimental results can be found in the literature in the publications of the working group [8, 30, 31].

Table 1. Characteristic velocity values for SM1 flame.

Flame	U_s [m/s]	W_s [m/s]	U_j [m/s]	U_e [m/s]	S_g
SM1	38.2	19.1	32.7	20	0.54

3. Numerical Analysis

In this section, the geometry used in the study, the mesh structure created for this geometry, the independence of the mesh structure, and the solution algorithms selected for the numerical analysis of the physical problem are described. The turbulence models RNG k-ε and SST k-ω, which are used to calculate the flow field in the solution phase, are described in detail in the following sections of this chapter. Detailed information on other solution algorithms can be found in the ANSYS Fluent Theory Manual [32], and other references in the literature.

3.1 Geometry, Mesh Structure and Mesh Independency

The dimensions of the three-dimensional flow field used in this study are shown in Fig. 2. The flow field is considered cylindrical. The outer diameter of the cylinder is 146mm and the length from the air and fuel inlets is 300mm. When creating the geometry, the geometry was extended by 35mm in front of the air and fuel inlets to take into account the effect of the 2° angle in the secondary air flow channel. To generate the mesh structure of the three-dimensional geometry, the mesh generation program within the ANSYS Fluent program was used. The mesh structure of the geometry is shown in

Fig. 3 and Fig. 4 as isometric and front view. The mesh is denser in the air and fuel inlet area and coarser towards the end of the geometry. The length of the first element in the inlet region is 0.175mm.
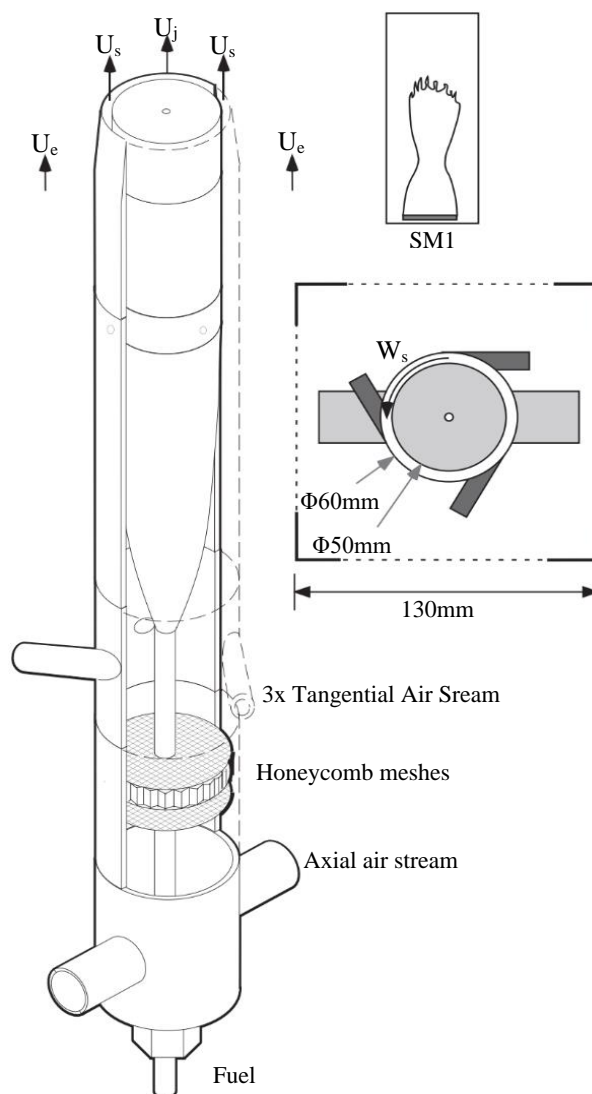
Figure 1. Schematic view of a swirl burner [4].
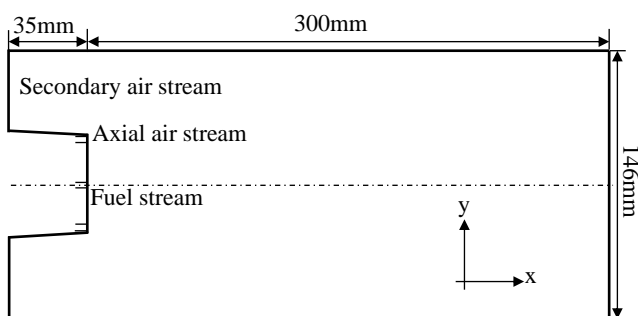
Figure 2. Measurements of three-dimensional geometry.

In order to ensure mesh independency in the analyses, meshes consisting of 2.1M (million), 3.1M and 5.2M structural elements were created. The three mesh structures were numerically analyzed using the SST k-ω turbulence model, appropriate boundary conditions and solution methods. The temperature change in the radial direction in the x/D=1.5 plane is given in Fig. 5. As can be seen from Fig. 5, the difference between the analysis results of the mesh structure with 3.1M elements and the mesh structure with

5.2M elements is quite low. Taking advantage of this result, the mesh structure consisting of 3.1M structural elements was used for all future analyses.
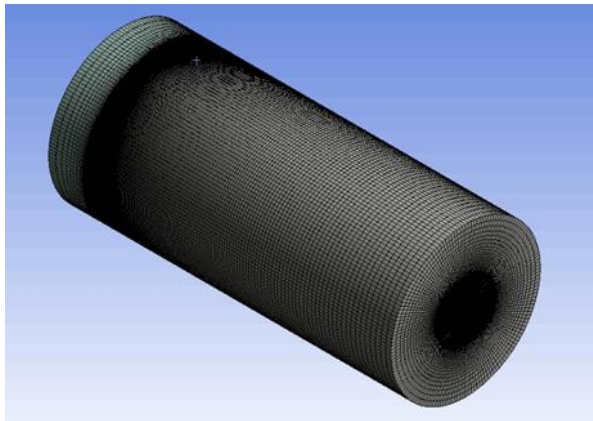

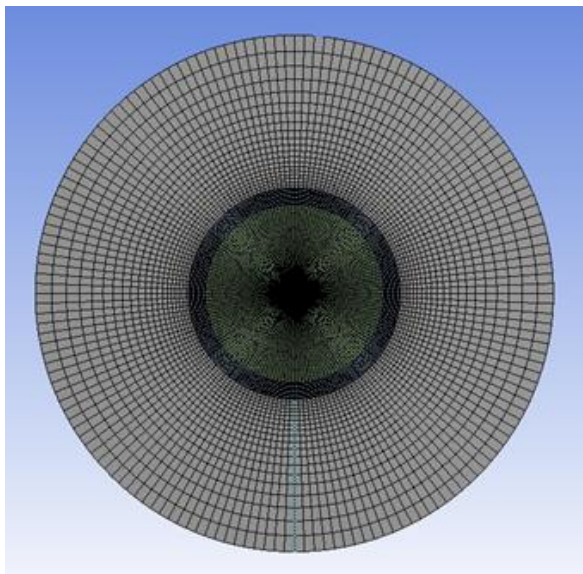*Figure 3. Isometric view of the mesh structure.*

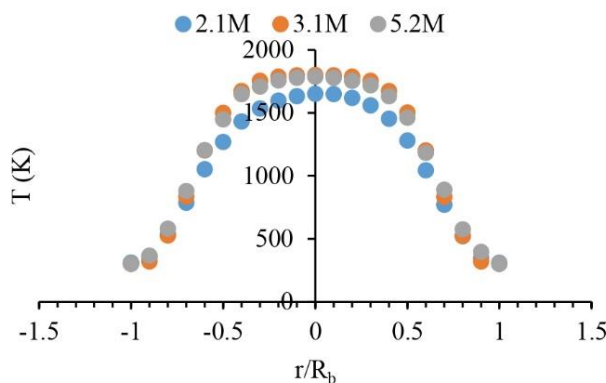*Figure 4. Front view of the mesh structure.*

Figure 5. Comparison of temperature values in radial direction for different mesh structures for x/D=1.5.

3.2 Numerical Solution Method

The numerical analysis code of ANSYS Fluent 2020 R1 program was used in the study. RNG k-ε and SST k-ω models were used as turbulence models. P1 was used for radiation and the steady diffusion flamelet sub-model within the non-premixed combustion model was used to model the combustion reaction. The analyses were run in the continuous regime. SIMPLE (Semi Implicit Method for Pressure Linked Equations) model was chosen for the pressure-velocity coupling solution. The PRESTO! method was chosen for pressure calculations, while the QUICK method was chosen for momentum calculations. For other conservation equations and scalar quantities, the second order forward approximation was preferred. The convergence criterion for all equations was taken as 10^{-6}.

3.3 Turbulent Flow Models

The RANS numerical method is a method used in computational fluid mechanics to solve the flow field. They are formed by Reynolds averaging the Navier-Stokes equations. As a result of applying the Reynolds averaging process to the Navier-Stokes equations and organizing these equations, the Reynolds stress term expressed as $-\rho\overline{u_i'u_j'}$ must be solved in order to solve the equations. The most common method used to solve this stress is the Boussinesq approach. Detailed information about this approach can be found in the work of Schmitt F. G. [33]. In order to solve the expression obtained by applying the Boussinesq approximation, the turbulent viscosity μ_t must be solved. After the partial success of the first couplings used for the calculation of turbulent viscosity, it was observed by researchers that this quantity is a property of the flow, not of the fluid, and that convection effects should be taken into account. As a result, methods that take into account convection effects have been proposed. The two-equation RNG k-ε and SST k-ω turbulence models used in this study are among these proposed models.

3.3.1 RNG k-ε turbulence model

The RNG k-ε turbulence model was developed using a statistical method called Renormalization group theory. Compared to the standard k-ε model, the RNG k-ε model takes turbulence fluctuations (eddies) into account and provides an analytical expression for the turbulent Prandtl number. The RNG k-ε model significantly improves the simulation accuracy of the flow by taking into account the effect of large-scale motions, regulating the viscosity governing the operation of small-scale effects, and systematically removing small-scale motions from the control equations. The equations for the quantities k and ε in the RNG k-ε turbulence model are given in Eq. 1 and Eq. 2.

$$\frac{d}{dt}(\rho k)=\frac{\partial}{\partial x_i}\left(\alpha_k\mu_{eff}\frac{\partial k}{\partial x_i}\right)+G_k+G_b-\rho\varepsilon-Y_M \tag{1}$$

$$\frac{d}{dt}(\rho\varepsilon)=\frac{\partial}{\partial x_i}\left(\alpha_\varepsilon\mu_{eff}\frac{\partial\varepsilon}{\partial x_i}\right)+C_{1\varepsilon}\frac{\varepsilon}{k}\left(G_k+C_{3\varepsilon}G_b\right)-C_{2\varepsilon}\rho\frac{\varepsilon^2}{k}-R_\varepsilon \tag{2}$$

In the equations, G_k is the formation of turbulent kinetic energy with respect to mean velocity gradients, G_b is the formation of turbulent kinetic energy with respect to buoyancy, and Y_M is the contribution of the fluctuating dilatation in compressible turbulence to the overall dissipation rate. The expressions α_k and α_ε are the inverse effective Prandtl numbers for k and ε, respectively. The R_ε expression in Eq. 2 is absent in the standard k-ε model and the R_ε expression is as in Eq. 3.

$$R_\varepsilon=\frac{C_\mu\rho\eta^3(1-\eta/\eta_0)\varepsilon^3}{k(1+\beta\eta^3)} \tag{3}$$

$$S_{ij}=\frac{1}{2}\left(\frac{\partial u_i}{\partial x_j}+\frac{\partial u_j}{\partial x_i}\right) \tag{4}$$

In this expression, η is equal to $S(k/\varepsilon)$. The expression for *S* is equal to $\sqrt{2S_{ij}S_{ij}}$ and the expression for the stress

tensor S_{ij} is given in Eq. 4. Among the constants in these expressions, η_0 has a value of 4.38 and β has a value of 0.012. If the Reynolds number is small and the fluid flow at the wall edge is considered, the turbulence viscosity is calculated as in Eq. 5.

$$d\left(\frac{\rho^2 k}{\sqrt{\varepsilon\mu}}\right)=1,72\frac{\hat{v}}{\sqrt{\hat{v}^3-1-C_v}}d\hat{v} \tag{5}$$

In this expression, $\hat{v}=\mu_{eff}/\mu$ and C_v is equal to 100. If the Reynolds number is large, the turbulence viscosity is calculated as in Eq. 6. The effective viscosity μ_{eff} is calculated by the formula in Eq. 7. The μ value in Eq. 7 represents the fluid viscosity. The value of C_μ in Eq. 6 is 0.0845.

$$\mu_t=\rho C_\mu\frac{k^2}{\varepsilon} \tag{6}$$

$$\mu_{eff}=\mu+\mu_t \tag{7}$$

The values of the model constants used for the RNG k-ε turbulence model in the ANSYS Fluent program are $\alpha_k=1.39$, $\alpha_\varepsilon=1.39$, $C_{1\varepsilon}=1.42$ and $C_{2\varepsilon}=1.68$.

3.3.2 SST k-ω turbulence model

The SST k-ω turbulence model is one of the most common models used to observe the effect of turbulence in flow analysis. It is a model with two equations. One equation solves the turbulence kinetic energy (k) term as in the k-ε model, while the other equation solves the specific dissipation rate (ω). The k-ω model has been developed by researchers due to the fact that the solutions with the k-ε model do not give appropriate results, especially in regions close to the wall. First, the standard k-ω model was introduced by David D. Wilcox. Later, the k-ω Base-Line (BSL) model was developed by considering the deficiencies and the SST k-ω model was introduced to the literature by F. R. Menter in 1994. The transport equations and algorithm of the model are explained in the following section of the chapter. Also, the details of the turbulence model can be found in the literature [34].

The SST k-ω model behaves like the k-ε turbulence model in the free flow region, thus eliminating the sensitivity of the standard k-ω turbulence model in the free flow region. The model also provides better flow separation solutions than many other models and takes into account the behavior of inverse pressure gradients. The equations of the model are given in Eq. 8 and Eq. 9.

$$\frac{\partial}{\partial t}(\rho k)+\frac{\partial}{\partial x_i}(\rho k u_i)=\widetilde{P}_k-\beta^*\rho k\omega$$
$$+\frac{\partial}{\partial x_i}\left[(\mu+\sigma_k\mu_t)\frac{\partial k}{\partial x_i}\right] \tag{8}$$

$$\frac{\partial}{\partial t}(\rho\omega)+\frac{\partial}{\partial x_i}(\rho\omega u_i)=\alpha\frac{1}{v_t}\widetilde{P}_k-\beta\rho\omega^2+\frac{\partial}{\partial x_i}$$
$$\cdot\left[(\mu+\sigma_\omega\mu_t)\frac{\partial\omega}{\partial x_i}\right]+2(1-F_1)\rho\sigma_{\omega,2}\frac{1}{\omega}\frac{\partial k}{\partial x_i}\frac{\partial\omega}{\partial x_i} \tag{9}$$

In the equations, k is the kinetic energy of turbulence, ω is the specific dissipation rate, ρ is the density, u is the velocity vector and μ is the dynamic viscosity. When calculating the model parameters, the constants in the k-ε and k-ω models are calculated using the blending function using

the expression $\theta=F_1\theta_1+(1-F_1)\theta_2$. The blending function F_1 used here is given in Eq. 10.

$$F_1=\tanh\left\{\left\{\min\left[\max\left(\frac{\sqrt{k}}{\beta^*\omega y},\frac{500v}{y^2\omega}\right),\frac{4\rho\sigma_{\omega,2}k}{CD_{k\omega}y^2}\right]\right\}^4\right\} \tag{10}$$

$$CD_{k\omega}=\max\left(2\rho\sigma_{\omega,2}\frac{1}{\omega}\frac{\partial k}{\partial x_i}\frac{\partial\omega}{\partial x_i},10^{-10}\right) \tag{11}$$

The expression for $CD_{k\omega}$ in the expression for the blending function is given in Eq. 11. The y value in these expressions represents the distance from the nearest wall. In the model, μ_t represents the turbulence fluctuation viscosity. The formula for μ_t is given in Eq. 12.

$$\mu_t=\frac{\alpha_1\rho k}{\max(\alpha_1\omega,SF_2)} \tag{12}$$

S in Eq. 12 is equal to $\sqrt{2S_{ij}S_{ij}}$. The F_2 value in this expression is the second blending function of the model. The expression for F_2 can be seen in Eq. 13.

$$F_2=\tanh\left[\left[\max\left(\frac{2\sqrt{k}}{\beta^*\omega y},\frac{500v}{y^2\omega}\right)\right]^2\right] \tag{13}$$

$\widetilde{P}_k$ in Eq. 8 and Eq. 9 is the production term. In Eq. 14, the expression $\widetilde{P}_k$ can be seen. In Eq. 13 there is a limit function to prevent the development of turbulence in the separation regions of the flow. The expression for P_k is given in Eq. 15.

$$\widetilde{P}_k=\min(P_k,10\cdot\beta^*\rho k\omega) \tag{14}$$

$$P_k=\mu_t\frac{\partial u_i}{\partial x}\left(\frac{\partial u_i}{\partial x_j}+\frac{\partial u_j}{\partial x_i}\right) \tag{15}$$

More detailed information about this model can be obtained from various sources in the literature and ANSYS Fluent Theory Guide [32]. The model constants and values used in the ANSYS Fluent program can be seen in Table 2.

Table 2. Model constants for the SST k-ω turbulence model.

Constant	Value	Constant	Value
$\sigma_{k,1}$	1.176	α_∞^*	1.000
$\sigma_{k,2}$	1.000	α_0	1/9
$\sigma_{\omega,1}$	2.000	β_∞^*	0.090
$\sigma_{\omega,2}$	1.168	R_β	8.000
α_1	0.310	R_k	6.000
$\beta_{i,1}$	0.075	R_ω	2.950
$\beta_{i,2}$	0.0828	μ_{t0}	0.0828
α_∞	0.52	ζ^*	1.500

4. Results and Comparison

This section, where the numerical analysis results are evaluated, consists of two main parts. In the first part, the axial velocity and temperature results of the analyses performed with the two-equation RNG k-ε and SST k-ω turbulence models are compared with the experimental results. In this section, the temperature contours obtained with both turbulence models are also evaluated in terms of the flame shape obtained.
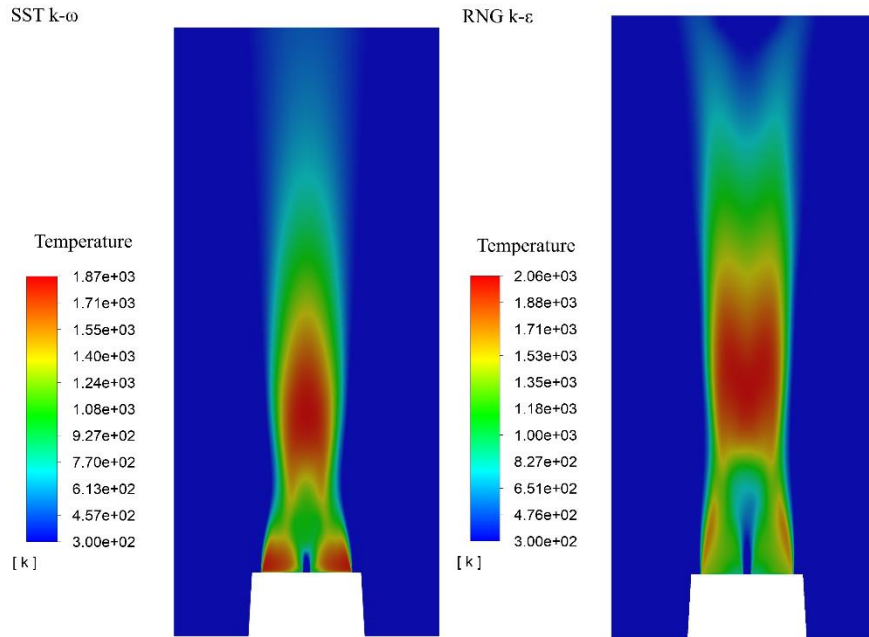
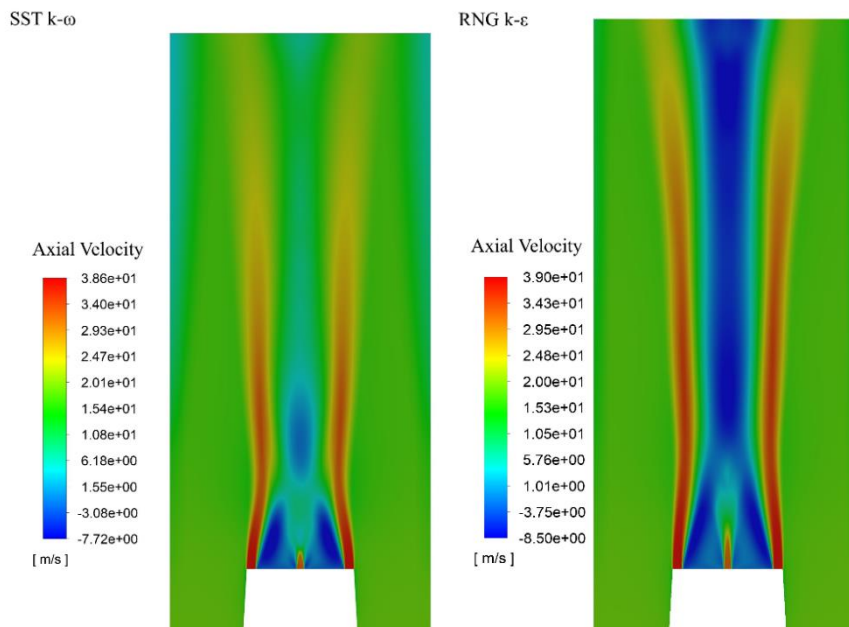*Figure 6. Temperature contours of SST k-ω and RNG k-ε turbulence model solutions.*

Figure 7. Axial velocity contours of SST k- ω and RNG k-ε turbulence model solutions.

In the second part, the numerical modeling results of axial velocity, tangential velocity, temperature, mean mixture fraction, mass fractions of H_2O, CO and CO_2 components obtained with the SST k-ω and LES turbulence models were compared with the experimental results and the agreement with the experimental results was examined. Pure CH_4 was used as a fuel in all analysis.

4.1 Results for RNG k-ε vs SST k-ω Turbulence Models

Except for the turbulence model, all other solution algorithms are the same. In this section, the temperature contours obtained with the two turbulence models are first analyzed. According to the measurements made by the researchers, the SM1 flame has two flow regions called the first recirculation region and the second recirculation region [8]. The first recirculation zone ends 43mm from the bluff body surface, while the second recirculation zone starts 65mm from the bluff body surface and ends 110mm from the

bluff body surface. The recirculation zone is an important characteristic behavior for swirling flames. The flow in these regions is quite complex. Therefore, the first goal of numerical approaches is to accurately calculate these recirculation zones [14]. The recirculation regions of the SM1 flame obtained by numerical analysis of SST k-ω and RNG k-ε are shown in Fig 6.

As can be seen in Fig. 6, the characteristics of the SM1 flame are better predicted by the SST k-ω turbulence model. Both the upper recirculation region and the lower recirculation region resulting from vortex breakdown are more pronounced. The neck region of the flame is also more pronounced than the solution of the RNG k-ε turbulence model. In the solution obtained from the SST k-ω turbulence model, the flame spreads more on the bluff body surface. In the results of the RNG k-ε turbulence model, the flame adheres to the bluff body surface from the outer periphery,
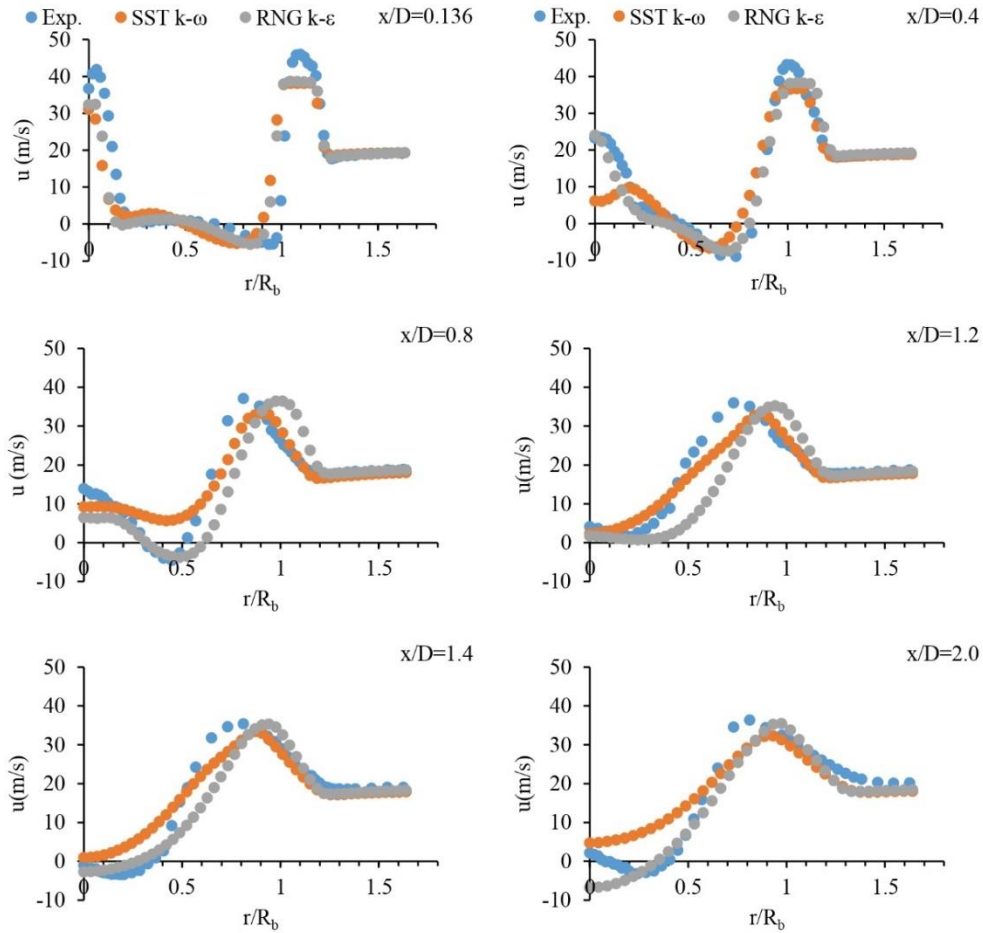
Figure 8. Comparison of axial velocity results of SST k-ω and RNG k-ε turbulence models with experimental data.
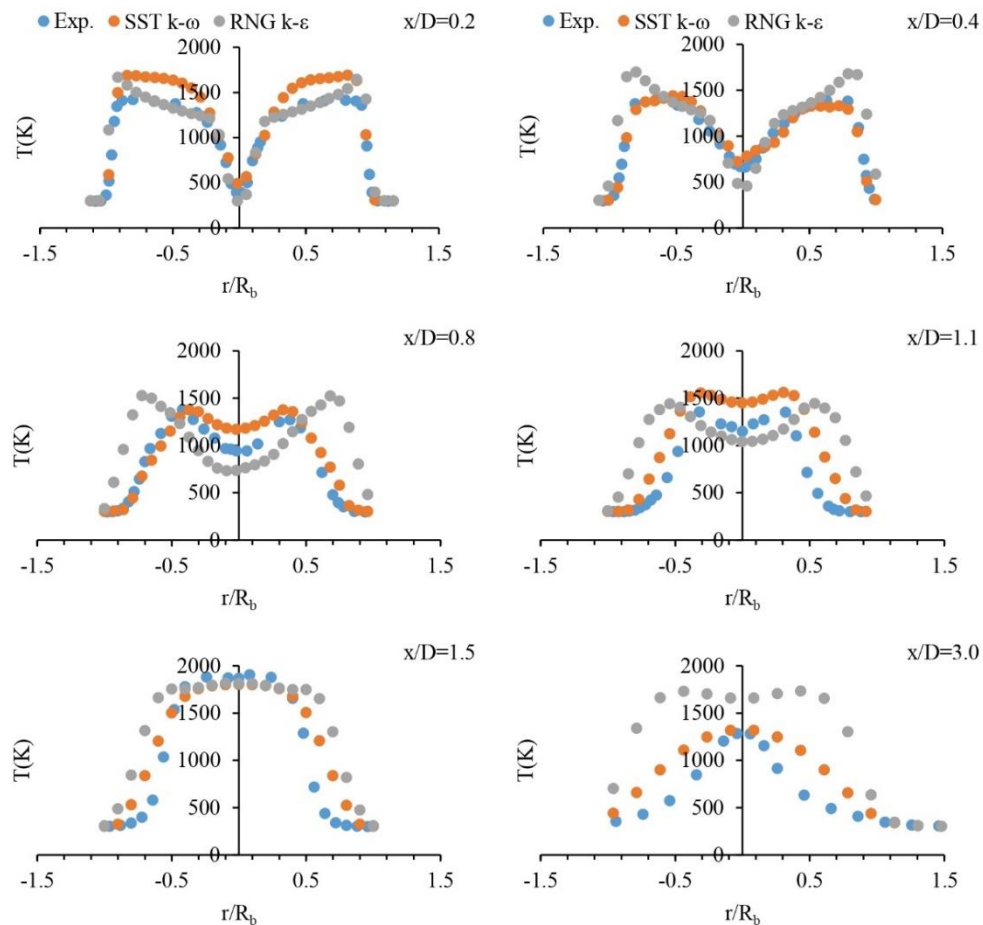
Figure 9. Comparison of temperature results of SST k-ω and RNG k-ε turbulence models with experimental data.

and a colder temperature contour is obtained on the bluff body surface. This is not consistent with the experimentally measured temperature values. In the lower recirculation zone, the results obtained with the SST k-ω turbulence model show that the vortex breakdown bubble is narrower and oval in shape, while the results of the RNG k-ε turbulence model show a wider and rectangular structure. In the comparison for the temperature values obtained from the measurement points in this region, the SST k-ω turbulence model is more consistent with the experimental data.

Axial velocity contours obtained from the numerical solutions of the SST k-ω and RNG k-e turbulence models are presented in Fig. 7. It is noticeable from Fig. 7 that the flame shapes are similar to the velocity profiles. Similar to the temperature contours, the results for the SST k-ω turbulence model show a more pronounced neck of the flame, while the results for the RNG k-ε turbulence model show a higher and thicker neck. In addition, the velocity values show a smaller decrease along the flow domain in the analysis with the RNG k-ε turbulence model. This leads to a longer flame length for the solution of the RNG k-ε turbulence model, which is noticeable in Fig. 6.

The variation of the axial velocities obtained from numerical analysis at different distances upon the bluff body surface is analyzed with the experimental results in Fig. 8. When the diagrams in Fig. 8 are examined, it is seen that the RNG k-ε model gives similar results with the SST k-ω turbulence model in terms of axial velocities and the analysis of both turbulence models for axial velocity values are compatible with the experimental results. At axial distances x/D=0.8 and x/D=1.2, in the range r/R_b=0.6 and r/R_b=1.2 (R_b =$D/2$), it is seen that the RNG k-ε turbulence model fails to capture the experimental results and the velocity profile shifts slightly off-center.

When the temperature data in Fig. 9 are analyzed, the results in the contour plots are better understood. The RNG k-ε turbulence model predicts higher temperatures than the SST k-ω turbulence model, especially in the upper recirculation region, and predicts the temperature values in a narrower region in the radial direction. This is also seen in the RNG k-ε temperature contour in Fig. 6. Except for the axial distances x/D=0.2 and x/D=0.4, the RNG k-ε model calculates the flame wider than the experimental results and the SST k-ω model at all other measurement points, but at the measurement point x/D=3.0, it both calculates the flame wider and overestimates the flame temperatures. The temperature data in Fig. 9 are also consistent with the temperature contours. The fact that the two turbulence models give different results for temperature values when the solution algorithm used in both models is the same suggests that the turbulence-chemistry interaction between the turbulence model and the steady diffusion flamelet model does not behave similarly for each turbulence model. As a result of the numerical analysis, it is concluded that the SST k-ω turbulence model models the SM1 flame better than the RNG k-ε turbulence model. In the second part of the evaluation of the results, the results obtained with the SST k-ω.

4.2. Results for SST k-ω and LES Turbulence Model

The results of the SST k-ω model for the SM1 flame, which are consistent with the experimental data, are compared with the results of the analysis of the SM1 flame with the LES turbulence model code (PUFFIN) developed by Malalasekara et al [24]. The experimental results are also included in all diagrams used for comparison in order to simultaneously see how well the turbulence models match the experimental data. Figure 10 shows the axial velocity data.

As can be seen from Fig. 10, the numerical results show a similar trend with the experimental results. The negative velocity values at the axial points x/D=0.136 and x/D=0.4 within the upward recirculation zone indicate the reverse flow due to the presence of the bluff body surface and are captured by both the SST k-ω and the LES turbulence model. The value of the axial velocity in the x/D=0.4 plane is underestimated by the SST k-ω turbulence model. This is because the SST k-ω turbulence model, which is a RANS turbulence model, has a limited capacity compared to the LES turbulence model in shear stress dominated flows. The recirculation region in the downstream flow due to the presence of vortex breakdown leads to negative axial velocities around the centerline. In this region, both turbulence models can calculate the swirl flow with acceptable accuracy. The data of the SST k-ω and LES turbulence models have a similar orientation with slight differences in the radial direction.

Figure 11 shows the results of the tangential velocity. For the measurement points x/D=0.136 and x/D=0.4, both turbulence models failed to capture the experimental data in the range r/R_b=0.2-1.0. This is due to the shear layer instability in the upper recirculation region and the fuel jet dispersion not being modeled well enough by the turbulence models [24]. In the lower recirculation region starting from the measurement point x/D=1.2, the SST k-ω model shows much more consistent behavior with the experimental results than the previous measurement points. The results of the variation of the tangential velocity of the LES turbulence model are better than the SST k-ω turbulence model for all measurement points.

Figure 12 shows the variations of the mean mixture fraction, f, at different axial distances from the fuel inlet cross section. As can be seen in the diagrams, the results of the SST k-ω and LES turbulence models are similar and show a behavior consistent with the experimental results. In the results of both models, the mean mixture fraction values are lower than the experimental data in the radial range r/R_b=0.4-0.8, especially in the regions close to the bluff body surface such as x/D=0.2 and x/D=0.4. This is due to the fact that turbulence models cannot calculate the propagation of the fuel jet due to tangential velocity well enough and model the flow of the fuel jet as straight. The mean mixture fraction values calculated lower than the experimental data were close to the stoichiometric mixing values. The stoichiometric mixing ratio is indicative of the flame front and is the ratio at which the calculated flame temperatures reach the highest value. For this reason, in areas where the mean mixture fraction is low, the flame temperature is higher than the experimental results. This is also seen in the temperature distribution diagram in Fig. 13. It can be observed from the diagrams that the SST k-ω model obtains lower values than the experimental results, especially near the centerline, at the x/D=0.8 and x/D=1.1 axial measurement points corresponding to the neck region of the SM1 flame. In these regions, the LES turbulence model shows more consistent behavior with the experimental data.

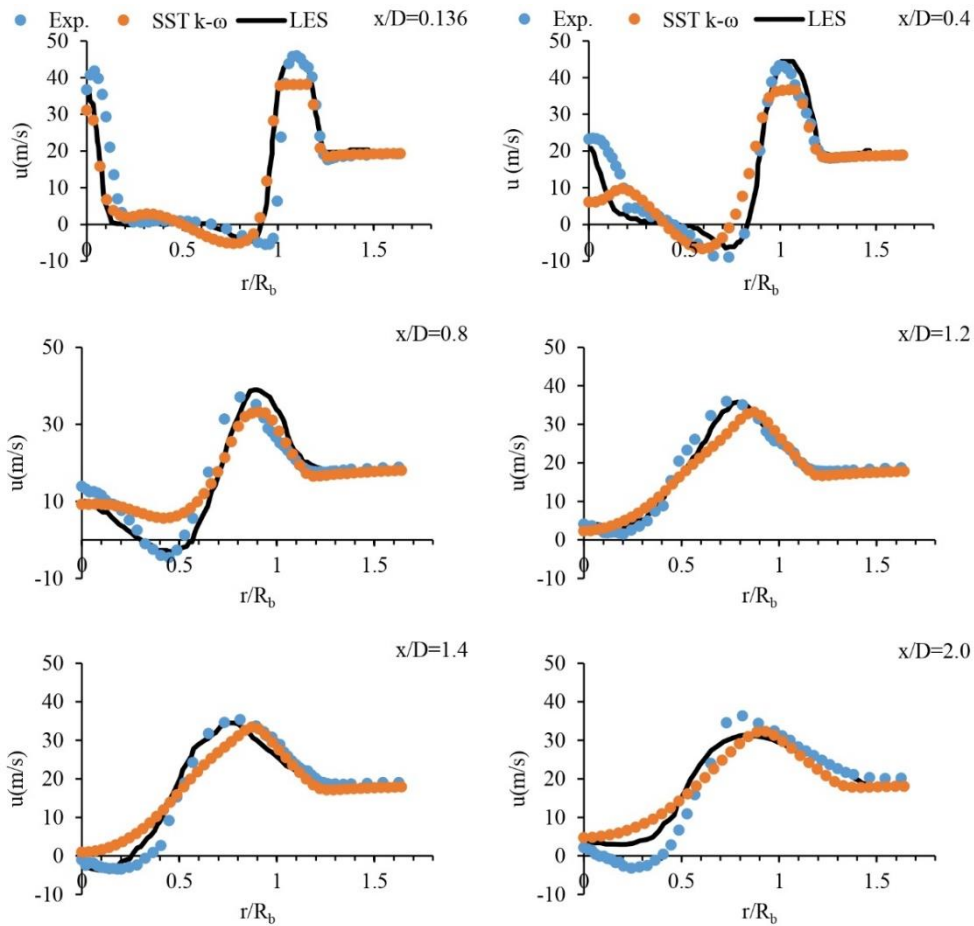In the lower recirculation zone, the SST k-ω turbulence model predicted the experimental data, especially the

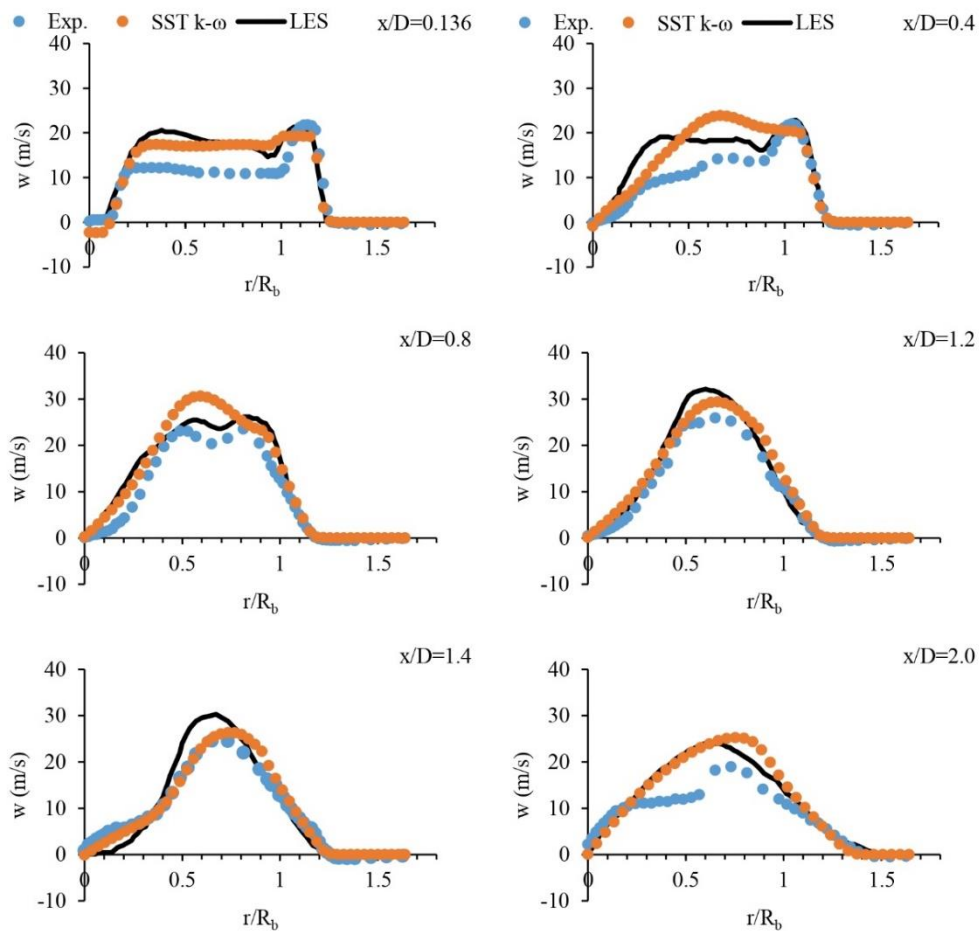*Figure 10. Comparison of axial velocity values of SST k-ω and LES turbulence models with experimental data.*

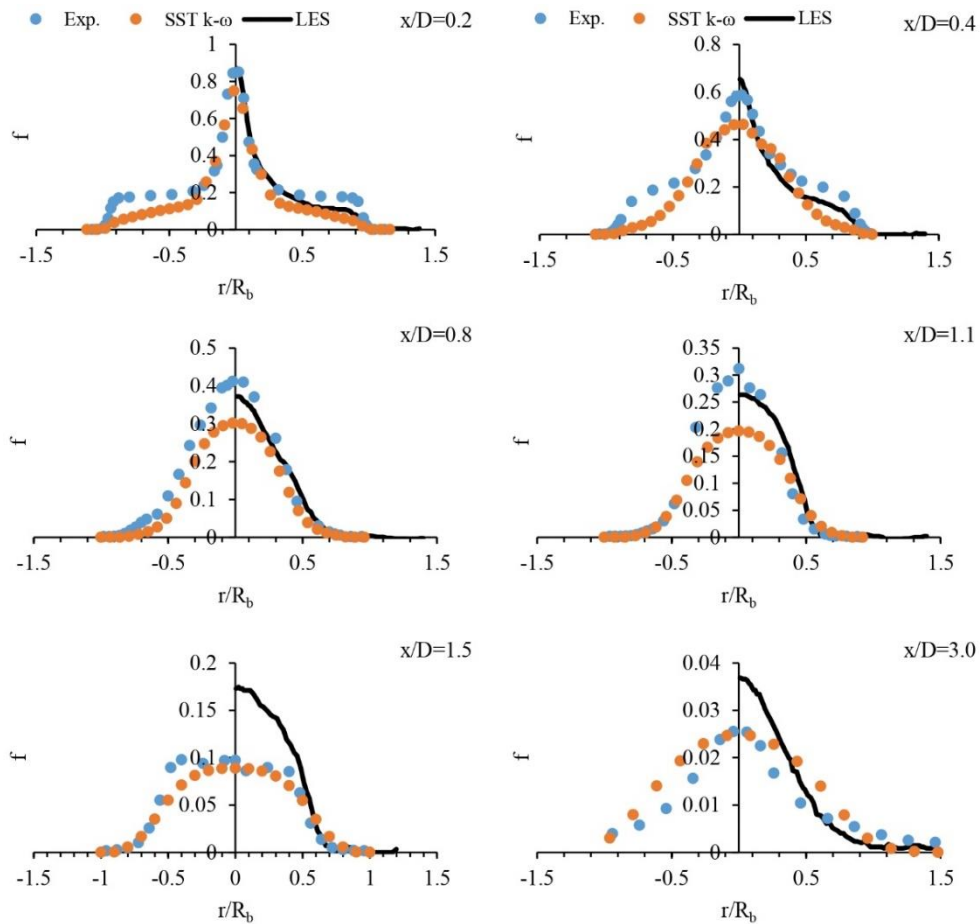*Figure 11. Comparison of tangential velocity values of SST k-ω and LES turbulence models with experimental data.*

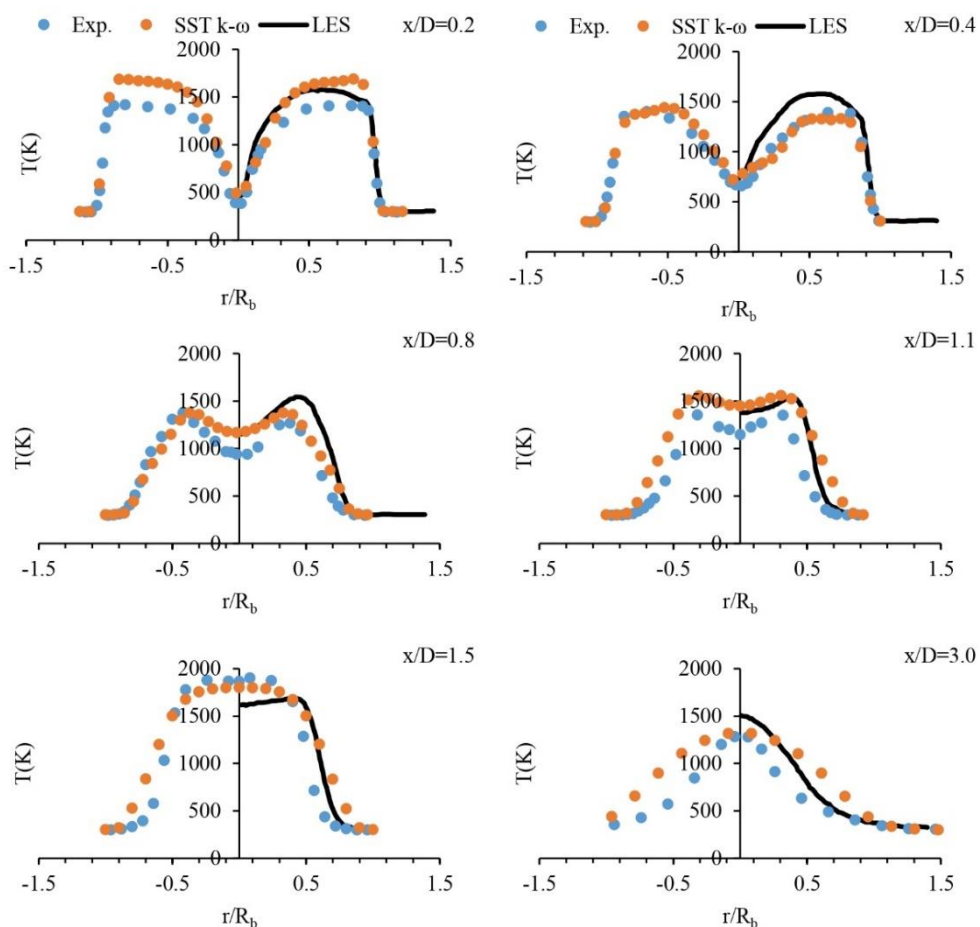*Figure 12. Comparison of mean mixture fraction values of SST k-ω and LES turbulence models with experimental data.*

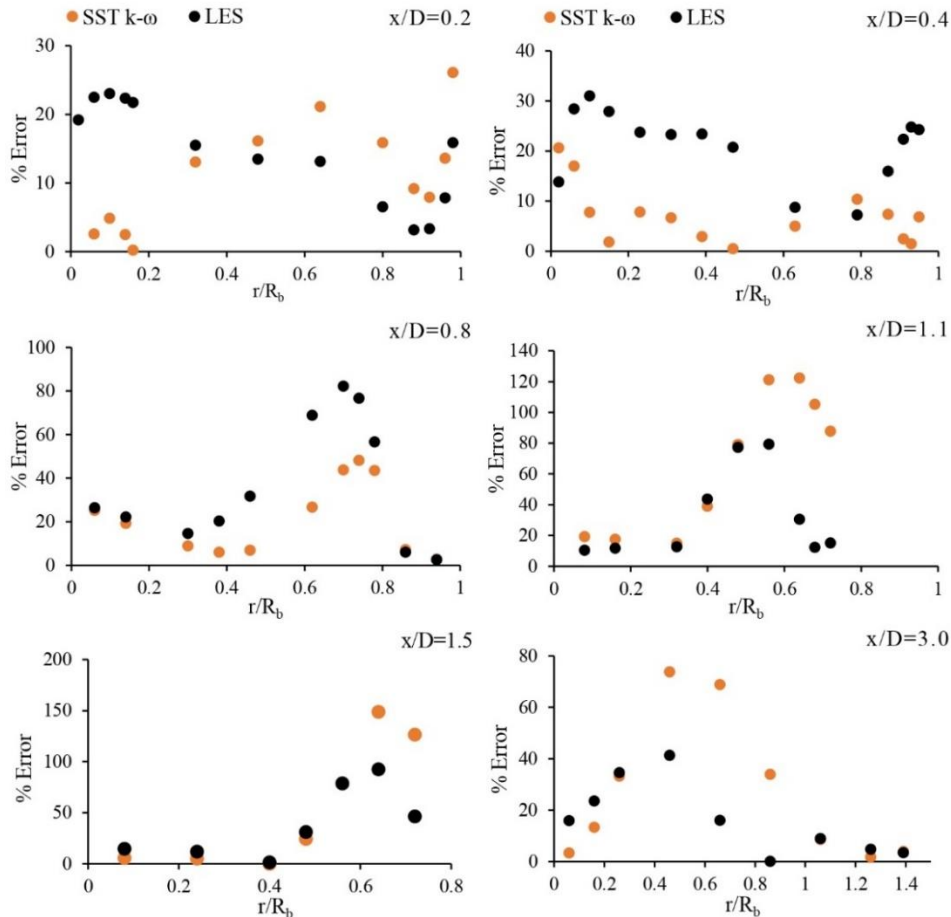*Figure 13. Comparison of temperature values of SST k-ω and LES turbulence models with experimental data.*

Figure 14. Comparison of %Error values of temperatures of SST k-w LES.

maximum temperature values, much better than the LES turbulence model. The temperature values calculated by the LES turbulence model in the lower recirculation zone are also in agreement with the predictions of the mean mixture fraction value shown in Fig. 12 for this zone, and there are deviations from the experimental measurements in the maximum temperature values. Malalasekara et al. attribute this to the fact that the measured region coincides with the stagnation point of the central recirculation zone [24].

Figure 13 shows diagrams comparing the experimental and numerical results of temperature values for different axial points. Considering the complex nature of the flow field and the combustion reaction, the results obtained are quite satisfactory. As mentioned above, in the *x/D* planes close to the fuel inlet plane, the temperature values of the SST k-ω and LES turbulence model analyses are predicted higher than the measured values. In other *x/D* planes, the numerical model and experimental results are consistent. Especially in the lower recirculation region, the SST k-ω model predicted the flame temperatures more accurately in the *x/D*=1.5 and *x/D*=3.0 planes. However, since it overestimates the size of the vortices in the vortex breakdown bubble, the temperature distribution is wider in the radial direction than the experimental results. The results of the analysis with the LES turbulence model agree with the results of the SST k-ω model in the upper recirculation region, while in the lower flow region near the centerline, the temperature values are underestimated for *x/D*=1.5 and overestimated for *x/D*=3.0. The reason for this difference can be seen from the mean mixture fraction diagrams for the LES turbulence model in Fig. 12. Malalasekara et al. attributed the differences in the temperature value in the lower recirculation zone to the high shear stress flows in this region

and the inadequacy of the combustion model used. However, it was emphasized that the numerical results are in the same direction as the experimental temperature data [24]. The temperature data from the LES turbulence model, which effectively models the velocity field throughout the entire flow region in accordance with experimental data, deviates from the temperature data predicted by the SST k-ω turbulence model. This discrepancy may stem from the combustion model code used in the analyses by Malalasekara et al. [24], which could exhibit less efficiency compared to the combustion model.

Figure 14 shows the variations of the temperature % error values of the numerical results obtained with the SST k-ω and LES turbulence models in the radial direction for different measurement points. The situation observed in Fig. 12 and Fig. 13 is also seen in Fig. 14. Both models calculate the temperatures with sufficient accuracy, especially in the upper recirculation zone. When examining the radial distributions of errors in the lower recirculation region, it is observed that the numerical results predict a wider flame than actual. Particularly, the high temperatures calculated within the range of r/R_b=0.5 to r/R_b=1.0 for measurement points between *x/D*=0.8 and *x/D*=3.0 lead to high error percentages. This may be due to the inability of turbulence models to capture the chaotic flow in the lower recirculation region or to errors in the calculation of reactions due to turbulence-chemistry interaction. The results, which are sufficient for validation purposes, can be analyzed with different turbulence-chemistry interaction models for further investigation.

Between Fig. 15 and Fig. 17, the mass ratios of H_2O, CO_2 and CO components are compared with the experimental results. As can be seen in the diagrams for the H_2O

component in Fig. 15, the theoretical results have similar trends with the experimental data. The results of the SST k-ω turbulence model generally overestimated the mass fraction value of H_2O, especially in the centerline region. At the measurement point x/D=1.5, very close results were obtained. The LES turbulence model, similar to the SST k-ω turbulence model, gave results close to the experimental data and predicted high and low results at some of the H_2O measurement points. The variations in the mass fraction of generally have similar maximum values and radial variations to the temperature distribution.

As the mass fraction variations of CO_2 in Fig. 16 are analyzed, the agreement of the SST k-ω model with the experimental data is very good in the upper recirculation region and in the neck region of the flame, except for the x/D=0.4 plane. In the lower recirculation region the results are slightly higher than the experimental data, but the overall prediction of the numerical results is good. It was reported by Malalasekara et al. that the results of the analysis with the LES turbulence model are slightly underestimated in the first two x/D planes and significantly underestimated in the x/D=1.5 plane. They also emphasized that this behavior is consistent with the temperature and the mean mixture fraction values [24].

Figure 17 compares the mass fractions of CO. The profile of CO mass fraction changes shows a similar trend and similar maximum values as the temperature profile in the x/D planes close to the bluff body surface. The CO profile obtained with the SST k-ω turbulence model shows lower values than the experimental results in the x/D planes close to the bluff body surface. The values associated with CO are close to the mixture's lean flammability limit. This situation

leads to the predicted values of CO being lower than the experimental data within the upper recirculation region. In the lower recirculation part of the flow, this situation improves and the numerical results show a similar behavior to the experimental results like temperature curves. The results obtained with the LES turbulence model show a similar behavior. However, especially in the lower recirculation zone where vortex breakdown occurs, a high mass fraction of CO has been estimated for the measurement point at x/D=3.0.

5. Conclusion

In this study, the experimental results of the non-premixed swirl flame SM1 from the Sydney swirl flame family, which is characterized by globally open and stable boundary conditions, were numerically modeled.

The proposed models for the swirl flow problem are evaluated by reviewing the studies in the literature. As a result of this evaluation, it was decided to use the two-equation SST k-ω and RNG k-ε models. The numerical analyses are compared with the experimental results and it is observed that the prediction values of the numerical analysis using the SST k-ω turbulence model are more compatible with the experimental data.

In the second stage of the study, the results obtained for the SM1 flame with the LES turbulence model, which has a high accuracy in turbulence modeling, were compared with the results obtained with the SST k-ω turbulence model. In the comparison for different variables, it is observed that the LES turbulence model predicts the experimental results better than the SST k-ω turbulence model, especially for the velocity variables, as expected.

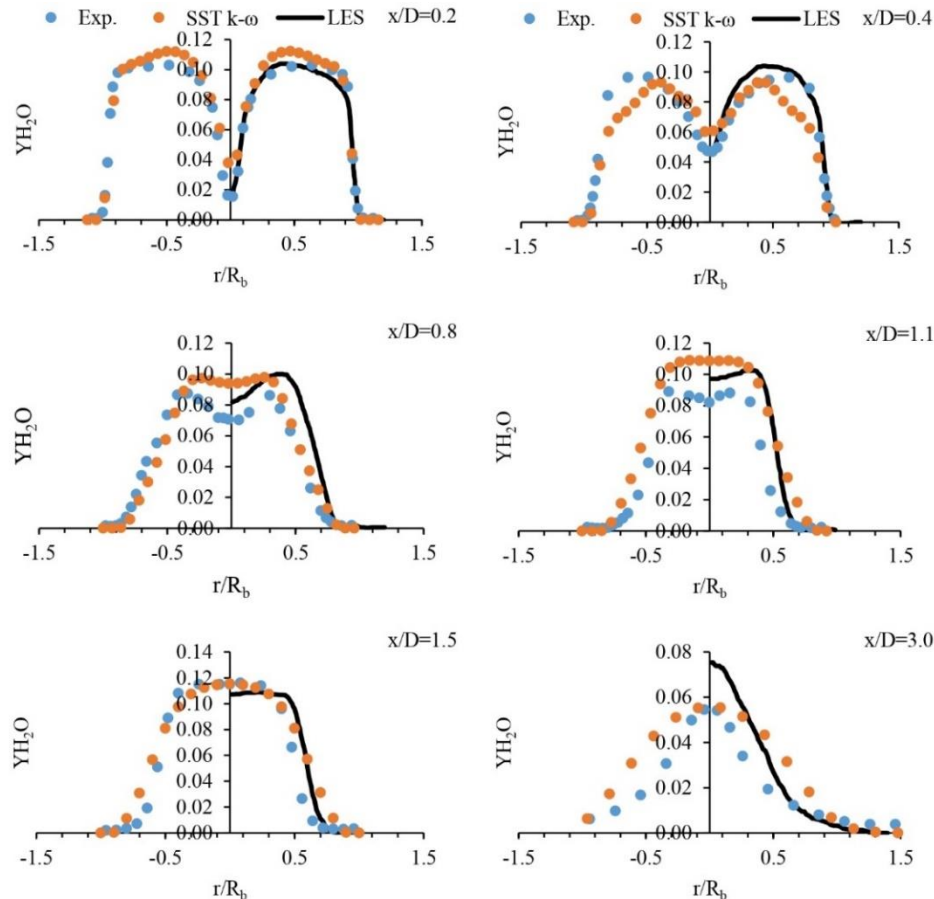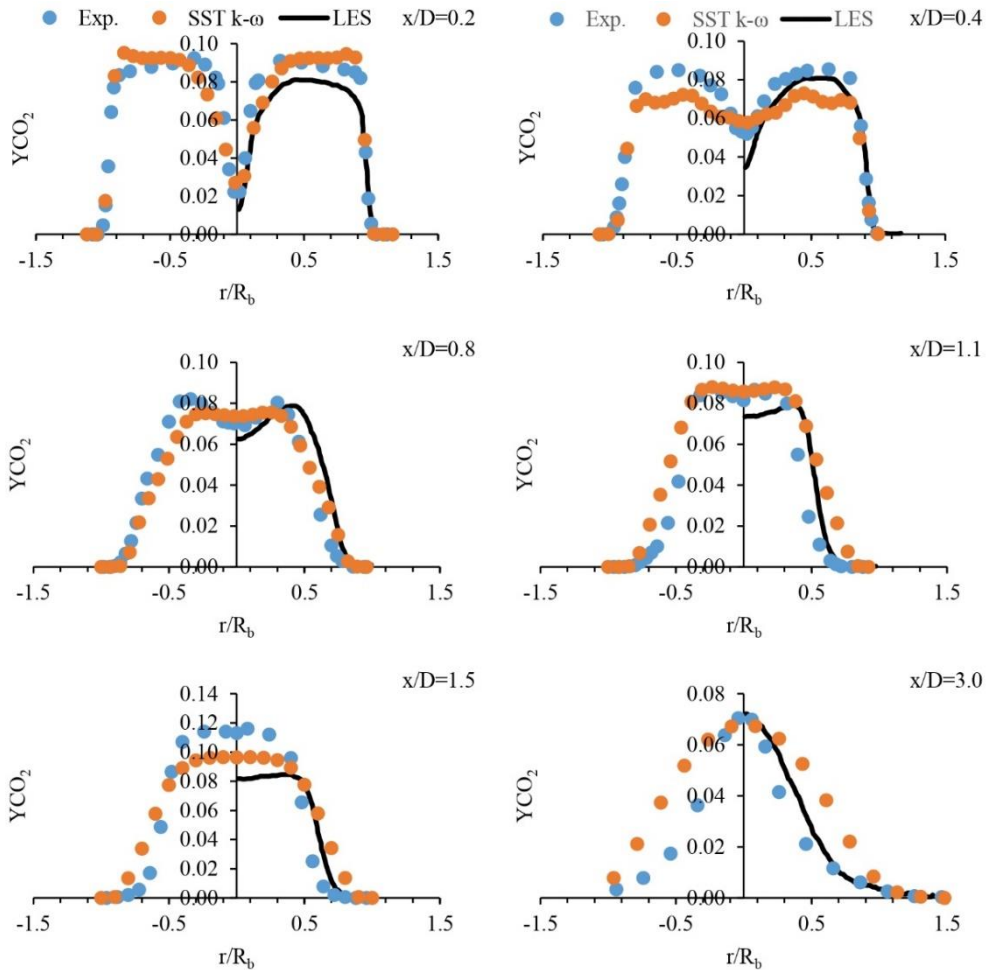Figure 15. Comparison of H_2O mass fraction values of SST k-ω and LES turbulence models with experimental data.

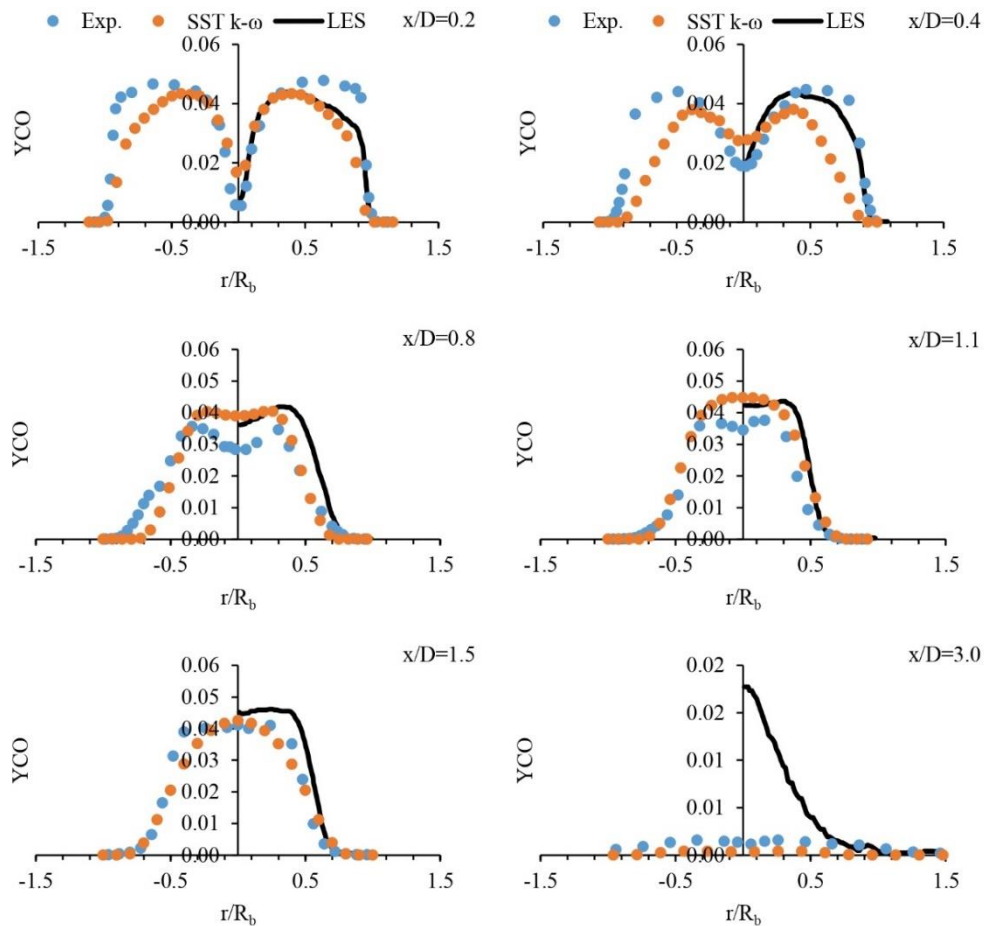*Figure 16. Comparison of CO₂ mass fraction values of SST k-ω and LES turbulence models with experimental data.*

Figure 17. Comparison of CO mass fraction values of SST k-ω and LES turbulence models with experimental data.

When the combustion reaction and the values of the mean mixture fraction, temperature and mass fraction of the components are compared, it is observed that both turbulence models are consistent with the experimental results and even SST k-ω turbulence model gives better results in some x/D planes.

The percentage error values of the calculated temperature values relative to the experimental results have similarly demonstrated that the two turbulence models yield similar solutions in terms of combustion and combustion-related variables. The LES algorithm solves large eddies and models small scales, but combustion occurs structurally at small scales. Therefore, in order to obtain accurate results in modeling combustion reactions, it is possible to make satisfactory predictions without the use of highly advanced numerical techniques such as LES.

By using a geometry that accurately represents the burner, a mesh structure with an ideal distribution, realistic boundary conditions and an accurate solution algorithm, the experimental data of swirl flow flames can be well predicted by the RANS turbulence model. This is also demonstrated in the comparison made in this study. Therefore, RANS turbulence models can be used to model such flames instead of high core-hour cost solution algorithms such as the LES turbulence model, which has a much lower core-hour cost and saves energy and time.

To improve and extend the scope of the study conducted, alternative turbulence-chemistry interaction models will be employed, and their impact on the numerical data will be investigated. Also, exploring the potential of using other alternative fuels or fuel blends in bluff-body stabilized swirl flames to further optimize combustion efficiency and reduce emissions can be done in future.

Nomenclature

α_k	Inverse effective Prandtl number for k
α_ε	Inverse effective Prandtl number for ε
$\alpha_0, \alpha_1, \alpha_\infty, \alpha_\infty^*$	Equation constants
$\beta, \beta_{i,1}, \beta_{i,2}, \beta_\infty^*$	Equation constants
$C_{1\varepsilon}, C_{2\varepsilon}, C_{3\varepsilon}$	Equation constants
C_μ, C_v	Equation constants
D	Diameter of bluff-body (m)
ε	Turbulent dissipation rate (m²/s³)
F_1, F_2	Blending functions
G_b	Turbulence kinetic energy with respect to buoyancy(W/m³)
G_k	Turbulence kinetic energy with respect to mean velocity gradients (W/m³)
k	Kinetic energy of turbulence (m²/s²)
μ	Dynamic viscosity (kg/m·s)
μ_{eff}	Effective viscosity (kg/m·s)
μ_t	Turb. fluctuation viscosity (kg/m·s)
μ_{t0}	Equation constant
ω	Specific dissipation rate (s⁻¹)
ρ	Density (kg/m³)
R_b	Radius of bluff-body (m)
R_β, R_k, R_ω	Equation constants
S_{ij}	Stress tensor
$\sigma_{k,1}, \sigma_{k,2}, \sigma_{\omega,1}, \sigma_{\omega,2}$	Equation constants
u_i, u_j	Velocity component in corresponding direction (m/s)
U_s	Axial air velocity (m/s)
U_j	Fuel jet velocity (m/s)
U_e	Secondary air axial velocity (m/s)
W_s	Tangential air velocity (m/s)
x	Axial distance from fuel inlet (m)
y	Distance from nearest wall (m)
Y_M	Contribution of the fluctuating dilatation in compressible turbulence to the overall dissipation rate (W/m³)

References:

[1] A. S. M. Al-Obaidi and T. Nguyenhuynh, "Renewable vs. conventional energy: Which wins the race to sustainable development?," *IOP Conf. Ser. Mater. Sci. Eng.*, vol. 434, no. 1, 2018.

[2] S. R. Brinkley Jr., B. Lewis, "The Thermodynamics of Combustion Gase General Considerations" April 1952. https://www.semanticscholar.org/paper/The-Thermodynamics-of-Combustion-Gases%3A-General-Brinkley-Lewis/3f1cbf613422d0b230ab716630acec0b3d34ecd4 (Accessed 22 December 2023).

[3] S. Sugawara and I. Michiyoshi, "The Thermo-Aerodynamical Analysis of Combustion Gas Flow (1st Report)," *Bulletin of JSME*, 1959. https://www.jstage.jst.go.jp/article/jsme1958/2/5/2_5_138/_pdf/-char/en (Accessed 22 December 2023).

[4] J. H. S. Lee and C. Guirao, "Fast Reactions in Energetic Systems," in *Fast Reactions in Energetic Systems*, C. Capellos and R. F. Walker, Eds. NATO Advanced Study Institutes, 1981, pp. 245–313.

[5] B. M. R. De Meester, B. Naud, U. Maas, "Hybrid RANS/PDF Calculations of a Swirling Bluff Body Flame ('SM1'): Influence of the Mixing Model," in *MCS 7*, 2011, vol. 13, no. 1, pp. 43–50.

[6] B. Kashir, S. Tabejamaat, and N. Jalalatian, "A numerical study on combustion characteristics of blended methane-hydrogen bluff-body stabilized swirl diffusion flames," *Int. J. Hydrogen Energy*, vol. 40, no. 18, pp. 6243–6258, 2015.

[7] "TNF Workshop." https://tnfworkshop.org/ (Accessed 22 December 2023).

[8] P. A. M. Kalt, Y. M. Al-Abdeli, A. R. Masri, and R. S. Barlow, "Swirling turbulent non-premixed flames of methane: Flow field and compositional structure," *Proc. Combust. Inst.*, vol. 29, no. 2, pp. 1913–1919, 2002.

[9] A. R. Masri, P. A. M. Kalt, and R. S. Barlow, "The compositional structure of swirl-stabilised turbulent nonpremixed flames," *Combust. Flame*, vol. 137, no. 1–2, pp. 1–37, 2004.

[10] M. Safavi and E. Amani, "A comparative study of turbulence models for non-premixed swirl-stabilized flames," *J. Turbul.*, vol. 19, no. 11, pp. 1017–1050, 2019.

[11] A. Radwan, K. A. Ibrahim, A. Hanafy, and K. M. Saqr, "On rans modeling of unconfined swirl flow," *CFD Lett.*, vol. 6, no. 4, pp. 159–174, 2014.

[12] Y. Yang and S. K. Kær, "Large-eddy simulations of the non-reactive flow in the Sydney swirl burner," *Int. J. Heat Fluid Flow*, vol. 36, pp. 47–57, 2012.

[13] T. M. R. Rahman, W. Asrar, and S. A. Khan, "An investigation of RANS simulations for swirl-stabilized isothermal turbulent flow in a gas turbine burner," *CFD*

Lett., vol. 11, no. 9, pp. 14–31, 2019.

[14] X. Yang, Z. He, S. Dong, and H. Tan, "Combustion Characteristics of Bluff-Body Turbulent Swirling Flames with Coaxial Air Microjet," *Energy and Fuels*, vol. 31, no. 12, pp. 14306–14319, 2017.

[15] J. P. West, C. P. T. Groth, and J. T. C. Hu, "Assessment of hybrid RANS/LES methods for gas-turbine combustor-relevant turbulent flows," *22nd AIAA Comput. Fluid Dyn. Conf.*, no. June, pp. 1–20, 2015.

[16] J. Fu, Y. Tang, J. Li, Y. Ma, W. Chen, and H. Li, "Four kinds of the two-equation turbulence model's research on flow field simulation performance of DPF's porous media and swirl-type regeneration burner," *Appl. Therm. Eng.*, vol. 93, pp. 397–404, 2016.

[17] R. Weber, B. M. Visser, and F. Boysan, "Assessment of turbulence modeling for engineering prediction of swirling vortices in the near burner zone," *Int. J. Heat Fluid Flow*, vol. 11, no. 3, pp. 225–235, 1990.

[18] A. Gupta and R. Kumar, "Three-dimensional turbulent swirling flow in a cylinder: Experiments and computations," *Int. J. Heat Fluid Flow*, vol. 28, no. 2, pp. 249–261, 2007.

[19] F. C. Christo and B. B. Dally, "Modeling turbulent reacting jets issuing into a hot and diluted coflow," *Combust. Flame*, vol. 142, no. 1–2, pp. 117–129, 2005.

[20] M. Lu, Z. Fu, X. Yuan, J. Wu, and S. W. Sabir, "Numerical Simulation of Turbulent Non-premixed Combustion Processes for Methane and Dimethyl Ether Binary Fuels," *ACS Omega*, vol. 6, no. 10, pp. 6629–6642, 2021.

[21] P. Wang, J. Fröhlich, and U. Maas, "Impact of location and flow rate oscillation of the pilot jet on the flow structures in swirling premixed flames," *J. Turbul.*, vol. 11, pp. 1–20, 2010.

[22] B. Wegner, A. Maltsev, C. Schneider, A. Sadiki, A. Dreizler, and J. Janicka, "Assessment of unsteady RANS in predicting swirl flow instability based on LES and experiments," *Int. J. Heat Fluid Flow*, vol. 25, no. 3, pp. 528–536, 2004.

[23] L. Chen and A. F. Ghoniem, "Simulation of oxy-coal combustion in a 100 kW th test facility using RANS and LES: A validation study," *Energy and Fuels*, vol. 26, no. 8, pp. 4783–4798, 2012.

[24] W. Malalasekera, K. K. J. Ranga-Dinesh, S. S. Ibrahim, and A. R. Masri, "LES of recirculation and vortex breakdown in swirling flames," *Combust. Sci. Technol.*, vol. 180, no. 5, pp. 809–832, 2008.

[25] H. El-Asrag and S. Menon, "Large eddy simulation of bluff-body stabilized swirling non-premixed flames," *Proc. Combust. Inst.*, vol. 31 II, no. 2, pp. 1747–1754, 2007.

[26] L. Y. Hu, L. X. Zhou, and Y. H. Luo, "Large-eddy simulation of the Sydney swirling NonPremixed flame and validation of several subgrid-scale models," *Numer. Heat Transf. Part B Fundam.*, vol. 53, no. 1, pp. 39–58, 2008.

[27] J. Xu, D. Huang, R. Chen, and H. Meng, "An Improved NO Prediction Model for Large Eddy Simulation of Turbulent Combustion," *Flow, Turbul. Combust.*, vol. 106, no. 3, pp. 881–899, 2021.

[28] K. Luo, J. Yang, Y. Bai, and J. Fan, "Large eddy simulation of turbulent combustion by a dynamic second-order moment closure model," *Fuel*, vol. 187, pp. 457–467, 2017.

[29] Y. Zhiyin, "Large-eddy simulation: Past, present and the future," *Chinese J. Aeronaut.*, vol. 28, no. 1, pp. 11–24, 2015.

[30] Y. M. Al-Abdeli and A. R. Masri, "Recirculation and flowfield regimes of unconfined non-reacting swirling flows," *Exp. Therm. Fluid Sci.*, vol. 27, no. 5, pp. 655–665, 2003.

[31] Y. M. Al-Abdeli and A. R. Masri, "Stability characteristics and flowfields of turbulent non-premixed swirling flames," *Combust. Theory Model.*, vol. 7, no. 4, pp. 731–766, 2003.

[32] Ansys Inc., "ANSYS FLUENT Theory Guide," *ANSYS Inc., USA*, vol. Release 20, no. R1,http://www.afs.enea.it/project/neptunius/ docs/fluent/html/th/main_pre.htm (Accessed 22 December 2023).

[33] F. G. Schmitt, "About Boussinesq's turbulent viscosity hypothesis: historical remarks and a direct evaluation of its validity," *Comptes Rendus - Mec.*, vol. 335, no. 9–10, pp. 617–627, 2007.

[34] Y. Liu, X. Guan, and C. Xu, "An improved scale-adaptive simulation model for massively separated flows," *Int. J. Aerosp. Eng.*, vol. 2018, 2018.

Research Article

Thermohydraulic Analysis of Coolant Entry Patterns in a High-Temperature Pebble Bed Reactor: Insights and Characterization

[1*]A. Gámez Rodríguez [ID], [2]D. Milián Pérez [ID], [3]C. A. Brayner de Oliveira Lira [ID]

[1,2] Departamento de Energia Nuclear, Universidade Federal de Pernambuco (UFPE), Cidade Universitária, Avenida Professor Luiz Freire 1000, CEP: 50670-901, Recife, PE, Brasil.
[1,2,3] Centro Regional de Ciências Nucleares (CRCN-NE/CNEN), Cidade Universitária, Avenida Professor Luiz Freire 200, CEP: 50740-545, Recife, PE, Brasil.
E-mail: [1*]abel.rodriguez@ufpe.br

Abstract

Conducting three-dimensional thermohydraulic analysis of an entire nuclear reactor poses significant challenges due to the considerable geometric volume and complex internal structures involved. The top reflector is one of the internal structures found in high-temperature pebble bed Small Modular Reactors (SMR). This structure serves several critical functions, including neutron reflection, control and distribution of helium inlet into the core, neutron and thermal shielding, among others. In this kind of system, the detailed representation of the top reflector includes the representation of more than 460 channels of 2.5cm of diameter. Considering that the reactor has almost a ten of meters then dimension scales of various orders must be represented, which is a challenge. In this sense, a three-dimensional Computational Fluid Dynamics (CFD) thermohydraulic analysis of the entry pattern to the core of a High Temperature SMR using ANSYS CFX has been done. This study presents a comparison between five coolant entry patterns into the core. Initially, two prototype models of 460x⌀2.5cm, one with vertical channels and another with inclined channels, are modeled. Additionally, two prototype models of 20x⌀12cm of equivalent area, with vertical and inclined channels are also included. Finally, a simplified porous media model with the same equivalent area is considered. The thermohydraulic behavior of the coolant before and after passing through the top reflector was then analyzed for these five patterns. An analysis of fuel elements temperature in the core was conducted. It is important to highlight that this study is qualitative and has the goal of identifying and characterizing the impact that the coolant entry pattern into the reactor core has on the main thermohydraulic parameters in this region. The study exposes a strong correlation between the porous media model and all prototype models in terms of the maximum fuel temperature, average fuel temperature, and helium velocity. In this study, the potential applicability of the porous media models for an integral full-scale reactor simulation in the future was demonstrated. As a benefit, the porous media model reduces the mesh quantity compared to a prototypic model.

Keywords: CFD; HTR; porous media; top reflector detailed representation; thermohydraulic analysis.

1. Introduction

In the past decades, energy consumption has been increasing steadily around the world, and this trend is expected to continue in the future. Over the last decade, electricity demand rose by 25%, and it is estimated that between 30% and 43% annual growth in demand will occur up to 2030. To support this growth, it is estimated that the global energy supply should grow between 1.0% and 1.3% per year [1], [2]. The nuclear industry, with more than six decades of developing and improving technologies, has proven to be an outstanding potential solution to meet the growing energy demand safely and economically. The capabilities of the nuclear industry are being reinforced by the innovations planned for the generation IV (Gen-IV) reactor technologies, which offer significant improvements compared to current nuclear technologies in terms of closing the fuel cycle, waste minimization and enhanced resource use, inherent safety, economics, and proliferation resistance

and security [1]. In recent years, there has also been a growing interest in merging the Gen-IV and the small modular reactor technologies. At the moment, all the Gen-IV technologies are in the research and development stages. All the research and development activities related with those advanced systems are being followed closely by the Generation IV International Forum (GIF).

In the two decades that have passed, since the establishment of the GIF in 2000, various Gen-IV reactor technologies have been evaluated. The Very-High-Temperature Reactor (VHTR) has been identified as one of the most promising reactor concepts for the next generation of nuclear reactors by the International Atomic Energy Agency (IAEA) [3]–[6]. It utilizes ceramic fuel, graphite as a moderator, and helium gas as a coolant. The VHTR builds on the experience gained from a group of experimental and commercial High-Temperature Gas-Cooled Reactors (HTGR) that were built and operated during the latter half of

the 20th century, along with two ongoing projects. The former includes Dragon in the United Kingdom, Peach Bottom and Fort St. Vrain in the United States, and AVR (German: Arbeitsgemeinschaft Versuchsreaktor) and the Thorium High-Temperature Reactor (THTR) in Germany. The latter are the High-Temperature Test Reactor (HTTR) in Japan and the HTR-10 in China, which became operational in early 2000, respectively. These experiences and advancements have led to the development of the VHTR, which holds great promise for the future of nuclear energy [7].

Making predictions about the thermohydraulic behavior of High Temperature Reactors is a crucial contribution to advancing VHTR technology. Despite the advances made in the development and study of VHTRs, there are still some key challenges that need to be addressed before the commercial deployment of this technology can be realized. These challenges include improving the nuclear safety characteristics, addressing the cost-effectiveness of the technology, developing appropriate fuel and waste management strategies, and addressing issues related to the supply chain and infrastructure. Ongoing research, development, and demonstration of important systems design and analysis are needed to overcome these challenges and ensure the successful implementation of VHTR technology [5], [6], [8].

The use of digital engineering, integrated numerical tools and high-level software for the simulation of these systems constitute an effective initial alternative to scale model proof. Reducing, time cost, the number of new experimental facilities and tests required during the experimental testing phase [9], [10]. Indeed, one of the current challenges in the engineering community is to obtain fast and realistic results of different configurations of diverse prototypes using experimentation in controlled conditions. This challenge almost always is extremely difficult and expensive. Mainly including expensive measurement techniques, and advanced sensors. Sometimes, involving measurement of inaccessible volume, or small for intrusive/non-intrusive measurement. And more difficult considering hostile environments such as the high temperature, chemical contaminants, radioactive, etc. In this sense, the Computational Fluid Dynamics (CFD) appears to be a logical way to complement experimentation [11]. On the other hand, to validate CFD models accurately simulating the thermohydraulic processes within the reactors, experimental data is essential.

In this sense, the experimental reactor HTR-10 was selected as a reference reactor of high temperature pebble bed gas-cooled reactor by the IAEA to study the performance of some technology components under different conditions [6]. The HTR-10 stands as one of the SMRs utilizing this technology and is currently operational [5]. Making predictions about the thermohydraulic behavior of High Temperature Reactors (HTR) is a crucial contribution to advancing VHTR technology. The computational prediction of the thermohydraulic behavior of this reactor involves different physic-neutronic approach and detailed structural information. Multiscale approach and multiphysics coupled techniques are others of the challenges in the simulation of real situations [12]. Thus, performing a comprehensive three-dimensional thermohydraulic analysis of an entire nuclear reactor poses a significant challenge due to the vast geometric volume and intricate structures involved [13].

However, the correct prediction of the coolant behavior inside the internal structures and the impact of different configurations of these internal structures in the reactor core continue to be challenges to the international research community. Optimized design and the safety performance of the internal structures continue to be the stay of the art. The top reflector is one of the internal structures found in high-temperature pebble bed SMRs. This structure serves several critical functions, including neutron reflection, control and distribution of helium inlet into the core, neutron and thermal shielding, among others.

To the best of the authors' knowledge, no detailed descriptions of the internals of the top reflector are available in the literature. According to [14], [15], the bricks below the cold plenum have 460 machined holes with 2.5cm of diameter through which cold helium flows down from the cold gas chamber into the reactor core. Nothing was indicated about the distribution or the inclination of these holes in the reflector bricks. Knowing only the number of channels and their diameter, it is impossible to adequately represent that section of the reactor geometry. That is why, over the years several articles have been made around the HTR-10, and in all of them, it has been modeled using different approximations of the internal construction details of the top reflector.

In [16] was studied one postulate design accident applying 3D modelling. In that study, the investigation centered on the hydrogen generation resulting from the reaction between graphite and water subsequent to a steam generator tube rupture. The study did not represent the characteristic coolant flow pattern within the core region but assumed a homogeneous vertical flow as the coolant inlet condition. Additionally, in [17] was analyzed the air ingress occurred after the Loss-of-Coolant Accident (LOCA) with double-ended rupture of the gas duct tube in the same pebble-bed reactor. In that paper were represented a few verticals channels to simulate the path of the coolant through the top reflector as a connection between the cold plenum and the reactor core. Other studies using the coarse mesh-based system-level codes have been used for HTGR safety analysis according to [13]. Other 2D axisymmetric thermohydraulic codes were used to analyze steady state and transient behavior of the HTR-10 using the porous media approximation according to [14]. Another example was [12], where 20 inclined channels of diameter 12 centimeters were utilized, employing an equivalent area simplification.

As observed, all these studies utilized varying approximations to represent the coolant's entry pattern into the core. However, no experimental studies or simulation investigations were found that address the potential impact of the coolant entry pattern into the core of this type of reactors. This gap in the existing literature underscores the originality and significance of the present study, which aims to fill this knowledge void and provide valuable insights into the thermohydraulic behavior of the reactor core under different coolant entry scenarios.

In this sense, the goal of this paper is to identify and characterize the impact in the main thermohydraulic parameters due to the approximation used to represent the coolant entry pattern into the core of the pebble bed high temperature reactor prototypes. In this paper, the three-dimensional CFD thermohydraulic analysis of the entry pattern to the core of the HTR-10 using ANSYS CFX has been done. This study presents a comparison between different patterns of the entry of coolant into the core: two
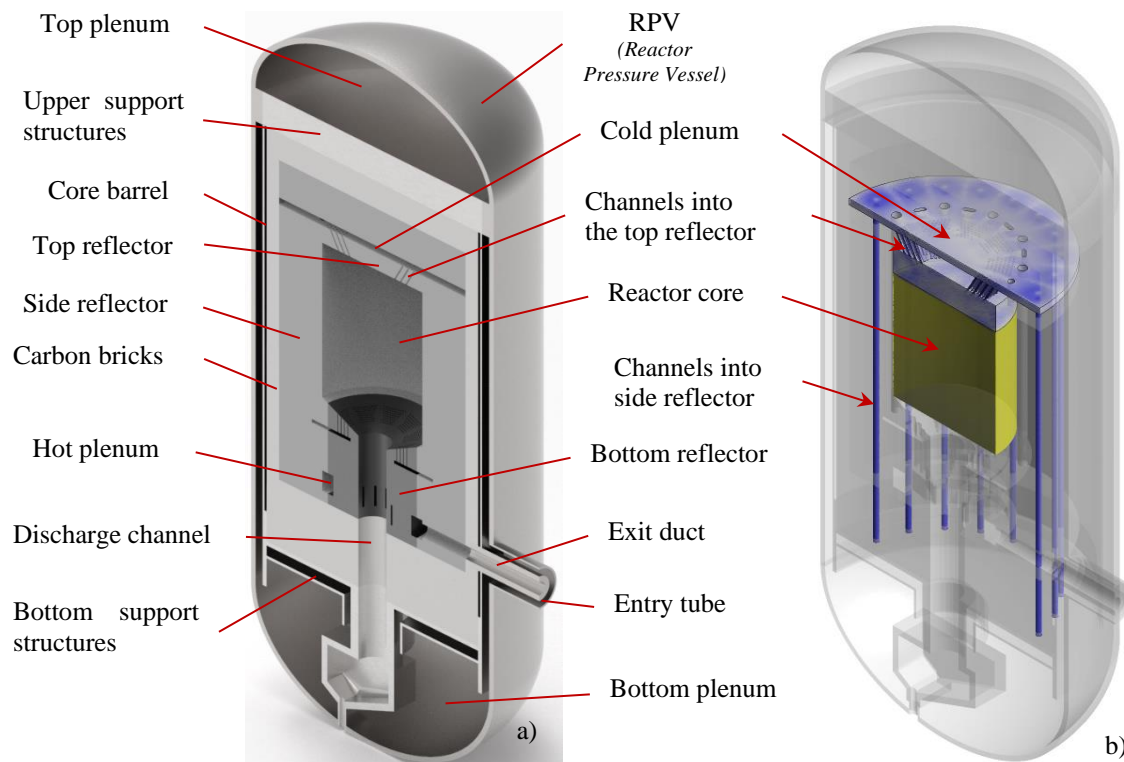
Figure 1. The main CAD geometries of the reactor structures a); blue and yellow the regions simulated in this study b).

prototype models of 460x⌀2.5cm distributed vertical and inclined channels, and two models of 20x⌀12cm of equivalent area vertical and inclined channels, also a simplified porous media model.

A thermohydraulic analysis of the coolant was conducted after examining five different representations of the coolant crossing through the top reflector. An analysis of the impact of the different ways of representing the coolant entrance to the reactor core on the temperature of the fuel elements was also carried out.

2. Methodology and Mathematical Model

To simulate the thermohydraulic characteristics of the coolant within the specified region inside the HTR-10 reactor, we used the model proposed by [12] as a reference. Geometric representation of the reactor structures was achieved using 3D CAD software such as Dassault Systèmes SOLIDWORKS and ANSYS SpaceClaim. These were used to represent the regions defined as coolant (fluid domains) and a mixture region of fuel and helium (porous domains). All of these regions were defined by the void space inside the specific structural components. The level of detail of the represented geometric models was defined based on the required precision, the scale resolved in the study and the available computational resources. The required precision in our geometric models was determined based on the specific parameters and phenomena under investigation. In particular, we considered factors such as the size of the channels in the top reflector, the variations of the coolant flow, and the thermal characteristics within the pebble-bed reactor. It's worth noting that all these geometric parameters were defined by IAEA [14], except for the distribution of the 460 channels of coolant in the top reflector. The lack of detailed description in [14] regarding the distribution of the 460 channels of coolant in the top reflector serves as a key motivation for conducting this study. In this sense, a three-

dimensional full-scale representation was created for the following regions: the vertical channels into the side reflector, the cold plenum, the prototypes pattern to represent the channels into the top reflector, the cavity before the pebble-bed in the reactor core, and the pebble-bed itself, as shown in Figure 1.

It is crucial to emphasize that this study is qualitative and aims to identify and characterize the impact of the coolant entry pattern into the reactor core on the main thermohydraulic parameters in this region. Following this premise, only the regions of coolant circulation closest to the study area were represented, focusing exclusively on studying the impact of different flow patterns at the core inlet. Therefore, thermal exchanges between the coolant and any structural element before entering the reactor core have been neglected. In all of the cases, no contact between the coolant and the structural elements will be considered, which will lead to ideal adiabatic conditions in these regions. This consideration will imply that the estimated temperatures are much more conservative than the real operating temperatures. For this, ANSYS CFX 19.0 software was employed [12], [18], [19]. Energy transport equation was used to consider the heat transfer between the fuel surface temperature and the coolant. The porous media approach was adopted to simulate the closely packed pebbles in the core.

In the present simulation, a non-uniform distribution of the packed pebble porosity was assumed to simulate wall effects. The base description of the integral 3D thermohydraulic simulation of the steady state of this reactor was proposed by [12].

2.1 Patterns of the Entry of Coolant into the Reactor Core

Figure 2 shows the coolant pattern of the simulated region inside the reactor and the patterns of coolant entry into the reactor core. Initially, two prototype models consisting of
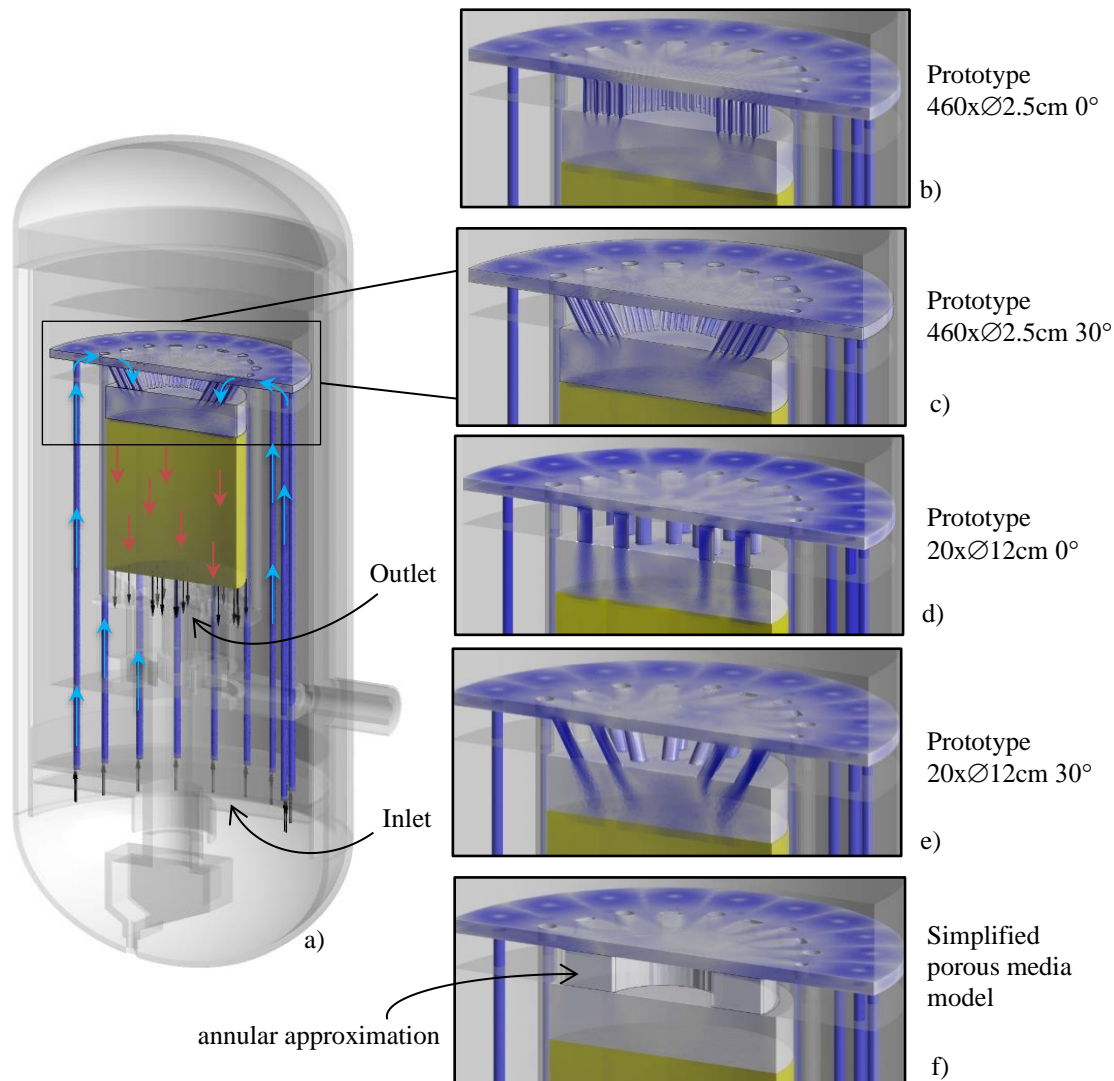
Figure 2. Schematic fluid flow of the simulated region inside the reactor a), and the coolant flow representation from the five analyzed patterns b) to f).

460 small channels, each with a diameter of 2.5cm, are distributed around the top reflector, as outlined in [15]. These channels are depicted either vertically (Figure 2 b) or at a 30-degree angle (Figure 2 c). Also, two models of 20 channels with 12cm of diameter representing the equivalent area used by [12]. Likewise, the larger channels were also represented vertically (Figure 2 d) or at a 30-degree angle, as illustrated in Figure 2 e). Finally, a simplified vertical porous media model as shown in (Figure 2 f). The five models have the same transversal equivalent area. However, their primary distinction lies in the pattern of turbulent flow generated within the top cavity of the core.

Based on these patterns, an analysis of the thermohydraulic behavior of the coolant before and after crossing the top reflector was carried out. Also, the impact of the use of these patterns in the prediction of average thermohydraulic parameters in the pebble-bed hot core zone was studied.

2.2 The Domain of Numerical Models and Boundary Conditions

The methodology employed in this article has been previously discussed in [12]. Specifically, in this paper, an equivalent mass flow rate to the helium flow under normal operating conditions of the HTR-10 reactor will be considered as the inlet condition. This flow is defined in the vertical direction in the cooling pipes of the side reflector, as shown in Figure 2. As the outlet condition, the transverse region of the reactor core just before the conical contraction has been selected, as illustrated in Figure 2.

A symmetry condition was placed on an axial plane, both in the region occupied by the entry patterns, the upper plenum, and the interior region of the reactor core, similar to what is shown in the methodology [12]. Also, the adiabatic no-slip wall option was considered for all other surfaces of the analyzed models. This last selection, will induce elevated temperature values throughout the fuel element bed region, as there will be no thermal exchange with the structural elements and reflectors through which helium flows. Nevertheless, this will illustrate the differences between the studied models without the influence of thermal exchange with these structures. This allows us to evaluate the impact of representing the coolant entry pattern into the reactor core.

2.3 Mathematical Models

In order to computationally simulate the flow of helium and the region occupied by the fuel elements, a comprehensive mathematical model was employed. This model encompasses the fundamental equations governing fluid dynamics, including the continuity equation, momentum conservation equation, and energy conservation equation. Additionally, the model incorporates the state

equation and two supplementary equations for the turbulence model. In general, ANSYS CFX uses a coupled solver, which solves the hydrodynamic equations (for u, v, w, p) as a single system. This solution approach involves a fully implicit discretization of the equations at any given time step. For steady-state problems, the time-step acts as an 'acceleration parameter', guiding the approximate solutions toward a physically based steady-state solution. This reduces the number of iterations required for convergence to steady-state or to calculate the solution for each time step in a time-dependent analysis [20].

Therefore, the simulation was executed using ANSYS's suite of codes: CFX-Pre for model setup, CFX-Solver for solving the equations, and CFD-POST for post-processing. The ANSYS CFX solver is specifically designed to calculate the unsteady Reynolds-averaged Navier-Stokes equations in their conservation form [20].

2.3.1 The Continuity Equation
The continuity equation or the mass conservation equation is shown below:

$$\frac{\partial \rho}{\partial t} + \nabla \cdot (\rho \boldsymbol{U}) = 0 \tag{1}$$

where t represents the time, ρ is the fluid density, and U is the velocity field.

The principle of momentum conservation states that the total forces exerted on a fluid element will consistently equal the change in momentum of that element. When accounting for both surface forces and forces acting within the body of an infinitesimal volume element, a simplified representation of the momentum conservation law can be formulated as follows:

$$\frac{\partial (\rho \boldsymbol{U})}{\partial t} = \nabla \cdot (\rho \boldsymbol{U} \otimes \boldsymbol{U}) = -\nabla p + \nabla \cdot \boldsymbol{\tau} + S_M \tag{2}$$

In this equation the parameter $\boldsymbol{\tau} = \mu \left[(\nabla \boldsymbol{U} + \nabla \boldsymbol{U}^T) - \frac{2}{3} \delta \nabla \cdot \boldsymbol{U} \right]$ is the stress tensor; p represents the pressure field, S_M is a source term that considers other effects [20].

2.3.2 The Thermal Energy Equation
Particularly, in fluid domains, the conservation of energy equation elucidates the mechanisms of heat transport attributed to fluid motion, conduction, and volumetric heat sources [20].

The most robust formulation for the energy equation within ANSYS CFX is the Total Energy formulation, which encompasses the total enthalpy. An alternative expression of the energy equation, which is suitable for low-speed flows from static enthalpy is the thermal energy equation:

$$\frac{\partial (\rho h)}{\partial t} + \nabla \cdot (\rho \boldsymbol{U} h) = \nabla \cdot (\lambda \nabla T) + \boldsymbol{\tau} : \nabla \boldsymbol{U} + S_E \tag{3}$$

In this formulation, the term $\boldsymbol{\tau} : \nabla \boldsymbol{U}$ represents the dissipation function representing the work done against viscous forces (viscous dissipation). Here, h denotes the enthalpy and λ represents the thermal conductivity. The terms S_E symbolize a heat source considered as a contributory factor to decay heat and fission power.

For the simulation of heat generation, a system of cylindrical and annular regions was employed, releasing heat from nuclear fission and radioactive decay. This approach, discussed previously in [12], was initially proposed by the IAEA in [14], and serves as a reference for the reactor power distribution under normal operation.

2.3.3 Equation of State
The transport equations described above must be complemented with constitutive equations of state for density and enthalpy to form a closed system. In the most general case, these states have the following form:

$$\rho = \rho(p, T) \tag{4}$$

$$dh = \frac{\partial h}{\partial T} |_p \, dT + \frac{\partial h}{\partial p} |_T \, dp = C_p dT + \frac{\partial h}{\partial p} |_T \, dp \tag{5}$$

$$C_p = C_p(p, T) \tag{6}$$

Together, all equations commented so far are solved in the CFD code simultaneously. Obtaining a detailed description at any point or region of interest.

2.4 Turbulence
One of the most important phenomena described by fluid dynamics is the phenomenon of turbulence. In this phenomenon, fluid movement is characterized by random or chaotic fluctuations in the form of swirls, vortices, etc. These fluctuations can be caused by surface imperfections and/or obstacles in the free flow of fluid and both small and large scales.

The extended Navier-Stokes equations are capable of representing both laminar and turbulent flows without requiring additional information, but this comes at the expense of high computational costs that can often be prohibitive. Furthermore, for flows with specific Reynolds numbers, a wide range of scale representations is required, some of which are significantly smaller than the finite volume mesh that can be reasonably utilized in numerical analysis. Direct Numerical Simulation (DNS) of these flows would require computational resources that are many orders of magnitude greater than those currently available. For that, turbulence models have been specifically developed to account for the effects of turbulence without recourse to a prohibitively fine mesh [20]. In general, turbulence models seek to modify the original Navier-Stokes equations, which are unstable, by introducing average and fluctuating quantities. These modifications give rise to the Reynolds Averaged Navier-Stokes (RANS) equations.

A group of turbulence models, headed by the RANS models, are widely used to represent most practical engineering problems. In this group, are used statistical turbulence models based on the Reynolds time mean equations, knowing only the effects of turbulence on the mean flow.

On the other hand, the preceding investigation [12], [14] showcased the application of the κ-ε turbulence model. In them, an outstanding correlation was established between simulating the steady state at maximum power for the HTR-10 reactor and experimental data, all achieved at a minimal computational cost. Hence, in this current study, we opt for the turbulence model grounded in the Reynolds equations

(temporal mean - RANS) with the two-equation turbulence model: standard κ-ε.

2.5 Pebble Bed Porous Media Simulation Approach

In this work, it was considered a porous media in the approximate region of the reactor core occupied by fuel pebbles which are cooled by the helium flow. In this region was used the Full Porous formulation that solve a finite temperature difference between the fluid phase and the solid phase. Full Porous is a non-thermal equilibrium model when the separate energy equations for each phase within the domain are computed and the temperature field is assumed as average temperatures.

All heat transfer effects between fuel elements and helium within the pebble bed were considered. This was accomplished through the implementation of the overall heat transfer coefficient in the reactor core region [12]. The coefficient used was proposed by the KTA after thorough experimental studies, considering conduction, convection, and thermal radiation [21]. The approach to representing the heat transfer within the reactor core using the porous media was analyzed in more detail in [12]. This detailed analysis supports the robustness and validity of the chosen methodology in capturing the essential aspects of heat transfer phenomena in the reactor core.

In [12], are discussed in detail the selection of the mathematical model to estimate the temperature in the center of the fuel elements, the isotropic porous media pressure losses, thermal and materials properties correlations, and others modeling related topics. The variation with pressure and temperature of helium properties, such as thermal conductivity, dynamic viscosity, and density, were implemented according to [22].

On the other hand, the reactor core is designed for a thermal power of 10 MW, with a gas pressure and mass flow in the primary circuit of 3.0 MPa and 4.32 kg/s, respectively in normal operation. It has a gas outlet temperature of 700 °C and a gas inlet temperature of 250 °C [23]. However, it is known that part of the helium coolant bypasses the main flow path (leaks) due to clearances among structural elements and graphite blocks. Conservatively, it is assumed that this bypassing part of the helium flows directly from cold helium entry to hot helium exit, making it non-effective for core cooling. The following flow rates and leakages are considered:

- The Rated Coolant Flow Rate (RCFR) is 4.32 kg/s.
- 1% of the RCFR passes through the fuel discharging tube to cool fuel elements in the tube.
- 2% of the RCFR flows through the control rod channels to cool the control rods.
- The maximum bypassing leakage among bottom graphite blocks is assumed to be 10% of RCFR.

Therefore, 87% of the RCFR flows through the pebble bed zone, effectively cooling fuel elements in the core. These approximations were widely used in [14] and more recently in [12].

2.6 Pressure Drop Through the Top Reflector Considering a Simplified Porous Media Model

As previously stated, in addition to the reactor core, the patterns of the entry of coolant into the reactor core were also represented using a vertical porous media simplification. As shown in Figure 2 f). For that, the simplified vertical porous media model represents the joint region between the cold helium plenum and the top cavity of the core region. In this approximation, was considered that the 460x$\varnothing$2.5cm straight coolant channels as the vertical direction inside the top reflector bricks as a simple annular region of 160cmx78cmx25cm. Was imposed in this annular region a bulk porosity equivalent to the relation between the volume occupied by the 460x$\varnothing$2.5cm channels and the volume of an annular region as shown in Figure 2. Also, it was considered the permeability and inertial resistance factor in the vertical direction (streamwise direction) only. The resistance in the transverse direction was be assumed substantially highest to prevent unphysical horizontal cross flow. This effect was implemented using the Directional Loss Model, allowed in Ansys CFX [18]. For this, the resistance along the flow direction from Darcy-Weisbach model was used.

To estimate the Reynold number that characterize the movement of coolant through the 460x$\varnothing$2.5cm channels ($Re_{2.5cm}$) was used the following consideration:

- Only the 87% of the reactor mass flow rate cross the top reflector through the 460 channels of $\varnothing$2.5cm to the reactor core as was indicated in the section 2.5 and used in [14].
- The same distribution of the mass flow rate crossing all the channels.
- The coolant crosses the channels to 250 °C, then

$$Re_{2.5cm} = \frac{\dot{m}_{2.5cm} * d_{2.5cm}}{A_{2.5cm} * \mu} = 14\ 152 \tag{7}$$

Where:
$\dot{m}_{2.5cm}$: mass flow rate crossing an individual channel.
$\dot{m}_{2.5cm} \approx 8.17E - 03\ [kg\ s^{-1}]$
$d_{2.5cm}$: diameter of a channel, $\varnothing$2,5cm.
$A_{2.5cm}$: Cross section area of a channel.
μ: Dynamic viscosity of the coolant corresponding to 250 °C.

For the solution of the corresponding pressure loss due to coolant through the top reflector for the simplified vertical porous media model, was used the universal formula proposed by Darcy-Weisbach [24]. The Eq. (8) describes the pressure loss, denoted as ΔP, resulting from inertial effects in a cylindrical pipe with a uniform diameter.

$$\frac{\Delta P}{L} = f \frac{\rho}{2} \frac{\bar{V}^2}{D} \tag{8}$$

In this work, L was considered as the length of the coolant path inside the top reflector, D the hydraulic diameter, $\bar{V}$ the mean flow velocity and f the dimensionless Darcy friction factor, Eq. (9).

Considering that, in the HTR-10 at normal operations, the Reynolds number of the helium flow in the coolant channels is above 10 000 then the viscous effects can be neglected. In this Reynolds number range for the turbulent flow, the estimative of the Darcy friction factor f was calculated from the Colebrook–White correlation [24]:

$$\frac{1}{\sqrt{f}} = -2 * \log\left(\frac{\frac{e}{d_{2.5cm}}}{3.7} + \left(1 + \frac{2.51}{Re\sqrt{f}}\right)\right) \tag{9}$$

where e is roughness, and $Re>4000$.

2.7 Mesh Independence Study

A combination of tetrahedral and hexahedral elements in the flow domain and prism elements close to walls was used. The mesh generating software ANSYS Meshing was chosen to generate the meshes. In all of cases were ensure a y+ < 50 considering the $\kappa-\varepsilon$ turbulent model and scalable wall function. Also, in areas where local details were needed, the local mesh refinement was used to capture fine geometrical details. Additionally, it was checked that parameters like orthogonal quality, expansion factor and aspect ratio are within the recommended values [18]. A good mesh quality is essential for performing a good CFD analysis but it's not enough [18]. A preliminary analysis of the results is required to reach a mesh-independent solution and eliminate the false information induced by numerical reasons, e.g., computational geometry (mesh size – number of elements, etc.) and numerical scheme applied [25]. In this sense, a mesh sensitivity study was performed to analyze the suitability of the mesh.

In all prototypes, four different meshes (design points) with increasing mesh densities were analyzed. For this mesh sensitivity study, it is necessary to select the key parameters to be analyzed. Since the aim of this paper is to identify and characterize the impact on the main thermohydraulic parameters due to the approximation used to represent the coolant entry pattern into the core of the pebble bed high-temperature reactor prototypes, the mesh sensitivity study analyzed the average and maximum coolant temperature, as well as the average velocity inside the hot core zone.
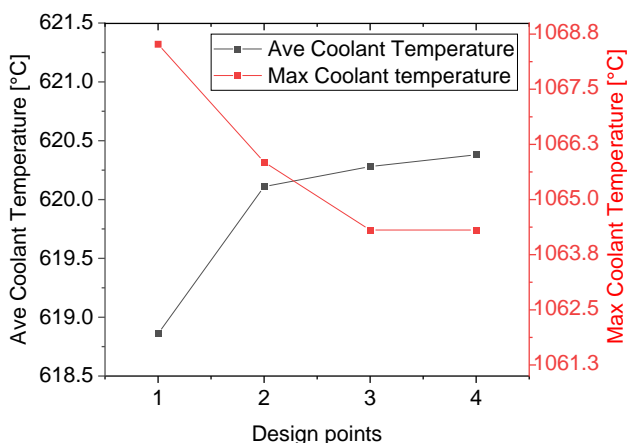
Figure 3. Coolant temperature inside the hot core zone for different meshes from Prototype 20x⌀12cm 30°

Also, the Grid Convergence Index (GCI) value, proposed by Roache in 1998 [26], was considered, which corresponds to the numerical uncertainty. In this case, the minimum numerical error considered was less than 1%. The Figure 3 and Figure 4 show the control parameters from four meshes with 0.6, 1.5, 4.3, and 7.6 million elements respectively.
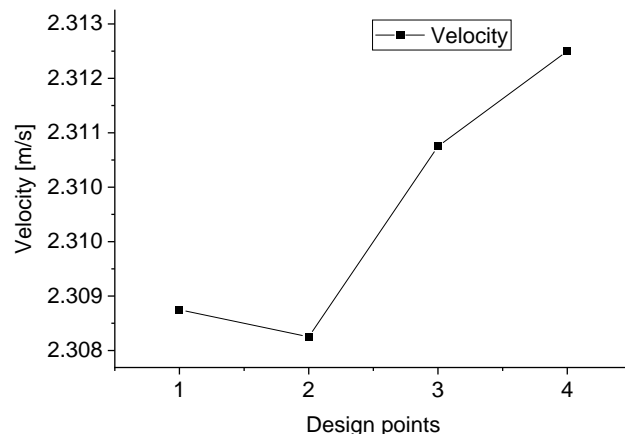
Figure 4. Velocity inside the hot core zone for different meshes from Prototype 20x⌀12cm 30°.

Figure 4 shows the average velocity values for the four different meshes for the Prototype 20x⌀12cm 30°. The four design points have a relative difference of less than 1% in all analyzed parameters for this entry pattern. These results show that there are no significant differences between them among the studied meshes. The same behavior was observed in the other prototypes.

As it is known that, the meshes with the least number of elements are the meshes that have the least computational requirements, then the meshes with the least number of elements were selected for the studies to be carried out. The Table 1 shows the properties and quality of the selected meshes. Is important to note that the analyzed prototypes of 20x⌀12cm have a similar mesh quantity to the simplified porous media model with around 1 million elements.

2.8 Computational Resources and Convergence

The time needed to converge a complex CFD analysis is more complicated than only considering the number of cores available and the mesh size. Other aspects of the hardware, such as memory, storage and interconnect speed will also make a difference, as will the specific choice of code and the temporal and spatial characteristics of the phenomena within the solution. All calculations were performed considering an RMS residual of 1E-05, which is typically sufficient for the majority of engineering applications. The Table 2 summarizes the computational resources needed for the solution of the five models.

Table 1. Properties of the selected meshes.

Selected Design Point	Prototype 460x⌀2.5cm 0°	Prototype 460x⌀2.5cm 30°	Prototype 20x⌀12cm 0°	Prototype 20x⌀12cm 30°	Simplified porous media model
Nodes 10^6	1.88	2.65	0.35	0.38	0.59
Elements 10^6	5.10	5.54	0.63	0.62	1.06
Aspect Ratio	53.00	54.00	40.00	15.00	82.00
Orth. Quality	32.60	32.50	27.40	32.70	31.60
Expansion Fact.	247.00	52.00	239.00	189.00	87.00

Model	Core	Memory [MBytes]	CPU time [s]	Iteration
Prototype 460x⌀2.5cm 0°	32	10149.29	1.339E+04	294
Prototype 460x⌀2.5cm 30°	32	9289.69	2.825E+04	600
Prototype 20x⌀12cm 0°	16	3273.12	9.257E+03	337
Prototype 20x⌀12cm 30°	16	3326.18	1.972E+03	448
Simplified porous media model	16	4043.77	6.912E+03	233

3. Results and Discussion

The ensuing section, delves into a qualitative examination aimed at identifying and characterizing the impact that the coolant entry pattern into the reactor core, on key thermohydraulic parameters within the reactor core. Specifically, our focus will be on comprehensively discussing the behavior of coolant velocity, pressure drops, and the temperatures of both the coolant and the fuel elements.

3.1 Velocity Discussion

The first thermohydraulic parameter to analyze is the coolant velocity. Following Figure 5, the depiction of the helium velocity profile before and after crossing the top reflector region is shown.

The colorimetric scale of Figure 5 a) was set from 0 to 10 m/s with the aim of highlighting, with greater contrast, the different flow regions, especially the coolant entry region into the reactor core. However, the maximum velocity reached at the top of the coolant channels was approximately 17 m/s in the five analyzed cases. As shown in Figure 5 a), the coolant rises through the ducts inside the reflectors and carbon bricks up to the cold plenum. Then, the coolant crosses the top reflector on its way up to the top core cavity using one of the five proposed models.

Figure 5 b) to f) show the flow distribution at this crossing for the five analyzed cases. In the prototype models with channels of 460x⌀2.5cm, the formation of small jets of coolant is observed. Those jets penetrate a small portion of the upper cavity of the core. The development of these small jets of coolant does not reach the bed of fuel elements, they diffuse before reaching the pebble-bed. On the other hand,
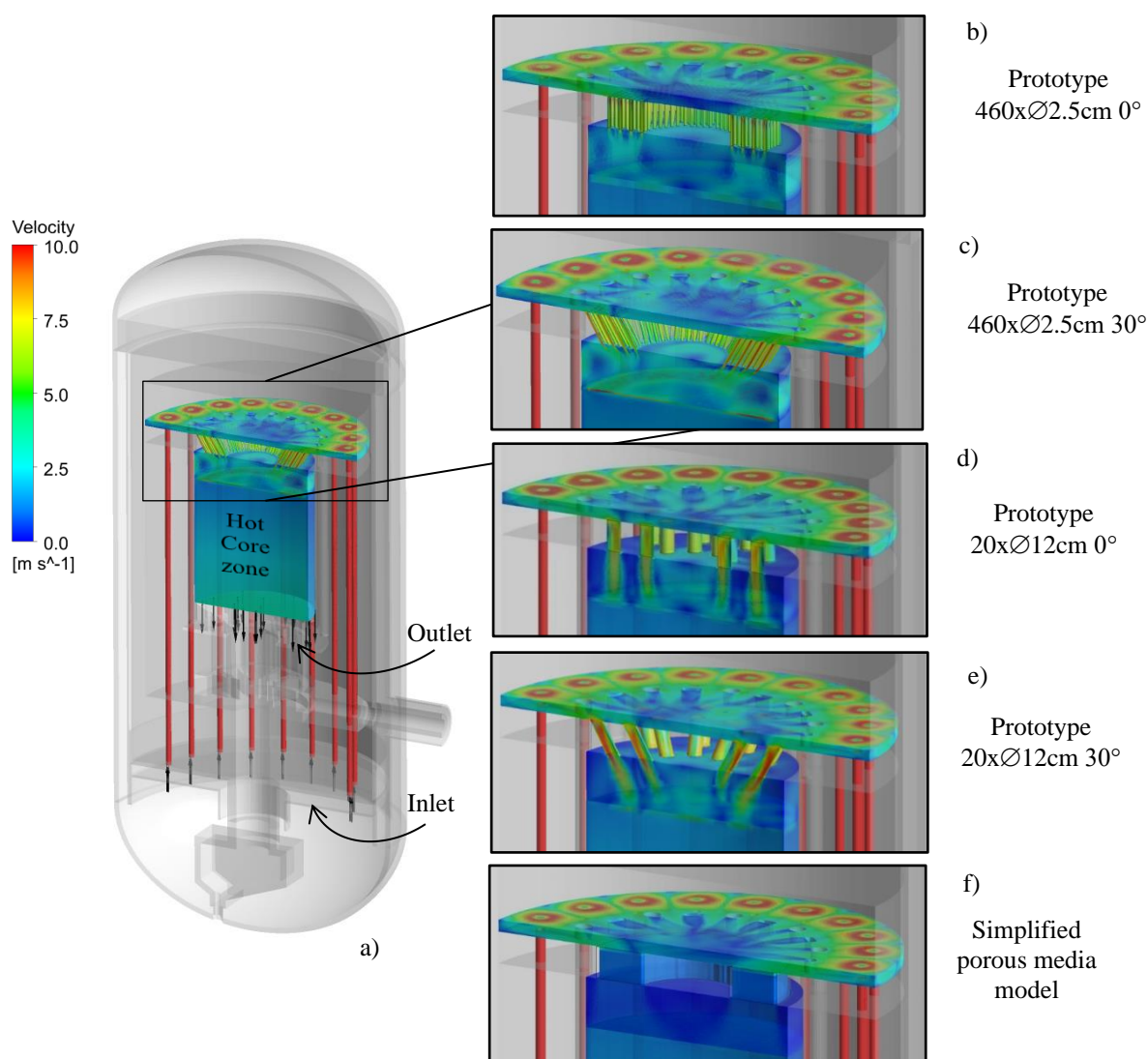

Figure 5. Modeled Coolant region inside the HTR-10 a), and the 3D volumetric representation of the velocity distribution profiles for the five computational models b) to f).

the jets of coolant in the prototypes of 20x⌀12cm develop as they pass through the core cavity, indicating a lower impact of the diffusive effects. In the simplified porous media model, the formation of jets is not observed.
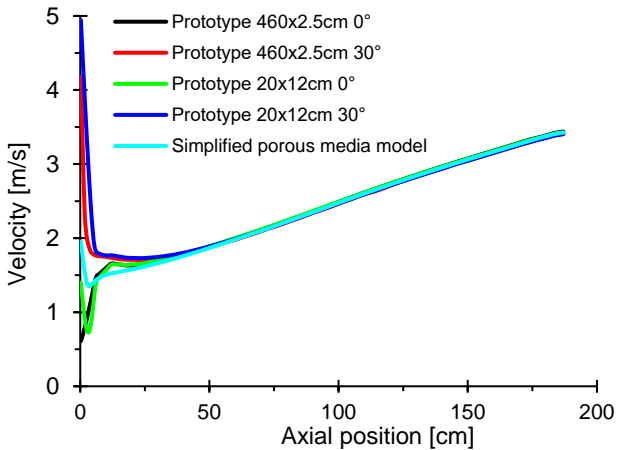

Figure 6. Velocity profiles at the center line of the reactor core.

After the coolant crosses the top cavity, the five schemes show a similar tendency. As expected, the coolant increases its speed as it passes through the core of fuel elements. Figure 6 display a linear increase in velocity from 1.78m/s at the beginning to 3.42m/s at the end of the pebble bed. This effect is due to the fact that when it crosses the fuel elements, the coolant is heated and its viscosity decreases. It is known that this reactor can increase its temperature by up to 3 times (250 °C - 950 °C) in normal operation.

Figure 7 shows using a colorimetric scale ranging from blue to white, the velocity profile at different distances of penetration of the coolant in the reactor core (0cm, 80cm and 170cm), for the five computational models studied. It is shown that at the beginning of the fuel elements (position, 0 cm) the coolant arrives with different patterns in each case. However, this difference disappears when entering the pebble bed (positions 80cm and 170cm). On the other hand, if the velocity profiles are represented in the radial positions at different depths, as shown in Figure 8, it is possible to notice that at 80cm and 170cm penetration the 5 models present practically the same prediction.

Performing a detailed analysis of the radial velocity distribution, it can be concluded that, for 50cm of penetration of the coolant in the fuel element bed, there is still a difference between the models (see Figure 7). This relative difference concerning to the average of the five computational models is small and can reach up to 6% at 50cm.

In summary, even though the analyzed models have different coolant distribution patterns at the beginning of the pebble of the fuel elements, these differences have a small impact on the prediction of the fluid movement inside the pebble. The estimated mean velocity coolant inside the pebble bed core was approximately 2.30 m/s, as shown in Figure 8 and Figure 9.

These results contribute valuable insights into the dynamic behavior of the coolant, aiding in the evaluation and enhancement of the reactor's design for optimal thermohydraulic efficiency.
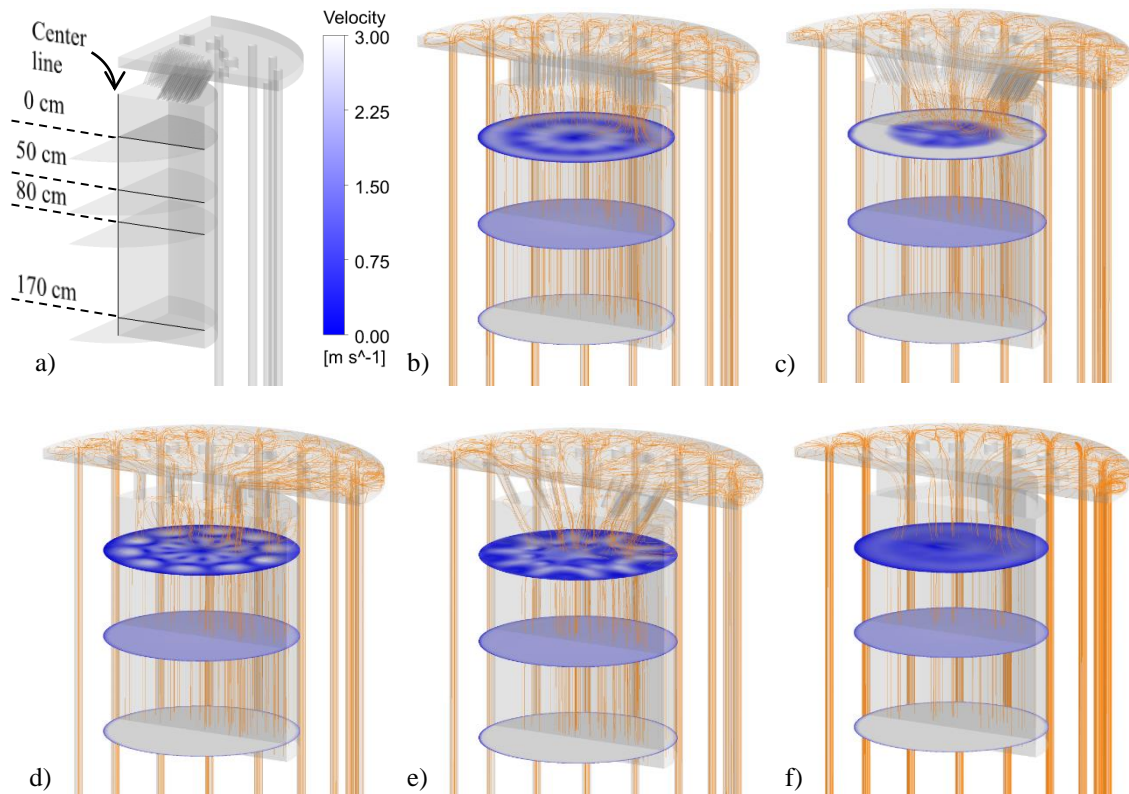

Figure 7. Velocity profiles at different penetration distances of the coolant in the reactor core: a) position lines, b) Prototype 460x⌀2.5cm 0°, c) Prototype 460x⌀2.5cm 30°, d) Prototype 20x⌀12cm 0°, e) Prototype 20x⌀12cm 30°, f) Simplified porous media model.
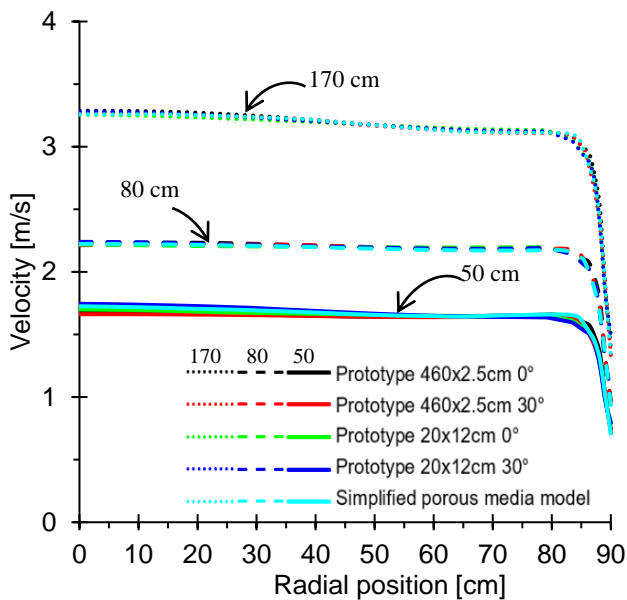
Figure 8. Radial velocity at three different heights, 50cm, 80cm and 170cm from the beginning of the pebble fuel elements.
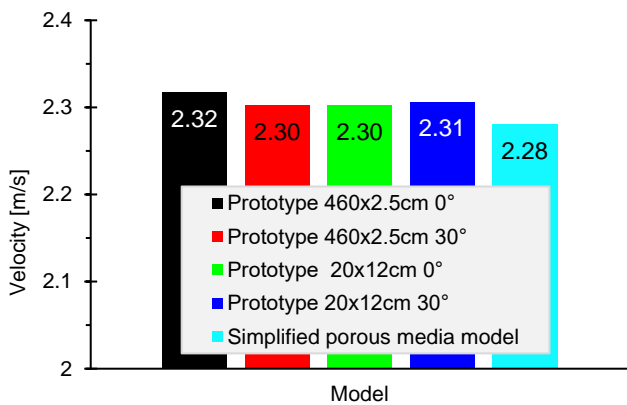

Figure 9. Average velocity in the Hot Core Zone.

3.2 Coolant and Fuel Elements Temperatures

The second thermohydraulic parameter to analyze was the coolant and fuel temperature. It is known that the highest temperatures are reached inside the fuel elements, which is where the heat by nuclear fission and radioactive decay is generated. After the heat is generated by nuclear fission inside the fuel elements, it heat is conducted to the external fuel surface. In general, for the extraction of this heat, the coolant and the structural elements act by convection, conduction, and radiation actively. Once the coolant is heated, this heat is conducted towards the steam generator. According to [12], [14], it is estimated that the highest temperatures in this reactor are found in the lower central region of the core. Therefore, with the interest of studying the behavior of the maximum temperatures in the coolant inside the reactor, the temperature in the center line will be analyzed.

Figure 10 shows the coolant temperature in the centerline of the hot core zone. From this figure, it can be identified that the five computational models present the same increasing trend of the fuel elements temperature. The heating occurs from a value close to the coolant at the inlet of the pebble bed until reaching the maximum temperature in the lower central

region of the core as seen in Figure 9. Also, it can be appreciated in Figure 9, that after reaching a depth of 180cm, the temperature of the coolant stops increasing. This is due to the used model of heat generation, having a drastic decrease in the power density for the last 7cm of the approximate active core, according to [14]. In this way, the last 7cm of the curves coincide with the region where the temperature stops increasing.

The highest temperature was obtained from the model of the Prototype 460x2.5cm 0°, which is the most conservative pattern from the point of view of safety. On the other hand, the model with the Prototype 20x12cm 30°, presents the least conservative tendency to estimate the highest temperature.
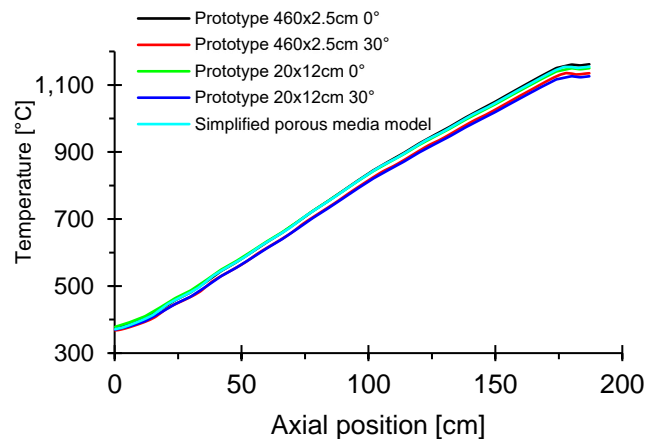

Figure 10. Coolant temperature in the centerline of the hot core zone.

The largest maximum relative difference between these two models was 35.7 °C, which represents approximately 3%. In summary, no significant differences were found in the estimated mean and maximum temperatures among the five computational models analyzed. It is important to note that this analysis is only qualitative since the objective of the article is to identify and characterize the impact of the coolant entry pattern into the reactor core on the main thermohydraulic parameters. For this reason, and with the aim of reducing the computational cost, adiabatic boundary conditions were considered in all surfaces as was indicated in the section 2.2. Thereby, estimated temperatures in all computational models were higher than those predicted by [12], [14]. In general, the values of the maximum temperatures in the normal operation in this reactor are lower. According to the [14] the fuel elements temperature must never exceed 1200 °C, which is the design limit temperature for the fuel elements.

In summary, the average and maximum estimated temperatures by the five models are shown in Table 3. From the analysis of the values shown in Table 3, it is concluded that the five models estimate the average values without significant differences. In the case of the maximum values, the Prototype of 460x2.5cm 0° estimates the highest values, both for the temperature of the coolant and the temperature on the surface of the fuel elements. The lowest maximum coolant temperature among the five models was obtained by the Prototype of 460x2.5cm 30° and the lowest fuel element surface temperature was obtained by the Prototype of 20x12cm 30°. The relative differences with respect to the mean value of the five models are less than 2%.

| Model | Temperature [C] | | | | | | | |
| | Coolant in the core zone | | | | Fuel elements Surface | | | |
	Ave.	Max.	Mean	Dif.	Ave.	Max.	Mean	Dif.
Prototype 460x∅2.5cm 0°	618.05	1104.75		0.9%	724.24	1161.70		1.4%
Prototype 460x∅2.5cm 30°	617.94	1080.38		1.3%	723.98	1135.50		0.9%
Prototype 20x∅12cm 0°	618.44	1092.85	1095	0.2%	724.55	1149.95	1145	0.4%
Prototype 20x∅12cm 30°	619.26	1098.45		0.3%	725.29	1125.99		1.7%
Simplified porous media model	618.04	1099.75		0.3%	724.24	1155.88		0.9%

3.3 Pressure Drop

The last thermodynamic parameter to analyze is the pressure in the five computational models. In general, the steady-state simulation was performed at the nominal pressure of 3MPa as indicated [14]. This pressure is less than the safety limit (3.3MPa) approved by the China National Nuclear Safety Authority (NNSA) as operation limit to ensure the system and components safety [27].

The estimated pressure drop in the pebble bed was in agreement with the equations model discussed in [12]. In all the cases, the coolant pressure drops slightly till reaching the top helium plenum, then continues decreasing along the path inside the top reflector. Subsequently, a more pronounced pressure drop was observed as the coolant passed through the pebble bed. Similar behavior was reported in [12].
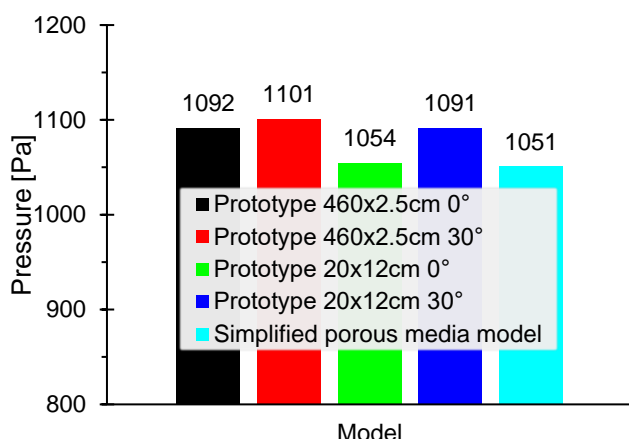

Figure 11. Total pressure drop in the five computational models.

The total pressure drop in the five computational models was shown in Figure 11. The five computational models show a similar total pressure drop, of approximately 1078 Pa.

Figure 12 shows the behavior of the pressure drop along the axial axis in the reactor core center line. As observed, the pressure remains approximately constant above 600 Pa in the region before the pebble bed entry. After the coolant enters the pebble bed, the pressure drops across the pebbles until the cone region. As observed for the temperature behavior, the entry pattern only has a small impact at the beginning of the pebble-bed modeling. In the first 25 cm of the top of the pebble-bed, this difference reaches less than 1% of the mean value between them.

4. Conclusions

This paper is part of the ongoing efforts to contribute to the prediction of the thermohydraulic behavior of one of the most promising Generation IV systems, the Very High
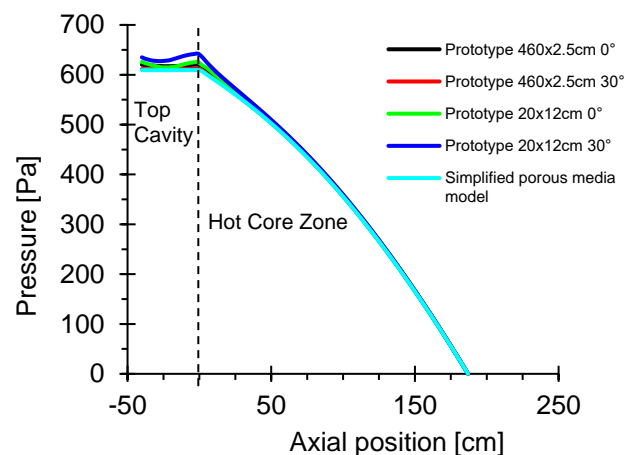

Figure 12. Pressure drop in the reactor core centerline.

Temperature gas-cooled Reactor, using three-dimensional modeling. For this purpose, this paper addresses one of the great challenges of nuclear thermohydraulic, which is the detailed full-scale modeling of complex structures. In this study, a comparison between five alternatives to represent the top reflector internal structures in a high temperature pebble bed SMR was developed. The primary objective of this study was to identify and characterize the influence of the coolant entry pattern into the reactor core on key thermohydraulic parameters. 460x2.5cm

From the analysis of the velocity profiles, it was found that the five models provoke different patterns of coolant distribution in the upper cavity of the reactor core. It was observed that the coolant entry patterns generated from the 460x2.5cm prototypes spread small jets and then diffuse quickly without penetrating the fuel element bed. On the other hand, the 20x12cm prototypes generate jets that reach the vicinity of the fuel element bed. The main difference was found in the distribution of coolant at the beginning of the bed of fuel elements, which quickly disappears. This difference between the 5 models is less than 6% in the first 10 cm of penetration in the pebble bed. The five inlet patterns maintain the same coolant distribution throughout virtually the entire fuel element bed. The temperature analysis revealed that all five models exhibit a consistent rate of temperature increase as they pass through the fuel elements. The greatest difference was evidenced between the model corresponding to the prototype 460x2.5cm 0° and 20x12cm 30°, being only 35.7 °C. The model that presents the highest values, therefore more conservative, is the prototype model of 460x2.5cm 30°. On the other hand, the lowest temperatures were obtained at 20x12cm 30°. The relative differences to the mean value of the five models are less than 2%. All five computational models exhibit a comparable total pressure drop, averaging around 1078 Pa. As observed for the temperature behavior, the entry pattern only has a small impact at the beginning of the pebble-bed modeling.

In the first 25cm of the top of the pebble-bed, this difference reaches less than 1% of the mean value between them.

Explicitly, it was demonstrated that even though the analyzed models exhibit distinct coolant distribution patterns at the initial stage of the pebble bed of fuel elements, these variations have a minimal impact on predicting the global temperatures and fluid movement inside the pebble. This distinct lack of differences in the overall results of the main parameters of interest, regardless of the entry pattern model used, might justify why, despite the reactor operators not sharing specific details about the top reflector internal structure, researchers have conducted successful simulation of the HTR-10 reactor over the years.

This conclusion is reinforced as even the porous media model shows a strong correlation with the prototype models concerning the maximum fuel temperature, average fuel temperature, and helium velocity. The prediction of the pressure drop from the Darcy-Weisbach approach is an acceptable prediction as well. In this study, the potential applicability of the porous media models for an integral full-scale reactor simulation in the future was demonstrated. As a benefit, the porous media model as well the simplified models reduces the mesh quantity from a detailed prototypic model. Correspondingly, the computation time was reduced.

Nomenclature

SMR	Small Modular Reactors
AVR	German: Arbeitsgemeinschaft Versuchsreaktor
CAD	Computer Aided Design
CFD	Computational Fluid Dynamics
DNS	Direct Numerical Simulation
GIF	Generation IV International Forum
HTGR	High-Temperature Gas-Cooled Reactors
HTR	High Temperature Reactor
HTTR	High-Temperature Test Reactor
IAEA	International Atomic Energy Agency
KTA	German: Kerntechnischer Ausschuss
LOCA	Loss-of-Coolant Accident
NNSA	China National Nuclear Safety Authority
RANS	Reynolds Averaged Navier-Stokes
RCFR	Rated Coolant Flow Rate
RPV	Reactor Pressure Vessel
RSM	Root Mean Square
THTR	Thorium High-Temperature Reactor
VHTR	Very-High-Temperature Reactor
ρ	density $[kg/m^3]$
τ	stress tensor $[Pa]$
t	time $[s]$
λ	thermal conductivity $[W/mK]$
μ	dynamic viscosity $[Pa\ s]$
U	velocity $[m/s]$
p	pressure $[Pa]$
S_M	momentum source $[kg\ m/s]$
h	enthalpy $[J]$
T	temperature $[K]$
S_E	heat source $[W]$
C_p	specific heat capacity at constant pressure $[J/kg\ K]$
L	length of the coolant path inside the top reflector $[m]$
f	Darcy friction factor
$\bar{V}$	mean flow velocity
D	hydraulic diameter $[m]$
e	roughness
Re	Reynolds Number
$\dot{m}_{2.5cm}$	mass flow rate crossing an individual channel $[kg/s]$
$d_{2.5cm}$	diameter of a channel $[m]$
$A_{2.5cm}$	cross section area of a channel $[m^2]$

References:

[1] OECD/NEA, "Advanced Nuclear Reactor Systems and Future Energy Market Needs," 2021.

[2] IEA, "World Energy Outlook 2021," Paris, 2021.

[3] OECD/NEA, "Generation IV International Forum, Technology Roadmap Update for Generation IV Nuclear Energy Systems," Paris, 2014.

[4] IAEA, "Guidance on Nuclear Energy Cogeneration," Vienna, 2019.

[5] GIF, "GIF R&D Outlook for Generation IV Nuclear Energy Systems: 2018 Update," 2018.

[6] B. Zohuri, "Generation IV nuclear reactors," in *Nuclear Reactor Technology Development and Utilization*, A. N. Salah Ud-Din Khan, Ed., Elsevier, 2020, pp. 213–246. doi: 10.1016/B978-0-12-818483-7.00006-8.

[7] IAEA, "Nuclear Power Reactors in the World," 2021.

[8] GIF, "Generation IV International Forum 2020 Annual Report," 2020.

[9] GIF/RSWG, "Basis for the Safety Approach for Design & Assessment of Generation IV Nuclear Systems," Vienna, 2021.

[10] D. E. Shropshire, A. Foss, and E. Kurt, "Advanced Nuclear Technology Cost Reduction Strategies and Systematic Economic Review," 2021.

[11] Y. A. Hassan and H. Students, "Theoretical Foundations and Applications of Computational Fluid Dynamics in Nuclear Engineering," Trieste, 2022.

[12] A. Gámez Rodríguez, L. Y. Rojas Mazaira, C. R. García Hernández, D. Dominguez Sanchez, and C. A. Brayner Oliveira Lira, "An integral 3D full-scale steady-state thermohydraulic calculation of the high temperature pebble bed gas-cooled reactor HTR-10," *Nucl. Eng. Des.*, vol. 373, no. December 2020, 2021, doi: 10.1016/j.nucengdes.2020.111011.

[13] C. Wang, Y. Liu, X. Sun, and P. Sabharwall, "A hybrid porous model for full reactor core scale CFD investigation of a prismatic HTGR," *Ann. Nucl. Energy*, vol. 151, p. 107916, 2021, doi: 10.1016/j.anucene.2020.107916.

[14] IAEA, "Evaluation of High Temperature Gas Cooled Reactor Performance: Benchmark Analysis Related to the PBMR-400, PBMM, GT-MHR, HTR-10 and the ASTRA Critical Facility," IAEA, Vienna, 2013.

[15] Z. Zhang, J. Liu, S. He, Z. Zhang, and S. Yu, "Structural design of ceramic internals of HTR-10," *Nucl. Eng. Des.*, vol. 218, no. 1–3, pp. 123–136, 2002, doi: 10.1016/S0029-5493(02)00205-4.

[16] Y. M. Ferng and C. T. Chen, "CFD investigating

thermal-hydraulic characteristics and hydrogen generation from graphite-water reaction after SG tube rupture in HTR-10 reactor," *Appl. Therm. Eng.*, vol. 31, no. 14–15, pp. 2430–2438, 2011, doi: 10.1016/j.applthermaleng.2011.04.007.

[17] Y. M. Ferng and C. W. Chi, "CFD investigating the air ingress accident for a HTGR simulation of graphite corrosion oxidation," *Nucl. Eng. Des.*, vol. 248, pp. 55–65, 2012, doi: 10.1016/j.nucengdes.2012.03.041.

[18] I. ANSYS, *ANSYS CFX Solver Modeling Guide*, 19.0. Canonsburg, PA, 2018.

[19] D. Milian Pérez, A. Gámez Rodríguez, L. Hernández Pardo, M. L. Daniel Evelio, and B. de O. L. Carlos Albrto, "Implementation of a Multi-cell Approach in the Multi-Physics Calculations of an Aqueous Homogeneous Reactor," *Int. J. Thermodyn.*, vol. 24, no. 4, pp. 125–133, 2021, doi: 10.5541/ijot.895287.

[20] I. ANSYS, *ANSYS CFX-Solver Theory Guide*, 19.0. Canonsburg, PA, 2018.

[21] KTA, "Reactor Core Design of High-Temperature Gas-Cooled Reactors Part 2: Heat Transfer in Spherical Fuel Elements," KTA, 1983.

[22] KTA, "Reactor Core Design for High-Temperature Gas-Cooled Reactor Part 1: Calculation of the Material Properties of Helium," KTA, 1978.

[23] Z. Gao and L. Shi, "Thermal hydraulic calculation of the HTR-10 for the initial and equilibrium core," *Nucl. Eng. Des.*, vol. 218, no. 1–3, pp. 51–64, 2002, doi: 10.1016/S0029-5493(02)00198-X.

[24] J. C. L. Pritchard, J. Philip, *Introduction to Fluid Mechanics*, 8th ed. John Wiley & Sons, Inc, 2011.

[25] H. Wang and Z. J. Zhai, "Analyzing grid independency and numerical viscosity of computational fluid dynamics for indoor environment applications," *Build. Environ.*, vol. 52, pp. 107–118, 2012, doi: 10.1016/j.buildenv.2011.12.019.

[26] P. J. Roache, *Verification and validation in computational science and engineering*. Albuquerque, N.M: Hermosa Publishers, 1998.

[27] S. Hu, R. Wang, and Z. Gao, "Safety demonstration tests on HTR-10," *2nd Int. Top. Meet. High Temp. React. Technol.*, pp. 22–24, 2004.